Investigations of Nanomaterials and Porous Materials

A thesis submitted in partial fulfillment
of the requirements of the degree of

Doctor of Philosophy

By

Gautam Gundiah

Chemistry and Physics of Materials Unit

Jawaharlal Nehru Centre for Advanced Scientific Research
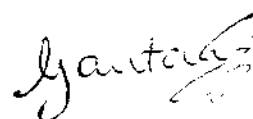
(Deemed University)

Bangalore – 560 064 (INDIA)

To Amma and Appa

Declaration

I hereby declare that this thesis entitled **"Investigations of Nanomaterials and Porous Materials"** is an authentic record of research work carried out by me under the supervision of Prof. C. N. R. Rao, FRS, at the Chemistry and Physics of Materials Unit, Jawaharlal Nehru Centre for Advanced Scientific Research, Bangalore, India.
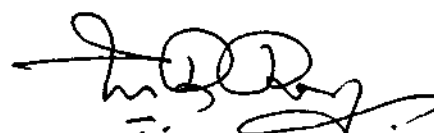
In keeping with the general practice of reporting scientific observations, due acknowledgement has been made whenever work described here has been based on the findings of other investigators. Any oversight due to error of judgement is regretted.

Gautam Gundiah

Certificate

Certified that the work described in this thesis titled **"Investigations of Nanomaterials and Porous Materials"** has been carried out under my supervision at the Chemistry and Physics of Materials Unit, Jawaharlal Nehru Centre for Advanced Scientific Research, Bangalore, India.

Prof. C. N. R. Rao

iii

Acknowledgements

It is indeed a great pleasure to express my respect and sincere gratitude to Prof. C. N. R. Rao, FRS, for suggesting the problems and his immense support and guidance during the course of this research work. The best advisor and teacher I could have wished for, he is actively involved in the work of all his students, and clearly always has their best interest in mind. I am grateful to him for giving me the opportunity to work on several different areas of research. I thank him for his keen interest in my personal welfare during difficult times.

It has been a pleasure working with Dr. A. Govindaraj in the Carbon Lab. His enthusiasm and hard-working nature deserve a special mention and it has been a tremendous learning experience for me.

I am extremely grateful to Prof. G. U. Kulkarni for introducing me to scanning probe microscopy. I cannot thank him enough for being patient and understanding whenever I approached him with any doubts or queries. The discussions that we have had have benefited me immensely.

I thank Dr. Neeraj, Dr. M. Eswaramoorthy, Deepak, Madhav, Motin, Neena, Ujjal, Dr. John Thomas, Mrs. Usha (JNCASR, Bangalore), Dr. S. Heun (Trieste, Italy), Dr. N. Rajalakshmi, K. S. Dhathathreyan (SPIC, Chennai), Samrat and Prof. U. Maitra (IISc) for the fruitful collaborations. The help rendered by. Dr. S. Natarajan during the initial stages of my research with aluminosilicates is kindly acknowledged.

I am thankful to the faculty members of JNCASR- Prof. G. U. Kulkarni, Prof. S. Natarajan, Prof. K. S. Narayan, Dr. N. Chandrabhas, Dr. S. Balasubramanian, Dr. A. R. Raju, Dr. S. Narasimhan, Dr. U. V. Waghmare, Dr. S. Pati and Dr. S. Sastry for their informative courses and discussions on several occasions. My teachers at IISc (Prof. U. Maitra, Prof. J. Chandrasekhar, Prof. S. Ramasesha, Prof. T. N. Gururow, Prof. V. Krishnan) are gratefully acknowledged for the excellent courses.

I have been fortunate to have had excellent labmates in all the labs that I have

Preface

The study of nanomaterials forms a major part of the present-day materials science research. This thesis consists of two parts- Part 1 dealing with the synthesis, characterization and some interesting properties of nanomaterials and Part 2 containing the results of investigations on porous materials.

Part 1 deals with the synthesis and characterization of nanomaterials such as inorganic nanowires and nanotubes. After a brief review of nanomaterials, the results obtained on nanowires by the carbon-assisted route are described. The method has been employed to prepare nanowires of elements (Si), oxides (SiO_2, Ga_2O_3 and ZnO), carbides (SiC) and nitrides (Si_3N_4). These investigations demonstrate the versatility of the carbon-assisted route for the synthesis of inorganic nanowires. A hydrogel has been used for the first time to prepare inorganic nanotubes. Thus, nanotubes of inorganic oxides such as SiO_2, TiO_2, ZrO_2, WO_3 and ZnO have been synthesized by the use of the hydrogel as the template. This method has been extended to synthesize nanotubes of $ZnSO_4$ and $BaSO_4$. The ability of single- and multi-walled carbon nanotubes to store hydrogen has been investigated, and a maximum of 3.7 wt% of hydrogen uptake observed. The last section in this part of the thesis describes the patterning of magnetic γ-Fe_2O_3 nanocrystals by an atomic force microscopy based dip-pen nanolithography method and the independent characterization of the patterns.

In Part 2, the focus is on macroporous and mesoporous materials. Macroporous networks of binary oxides such as SiO_2, TiO_2 and ZrO_2 as well as ternary oxides such as $PbTiO_3$ have been obtained by templating ordered polystyrene spheres followed by their removal. Macroporous carbon networks of different sizes have been synthesized by using ordered array of silica spheres with different sizes as the template. Macroporous aluminosilicate networks with mesoporous walls were obtained employing PMMA spheres. Mesoporous aluminosilicate spheres containing different amounts of Al have also been prepared.

Contents

PART 1
INVESTIGATIONS OF NANOMATERIALS   1

Part 1

INVESTIGATIONS OF

NANOMATERIALS

SUMMARY

This part of the thesis deals with the synthesis of various one-dimensional inorganic nanostructures such as nanowires and nanotubes as well as a study of certain properties of nanotubes and nanowires. Nanowires of several materials have been prepared by the carbon-assisted route. A new-route using hydrogels have been employed to obtain nanotubes of oxides as well as sulfates. Properties of carbon nanotubes such as hydrogen storage have also been explored. Dip-pen nanolithography has been used to obtain patterns of γ-Fe_2O_3 on various substrates. A brief description of the results is presented below.

Among the several strategies developed for the synthesis of inorganic nanowires, the carbothermal route perfected by us is noteworthy since it provides a general method for preparing crystalline nanowires of many of these materials. The method itself is quite simple and involves heating a mixture of an oxide with carbon in an appropriate atmosphere. Using this method, nanowires of various materials such as elemental silicon, oxides such as Ga_2O_3, ZnO and SiO_2, SiC and Si_3N_4 have been synthesized. The reactions have been carried out using various precursors of metals such as oxides, alkoxides or oxalates. The reactivity of the carbon source is found to play a major role in the product obtained. The flow rate of the gases was found to be crucial in determining the nature and quality of the nanostructures, from nanosheets to nanobelts and nanowires. The nanowires have been characterized by techniques such as electron microscopy, X-ray diffraction and photoluminescence. Wherever required, we have also performed Raman Scattering as well as infra-red spectroscopy on the nanowires.

A tripodal cholamide-based hydrogel has been employed as a template for the first time to synthesize inorganic nanotubes. Besides nanotubes of oxides such as SiO_2, TiO_2, ZrO_2, WO_3 and ZnO, nanotubes of sulfates such as the water-soluble $ZnSO_4$ as well as of $BaSO_4$ have been obtained using this method. An advantage of the use of the hydrogel, as compared to other organogels, is that metal alkoxides

are not required for the synthesis of the oxide nanotubes. This enabled us to obtain nanotubes of materials that have been difficult to obtain by traditional means. The nanotubes have been characterized by X-ray diffraction and transmission electron microscopy.

Adsorption of hydrogen at 300 K has been investigated on well-characterized samples of carbon nanotubes, besides carbon fibres by taking care to avoid many of the pitfalls generally encountered in such measurements. The system used in the study was custom-built and tested adequately before use. The nanotube samples include single- and multi-walled nanotubes prepared by different methods, as well as aligned bundles of multi-walled nanotubes. The nanotubes were characterized electron microscopic as well as other techniques. The effect of acid treatment of the nanotubes has been examined. A maximum adsorption of *ca.* 3.7 wt% is found with aligned multi-walled nanotubes.

Dip-pen nanolithography is a technique employed to pattern molecules using the water meniscus formed between the cantilever of an atomic force microscope and suitable substrates. We have successfully obtained magnetic nanopatterns of γ-Fe_2O_3 nanocrystals on mica and silicon substrates. The chemical and magnetic nature of the patterns have been characterized employing LEEM, XPEEM and MFM measurements. *

---

*Papers based on these studies have appeared in Chem. Phys. Lett., (2003); J. Mater. Res., (2004); Chem. Phys. Lett., (2002); Topics in Catalysis, (2003); J. Mater. Chem., (2002); J. Mater. Chem., (2003); J. Mater. Chem., (2003); Appl. Phys. Lett., (2004).

1.1 Nanomaterials: A brief overview

1.1.1 Introduction

Nanomaterials- materials that have features in between those of atoms and bulk material with at least one dimension in the nanometer regime- have received steadily growing interest due to their fascinating properties and applications superior to their bulk counterparts [1–3]. The properties of these materials are significantly different from those of atoms as well as their bulk counterparts. The importance of nanotechnology was pointed out by Richard P. Feynman as early as 1959, in his often-cited lecture entitled "There is plenty of room at the bottom". The ability to generate such minuscule structures is essential to much of modern science and technology. For example, in microelectronics, smaller has meant greater performance ever since the invention of integrated circuits; more components per chip, faster operation, lower cost and less power consumption. In other areas such as information storage too, efforts are on to develop magnetic and optical storage components with critical dimensions being tens of microns [4]. Besides, there are also a wealth of interesting and new phenomena associated with nanostructures, such as size-dependant excitation or emission [5], quantized (or ballistic) conductance [6], Coulomb blockade (or single-electron tunneling) [7] and metal-insulator transition [8].

Size effects constitute a fascinating aspect of nanomaterials. Bulk metals possess a partially filled electronic band and their ability to conduct electrons is due to the availability of a continuum of energy levels above the Fermi energy, E_F. However when bulk metal is broken down, the continuum of electronic states breaks down and ultimately, the material becomes insulating. The emerging discreetness of energy levels would not manifest themselves as long as the gap is less that $k_b T$. For semiconductors, the E_F is in between the filled and the unfilled levels. As

5

the size of the system decreases, the energy levels become discrete, with a similar spacing as in metals. Thus, the bandgap of the semiconductor effectively increases. In Figure 1.1.1, we show how the electronic structure of metal and semiconductor nanocrystals differ from those of bulk and isolated atoms.

Based on their dimensionality, nanostructures are classified as zero-, one- or two-dimensional. A schematic illustration showing the density of states versus energy for the various dimensional nanostructures is shown in Figure 1.1.2. There is a great change in the density of states for different dimensions. Even though the density is constant in 2D, the density of states is a step function with steps occuring at the energy of each quantized level. The case of 1D is complicated by the degeneracy of energy levels. We see the presence of singularities in 1D. The density of states for 0D shows quantization at particular energy values.

In the past two decades, significant progress has been made with regard to the synthesis and assembly of zero-dimensional (0D) nanostructures (or quantum dots) [9, 10]. Nanocrystals can be synthesized by two different routes, namely by the continuous division of matter in bulk (top-down approach) or by the controlled growth of constituent atoms (bottom-up approach). Physical methods such as resistive evaporation, laser ablation or arc-discharge are employed in the former process. The bottom to top approach involves chemical routes wherein metal salts are reduced in the presence of suitable capping ligands that prevent aggregation. A variety of reducing agents have been employed including alcohols, glycols, metal borohydrides and certain specialized reagents such as Li or Na naphthalide and tetrakis(hydroxylmethyl)phosphonium chloride. Various metal particles with sizes ranging from a few nanometers to a few microns have been made by the polyol process [11, 12] in which metal salts are reduced with high boiling alcohols such ethylene glycols. Long chain thiols, amines and fatty acids have emerged as suitable capping agents for metal nanocrystals. Semiconducting nanoparticles could be obtained by kinetic control of precipitation reaction [13, 14]. Nanocrystals of inorganic oxides and hydroxides are generally obtained by controlled hydrolysis [15]. A reverse (inverted) micelle method has also been used to obtain nanoparticles [16].
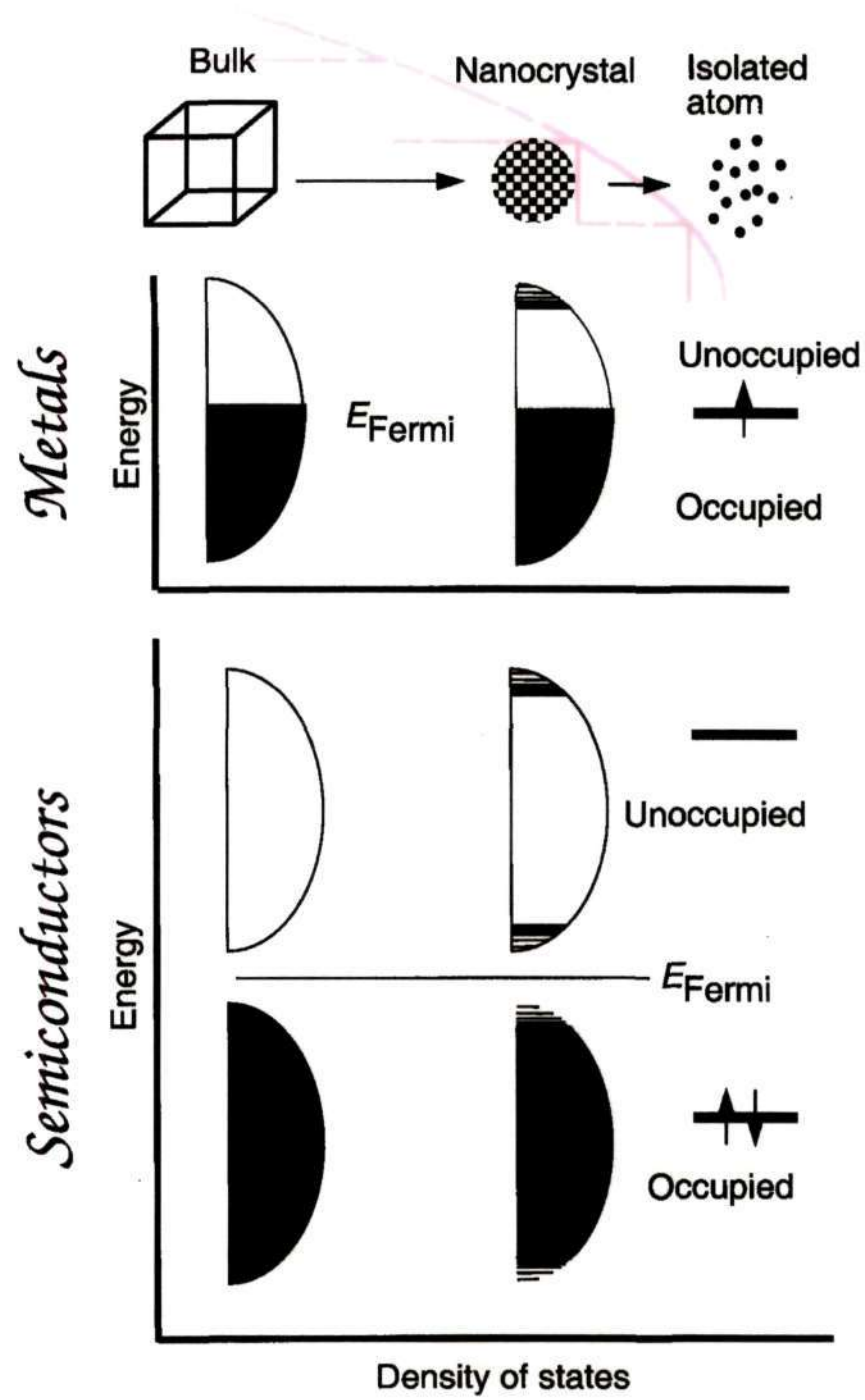
Figure 1.1.1: Density of states for metal and semiconductor nanocrystals compared to those of the bulk and of isolated atoms.
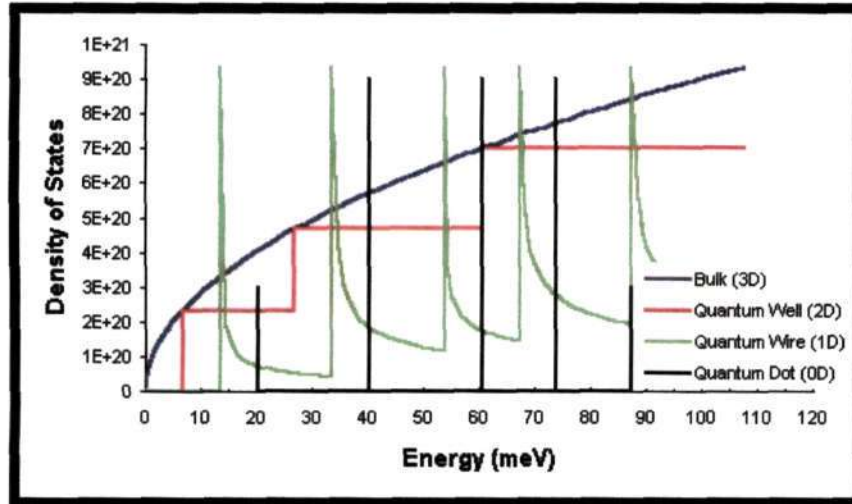
Figure 1.1.2: Density of states for bulk (3D blue), quantum well (2D red), quantum wire (1D green) and quantum dot (0D black)

Using nanoparticles as active components, various types of nanoscale devices have been fabricated. Notable examples include quantum-dot lasers [17], single-electron transistors [18], memory units [19], sensors [20], optical detectors [21] and light-emitting diodes [22]. For most of these applications, it is believed that the dimension of an individual quantum dot may represent the ultimate limit to the miniaturization of currently existing functional devices. Two-dimensional (2D) nanostructures have also been extensively studied by the semiconductor community since they can be conveniently synthesized using techniques such as molecular beam epitaxy.

1.1.2 Nanotubes

Ever since the discovery of carbon nanotubes by Iijima [23], there has been great interest in the synthesis and characterization of other one-dimensional (1D) nanostructures. Carbon nanotubes are either single- or multi-walled. A single-walled carbon nanotube (SWNT) can be viewed as a seamless cylinder obtained by rolling-up a section of a 2D graphene sheet (for reviews on carbon nanotubes, see, for example, [24, 25]). The structure of a SWNT is uniquely characterized by the roll-up vector, $\mathbf{C}_h = n\mathbf{a}_1 + m\mathbf{a}_2 \equiv (n,m)$ where $\mathbf{a}_1$ and $\mathbf{a}_2$ are the graphene

primitive vectors and *n,m* are integers (Figure 1.1.3(a)). The translation vector, **T**, is directed along the axis of the SWNT axis and perpendicular to C_h; the magnitude of **T** corresponds to the length of the (*n,m*) SWNT unit cell. Once (*n,m*) are specified, other structural properties such as the diameter and chiral angle can be determined. Among the large number of possible C_h vectors, there are two inequivalent, high-symmetry directions. These are termed as "zigzag" and "armchair" and are designated by (*n,0*) and (*n,n*) respectively, as shown in Figure 1.1.3(b).

Several strategies have been employed for the synthesis of carbon nanotubes [25]. They are generally made by the arc evaporation of graphite or by the pyrolysis of hydrocarbons such as acetylene or benzene over metal nanoparticles in a reducing atmosphere. Pyrolysis of organometallic precursors provides a one-step synthetic method for making carbon nanotubes [26]. In addition to the above methods, nanotubes have been prepared by laser ablation of graphite or electron-beam evaporation. Electrochemical synthesis as well as growth inside the pores of alumina membranes have also been reported.

Following the discovery of carbon nanotubes, researchers begun extending the synthesis to inorganic nanotubes such as BN, which have structures similar to graphite. Nanotubes of MoS_2 and WS_2 are conveniently prepared starting with the respective stable oxides [27–29]. Trisulfides of Mo and W have been decomposed to directly obtain the disulfide nanotubes [30]. The hydrothermal route has been used to obtain nanotubes of several oxides such as SiO_2 [31], V_2O_5 [32], and ZnO [33]. Surfactant-assisted synthesis of CdSe and CdS nanotubes has been reported by the reaction of metal oxide with the sulfiding/selenidizing agent in the presence of a surfactant [34]. By coating carbon nanotubes with oxide gels and then burning off the carbon, one obtains nanotubes and nanowires of a variety of metal oxides including ZrO_2, SiO_2, and MoO_2 [35–37]. Sol-gel synthesis of oxide nanotubes is also possible in the pores of alumina membranes.

There are several applications that have been proposed for carbon nanotubes, some of which have already been realized, while others are being developed rapidly.
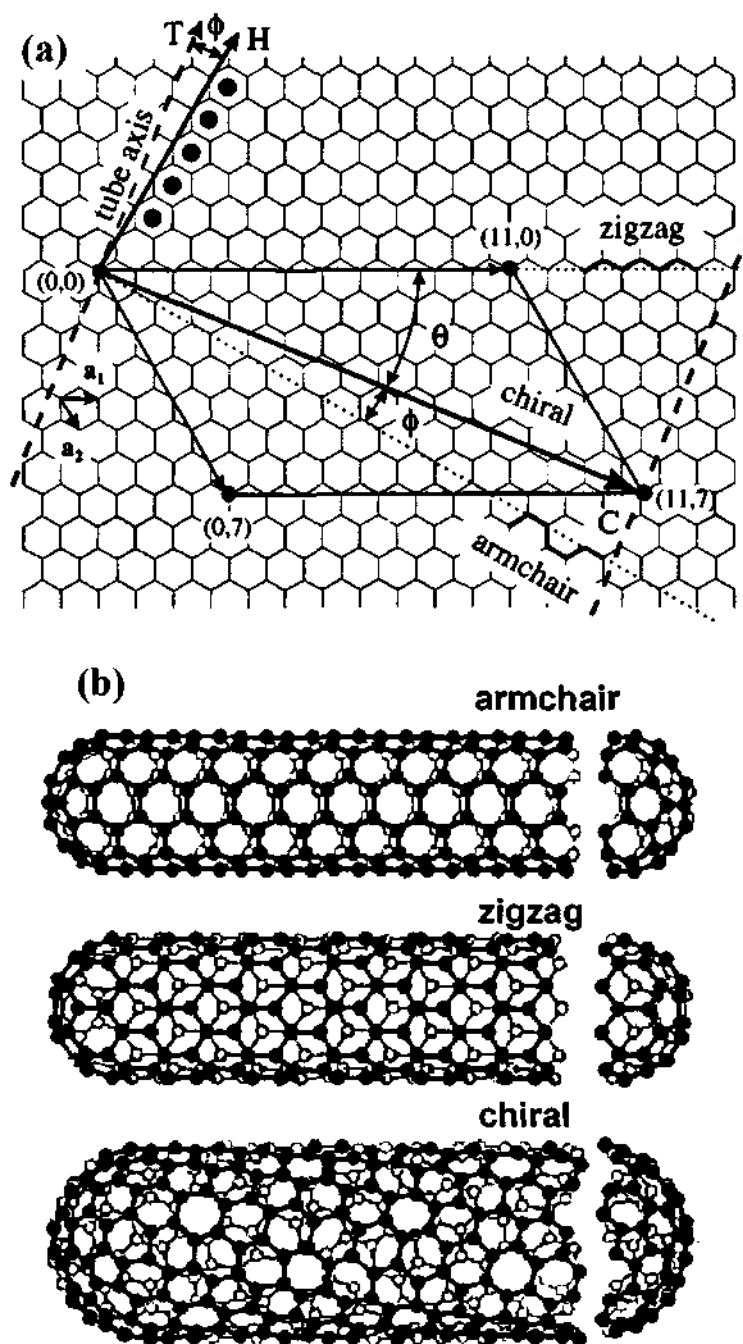
Figure 1.1.3: Schematic representation of the folding of a graphene sheet into zigzag, armchair and chiral nanotubes

SWNTs and MWNTs have been extensively used as field-emission electron sources [38, 39] for flat panel displays [40], lamps [41] and gas discharge tubes providing surge protection [42]. A potential applied between a carbon nanotube-coated surface and an anode produces high local fields, as a result of the small radius of the nanotube tip and its length. These local fields cause electrons to tunnel from the tip into the vacuum. Electric fields direct the field-emitted electrons towards the anode, where a phosphor produces light for the flat panel display application. Nanotubes provide stable field-emission, long lifetimes and low emission threshold potentials [38, 42]. Current densities as high as 4 Acm^{-2} have been obtained, compared with the 10 Acm^{-2} needed for flat panel field emission displays and the > 0.5 Acm^{-2} required for microwave power amplifier tubes.

Carbon nanotubes and fibers are believed to store vast amounts of hydrogen. Such studies assume importance due to the proposed utilization of hydrogen as a fuel instead of petroleum. Recent claims stating high hydrogen storage capacity of carbon fibers and nanotubes have aroused considerable interest and a great deal of controversy [43]. The US Department of Energy has set a system-weight benchmark (the ratio of system weight to hydrogen weight) of 6.5 wt%. In order to achieve this goal, there is a need for systematic studies using pure nanotube samples, minimizing the errors as far as possible.

Besides the above mentioned application, carbon nanotubes also find use in composites [44], sensors [45] and nanometer-sized semiconductor electronic devices [46].

1.1.3 Inorganic nanowires

Besides nanotubes, nanowires and nanorods constitute an important class of 1D nanostructures, which provide models to study the relationship between electrical transport, optical and other properties with dimensionality and size confinement. The various inorganic nanowires can also act as active components in devices as revealed by recent investigations.

In comparison to 0D and 2D nanostructures, the advancement of 1D nanowires

has been slow until recently due to the difficulties in synthesizing 1D nanostructures with well-controlled dimensions, morphology phase purity and chemical composition. 1D nanostructures can be synthesized by a variety of physical techniques such as electron-beam or focused-ion-beam writing [47, 48], proximal-probe patterning [49, 50] and X-ray or extreme-UV lithography [51]. Compared to these physical methods, chemical methods have been more versatile and effective in the synthesis of nanowires. Thus, techniques involving chemical vapour deposition (CVD), precursor decomposition, as well as solvothermal, hydrothermal and carbothermal methods have been widely employed (for recent reviews, see [52–54]). The following section presents details of the methods to synthesize nanowires. Several physical methods, especially microscopic techniques such as scanning electron microscopy (SEM), transmission electron microscopy (TEM), scanning tunneling microscopy (STM) and atomic force microscopy (AFM) are commonly used to characterize nanowires.

1.1.4 Synthetic strategies of nanowires

An important aspect of the 1D structures relates to their crystallization [55], wherein the evolution of a solid from a vapor, a liquid, or a solid phase involves nucleation and growth. As the concentration of the building units (atoms, ions, or molecules) of a solid becomes sufficiently high, they aggregate into small nuclei or clusters through homogeneous nucleation. With a continuous supply of the building blocks, the clusters serve as seeds for further growth to form larger clusters. In order to obtain crystals with homogenous compositions and uniform morphologies, the building-blocks need to be supplied at a well controlled rate. Several synthetic strategies have been developed for 1D nanowires with different levels of control over the growth parameters. Figure 1.1.4 schematically illustrates some of the synthetic strategies which include: (i) the use of the anisotropic crystallographic structure of the solid to facilitate 1D nanowire growth, Figure 1.1.4(a); (ii) the introduction of a solid-liquid interface, Figure 1.1.4(b); (iii) use of templates (with 1D morphologies) to direct the formation of nanowires, Figure 1.1.4(c); (iv) supersaturation control to modify the growth habit of a seed; (v) use of capping agents to kinetically control

the growth rates of the various facets of a seed, Figure 1.1.4(d); (vi) self-assembly of zero-dimensional (0D) nanostructures, Figure 1.1.4(e) and (vii) size reduction of 1D microstructures, Figure 1.1.4(f). They are conveniently categorized into (a) growth in vapor phase and (b) solution-based growth.

Vapor phase growth

Vapor phase growth is extensively used for producing nanowires. Starting with the simple evaporation technique in an appropriate atmosphere to produce elemental or oxide nanowires, vapor-liquid-solid, vapor-solid and other processes are also made use of.

Vapor-liquid-solid growth

The growth of nanowires via a gas phase reaction involving the vapor-liquid-solid (VLS) process has been widely studied. Wagner [56, 57], during his studies of growth of large single-crystalline whiskers, proposed in 1960s, a mechanism for the growth via gas phase reaction involving the so called vapor-liquid-solid process. He studied the growth of mm-sized Si whiskers in the presence of Au particles (Figure 1.1.5). According to this mechanism, the anisotropic crystal growth is promoted by the presence of the liquid alloy/solid interface. The growth of Si whiskers using Au as a solvent at high temperature has been explained based on the Si-Au phase diagram as shown in Figure 1.1.5. Si and Au form a liquid alloy when the temperature is higher than the eutectic point (370 °C). The liquid surface has a large accommodation coefficient and is therefore a preferred deposition site for the incoming Si vapor. After the liquid alloy becomes supersaturated with Si, precipitation of the Si whisker occurs at the solid-liquid interface. Si whiskers obtained are shown in the photograph in Figure 1.1.5. Until recently, the only evidence that nanowires grew by this mechanism was the presence of alloy droplets at the tips of the nanowires. Wu *et al.* [58] have reported real-time observations of Ge nanowire growth in an *in-situ* high-temperature TEM, which demonstrate the validity of the VLS growth mechanism. Their experimental observations suggest that there are three growth stages: metal alloying, crystal nucleation and axial

13
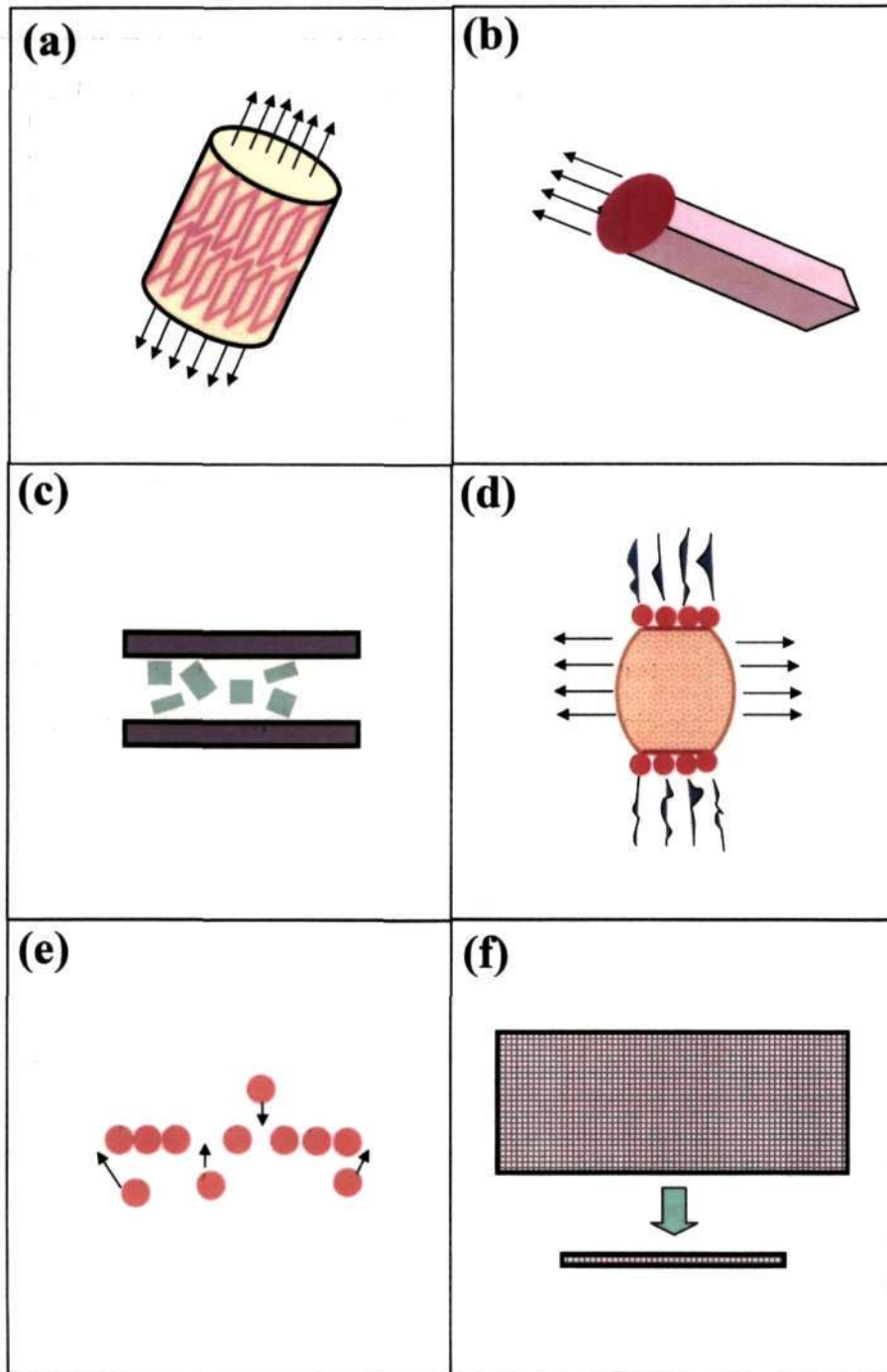
Figure 1.1.4: Schematic illustration of six strategies that have been demonstrated for achieving 1D growth
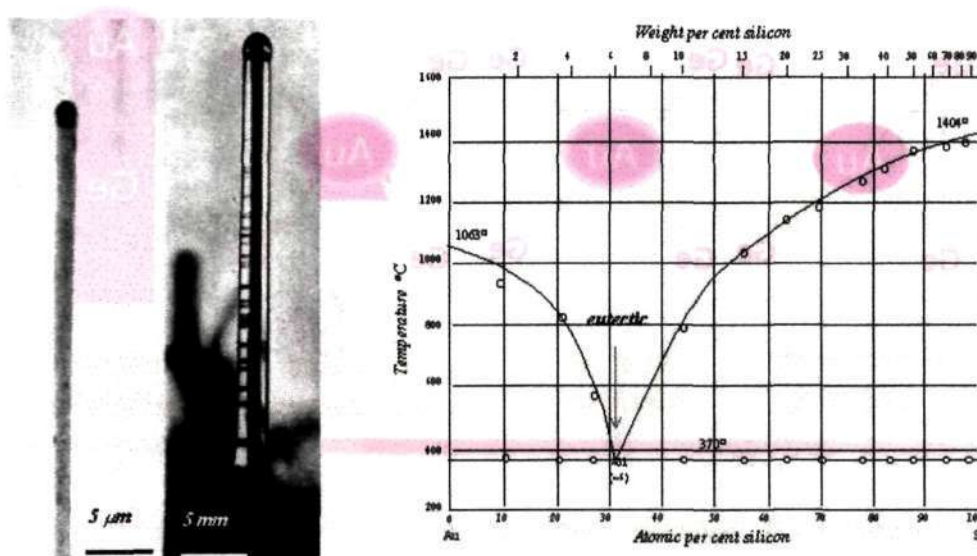
Figure 1.1.5: The Si-Au phase diagram along with photographs of the Si whiskers synthesized by the VLS process

growth. See Figure 1.1.6 for a schematic illustration of the VLS process. The TEM images obtained by them clearly confirm the validity of the VLS growth mechanism at the nanometer scale.

Since the diameter of the nanowires is determined by the diameter of the catalyst particles, this method provides an efficient means to obtain uniform-sized nanowires. Also, with the knowledge of the phase diagram of the reacting species, the growth temperature can be set in between the eutectic point and the melting point of the material. Physical methods such as laser ablation or thermal evaporation as well as chemical methods such as chemical vapor deposition can be used to generate the reactant species in vapor form, required for the nanowire growth. Catalyst particles can be sputtered onto the substrates or metal nanoparticles prepared by solution-based routes used as the catalysts. An advantage of this route is that patterned deposition of catalyst particles yields patterned nanowires. The VLS process has been employed to synthesize a variety of inorganic nanowires, a few examples being those of elements like Ge [58], oxides such as ZnO [59,60], nitrides such as GaN [61], chalcogenides like CdS [62] among others.

15
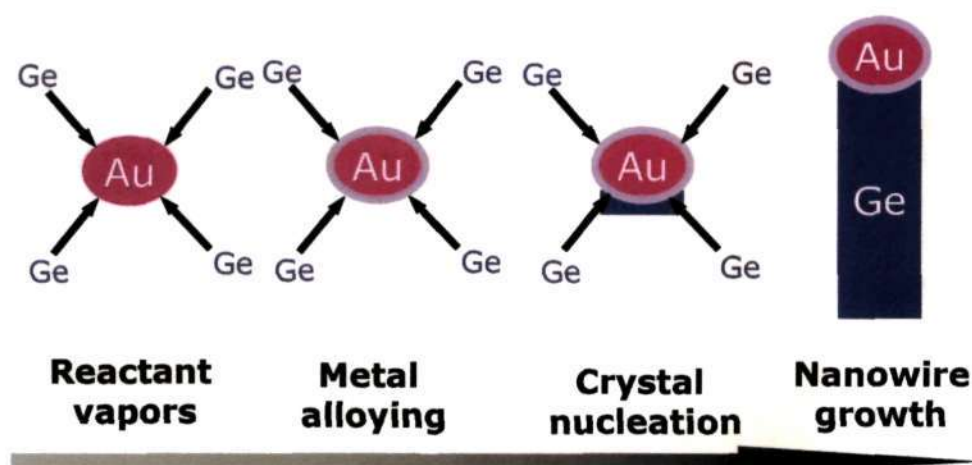
Figure 1.1.6: Schematic representation of the VLS growth mechanism

Oxide-assisted growth

In contrast to the well-established VLS growth, Lee and co-workers [63, 64] have proposed a nanowire growth mechanism called the oxide-assisted growth mechanism. No metal catalyst is required for the synthesis of nanowires by this means. Based on their experimental observations, the workers find that the growth of Si nanowires is greatly enhanced when SiO_2-containing Si powder targets were used. Limited quantities of Si nanowires were obtained with a target made of pure Si powder (99.995 %)

Lee *et al.* propose that the growth of the Si nanowires is assisted by the Si oxide, where the Si_xO ($x>1$) vapor generated by thermal evaporation or laser ablation plays the key role. Nucleation of the nanoparticles is assumed to occur on the substrate as shown in equations (1) and (2).

$$Si_xO \longrightarrow Si_{x-1} + SiO \ (x > 1), \qquad \cdots \quad (1)$$
$$2SiO \longrightarrow Si + SiO_2 \qquad\qquad\qquad \cdots \quad (2)$$
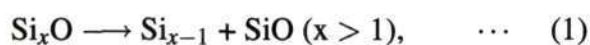
These decompositions result in the precipitation of Si nanoparticles, which act as the nuclei of the silicon nanowires covered by shells of silicon oxide. The precipitation, nucleation and growth of the nanowires occur in the area near the cold finger, suggesting that the temperature gradient provides the external driving force for the

formation and growth of the nanowires.

Nanowires synthesized by the oxide-assisted growth mechanism include those of silicon and germanium [63].

Vapor-solid growth

The vapor-solid (VS) method for whisker growth also holds for the growth of 1D nanomaterials [56]. In this process, evaporation, chemical reduction or gaseous reaction first generates the vapor. The vapor is subsequently transported and condensed onto a substrate. The VS method has been used to prepare whiskers of oxide as well as metals with micrometer diameters. It is, therefore, possible to synthesize the 1D nanostructures using the VS process if one can control the nucleation and the subsequent growth process. Using the VS method, nanowires of oxides of Zn, Sn, In, Cd, Mg, Ga and Al have been obtained.

Carbothermal reactions

Nanowires of a variety of oxides, nitrides and carbides can be synthesized by carbothermal reactions. The process is a simple one, involving the heating of carbon with an oxide in flowing gas. The first step involves the formation of sub-oxidic species which reacts with C, O_2, N_2 or NH_3 to produce the desired nanowires. The carbon sources that can be used include carbon nanotubes or graphite (that are stable to oxidation on heating) as well as activated carbon or charcoal (that get easily oxidized on heating in air). Thus, heating a mixture of Ga_2O_3 and carbon in N_2 or NH_3 produces GaN nanowires. Carbothermal reactions generally involve the following steps: The first step normally involves the formation of a metal suboxide by the reaction of the metal oxide with carbon. Depending on the desired product, the suboxide heated in the presence of O_2, NH_3, N_2 or C yields oxide, nitride or carbide nanowires respectively.

17

$$metal\ oxide + C \longrightarrow metal\ suboxide + CO$$

$$metal\ suboxide + O_2 \longrightarrow metal\ oxide\ nanowires$$

$$metal\ suboxide + NH_3 \longrightarrow metal\ nitride\ nanowires + CO + H_2$$

$$metal\ suboxide + N_2 \longrightarrow metal\ nitride\ nanowires + CO$$

$$metal\ suboxide + C \longrightarrow metal\ carbide\ nanowires$$
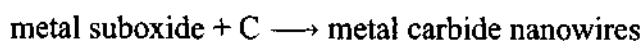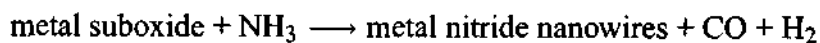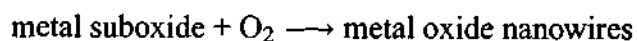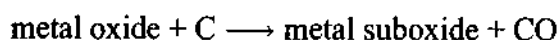
Solution-based growth of nanowires

This synthetic strategy for nanowires makes use of anisotropic growth dictated by the crystallographic structure of the solid material, or confined and directed by templates, or kinetically controlled by supersaturation, or by the use of appropriate capping agent.

Highly anisotropic crystal structures

Many solid materials naturally grow into 1D nanostructures, and this habit is determined by the highly anisotropic bonding in the crystallographic structure. A well-known example is poly(sulphur nitride), $(SN)_x$, an inorganic polymer extensively studied for its metallic and superconducting properties, that can easily be grown into 1D nanostructures [65, 66]. Other materials such as selenium [67], tellurium [68] and molybdenum chalcogenides [69, 70] are also easily obtained as nanowires due to anisotropic bonding, which dictates the crystallization to occur along the c-axis, favoring the stronger covalent bonds over the relatively weak van der Waals forces between the chains.

Template-based synthesis

Template-directed synthesis represents a convenient and versatile method for generating 1D nanostructures. In this technique, the template serves as a scaffold against which other materials with similar morphologies are synthesized. That is, the *in situ* generated material is shaped into a nanostructure with a morphology complementary to that of the template. The templates could be nanoscale channels within mesoporous materials, porous alumina and polycarbonate membranes. The
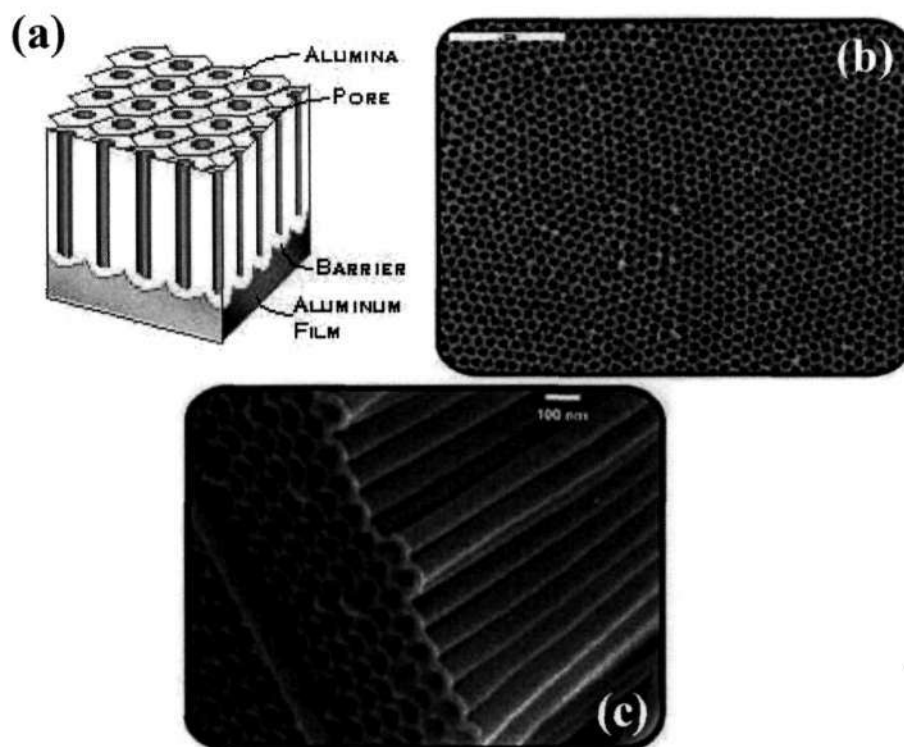
Figure 1.1.7: (a) Schematic illustration of an anodic alumina membrane. The SEM images of the membrane (b) before and (c) after filling with the inorganic precursor.

nanoscale channels are filled using, the solution, the sol-gel or the electrochemical method. The nanowires so produced are released from the templates by removal of the host matrix [71–73]. Unlike the polymer membranes fabricated by track etching, anodic alumina membranes (AAMs) containing a hexagonally packed 2D array of cylindrical pores with a uniform size are prepared using anodization of aluminium foils in an acidic medium (Figure 1.1.7). Several materials have been fabricated into nanowires using AAMs in the templating process. The various inorganic materials include Au, Ag, Pt, TiO_2, MnO_2, ZnO, SnO_2, In_2O_3, CdS, CdSe, CdTe, electronically conducting polymers such as polypyrole, poly(3-methylthiophene) and polyaniline as well as carbon nanotubules. The only drawback of this method is that it is difficult to obtain materials that are single-crystalline.

Besides alumina and polymer membranes with high surface areas and uniform pore sizes, mesoporous silica has been successfully used as a template for the synthesis of polymer and inorganic nanowires. Mesophase structures self-assembled

19

surfactant
molecules
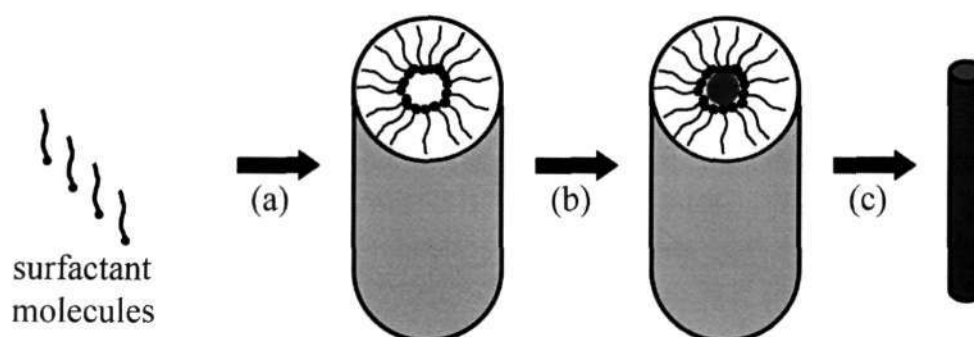
Figure 1.1.8: Schematic illustration showing the formation of nanowires by templating against mesostructures which are self-assembled from surfactant molecules; (a) formation of cylindrical micelle, (b) formation of the desired material in the aqueous phase encapsulated by the cylindrical micelle, (c) removal of the surfactant molecule with an appropriate solvent (or by calcination) to obtain an individual nanowire.

from surfactants (Figure 1.1.8) provide another class of useful and versatile templates for generating 1D nanostructures in relatively large quantities. It is well known that at critical micellar concentration (CMC) surfactant molecules spontaneously organize into rod shaped micelles [74, 75]. These anisotropic structures can be used immediately as soft templates to promote the formation of nanorods when coupled with appropriate chemical or electrochemical reaction. The surfactant needs to be selectively removed to collect the nanorods/nanowires. Based on this principle, nanowires of CuS, CuSe, CdS, CdSe, ZnS and ZnSe have been grown, by using surfactants such as Na-AOT or Triton X of known concentrations [34, 76].

Nanowires themselves can be used as templates to generate the nanowires of other materials. The template may be coated to the nanowire (physical) forming coaxial nanocables [77], or it might react with the nanowires forming a new material [78]. In the physical method (solution or sol-gel coating), surfaces of the nanowires are directly coated with conformal sheaths made of a different material to form coaxial nanocables. Subsequent dissolution of the original nanowires leads to nanotubes of the coated materials. The sol-gel coating method is a generic route to synthesize co-axial nanocables that may contain electrically conductive metal cores and insulating sheaths.

Govindaraj *et al.* [79] have demonstrated that a variety of metal nanowires of 1–1.4 nm diameter can be readily prepared by filling SWNTs, opened by acid treatment. Nanowires of Au, Pt, Pd and Ag have been synthesized by employing sealed-tube reactions as well as solution methods. In addition, incorporation of thin layers of metals in the intertubular space of the SWNT bundles has been observed.

Solution-liquid-solid process

Buhro and coworkers [80] have developed a low temperature solution-liquid-solid (SLS) method for the synthesis of crystalline nanowires of III-V semiconductors [81–83]. In a typical procedure, a metal (e.g. In, Sn, Bi) with a low melting point is used as a catalyst, and the desired material generated through the decomposition of organometallic precursors. Nanowhiskers of InP, InAs and GaAs have been prepared by low temperature ($\sim$ 203 °C) solution phase reactions. The products obtained are generally single- crystalline.

Korgel *et al.* [84] have used the supercritical fluid-liquid-solid (SFLS) method to synthesize bulk quantities of defect-free silicon and germanium nanowires. In addition to these solution routes to elemental III-V semiconductor nanowires, it has been reported recently that by exploiting the selective capping capacities of mixed surfactants, it is possible to extend the synthesis of the II-IV semiconductor nanocrystals to that of semiconductor nanorods [85], a version of nanowires with relatively shorter aspect ratios.

1.1.5 Growth control and integration

A significant challenge in the chemical synthesis of nanowires is to rationally control the nanostructure assemblies so that their size, dimensionality, interfaces and their 2D and 3D superstructures can be tailor-made towards desired functionality. Many physical and thermodynamic properties are diameter-dependent. Several groups have synthesized uniform-sized nanowires by the VLS process using clusters with narrow size-distributions.

Controlling the growth orientation is important for the applications of nanowires.

By utilizing the conventional epitaxial crystal growth technique to the VLS process, a vapor-liquid-solid epitaxy technique has been developed for the controlled synthesis of nanowire arrays. Nanowires generally have preferred growth directions. For example, zinc oxide nanowires prefer to grow along their c-axis, that is along the <001> direction [59,60]. Also, Si nanowires grow along the <111> direction when grown by the VLS growth process, but can be made to grow along the <112> or the <110> direction by the oxide-assisted growth mechanism.

It is clear from the VLS nanowire growth mechanism that the initial positions of Au clusters or Au thin films control the positions of the nanowires. By creating desired patterns of Au using a lithographic technique, it is possible to grow ZnO nanowires of the same designed pattern since they grow vertically only from the region coated with Au and form the designed patterns of ZnO nanowire arrays [59,60]. Similarly, networks of nanowires with the precise placement of individual nanowires on substrates with the desired configuration is achieved by the surface patterning strategy [59,60].

Using the above methods, it is possible to pattern nanowires on length scales of hundreds of microns. The present day electronics demands the patterning of nanowires and nanotubes in the nanometer level. This has recently been achieved by Liu and co-workers [86]. Nickel nitrate solutions was deposited on silica substrates using an atomic force microscope cantilever tip to form nanometer-sized droplets. GaN nanowires were grown on the patterned nickel oxide islands by a simple chemical vapor deposition process. I-V curves were measured for the nanowires in the presence and absence of UV illumination. Under illumination, the conductivity of the nanowire was found to increase. The dip-pen nanolithography technique has been extensively used for patterning of molecules and recently to other metals as well as nanoparticles [87]. Such nanopatterns would be ideal candidates for the positioning of nanowires and needs to be further exploited.

Integration of nanowire building blocks into complex functional networks in a controlled fashion is a major challenge. The direct one-step growth process has been used [59,60]. In this process, the nanowires, grown by the VLS method, are

patterened on substrates by selectively depositing catalyst particles. Another way is to place the nanowire building blocks together into the functional structure to develop a hierarchical assembly. By using a simple dubbed microfluidic-assisted nanowire integration process, wherein the nanowire solution/suspension is filled in the microchannels formed between poly(dimethylsiloxane) (PDMS) micromould and a flat Si substrate, followed by the evaporation of the solvent, nanowire surface patterning and alignment has been achieved [88–90]. Langmuir Blodgett technique has also been used to obtain aligned, high-density nanowire assemblies [91].

1.1.6 Physical properties of nanowires

As compared to bulk materials, low-dimensional nanoscale materials, with their large surface areas and possible quantum confinement effect, exhibit interesting optical, electronic, mechanical and thermal properties. The understanding of such properties is essential for their applications in various areas.

Optical properties

As in the case of quantum dots, size-confinement also plays an important role in determining the energy levels of a nanowire once its diameter has been reduced below a critical value. Korgel and co-workers found that the absorption edge of silicon nanowires (obtained with hexane supercritical fluid as the solvent) was significantly blue-shifted as compared with the indirect bandgap ($\sim$ 1.1 eV) of silicon [84, 92, 93]. They also observed sharp, discrete features in the absorption spectra and relatively strong band-edge photoluminescence (PL) arising from quantum-confinement with possible contributions from surface states [94]. In addition, the variation in the growth direction of the silicon nanowires led to different optical signatures.

In contrast to quantum dots, light emitted from nanowires is highly polarized along their longitudinal axis. Lieber and co-workers [95] have observed this in the PL measurements on individual InP nanowires. Polarization-sensitive measurements reveal a striking anisotropy in the PL intensity recorded parallel and

perpendicular to the long axis of the nanowire. The order-of-magnitude polarization anisotropy was quantitatively explained in terms of the large dielectric contrast between these free-standing nanowires and the surrounding environment as opposed to quantum confinement effects.

UV lasing has been demonstrated from single ZnO nanowires at room temperature [96]. The line widths, wavelengths and power dependence of the nanowire emission demonstrate that the nanowires act as an active optical cavity. ZnO nanowire arrays also exhibit room temperature lasing [60]. Nanowires with diameters of 20–150 nm form natural lasing cavities. Under optical excitation, surface-emitter lasing action was observed at 385 nm, with an emission linewidth less than 0.3 nm. Shown in Figure 1.1.9, is the lasing action observed in the array of ZnO nanowires during the evolution of the emission spectra with increasing power. At lower excitation intensities, the spectrum consists of a single broad peak with full width at half maximum at $\sim$ 17 nm. As the pump power increases, the emission peak narrows due to the preferential amplifications of frequencies close to the maximum of the gain spectrum. When the excitation intensity exceeds a threshold of $\sim$ 40 kW/cm^2, sharp peaks emerge in the emission spectra with the linewidths of < 0.3 nm.

Mechanical properties

Whiskers have been investigated for their mechanical properties and have been found to have much greater strengths as compared to their bulk counterparts,. This has been attributed to a reduction in the number of defects per unit length that lead to mechanical failure. Atomic force microscopy has been used to determine the mechanical properties of individual, structurally isolated silicon carbide nanowire that were pinned at one end to MoS$_2$ surfaces [97]. The bending force was measured versus displacement along the unpinned lengths. Continued bending of the SiC nanowire ultimately led to fracture. The Youngs modulus obtained (610–660 GPa) was comparable to that predicted for [111]-oriented SiC (600 GPa) and the average values obtained previously for millimeter-sized whiskers. Thus, the nanowires are obvious candidates as reinforcing elements in ceramic, metal and polymer matrix
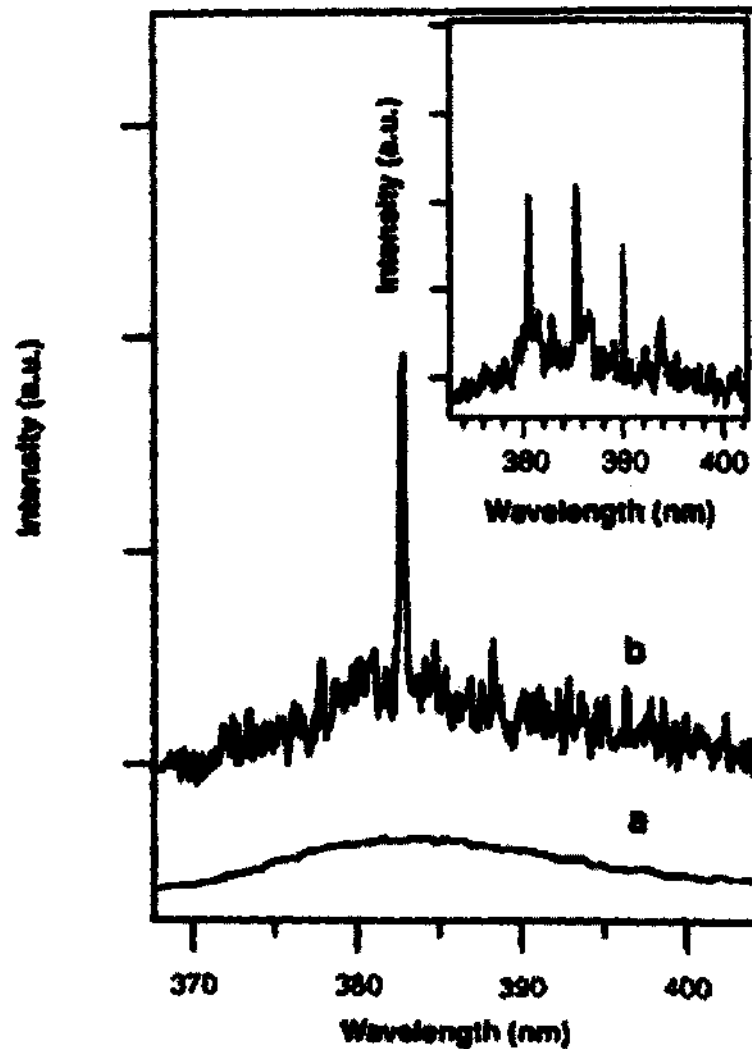
Figure 1.1.9: The power-dependent emission spectra recorded from a 2D array of ZnO nanowires, with the excitation energy being below (bottom trace) and above (top trace) the threshold

composites.

Thermal properties

Thermal stability of the nanowires assumes importance while considering their applications in nanoscale electronics. Size-dependent melting-recrystallization process of the carbon-sheathed semiconductor Ge nanowires has been studied by Yang and co-workers using an *in situ* high temperature transmission electron microscope [98, 99]. They observed that the melting point to be inversely

proportional to the diameter of the nanowire. The ability to manipulate individual nanowire cutting, interconnection and welding was also demonstrated.

A related study is the recent observation of Si-based nanowires with different morphologies and microstructures at different formation and annealing temperatures [100, 101]. It was observed that besides Si nanowires, many other kinds of Si-based nanostructures such as octopuslike, pinlike, tadpolelike and chainlike structures were also formed. The formation and annealing temperature was found to play a dominant role in the formation of these structures.

Such studies are useful to determine the optimum temperature for preparing high quality defect-free nanowires. Manipulation of the nanowires is useful for integrating the nanostructures into useful circuitry.

Electronic properties

Electrical transport is of great interest in 1D systems since predictable and controllable conductance will be crucial to many nanoscale applications. In recent times, efforts have focused on electrical transport in carbon nanotubes (see for example [24] and references therein). These studies have shown interesting fundamental features including ballistic conductance at room temperature [102, 103], Luttinger liquid behavior [104] and have demonstrated the potential for devices such as field effect transistors [105, 106]. However, there are limitations to applications based on carbon nanotubes. Firstly, the specific growth of metallic or semiconducting nanotubes is not possible. Studies dependent on the specific conducting behavior must thus rely on chance observation. Second, controlled doping of semiconducting nanotubes is not possible, although it is potentially critical for device applications. Semiconducting nanowires, however, can overcome these limitations of carbon nanotubes. These nanowires will remain semiconducting independent of diameters and it should be possible to take advantage of the vast knowledge from the semiconductor industry to dope the nanowires.

Using gate-dependent, two-terminal measurements, Lieber and co-workers have demonstrated that B-doped and P-doped silicon nanowires behave as p-type and

n-type respectively [107]. The estimates of carrier mobilities suggest diffusive transport in these nanowires. They have further used these nanowires as building blocks to form critical junctions [108]. Passive diode structures consisting of crossed p- and n-type nanowires exhibit rectifying transport similar to planar p-n junctions. Active bipolar transistors, consisting of heavily and lightly n-doped nanowires crossing a common p-type wire base, exhibit common base and emitter current gains as large as 0.94 and 16, respectively. In addition, p- and n-type nanowires have been used to assemble complementary inverter-like structures.

Recently, the assembly of p-type Si and n-type GaN nanowires has been reported to form crossed nanoscale p-n junctions and junction arrays in which the electronic properties and functions are controlled in a predictable manner to provide both diode and FET elements in high yields. Nanoscale p-n junctions and FET arrays have also been configured as OR, AND and NOR logic gates with substantial gains, and these gates have been interconnected to demonstrate computation with a half adder [109]. This is a step forward in the integration at the nanoscale level.

1.1.7 Concluding remarks

As seen above, nanowires have a host of interesting properties, different from their bulk counterparts. The first step in their utilization in functional devices is precise control on the synthesis. This includes control on the aspect ratios as well as chemical composition of the materials. The past few years have witnessed a surge in the synthesis of nanowires of various materials and their characterization. Future research would be aimed at the assembly of these nanowires as well as a study of their properties.

References

[1] See, for example, (a) *Handbook of Nanostructures Materials and Nanotechnology*, (Ed. H. S. Nalwa) Academic Press, New York, 2000; (b) *Nanomaterials: Synthesis, Properties and Applications*, (Ed. A. S. Edelstein, R. C. Cammarata), Institute of Physics, Philadelphia, PA, 1996.

[2] See, for example, (a) A special issue on nanoscale materials, *Acc. Chem. Res.*, 1999, **32**; (b) Special issue on nanostructures materials, *Chem. Mater.*, 1996, **8**, 1569; (c) G. A. Ozin, *Adv. Mater.*, 1992, **4**, 612.

[3] (a) R. Dagani, *C&EN News*, 2000, **October**, 27; (b) W. Schulz, *C&EN News*, 2000, **May**, 41.

[4] C. Ross, *Annu. Rev. Mat. Sci.*, 2001, **31**, 203.

[5] C. B. Murray, C. R. Kagan and M. G. Bawendi, *Annu. Rev. Mat. Sci.*, 2000, **30**, 545.

[6] J. M. Krans, J. M. van Rutenbeek, V. V. Fisun, I. K. Yanson and L. J. de Jongh, *Nature*, 1995, **375**, 767.

[7] K. K. Likharev and T. Claeson, *Sci. Am.*, 1992, **June**, 80.

[8] G. Markovich, C. P. Collier, S. E. Henrichs, F. Remacle, R. D. Levine and J. R. Heath, *Acc. Chem. Res.*, 1999, **32**, 415.

[9] P. Alivisatos, *Pure Appl. Chem.*, 2000, **72**, 3

[10] A special issue on semiconductor quantum dots, *MRS Bull.*, 1998, **2**, 15.

[11] F. Fievet, J. P. Lagier, B. Blin, B. Beaudoin and M. Figlarz, *Solid State Ionics*, 1989, **32/33**, 198.

[12] R. Seshadri and C. N. R. Rao, *Mater. Res. Bull.*, 1994, **29**, 795.

References
_____

[13] A. Henglein, *Ber. Bunsenges. Phys. Chem.*, 1995, **903**, 99.

[14] S. V. Gaponenko, *Optical Properties of Semiconductor Nanocrystals*, Cambridge University Press, Cambridge, 1998.

[15] M. Rajamathi and R. Seshadri, *Curr. Opinion Solid State Mater. Sci.*, 2002, **6**, 337.

[16] M. P. Pileni, *J. Phys. Chem.*, 1993, **97**, 6961.

[17] V. I. Klimov, A. A. Mikhailovsky, S. Xu, A. Malko, J. A. Hollingsworth, C. A. Leatherdale, H. J. Eisler and M. G. Bawendi, *Science*, 2000, **314**, 290.

[18] D. L. Klein, R. Roth, A. K. L. Lim, A. P. Alivisatos and P. L. McEuen, *Nature*, 1997, **389**, 699.

[19] H. Pettersson, L. Baath, N. Carlsson, W. Seifert and L. Samuelson, *Appl. Phys. Lett.*, 2001, **79**, 78.

[20] A. N. Shipway, E. Katz and I. Willner, *ChemPhysChem*, 2000, **1**, 18.

[21] J. Phillips, *J. Appl. Phys.*, 2002, **91**, 4590.

[22] S. Coe, W. K. Woo, M. Bawendi and V. Bulovic, *Nature*, 2002, **420**, 800.

[23] S. Iijima, *Nature*, 1991, **354**, 56.

[24] M. Ouyang, J. L. Huang and C. M. Lieber, *Acc. Chem. Res.*, 2002, **35**, 1018.

[25] C. N. R. Rao, B. C. Satishkumar, A. Govindaraj and M. Nath, *ChemPhysChem.*, 2001, **2**, 78.

[26] C. N. R. Rao and A. Govindaraj, *Acc. Chem. Res.*, 2002, **35**, 998.

[27] R. Tenne, L. Margulis, M. Genut and G. Hodes, *Nature*, 1992, **360**, 444.

[28] L. Margulis, G. Salitra and R. Tenne, *Nature*, 1993, **365**, 113.

[29] Y. Feldman, E. Wasserman, D. J. Srolovitch and R. Tenne, *Science*, 1995, **267**, 222.

[30] M. Nath, A. Govindaraj and C. N. R. Rao, *Adv. Mater.*, 2001, **13**, 283,

[31] A. P. Lin, C. Y. Mou and S. D. Liu, *Adv. Mater.*, 2000, **12**, 103,

[32] M. E. Spahr, P. Bitterli, R. Nesper, M. Müller, F. Kremeich, H. U. Nissen, *Angew. Chem. Int. Ed.*, 1998, **37**, 1263.

[33] J. Zhang, L. Sun, C. Liao and C. Yan, *Chem. Commun.*, 2002, 262.

[34] C. N. R. Rao, A. Govindaraj, F. L. Deepak, N. A. Gunari and M. Nath, *Appl. Phys. Lett.*, 2001, **78**, 1853.

[35] B. C. Satishkumar, A. Govindaraj, E. M. Vogl, L. Basumallick and C. N. R. Rao, *J. Mater. Res.*, 1997, **12**, 604.

[36] B. C. Satishkumar, A. Govindaraj, M. Nath and C. N. R. Rao, *J. Mater. Chem.*, 2000, **10**, 2115.

[37] C. N. R. Rao, B. C. Satishkumar and A. Govindaraj, *Chem. Commun.*, 1997, 1581.

[38] W. A. deHeer, A. Chatelain and D. Ugarte, *Science*, 1995, **270**, 1179.

[39] A. G. Rinzler, J. H. Hafner, P. Nikolaev, L. Lou, S. G. Kim, D. Tomanek, P. Nordlander, D. T. Cobert and R. E. Smalley, *Science*, 1995, **267**, 1550.

[40] N. S. Lee, D. S. Chung, I.T. Han, J. H. Kang, Y. S. Choi, H. Y. Kim, S. H. Park, Y. W. Jin, and W. K. Yi, *Diamond Relat. Mater.*, 2001, **10**, 265.

[41] Y. Saito and S. Uemura, *Carbon*, 2000, **38**, 169.

[42] R. Rosen, W. Simendinger, C. Debbault, H. Shimoda, L. Fleming, B. Stoner, and O. Zhou, *Appl. Phys. Lett.*, 2000, **76**, 1668.

[43] C. Zandonella, *Nature*, 2001, **410**, 734.

[44] S. R. C. Vivekchand, L. Sudheendra, M. Sandeep, A. Govindaraj and C. N. R. Rao, *J. Nanosci. Nanotech.*, 2002, **2**, 631.

References

[45] S. S. Wong, E. Joselvich, A. T. Woolley, C. L. Cheung and C. M. Lieber, *Nature*, 1998, **394**, 52.

[46] A. Bachtold, P. Hadley, T. Nakamichi, C. Dekker, *Science*, 2001, **294**, 1317.

[47] J. M. Gibson, *Phys. Today*, 1997, **October**, 56.

[48] S. Matsui and Y. Ochiai, *Nanotechnology*, 1996, **7**, 247.

[49] S. H. Hong, J. Zhu and C. A. Mirkin, *Science*, 1999, **286**, 523.

[50] J. A. Dagata, *Science*, 1995, **270**, 1625.

[51] M. D. Levenson, *Solid State Technol.*, 1995, **September**, 81.

[52] P. Yang, Y. Wu and R. Fan, *Int. J. Nanosci.*, 2002, **1**, 1.

[53] Y. Xia, P. Yang, Y. Sun, Y. Wu, B. Mayers, B. Gates, Y. Yin, F. Kim and H. Yan, *Adv. Mater.*, 2003, **15**, 353.

[54] C. N. R. Rao, F. L. Deepak, G. Gundiah and A. Govindaraj, *Progress in Solid State Chem.*, 2003, **31**, 5.

[55] E. I. Givargizov, *Highly Anisotropic Crystals*, (Eds. M. Senechal, S. College), Reidel, Dordrecht, The Netherlands, 1987.

[56] R. S. Wagner, *Whisker Technology*, (Ed: Levitt AP), Wiley-Interscience, New York, 1970.

[57] R. S. Wagner and W. C. Ellis, *Appl. Phys. Lett.*, 1964, **4**, 89.

[58] Y. Wu, P. Yang, *J. Am. Chem. Soc.*, 2001, **123**, 3165.

[59] M.H. Huang, Y. Wu, H. Feick, N. Tran, E. Weber and P. Yang, *Adv. Mater.*, 2001, **13**, 113.

[60] M.H. Huang, S. Mao, H. Feick, H. Yan, Y. Wu, H. Kind, E. Weber, R. Russo and P. Yang, *Science*, 2001, **292**, 1897.

[61] C. C. Chen and C. C. Yeh, *Adv. Mater.*, 2000, **12**, 738.

32

[62] Y. Wang, G. Meng, L. Zhang, C. Liang and J. Zhang, *Chem. Mater.*, 2002, **14**, 1773.

[63] S. T. Lee, N. Wang, Y. F. Zhang and Y. H. Tang, *MRS Bull.*, 1999, **36**.

[64] N. Wang, Y. H. Tang, Y. F. Zhang, C. S. Lee and S. T. Lee, *Phys. Rev. B*, 1998, **58**, R16024-R16026.

[65] J. J. Stejny, R. W. Trinder and J. Dlugosz, *J. Mater. Sci.*, 1981, **16**, 3161.

[66] J. J. Stejny, R. W. Dlugosz and A. Keller, *J. Mater. Sci.*, 1979, **14**, 1291.

[67] B. Gates, B. Mayers, B. Cattle and Y. Xia, *Adv. Funct. Mater.*, 2002, **12**, 219.

[68] B. Mayers and Y. Xia, *J. Mater. Chem.*, 2002, **12**, 1875.

[69] B. Messer, J. H. Song, M. Huang, Y. Wu, F. Kim and P. Yang, *Adv. Mater.*, 2000, **12**, 1526.

[70] J. Song, B. Messer, Y. Wu, H. Kind and P. Yang, *J. Am. Chem. Soc.*, 2001, **123**, 9714.

[71] C. R. Martin, *Science*, 1994, **266**, 1961.

[72] D. Almawlawi, C. Z. Liu, and M. Moskovits, *J. Mater. Res.*, 1994, **9**, 1014.

[73] M. Zheng, L. Zhang, X Zhang, J. Zhang and G. Li, *Chem. Phys. Lett.*, 2001, **334**, 298.

[74] Y. Xia, P. Yang, Y. Sun, Y. Wu, B. Mayers, B. Gates, Y. Yin, F. Kim and H. Yan, *Adv. Mater.*, 2003, **15**, 353.

[75] H. Ringsdorf, B. Schlarb and J. Verzmer, *Angew. Chem. Int. Ed.*, 1988, **27**, 113.

[76] A. Govindaraj, F. L. Deepak, N. A. Gunari and C. N. R. Rao, *Israel J. Chem.*, 2001, **41**, 23.

[77] Y. Yin, Y. Lu, Y. Sun and Y. Xia, *NanoLett.*, 2002, **2**, 427.

References

[78] B. Gates, Y. Wu, Y. Yin, P. Yang and Y. Xia, *J. Am. Chem. Soc.*, 2001, **123**, 11500.

[79] A. Govindaraj, B. C. Satishkumar, M. Nath and C. N. R. Rao, *Chem. Mater.*, 2000, **12**, 202.

[80] T. J. Trentler, K. M. Hickman, S. C. Geol, A. M. Viano, P. C. Gibbons and W. E. Buhro, *Science*, 1995, **270**, 1791.

[81] T. J. Trentler, S. C. Goel, K. M. Hickman, A. M. Viano, M. Y. Chiang, A. M. Beatty, P. C. Gibbons and W. E. Buhro, *J. Am. Chem. Soc.*, 1997, **119**, 2172.

[82] P. D. Markowitz, M. P. Zach, P. C. Gibbons, R. M. Penner and W. E. Buhro, *J. Am. Chem. Soc.*, 2001, **123**, 4502.

[83] O. R. Lourie, C. R. Jones, B. M. Bartlett, P. C. Gibbons, R. S. Ruoff and W. E. Buhro, *Chem. Mater.*, 2000, **12**, 1808.

[84] J. D. Holmes, K. P. Johnston, R. C. Doty and B. A. Korgel, *Science*, 2000, **287**, 1471.

[85] L. Manna, E. C. Scher and A. P. Alivisatos, *J. Am. Chem. Soc.*, 2000, **122**, 12700.

[86] J. Li, C. Lu, B. Maynor, S. Huang and J. Liu, *Chem. Mater.*, 2004, **16**, 1633.

[87] D. S. Ginger, H. Zhang and C. A. Mirkin, *Angew. Chem. Int. Ed.*, 2004, **43**, 30 and references therein.

[88] B. Messer, J. H. Song and P. Yang, *J. Am. Chem. Soc.*, 2000, **122**, 10232.

[89] Y. Huang, X. Duan, Q. Q. Wei and C. M. Lieber, *Science*, 2001, **291**, 630.

[90] Y. Wu, H. Yan, M. Huang, B. Messer, J. H. Song and P. Yang, *Chem. Eur. J.*, 2002, **8**, 1260.

[91] F. Kim, S. Kwan, J. Arkana and P. Yang, *J. Am. Chem. Soc.*, 2001, **123**, 4360.

[92] X. Lu, T. Harnath, K. P. Johnston and B. A. Korgel, *Nano Lett.*, 2003, **3**, 93.

[93] T. T. Harnath and B. A. Korgel, *J. Am. Chem. Soc.*, 2001, **124**, 1424.

[94] M. V. Wolkin, J. Jorne, P. M. Fauchet, G. Allan and C. Delerue, *Phys. Rev. Lett.*, 1999, **82**, 197.

[95] J. F. Wang, M. S. Gudiksen, X. F. Duan, Y. Cui and C. M. Lieber, *Science*, 2001, **293**, 1455.

[96] J. C. Johnson, H. Yan, R. D. Schaller, L. H. Haber, R. J. Saykally and P. Yang, *J. Phys. Chem. B*, 2001, **105**, 11387.

[97] E. W. Wong, P. E. Sheehan and C. M. Lieber, *Science*, 1997, **277**, 1971.

[98] Y. Y. Wu and P. Yang, *Appl. Phys. Lett.*, 2000, **77**, 43.

[99] Y. Wu and P. Yang, *Adv. Mater.*, 2001, **13**, 520.

[100] Z. W. Pan, Z. R. Dai, L. Xu, S. T. Lee and Z. L. Wang, *J. Phys. Chem. B*, 2001, **105**, 2507.

[101] H. Y. Peng, Z. W. Pan, L. Xu, X. H. Fan, N. Wang, C. S. Lee and S. T. Lee, *Adv. Mater.*, 2001, **13**, 317.

[102] C. T. White and T. N. Todorov, *Nature*, 1998, **393**, 240.

[103] S. Frank, P. Poncharal, Z. L. Wang and W. A. de Heer, *Science*, 1998, **280**, 1744.

[104] Z. Yao, H. W. Postma, L. Balents and C. Dekker, *Nature*, 1999, **402**, 273.

[105] S. J. Trans, A. R. M. Verschueren and C. Dekker, *Nature*, 1998, **393**, 49.

[106] R. Martel, T. Schmidt, H. R. Shea, T. Hertel and Ph. Avouris, *Appl. Phys. Lett.*, 1998, **73**, 2447.

[107] Y. Cui, X. Duan, J. Hu and C. M. Lieber, *J. Phys. Chem. B*, 2000, **104**, 5213.

[108] Y. Cui and C. M. Lieber, *Science*, 2001, **291**, 851.

[109] Y. Huang, X. F. Duan, Y. Cui, L. J. Lauhon, K. H. Kim and C. M. Lieber, *Science*, 2001, **294**, 1313.

1.2 Carbon-assisted synthesis of inorganic nanowires

1.2.1 Introduction

There has been intense interest in the synthesis and characterization of nanowires of inorganic materials such as metal oxides, sulfides, nitrides and carbides in the last three to four years. Among the several strategies developed for the synthesis of these materials, the vapor-solid and vapor-liquid-solid routes are the means to prepare crystalline nanowires of many of these materials which include oxides, nitrides, carbides and elements. We have employed the carbothermal route which involves heating a mixture of an oxide with an appropriate quantity of carbon in an appropriate atmosphere. For example, ammonia provides the atmosphere for the formation of nitrides. An inert atmosphere and a slight excess of carbon yield carbides. In these reactions, carbon helps to form an oxidic species, usually a sub-oxide, in the vapor phase, which then transforms to the final crystalline product. By perfecting the carbon-assisted synthesis, we have successfully prepared nanowires of elemental silicon, metal oxides, silicon carbide and silicon nitride. In what follows, we describe the scope of the investigations carried out on nanowires.

1.2.2 Scope of the present investigations

(a) Nanowires, nanobelts and related nanostructures of Ga_2O_3

β-Ga_2O_3 is a wide band gap semiconductor ($E_g = 4.9$ eV) with intense luminescent properties [1]. We have been interested in synthesizing nanowires, nanorods and other nanostructures of β-Ga_2O_3. Zhang et al. [2] prepared Ga_2O_3 nanowires by the evaporation of bulk Ga at 300 °C under a pressure of 100 Torr in a mixture of 90 % Ar and 10 % H_2 gases at a flow rate of 30 standard cubic centimeter per minute (sccm). β-Ga_2O_3 nanowires have been synthesized by Choi et al. [3]

using direct current arc discharge of GaN powders in a mixture of Ar and O_2 gases in the presence of a small amount of a transition metal catalyst. Wu *et al.* [4], on the other hand, have prepared Ga_2O_3 nanowires by the carbothermal reduction starting with a mixture of gallium oxide powder and graphite. The reactions were carried out at 980 °C for 2 h in flowing N_2 atmosphere (20 sccm). Liang *et al.* [5] have recently obtained β-Ga_2O_3 nanowires by heating a composite material of GaAs and pre-evaporated Au at 1240 °C in dry O_2 atmosphere.

We have developed a simple method to synthesize nanostructures of β-Ga_2O_3, starting with Ga_2O_3 powder mixed with activated carbon or carbon nanotubes. The nanostructures obtained include not only nanowires, but also nanobelts. The width of the nanowires could be controlled by adjusting the flow rate of the argon gas going through the furnace. Besides determining the direction of growth of the nanowires, we have measured the luminescent properties.

(b) ZnO nanowires

There has been a surge in the reports of synthesis of 1D nanostructures of ZnO after Huang *et al.* [6] demonstrated room temperature lasing in ZnO nanowire arrays obtained by a vapor transport process [7]. Low-temperature growth of aligned ZnO nanowires has been achieved by the evaporation of Zn metal onto NiO catalyst dispersed on an alumina substrate [8]. Substrates such as Cu on Si(100) have also been used for the growth of ZnO nanowires by the vapor-liquid-solid VLS) process [9]. Lee *et al.* [10] synthesized aligned zinc oxide nanowires at low temperatures by the condensation of Zn vapor on Co nanoparticles spread over silicon substrates in an Ar atmosphere. Evaporation of ZnO at high temperatures in the absence of a catalyst also yields ZnO nanowires [11]. Electrochemical techniques and porous alumina membranes have also been used to prepare ZnO nanowires, the latter giving ordered nanowire arrays [12, 13]. Solution-based [14] as well as microemulsion-mediated hydrothermal routes [15] can be employed to prepare ZnO nanowires. ZnO nanorods were grown recently on bare silica or silicon substrates at a temperature of 500 °C in a two-heating-zone furnace using zinc acetylacetonate hydrate as the precursor [16]. Vertically aligned ZnO nanorods are obtained by using

38

a metal organic vapor-phase epitaxy method in the absence of any catalyst [17].

We have been exploring simple ways to prepare ZnO nanowires by employing carbothermal procedures wherein activated carbon or carbon nanotubes is one of the reactants. We could prepare ZnO nanowires by the carbothermal reduction route starting with zinc oxalate or ZnO along with active carbon or carbon nanotubes. The nanowires obtained have been characterized by X-ray diffraction, scanning electron microscopy, transmission electron microscopy and photoluminescence.

(c) Crystalline silica nanowires

Among the various one-dimensional inorganic nanostructures, much attention has been devoted to the synthesis of nanotubes and nanowires of silica [18–21]. Using molten Ga as the catalyst, the vapor-liquid-solid process has been employed to obtain aligned silica nanowires [22, 23]. Use of other catalysts such as Sn also yields densely aligned silica nanowires by a similar process [24]. Other methods for the synthesis include the laser ablation of a mixture of Si, SiO_2 and Fe [25], thermal oxidation of Si wafers [26] and the oxidation of Si vapor catalyzed by Au [27]. Thermal treatment of Si powder with graphite is also found to yield silica nanowires [28]. A recent report employs the solid state transformation of silica films to obtain silica nanowires [29]. The transformation of silica nanowires to nanotubes has also been examined [30].

In all the preparations reported hitherto, the silica nanowires obtained are amorphous showing intense blue luminescence. We were interested to explore the possibility of producing crystalline silica nanowires. The nanowires might find useful applications in optical communications, nanosensors and other areas. Besides, it would be interesting to establish the exact conditions under which they form. For this purpose, we have employed the carbon-assisted process, which has proved effective in the synthesis of nanowires of several oxide materials. In this work, the first successful synthesis of single-crystalline α-cristobalite nanowires is described.

(d) Silicon nanowires

In recent times, silicon nanowires (SiNWs) have received considerable attention and several methods have been employed for their synthesis. These include thermal evaporation of Si powder [31], vapor-liquid-solid (VLS) method involving liquid metal solvents with low solubility for Si [32], laser ablation [33, 34], and the use of silicon oxide in mixture with Si [35, 36]. SiO_2-sheathed crystalline SiNWs have been obtained by heating Si-SiO_2 mixtures [37]. It has been recently reported that enhanced yields of SiNWs are obtained by heating a Si substrate coated with carbon nanoparticles at 1050 °C under vacuum [38].

We consider the role of carbon to be as in other carbothermal methods of synthesizing nanowires of oxides, nitrides and other materials, involving a vapor-solid mechanism wherein carbon reacts with the oxide probably producing a suboxide-type species. In the case of SiNWs, we make use of the oxide layer on elemental silicon for the reaction with carbon. We have carried out the carbon-assisted synthesis of SiNWs and report the important findings, of relevance to the vapor-solid and oxide-assisted growth of SiNWs.

(e) Silicon carbide, silicon oxynitride and silicon nitride nanowires

Silicon carbide (SiC) nanowires possess high elasticity and strength and are good candidates for making various types of composites. Nanowires of silicon nitride (Si_3N_4) may have potential applications in nanodevices and in the fabrication of composites. There are several reports on the preparation of SiC nanowires in the literature, but fewer on the preparation of Si_3N_4 nanowires. The methods employed for the synthesis of SiC nanowires have been varied. SiC nanowires were prepared by Dai *et al.* [39] by the reaction between carbon nanotubes and SiO or SiI_2 in a sealed tube under vacuum at 1300-1400 °C and 1100-1200 °C , respectively. Han *et al.* [40] employed a two-step reaction in which SiO vapour was first generated via the reduction of silica and then reacted with carbon nanotubes at 1400 °C in an Ar atmosphere to form SiC nanowires. β-SiC nanowires with and without amorphous silica (SiO_2) wrapping layers have also been obtained by the carbothermal reduction

of sol-gel-derived silica xerogels containing carbon nanoparticles, at 1800 °C and 1650 °C , respectively, in an Ar atmosphere [41]. SiC nanorods have also been prepared from solid sources of carbon and silicon by hot filament chemical vapour deposition [42]. Liang *et al.* [43] used the reaction between activated carbon and sol-gel derived silica embedded with Fe nanoparticles at 1400 °C in an H_2 atmosphere to produce β-SiC nanowires, while Hu *et al.* [44] prepared β-SiC nanowires by the reaction of silicon with carbon tetrachloride (CCl_4) and metallic sodium at 700 °C . Zhang *et al.* [45], on the other hand, used a floating catalyst method wherein $SiCl_4$ was reacted with benzene and floating Fe catalyst particles derived from ferrocene in the presence of H_2 and Ar at around 1150 °C . In the various procedures listed above, the diameters of the nanowires varied between 10 and 100 nm, while the lengths were in the micrometer (μm) range. The reaction of aligned carbon nanotubes with SiO has however been considered to be advantageous, the diameter and the length of the nanowires depending on the nature of the starting carbon nanotubes [46].

In spite of many of the studies mentioned above, there is a need for a simple procedure for the synthesis of SiC nanowires which uses common chemicals as starting materials and avoids extreme conditions. Since both SiC and Si_3N_4 are products of the carbothermal reduction of SiO_2, it should be possible to establish conditions wherein one set of specific conditions favours one over the other. We have carried out detailed investigations on the preparation of SiC nanowires starting with silica gel and activated carbon and by employing NH_3 or H_2 as the reducing agent, the former enabling us to obtain silicon nitride nanowires as well, under slightly modified conditions. The procedure employed by us for SiC nanowires has the advantage that it does not require carbon nanotubes or the use of SiO as the starting material. In addition to the synthesis of SiC nanowires, we have carried out studies to establish a procedure for the synthesis of pure silicon nitride nanowires as well. Han *et al.* [47] obtained nanorods of a mixture of α- and β-forms of silicon nitride along with Si_2N_2O, by heating a mixture of Si and SiO_2 powders with carbon nanotubes in a nitrogen atmosphere at 1400 °C . Silicon nitride whiskers have been prepared by the gas phase reaction between SiO, CO and N_2 at 1350 °C [48] while α-Si_3N_4 nanowires sheathed with Si and SiO_2 have been obtained by heating silicon
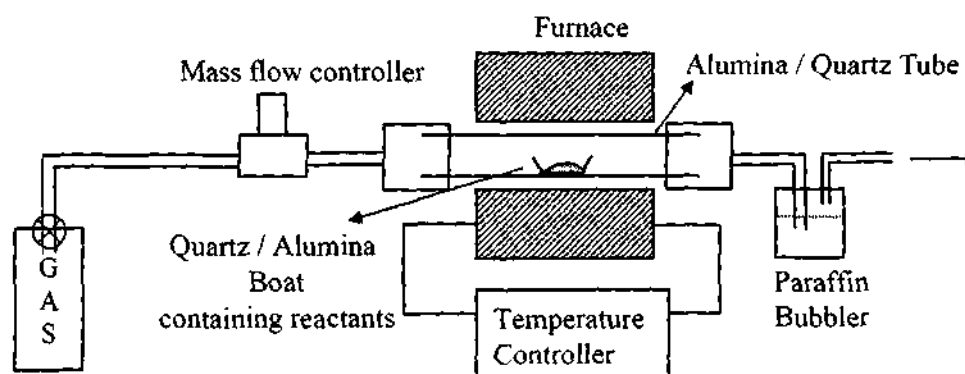
41

Figure 1.2.1: Experimental setup for synthesis of nanowires by the carbon-assisted route.

oxide nanoparticles with carbon in a flowing N_2 atmosphere at 1450 °C [49]. We have found that the reaction of SiO_2 gel with carbon nanotubes or activated carbon with Fe catalyst in the presence of NH_3 yields pure α-Si_3N_4 nanowires.

1.2.3   Experimental and related aspects

The setup employed for the synthesis of the nanowires is shown in Figure 1.2.1. It consists of stainless steel gas flow lines and a furnace fitted with quartz or alumina tube. While using a quartz tube, the reactants were placed in a quartz tube having a smaller diameter than the outer tube. In case of an alumina tube, the reactants were placed in a quartz or ceramic boat. The flow rate of the gas is crucial for the formation of the nanowires and is controlled by means of mass flow controllers. The exact details of the procedures used will be given below.

Synthesis of nanowires, nanobelts and related nanostructures of Ga_2O_3

For the preparation of β-Ga_2O_3 nanowires, we have employed several procedures. In procedure (i), gallium oxide powder was mixed with activated charcoal (Sarabhai Chemicals, India) according to the weight ratio of 1:1.5 and the mixture ground to a fine powder. The mixture was taken in a quartz tube (10 cm in length) with an outer diameter of 8 mm. This tube was kept in the centre of a quartz tube (10 mm outer diameter) placed horizontally in a tubular furnace. The mixture was heated at 1000 °C for 4 h in a flow of Ar gas at 40 sccm. The flow rate of Ar gas

was controlled by a unit mass flow controller. After a period of 4 h, air was let into the reaction tube and the product allowed to reach ambient temperature. This helped to burn out the unreacted carbon and to convert any suboxide of gallium into Ga_2O_3. A white, wool-like product was obtained at the outlet of the inner quartz tube along with a white powder at the outlet of the outer tube. These products were collected separately and analyzed. Procedure (ii) was the same as procedure (i) except that activated carbon prepared by the thermal decomposition of polyethylene glycol (600 units) at 700 °C in a N_2 atmosphere was used in place of activated charcoal. In procedure (iii), we employed multi-walled carbon nanotubes as the source of carbon. The multi-walled carbon nanotubes were prepared by the arc-discharge method outlined in the literature [50]. The rest of the procedure was the same as in (i). In order to see the effect that the flow rate plays on the final product, we performed the reaction at different flow rates of Ar (40, 60 and 80 sccm). As we increased the flow rate, the amount of product carried to the outlet increased. Thus, at a flow rate of 80 sccm, the amount of product obtained at the inner tube was negligible and the entire product was present at the outlet.

Synthesis of ZnO nanowires

For the synthesis of ZnO nanowires, we have employed several procedures. Procedure (i) involved the solid-state reaction between zinc oxalate and multi-walled carbon nanotubes (MWNTs). MWNTs were prepared by the arc discharge method outlined in the literature [50]. In a typical synthesis, zinc oxalate was mixed with MWNTs according to the weight ratio 1.5 : 1 and the mixture ground to a fine powder. The mixture was taken at one end of a quartz tube (10 cm in length) with an outer diameter of 8 mm. This tube was kept in the center of a quartz tube (16 mm outer diameter) placed horizontally in a tubular furnace. The mixture was heated to 900 °C for a period of 3 h in an Ar atmosphere of 25 sccm, and the temperature maintained for 1 h after which O_2 gas was mixed with Ar for a duration of 1 h. During the last 1 h, the flow of Ar was stopped and the sample was heated in flowing O_2 for 1 h and also allowed to cool to room temperature in flowing O_2. This helped to burn out any unreacted carbon and give the correct oxygen stoichiometry of ZnO.

A white product was obtained in the inner quartz tube that was further characterized.

Procedure (ii) was the same as procedure (i) except that active carbon was used in place of MWNTs. In procedure (iii), ZnO powder was used instead of zinc oxalate, the weight ratios of ZnO to MWNTs being 1 : 1. The mixture was finely ground and heated as in procedure (i). Procedure (iv) involved the mixing of ZnO and active carbon in the weight ratio of 1.5 : 1. We have carried out the reaction between Zn oxalate or ZnO with carbon in the presence of Ni catalyst. Thus, procedure (v) involved the reaction of zinc oxalate, MWNTs and Ni taken in the weight ratios of 1 : 1 : 0.13. These were finely ground and then heated to 900 °C as in procedure (i). In procedure (vi), the reaction of zinc oxide, MWNTs and Ni catalyst (weight ratios 1 : 1 : 0.005) was carried out at 900 °C .

Synthesis of silica nanowires

The procedure employed for the synthesis of the α-SiO_2 nanowires was as follows. Fumed silica (Sarabhai Chemicals, India) was thoroughly mixed and ground with activated charcoal (Sarabhai Chemicals, India, heated to 700 °C in a flowing H_2 / He mixture) or activated carbon (prepared by the decomposition of polyethylene glycol-600 units in an Ar atmosphere at 700 °C). The mixture was placed in an alumina boat and heated to 1300 °C (heating and cooling rates 3 °C .min^{-1}) for 5 h in flowing Ar (50 sccm) or a mixture of Ar (50 sccm) and H_2 (20 sccm). The relative molar ratio of the carbon source with respect to fumed silica was varied between 0.5 and 2. The product obtained in the alumina boat was a white or gray powder, which was further characterized.

Synthesis of silicon nanowires

The synthesis of silicon nanowires (SiNWs) has been carried out by employing the following procedures. Procedure (i) involved the solid state synthesis in which silicon powder (Aldrich Chemicals) was finely ground with activated carbon, keeping the molar ratio of Si to C at 1:1 or 1:0.5. The activated carbon was prepared by decomposing polyethylene glycol (600 units) in argon atmosphere at 700 °C for

3 h. The finely ground mixture was taken in an alumina boat and heated at 1200 °C for 3 h in a mixture of Ar (50 sccm) and H_2 (20 sccm). The reaction was also carried out under similar conditions in the absence of carbon to verify whether carbon plays a role in the formation of the nanowires. Procedure (ii) was similar to (i), except that the reactants were heated in an Ar atmosphere (without any H_2). The product obtained was grey or white in color and was collected as fine powders.

In procedure (iii), a silicon substrate was used as the source of silicon. The Si(100) substrates were cleaned by ultrasonication in acetone as well as distilled water. Amorphous carbon was sputtered on the substrates using a JEOL JEE-400 vacuum evaporator, with a sputtering time of 0.5-1 min. The carbon-coated Si substrates were heated to 1350 °C for 3 h in an atmosphere of Ar/H_2 (25 sccm each). The product formed as a layer on the substrate was grey or white in color. A blank run with the silicon substrate without any sputtered carbon was carried out under similar conditions.

Synthesis of silicon carbide, silicon oxynitride and silicon nitride nanowires

For the preparation of SiC nanowires, we have employed several methods. In procedure (i), silica gel prepared in admixture with activated carbon, was dried, and heated to 1360 °C (4-7 h) in an NH_3 or a H_2 atmosphere. Activated carbon was prepared by the thermal decomposition of polyethylene glycol (600 units) at 700 °C for 3 h in an Ar atmosphere. In a typical experiment, 2 ml of tetraethylorthosilicate (TEOS) was mixed with 10 ml of ethanol under stirring for 10–15 min. To this solution, 0.424 g of activated carbon was added (giving a C : Si molar ratio of 4 : 1), followed by 1 ml of aqueous HF (48 % A.R.) and the stirring continued. After gelation of the above solution, the gel was dried at 125 °C for 12–15 h. The gel containing finely distributed activated carbon was powdered, taken in an alumina boat and placed in a tubular furnace, purged earlier with NH_3 gas for 15 min. The gel powder was heated at an appropriate temperature in the 1100–1360 °C range for several hours with the flow of NH_3 maintained at 10 ml.min^{-1}. Instead of NH_3, H_2 was also used in this procedure. A grey, wool-like product was deposited on the walls of the alumina boat. This was collected and analyzed.

45

Procedure (ii) for the preparation of SiC nanowires involved a solid state synthesis in which fumed silica (Grade M-5, surface area 210 m^2g^{-1}, Cabot Corporation) was finely ground with activated carbon, keeping the molar ratio of C : Si at 4 : 1. The mixture was reduced under conditions similar to those in procedure (i). In procedure (iii), a homogenous gel was prepared by the reaction of ethylene glycol with citric acid in the presence of TEOS at elevated temperatures, by the following procedure. In a typical synthesis, 1.5 ml of ethylene glycol was mixed with 3.5 g of citric acid followed by the addition of 2 ml of TEOS. The sample was heated at 80 °C for 12 h, at 120 °C for 6 h and finally at 180 °C for 12 h. The dried gel so obtained was reduced as in procedure (i).

In order to prepare Si_3N_4 nanowires, we have used multi-walled carbon nanotubes as the carbon source instead of activated carbon. The nanotubes have higher thermal stability than activated carbon. The multi-walled nanotubes were prepared by the arc discharge method as well as by the pyrolysis technique outlined in the literature [50, 51]. The procedure was similar to procedure (i) used for the synthesis of SiC nanowires. NH_3 was used to provide a reducing atmosphere as well as to carry out nitridation. The reaction was also carried out in the presence of an Fe catalyst prepared *in situ* by taking ferric nitrate along with the other reactants. The proportion of Fe was varied between 0.1 and 0.5 mol %. Instead of using multi-walled carbon nanotubes prepared by the arc-discharge method, we have also used aligned multi-walled carbon nanotubes with or without catalytic Fe particles. Aligned multi-walled nanotubes were prepared by the pyrolysis of ferrocene along with acetylene in an Ar atmosphere [52]. Most of the reactions were carried out at 1360 °C and a few of them at 1100 °C . The grey colored, wool-like product in each case was collected and analyzed.

In order to prepare Si_3N_4 nanowires, we have also used the reaction of silica gel and NH_3 in the presence of activated carbon (as in procedure (i) for SiC nanowires) and catalytic iron particles. The Fe particles were incorporated by taking ferric nitrate along with TEOS and activated carbon during the preparation of the silica gel. Graphite powder was also used in place of the other carbon sources in procedure (i). The reaction of graphite powder at 1360 °C did not give us the carbide or the nitride

due to the stability of graphite as compared with the other carbon sources.

Techniques used for characterization

X-ray diffraction

Powder X-ray diffraction patterns were recorded using Cu-Kα radiation on a Rich-Siefert, XRD-3000-TT diffractometer. Samples were prepared by finely grinding the product and depositing on a glass slide.

Scanning electron microscopy

Scanning electron microscopy (SEM) images were obtained on a LEICA S440i scanning electron microscope. Energy dispersive analysis of X-rays (EDAX) was performed with a Oxford microanalysis group 5526 system attached to the SEM employing Links (ISIS) software and a Si(Li) detector. Samples for SEM and EDAX were prepared by spreading 10–20 mg of product onto a conducting carbon tape pasted on a aluminum stub, followed by sputter-coating with a gold film. EDAX analysis was carried out in the spot profile mode with a beam diameter of 1 μm at several places on the sample.

Transmission electron microscopy

Transmission electron microscopy (TEM) images were obtained with a JEOL JEM 3010 operating with an accelerating voltage of 300 kV. Samples for TEM studies were prepared by dispersing the nanostructures by sonication in CCl$_4$. A drop of the suspension was put on a holey carbon coated Cu grid and allowed to evaporate slowly.

Photoluminescence

Photoluminescence measurements were carried out at room temperature with a Perkin Elmer model LS50B luminescence spectrometer. The excitation wavelength used depended on the sample that was being studied.

Raman scattering

The Raman experiments were performed in a quasi-backscattering geometry. The Raman spectra were measured at room temperature using a Nd-YAG laser at 532 nm, and an Ar-ion laser at 488 and 514.5 nm. The Raman spectra show no remarkable resonance enhancement. The scattered light was collected using an optical fiber through a Super Notch filter, dispersed by a single monochromator with $f \sim 0.55$ m (Spex 550) and detected by a cooled CCD.

Infrared spectroscopy

Infrared spectra were recorded with a Bruker FT-IR spectrometer. The samples were prepared by grinding with KBr and pressing into a disk.

Differential Scanning Calorimetry

Differential Scanning Calorimetry analysis was carried out using a Perkin-Elmer instrument by taking a small quantity of the sample and heating at a constant rate.

1.2.4 Results and discussion

(a) Nanowires, nanobelts and related nanostructures of Ga_2O_3

The reaction of activated charcoal with gallium oxide powder by procedure (i) yields a mixture of nanosheets and nanowires of Ga_2O_3 at the outlet of the inner tube as revealed in Figure 1.2.2(a). The diameter of the nanowires is between 300 and 400 nm and the length extends to tens of microns. The nanosheets are rectangular with a width of around 5 μm and the length going upto tens of microns. XRD patterns of these nanostructures showed them to be β-Ga_2O_3 with a monoclinic structure (JCPDS card: No. 11-0370).

When the reaction was carried out with activated carbon by procedure (ii), we obtain nanorods of β-Ga_2O_3 at the outlet of the outer tube, as shown in Figure 1.2.2(b). These have diameters in the range 500-1000 nm and lengths between
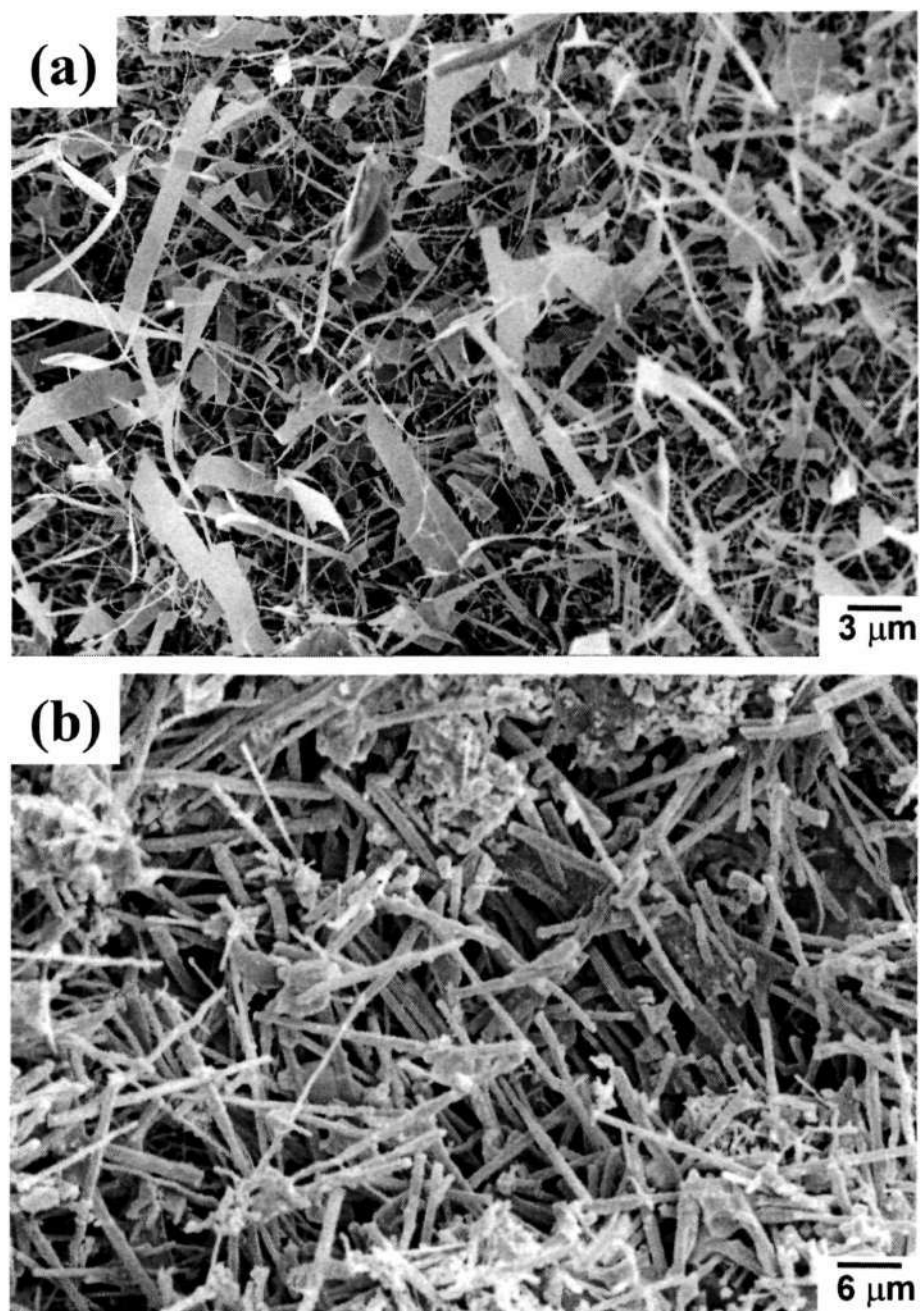
Figure 1.2.2: (a) SEM image of Ga_2O_3 nanosheets and nanowires prepared by procedure (i). (b) SEM image of Ga_2O_3 nanorods prepared by procedure (ii).

10 and 15 μm. XRD patterns confirmed the nanorods to be of β-Ga$_2$O$_3$. On increasing the flow rate of Ar from 40 to 60 sccm, there was a distinct change in the morphology. We obtained nanosheets and nanowires at a flow rate of 40 sccm with activated charcoal while at 60 sccm with activated carbon, we obtained nanorods.

Activated carbon has a large surface area and is oxidized around 500 °C , and is more reactive than multi-walled carbon nanotubes prepared by the arc-discharge method. The nanotubes have a considerably lower surface area and are oxidized around 700 °C . The reaction of Ga$_2$O$_3$ powder with multi-walled nanotubes by procedure (iii) at an Ar flow rate of 40 sccm yielded a mixture of nanosheets and nanobelts at the inner tube. The XRD pattern confirmed that the product obtained was β-Ga$_2$O$_3$. A SEM image of the sample collected at the inner tube (Figure 1.2.3(a)) reveals the morphology of the belts and sheets. The nanosheets have widths going upto 10 μm and lengths of tens of microns. The nanobelts, however, have a much smaller width as can be seen from the low magnification TEM image of a nanobelt in (Figure 1.2.4(a)). Nanobelts of semiconducting oxides such as SnO$_2$ and Ga$_2$O$_3$ have been prepared by Pan *et al.* [53] by the thermal evaporation of oxide powders under controlled conditions. The nanobelts obtained by us typically have widths of 150-200 nm, with lengths extending to tens of microns. The selected area electron diffraction (SAED) pattern of a nanobelt is shown in the inset in Figure 1.2.4 (a). The reflections correspond to the (104), ($\bar{2}$11) and ($\bar{2}$02) planes of β-Ga$_2$O$_3$. The SEM image of the product obtained at the outlet by procedure (iii) is shown in Figure 1.2.3(b). The product mainly consists of nanowires with a diameter of around 1 μm and a length of several microns. It appears that the lighter products such as the nanowires are carried to the outlet whereas the heavier nanobelts and nanosheets are deposited on the inner tube. When the reaction was carried out in the absence of any carbon source under similar conditions, we did not obtain any nanowires.

On increasing the flow rate of Ar to 60 sccm in procedure (iii) and maintaining the rest of the parameters the same, there was a marked change in the morphology and in the dimensions of the nanostructures. In Figure 1.2.5(a) we show a SEM image of the product obtained at the outlet of the inner tube. At this flow rate, the
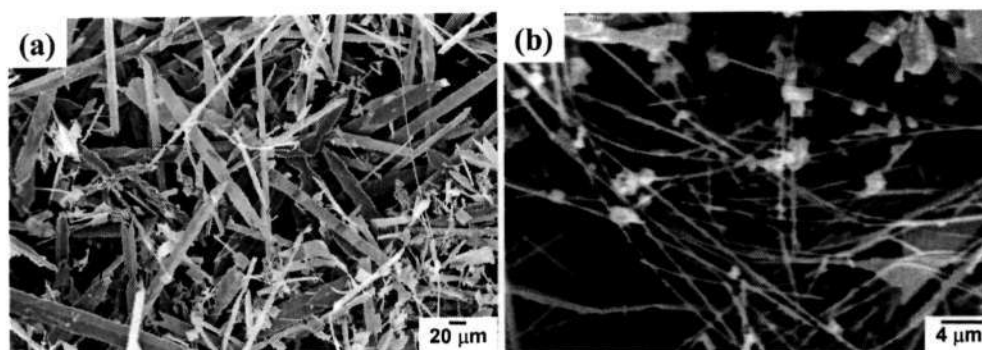
Figure 1.2.3: SEM images of nanostructures obtained by procedure (iii) when the Ar flow rate was maintained at 40 sccm and the product was collected at the (a) inner tube and (b) outlet.
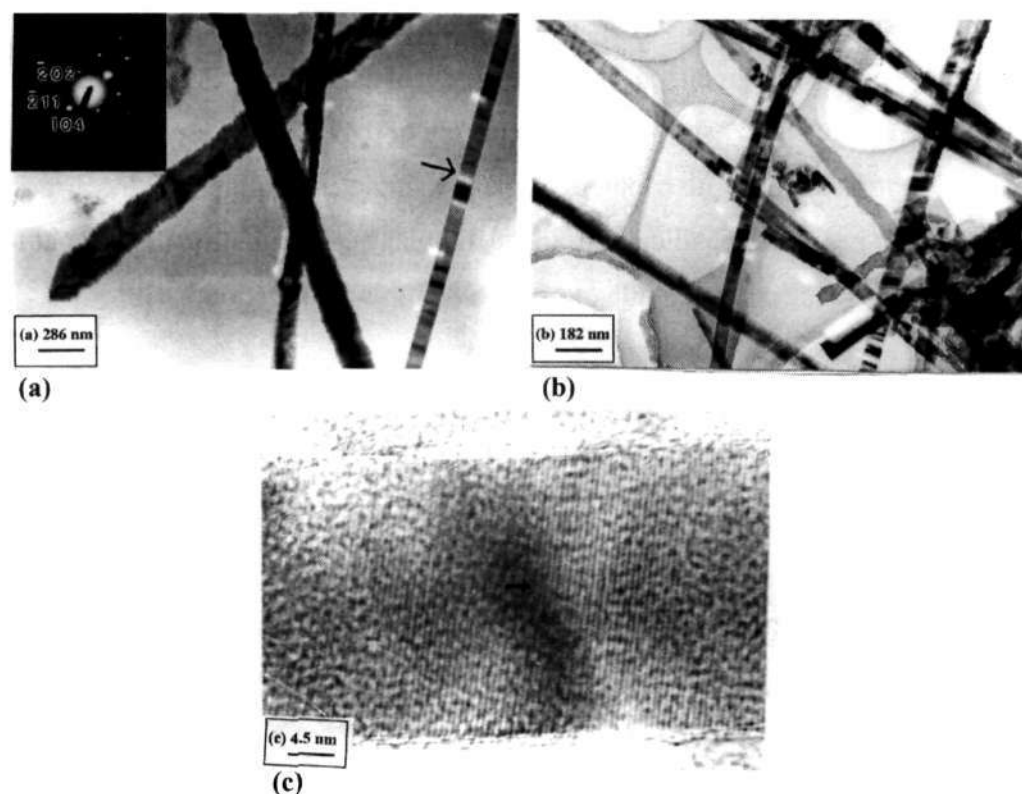
Figure 1.2.4: Low magnification TEM images of the nanowires obtained by the procedure (iii) (a) at a flow rate of Ar maintained at 40 sccm and the product collected at the inner tube. The arrow shows a nanobelt. Inset is the SAED pattern of the sample. (b) Flow rate of Ar maintained at 80 sccm and the product collected at the outlet. (c) HREM of a gallium oxide nanowire obtained on the inner tube by procedure (iii) on maintaining the flow of the Ar gas at 60 sccm. The arrow indicates the growth direction that makes an angle of $\sim 6°$ with the normal to the $(\bar{1}02)$ planes.

51

yield of nanowires was high, compared to that of the nanosheets or the nanobelts, which are predominantly formed at lower flow rates of Ar. The nanowires have a diameter of around 500 nm with lengths of several microns. Thinner nanowires were formed at the outlet as shown in the SEM image in Figure 1.2.5(b). These nanowires have a diameter of around 300 nm. On further increasing the flow rate of Ar to 80 sccm, no product accumulated at the inner tube. The entire product was present at the outlet and SEM images of this sample showed them to entirely comprising nanowires of a considerably smaller diameter than that obtained at lower flow-rates. The low magnification TEM image in Figure 1.2.4(b) shows nanowires with diameters of around 70 nm.

A high-resolution electron microscopic (HREM) image of a nanowire synthesized by procedure (iii) obtained at Ar flow-rate of 60 sccm is shown in Figure 1.2.4(c). The image clearly shows a lattice spacing of 0.47 nm, corresponding to the $(\bar{1}02)$ planes of β-Ga_2O_3. The nanowire is clearly single crystalline with the growth direction being nearly perpendicular to the $(\bar{1}02)$ planes. In actuality, the normal to the $(\bar{1}02)$ planes make a small angle of $6°$ with the growth direction.

The growth mechanism of the nanowires can be explained on the basis of a vapor-solid mechanism since there are no droplets present at the ends of the nanowires. The reactions that may be involved in the formation of the nanowires are as follows:

$$Ga_2O_3(s) + 2C(s) \longrightarrow Ga_2O(v) + 2CO(v) \qquad \cdots \quad (1)$$
$$Ga_2O_3(s) + 3C(s) \longrightarrow 2Ga(v) + 3CO(v) \qquad \cdots \quad (2)$$
$$Ga_2O(v) + O_2(g) \longrightarrow Ga_2O_3(s) \qquad \cdots \quad (3)$$
$$4Ga(v) + 3O_2(g) \longrightarrow 2Ga_2O_3(s) \qquad \cdots \quad (4)$$
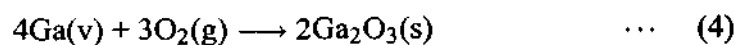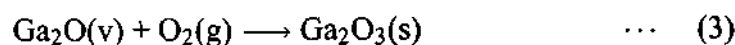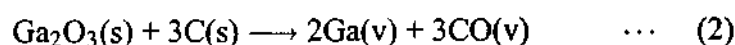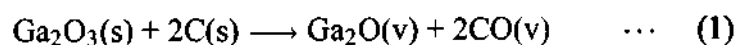
Gallium oxide has been extensively studied for its luminescent properties [1]. We carried out photoluminescence measurements at room temperature at an excitation wavelength of 265 nm. In Figure 1.2.6, we show the PL spectrum of the nanowires prepared by procedure (iii). Two broad peaks are seen at 324 and 405 nm. The intensity of the peak at 324 nm is considerably smaller than that of the peak at 405 nm. The peak at 405 nm is slightly shifted from the peak (436 nm)
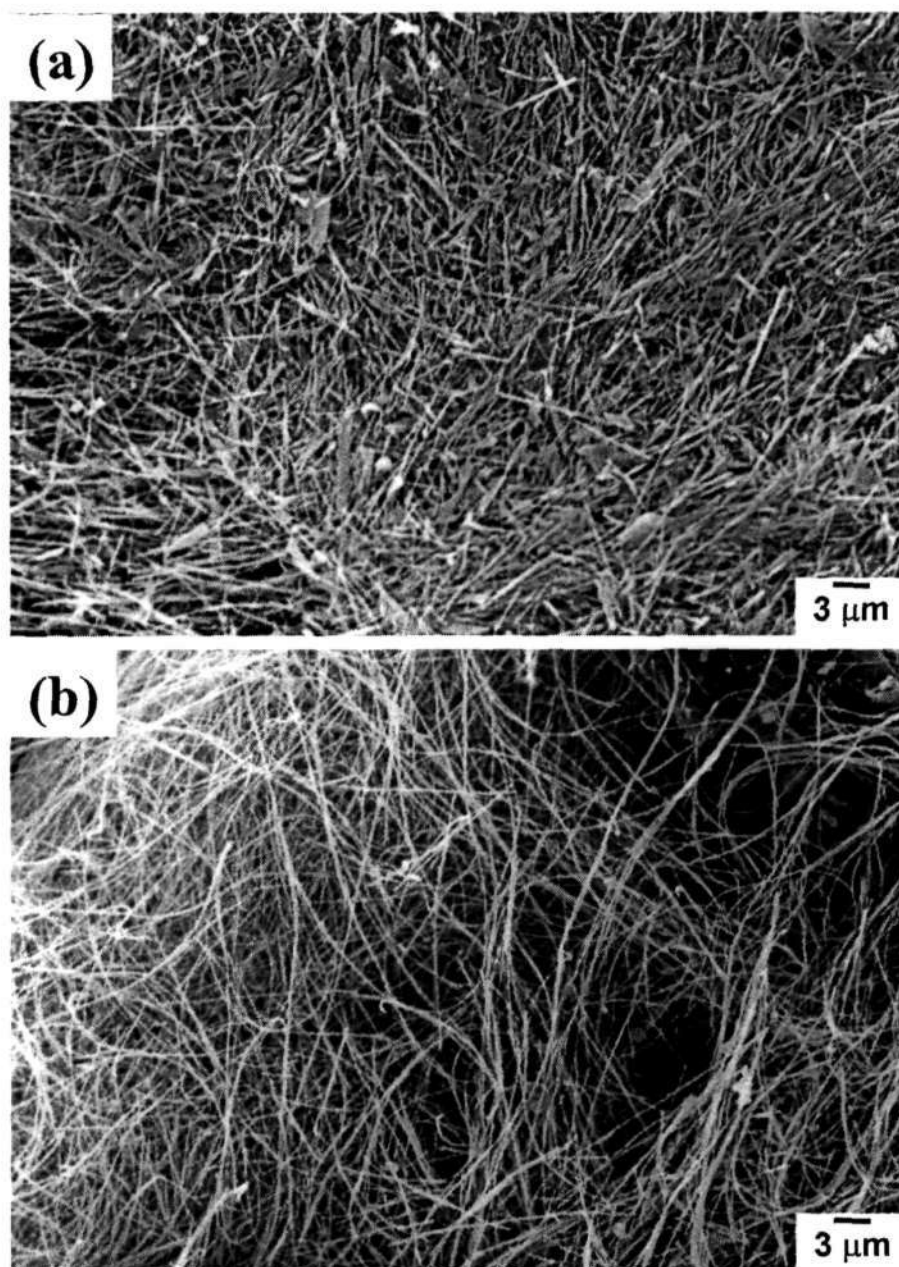
Figure 1.2.5: SEM image of gallium oxide nanowires obtained by procedure (iii) when the reaction was carried out under a flow rate of 60 sccm of Ar gas at (a) the *inlet* and (b) the outlet.

of β-Ga$_2$O$_3$ single crystal [54]. The blue-shift may be due to the small grain size in the nanowires compared to the bulk sample. The mechanism of PL in Ga$_2$O$_3$ is likely to involve the recombination of an electron on the donor and a hole on the acceptor formed by the gallium vacancies [1]. Vasil'tsiv *et al.* [55] propose that the acceptor would be formed by a gallium-oxygen vacancy pair. According to Binet and Gourier [54], after excitation of the acceptor, a hole on the acceptor and an electron on a donor would be created. These combine radiatively to emit a blue photon. By increasing the temperature, the blue emission can be quenched either by electron detrapping from a donor to the conduction band or by hole detrapping from an acceptor to the valence band. The holes and electrons recombine via a self-trapped exciton to emit an UV photon. In the β-Ga$_2$O$_3$ nanowires prepared by us, it is likely that oxygen vacancies and gallium-oxygen vacancy pair are produced, accounting for the presence of one peak in the UV region and another peak slightly shifted from the blue region in the PL spectrum.

In summary, we have been able to prepare different nanostructures of β-Ga$_2$O$_3$ by the reaction of gallium oxide with activated carbon and carbon nanotubes. These include nanosheets and nanobelts besides nanowires. The flow rate of the Ar gas determines the morphology of the final nanostructures, thin nanowires being favored by a high flow rate. The formation of nanobelts is significant since they would be ideal for understanding dimensionally confined transport phenomena in functional oxides and for building functional devices along individual nanobelts. *

(b) ZnO nanowires

The reaction of zinc oxalate with MWNTs at 900 °C by procedure (i) gave a good yield of ZnO nanowires as shown in the SEM image in Figure 1.2.7(a). The diameter of the nanowires is between 300 and 400 nm and the length extends to tens of microns. The XRD pattern of the nanowires showed them to be of the wurtzite phase (JCPDS file: 36–1451). There are no peaks corresponding to any of the starting materials. The diameter of the nanowires is generally larger than that of the reactant MWNTs, ruling out the possibility of a confined reaction. The

---

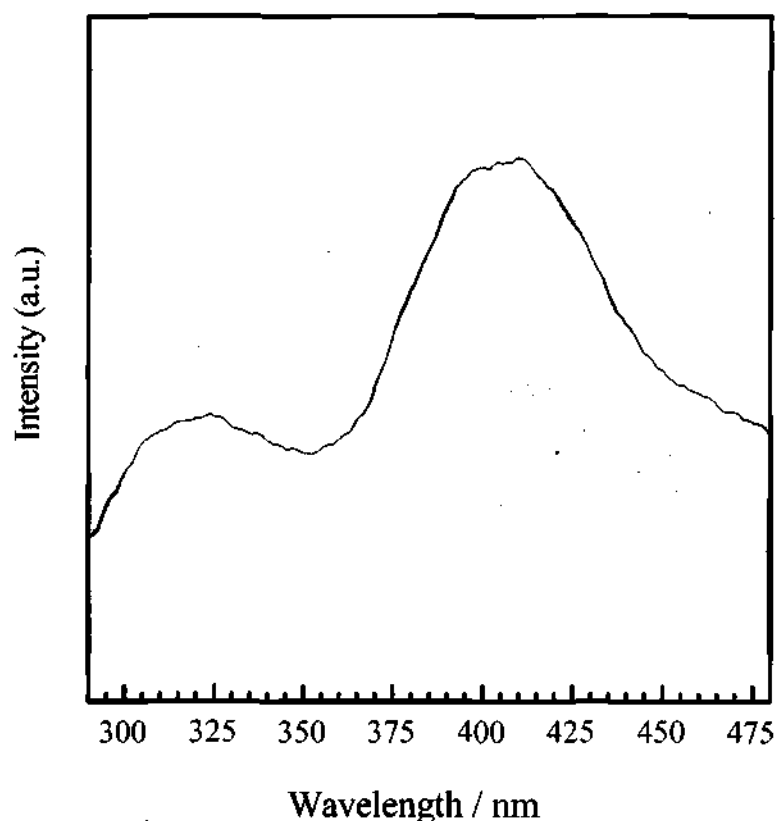*A paper based on this study has appeared in Chem. Phys. Lett., (2002).

Figure 1.2.6: PL spectrum of gallium oxide nanosheets obtained by procedure (iii) on maintaining the flow of the Ar gas at 40 sccm.

HREM image (Figure 1.2.8) reveals the nanowires to be single crystalline with a spacing of 0.26 nm corresponding to (002) planes. The <001> direction appears to be the growth direction of the ZnO nanowires. Other reports in the literature also indicate <001> to be the growth direction for the nanowires [7, 56]. The inset in Figure 1.2.8 gives the characteristic selected area electron diffraction (SAED) of single-crystalline nanowires.

In Figure 1.2.7(b), we show a SEM image of the nanowires obtained by procedure (ii). The nanowires have a diameter of ~400 nm with lengths extending to tens of microns. The XRD pattern confirmed the nanowires to be in the wurtzite phase. The PL spectrum, recorded by using an excitation wavelength of 335 nm, shows a characteristic narrow band at 414 nm and a weaker band at 480 nm (Figure 1.2.9). The 414 nm emission corresponds to the near-band-edge emission, while the long wavelength band is considered to be due to a deep-level or trap-state emission.
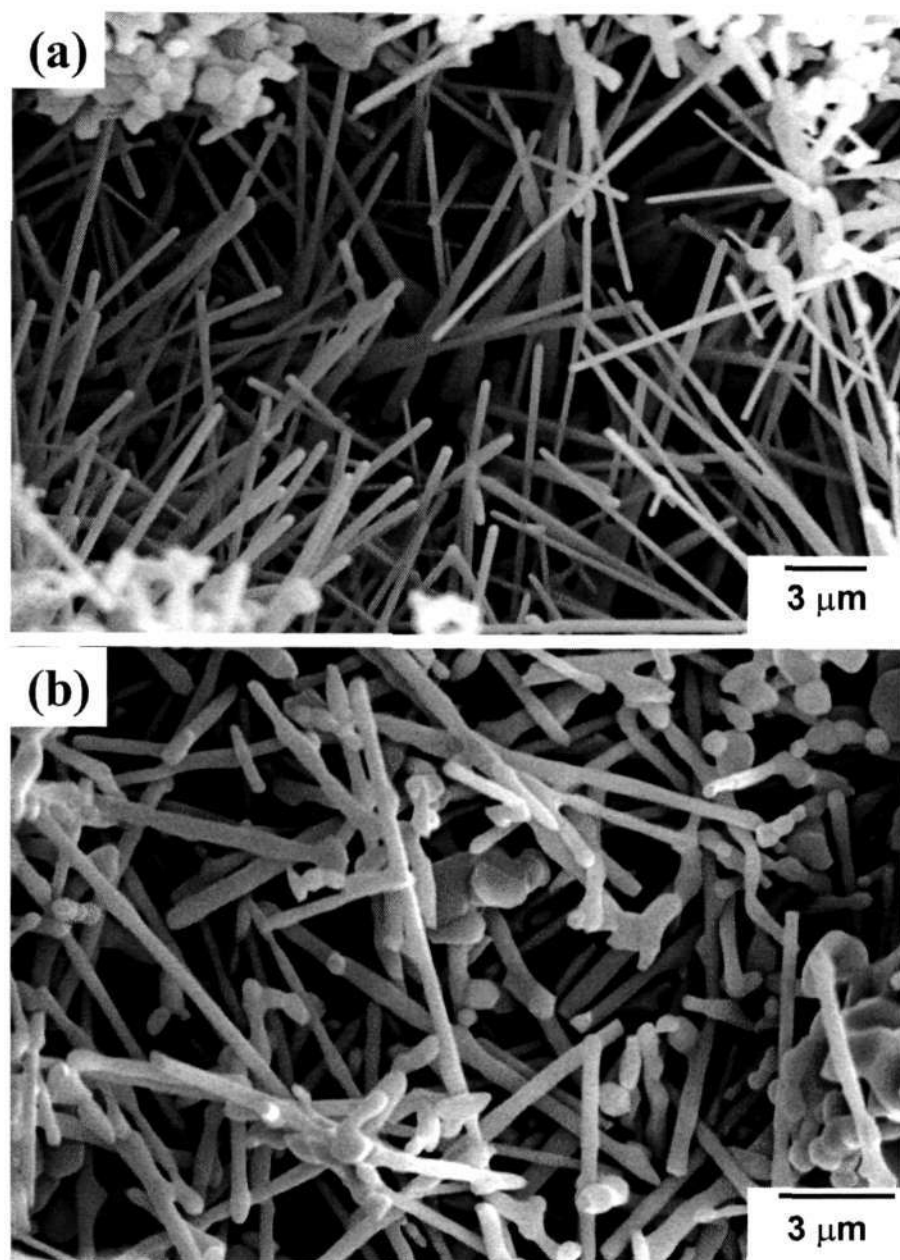
Figure 1.2.7: SEM images of ZnO nanowires obtained by (a) procedure (i) and (b) procedure (ii).
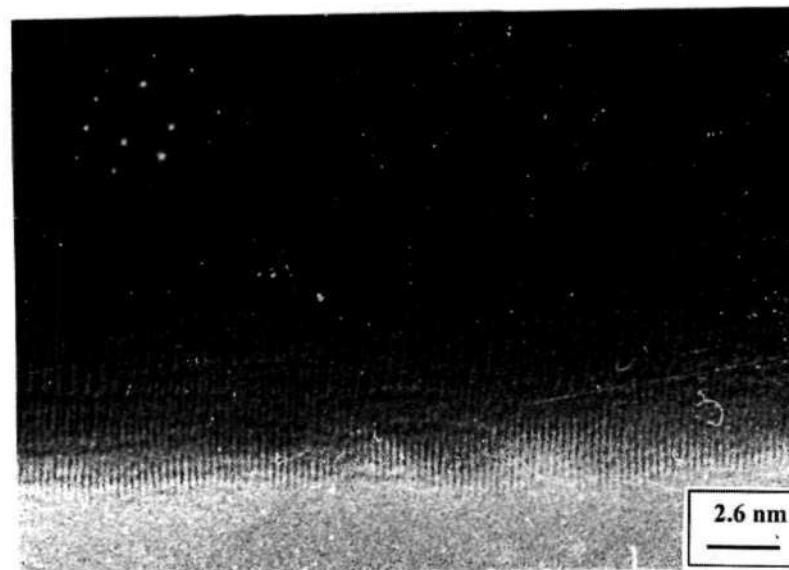
Figure 1.2.8: HREM image of a ZnO nanowire obtained by procedure (i). Inset shows the SAED of a single ZnO nanowires, indicating the single-crystalline structure of ZnO nanowires.

The latter transition is attributed to the singly ionized oxygen vacancy in ZnO, the emission resulting from the radiative recombination of a photogenerated hole with an electron occupying the oxygen vacancy [57].

We could obtain ZnO nanowires by procedure (iii) wherein ZnO was used as the precursor instead of zinc oxalate. In Figure 1.2.10(a), we show an SEM image of the nanowires that have a diameter of ∼400 nm with lengths of tens of microns. The XRD of the samples showed them to be of the wurtzite structure. Procedure (iv), which involved the reaction of ZnO with active C yielded nanowires that had diameters of ∼250 nm with much shorter lengths of a few microns as shown in the SEM image in Figure 1.2.10(b).

In order to find out whether the presence of a catalyst influences the morphology of the nanowires, we carried out the reactions in the presence of Ni catalyst, and the results are shown in Figure 1.2.11. The nanowires obtained by procedure (v) can be seen from the SEM image in Figure 1.2.11(a). The diameters in this case are around 350 nm with lengths of tens of microns. There seems to be no significant thinning of the nanowires due to the presence of catalyst. The nanowires obtained by

57
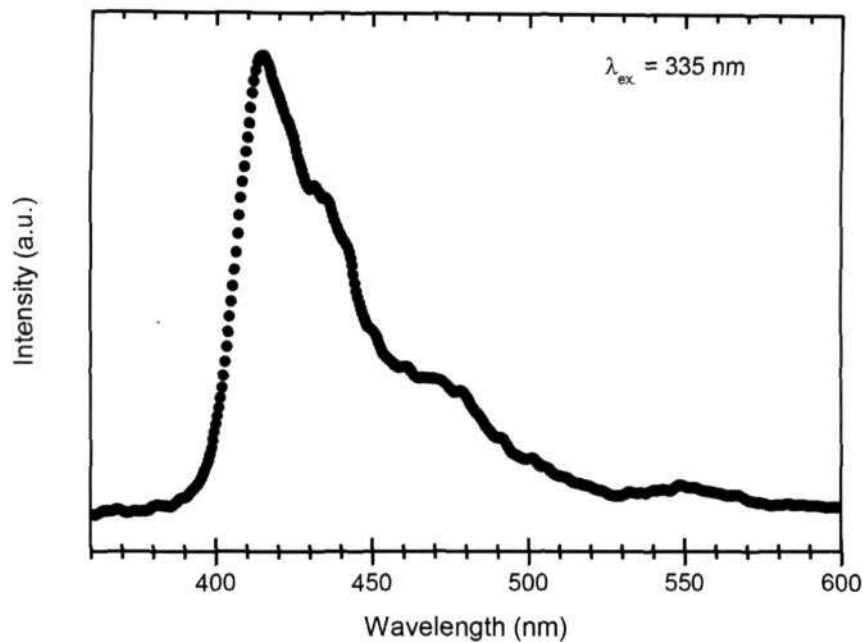
Figure 1.2.9: PL spectrum of ZnO nanowires obtained by procedure (ii).
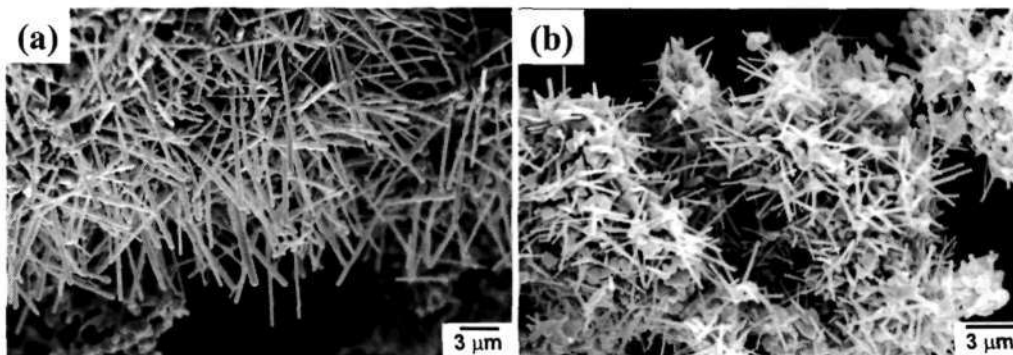
Figure 1.2.10: SEM images of ZnO nanowires obtained by (a) procedure (iii) and (b) procedure (iv).

procedure (vi) shown in the SEM image in Figure 1.2.11(b) also do not reveal any decrease in the diameters. The nanowires have a small aspect ratio with diameters of ~350 nm.

The growth of the nanowires can be explained on the basis of a vapor-solid mechanism since there are no droplets present at the ends of the nanowires. The reactions that may be involved in the formation of the nanowires from zinc oxalate are as follows:
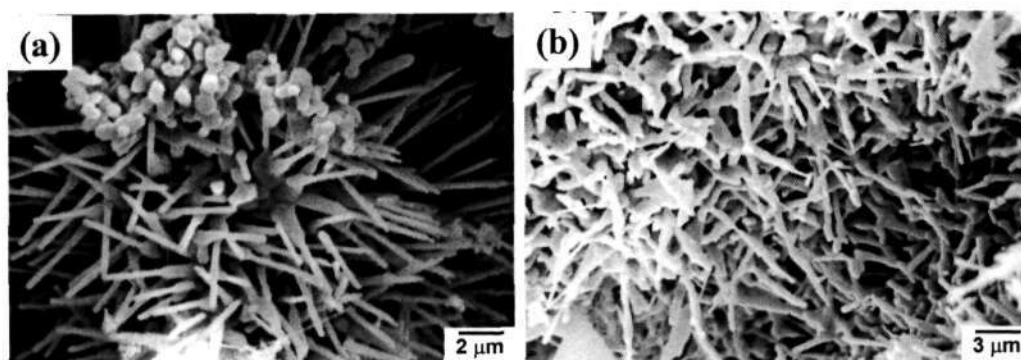
Figure 1.2.11: SEM images of ZnO nanowires obtained by (a) procedure (v) and (b) procedure (vi).

$$ZnC_2O_4(s) \longrightarrow ZnO(s) + CO_2(g) + CO(g) \qquad \cdots \quad (1)$$
$$ZnO(s) + C(s) \longrightarrow Zn(v) + CO(g) \qquad \cdots \quad (2)$$
$$2Zn(v) + O_2(g) \longrightarrow 2ZnO(s) \qquad \cdots \quad (3)$$
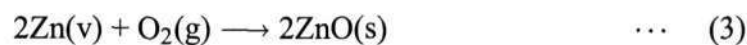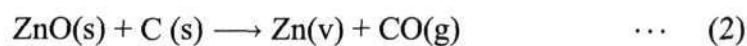
The first step involves in decomposition of zinc oxalate, which leads to the formation of ZnO as shown in (1). This is reduced to Zn in a vapor form that may get nucleated by the quartz tube and further get oxidized to ZnO when O_2 is introduced in the reaction. When ZnO is used as the reactant, steps (2) and (3) may occur. The advantage in using zinc oxalate is that there would be better mixing of the reactants after its decomposition. We obtain nanowires of similar diameter by using MWNTs as well as active carbon, which suggests that carbon may be acting as a reactant and the reaction may be proceeding through the steps (1)–(3) mentioned above.

Thus, nanowires of ZnO have been synthesized by a variety of procedures, all of which involve the use of carbon along with Zn oxalate or ZnO. Along with their interesting optical properties, the nanowires may also be useful as catalyst supports. [†]

[†]A paper based on this study has appeared in Topics in Catalysis, (2003).

(c) Crystalline silica nanowires

In Figure 1.2.12, we show SEM images of the SiO_2 nanowires obtained under different conditions. Shown in Figure 1.2.12(a) are crystalline silica nanowires obtained on heating a mixture of fumed silica and activated charcoal (molar ratio of 1:2) in 50 sccm Ar. The nanowires have a diameter between 50 and 100 nm, with lengths extending upto tens of microns. We notice the presence of a small quantity of unreacted carbon as identified by EDAX. The carbon content is, however, reduced or eliminated by starting with a low carbon:silica ratio. The XRD pattern of the
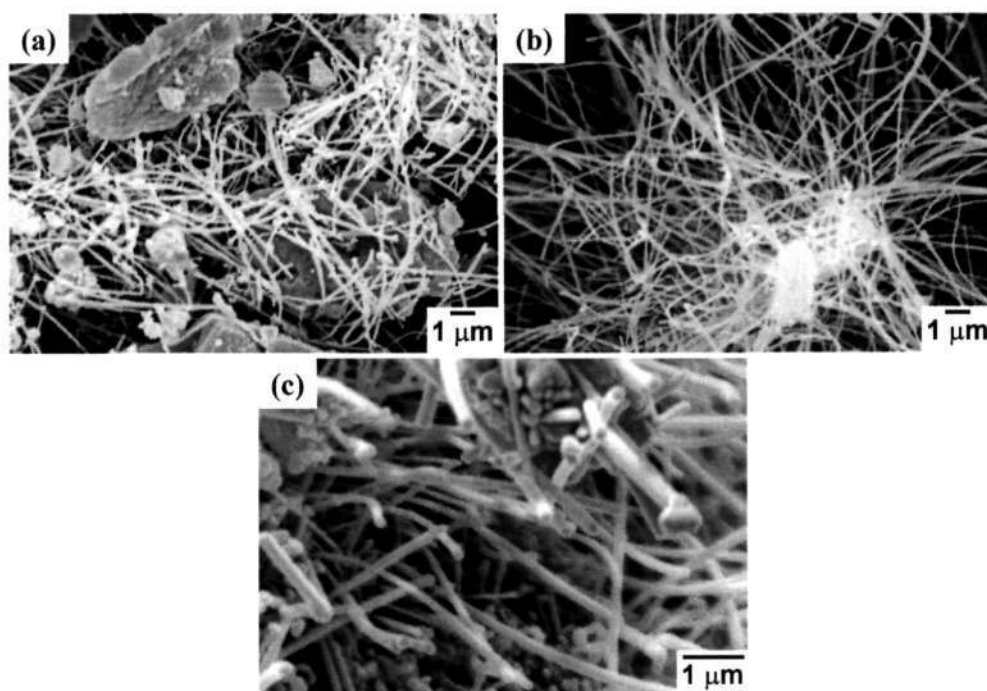
Figure 1.2.12: SEM images of the silica nanowires found in the alumina boat by the reaction of fumed silica with activated charcoal at 1300 °C for 5 h (a) with silica to carbon mole ratio 1:2 in 50 sccm Ar, (b) with a mole ratio 1:0.5 in 50 sccm Ar and (c) with a mole ratio 1:2 in 50 sccm Ar and 20 sccm H_2.

nanowires shown in Figure 1.2.13(a) corresponds to that of α-cristobalite with the tetragonal structure (lattice parameters: a = 4.97 Å, c = 6.92 Å, JCPDS card no: 39–1425). We observe no peaks due to silicon and other impurities. A low-magnification TEM image of the sample is shown in Figure 1.2.14(a). Selected area electron diffraction (SAED) patterns of several nanowires were recorded at
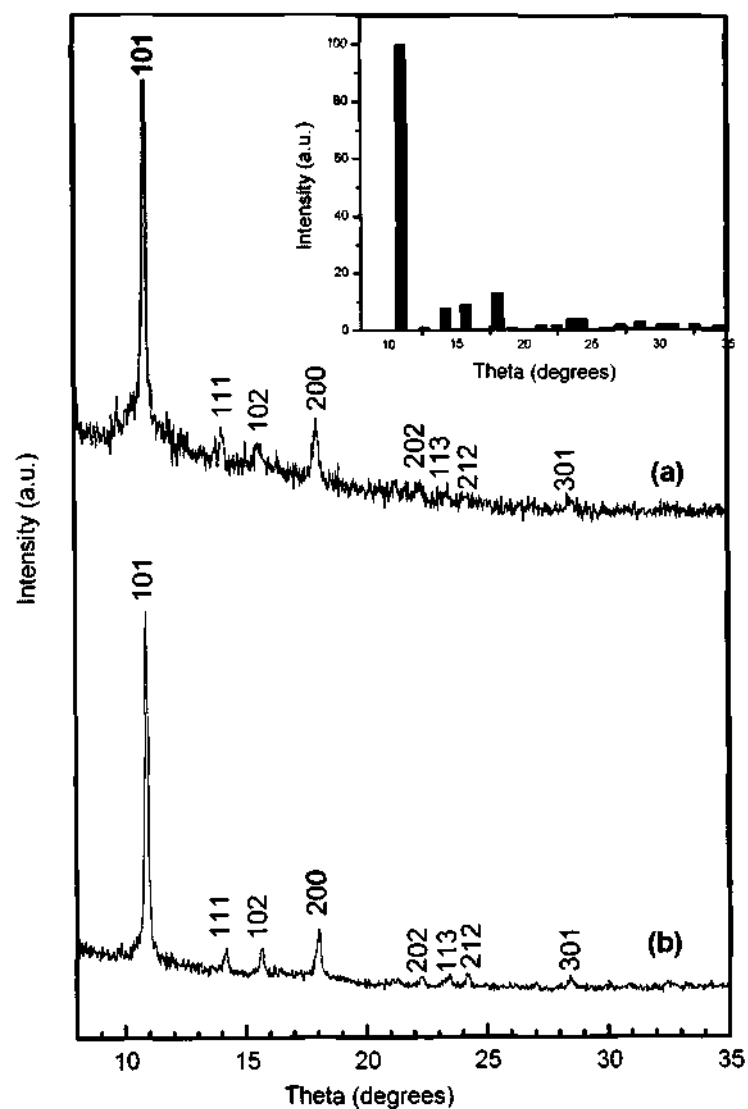
Figure 1.2.13: XRD patterns of the silica nanowires obtained by (a) the reaction of fumed silica and activated charcoal (mole ratio 1:2) at 1300 °C for 5 h in 50 sccm Ar and (b) the reaction of fumed silica and activated charcoal (mole ratio 1:1) at 1300 °C for 5 h in 50 sccm Ar + 20 sccm H_2. Inset shows the standard JCPDS pattern (card 39–1425).

61
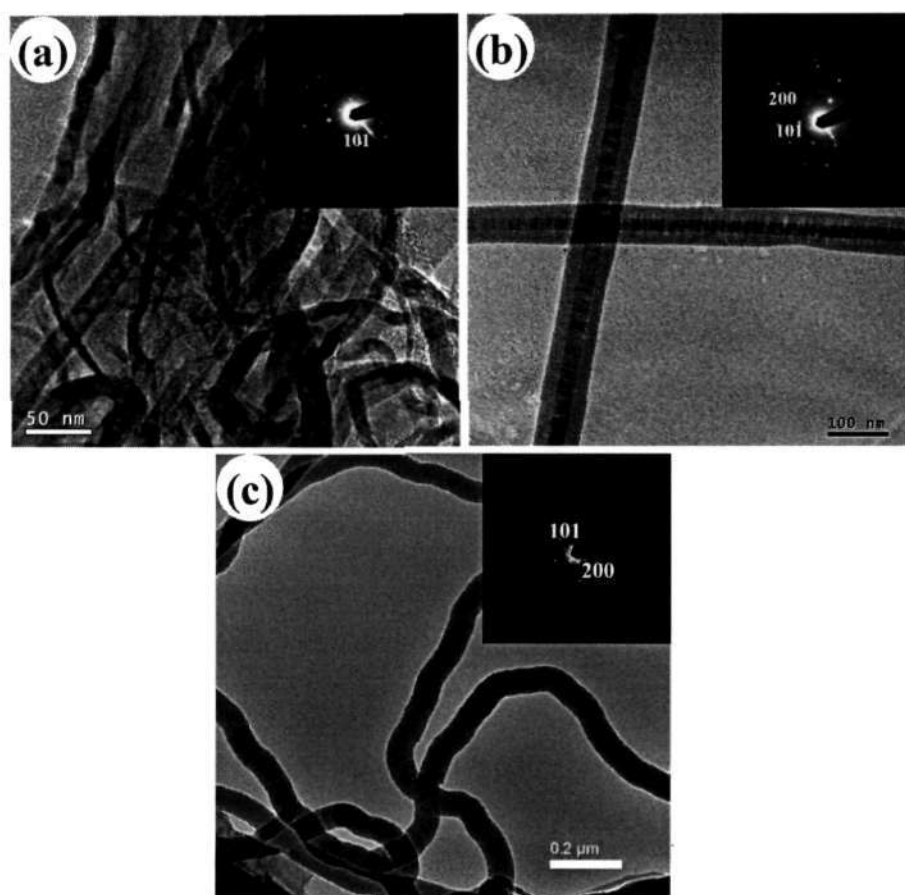
Figure 1.2.14: Low-magnification TEM images of silica nanowires obtained by the reaction of (a) fumed silica with activated charcoal (mole ratio 1:2) in 50 sccm Ar, (b) fumed silica with activated charcoal (mole ratio 1:0.5) in 50 sccm Ar and (c) fumed silica with activated carbon (mole ratio 1:1) in 50 sccm Ar and 20 sccm H_2 at 1300 °C for 5 h. The insets show the corresponding SAED patterns.

different points along the length of the wires. The inset in the Figure 1.2.14(a) shows a representative SAED pattern with the Bragg spots corresponding to (101), revealing the single-crystalline nature of the nanowires.

By carrying out the reaction of fumed silica with reduced amounts of carbon (molar ratio of 1:0.5) in 50 sccm Ar, we obtained a high yield of nanowires with no or negligible carbon content. We show a typical SEM micrograph of these nanowires in Figure 1.2.12(b). The nanowires have a uniform diameter of *ca.* 70 nm with lengths of tens of microns. The nanowires contain a crystalline core ($\sim$ 30 nm) sheathed by an amorphous layer as can be seen from the TEM image in Figure

1.2.14(b). Reducing the ratio of carbon to fumed silica appears to increase the amorphous coating on the crystalline core, while eliminating or minimizing the carbon content. The amorphous sheath is SiO_2 and not carbon. There is however some competition between the magnitude of the amorphous sheath and carbon content in the preparation. Based on independent experiments with nanowires and nanotubes, we have found that any amorphous carbon in the sample is eliminated entirely on heating in hydrogen around 1000 °C . We, therefore, conclude that no amorphous carbon is present in the silica nanowires subjected to hydrogen treatment at 1000 °C . The sheath is not due to SiC which requires a high $C:SiO_2$ ratio for formation. The SAED pattern, shown as an inset in Figure 1.2.14(b), reveals the nanowires to be single-crystalline α-cristobalite. The Bragg spots in this case arise due to (101) and (200) reflections of the tetragonal structure of α-cristobalite. With a 1:1 molar ratio of fumed silica and activated charcoal, however, we obtained a good crystalline α-cristobalite nanowires of diameters in the 70–100 nm range (Figure 1.2.14(c)). The diffraction pattern in the inset of Figure 1.2.14(c) reveals the crystalline nature of the nanowires.

The high resolution TEM image of a single silica nanowire presented in Figure 1.2.15 shows (102) planes with the expected spacing of 0.28 nm between the planes. The normal to the (102) planes makes an angle of $\sim 12°$ with the growth direction of the nanowire.

A good yield of α-cristobalite nanowires was also obtained when 20 sccm of H_2 gas was passed along with 50 sccm Ar while heating a 1:2 mixture of fumed silica to activated charcoal as evident from the SEM image shown in Figure 1.2.12(c). The use of H_2 helps to remove the unreacted carbon, as found by us in repeated experiments. We find a similar situation in the case of carbon nanotubes where again amorphous carbon is best removed by hydrogen treatment at 1000 °C . This can be seen by a comparison of Figure 1.2.12(a) and (c). We show a representative XRD pattern of the sample obtained by the reaction of a mixture of fumed silica and activated charcoal (molar ratio of 1:1) heated in a mixture of Ar (50 sccm) and H_2 (20 sccm) in Figure 1.2.13(b). The line-widths of the reflections in this XRD pattern are somewhat narrower suggesting greater crystallinity.
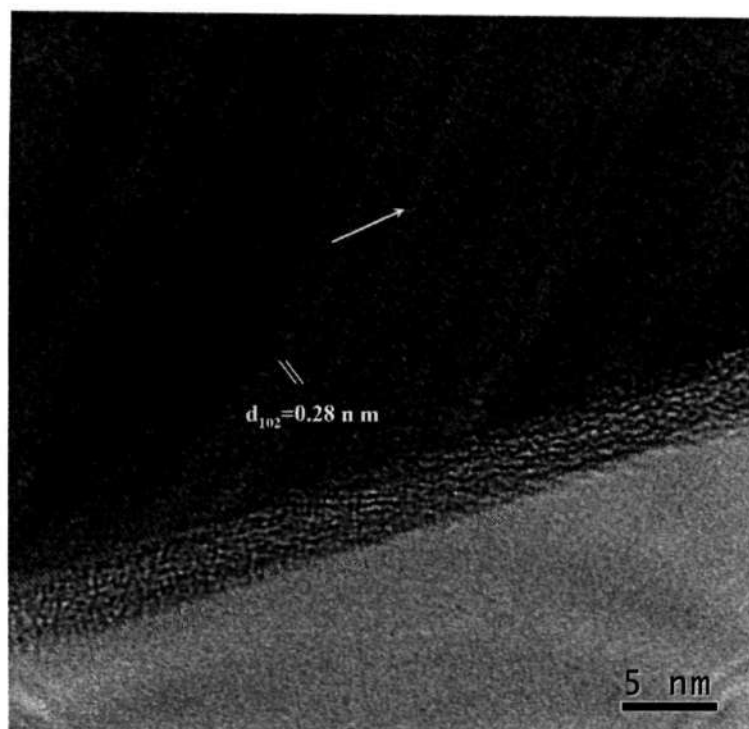
Figure 1.2.15: HREM image of a crystalline silica nanowire prepared by the reaction of fumed silica with activated charcoal (mole ratio 1:0.5) at 1300 °C for 5 h in 50 sccm Ar. The arrow denotes the direction of growth of the nanowire.

The photoluminescence spectrum of the α-cristobalite nanowires was recorded along with that of fumed silica. As shown in Figure 1.2.16(a), fumed silica exhibits a shoulder in the UV region at 375 nm and a broad band in the blue region centered at 440 nm. These features are nearly absent in the spectrum of the nanowires. The presence of intense blue emission in fumed silica arises from the high density of defects and oxygen related vacancies. We have recorded the Raman spectrum of the sample and observed two bands at 200 cm^{-1} (A1) and 424 cm^{-1} (A1 or B2) in addition to a weak band around 790 cm^{-1} (E) [see Figure 1.2.16(b)]. There is a lot of controversy regarding the band assignment in the literature of the α- and β- phases of cristobalite [58, 59]. The spectrum resembles that of the α-phase reported in the literature. DSC of the crystalline nanowires revealed a reversible transformation from the α-form to the β-form at 240 °C. This α-β transition is known to occur in cristobalite around this temperature [60]. Under the preparation conditions employed by us, the nanowires are first formed in the β-form, and are

64

Figure 1.2.16: (a) PL spectra of fumed silica and crystalline nanowires obtained by the different routes using 325 nm as the excitation wavelength and (b) Raman spect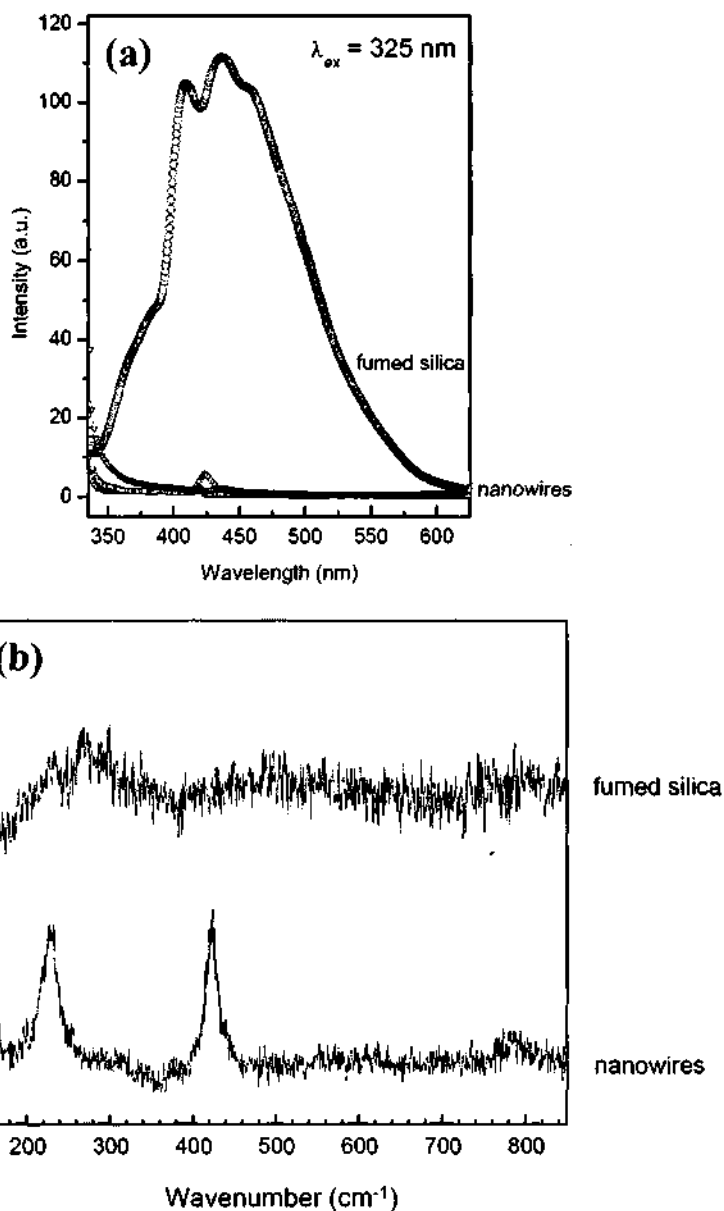ra of fumed silica and the nanowires prepared by the reaction of fumed silica with activated carbon (mole ratio 1:1) at 1300 °C for 5 h in a mixture of Ar (50 sccm) and H_2 (20 sccm).

65
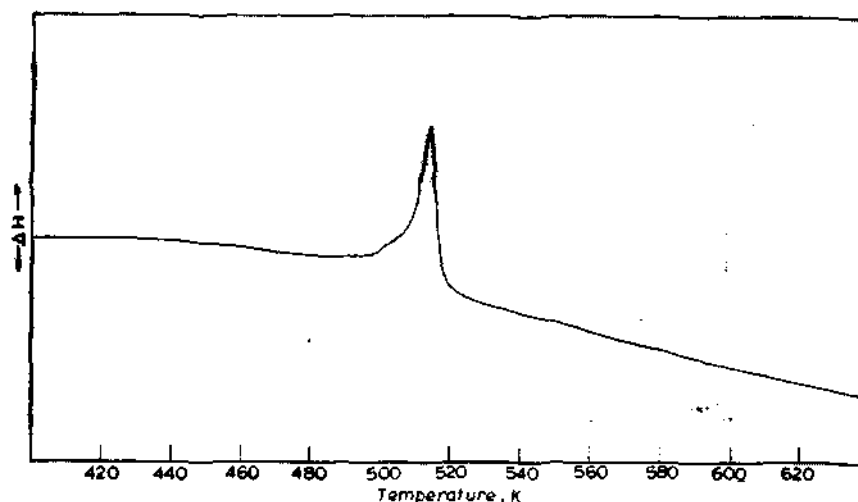
Figure 1.2.17: DSC curve of crystalline silica nanowires

then converted to the α-form on cooling to room temperature.

We could obtain α-cristobalite nanowires only with fumed silica but not with other sources of silica. This may be because fumed silica is amorphous, containing very tiny particles with a high surface area. Carbon plays a crucial role in the reaction in reducing silica to its reactive suboxide SiO_x. The presence of a high proportion of carbon relative to silica and use of hydrogen give rise to good crystalline nanowires. A lower proportion of carbon or the absence of hydrogen results in crystalline SiO_2 nanowires coated with an amorphous silica layer. The exothermic nature of the reduction of silica by carbon may give rise to considerable local heating which may help the crystallization of fumed silica into the cristobalite form. The reaction involved in the formation of crystalline silica can be written as follows:

$$SiO_2 + C \longrightarrow SiO + CO \qquad \cdots \quad (1)$$
$$2SiO + O_2 \longrightarrow SiO_2 \qquad \cdots \quad (2)$$
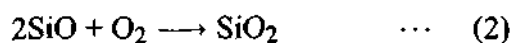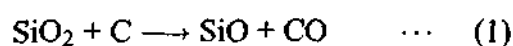
We do not feel that disproportionation of SiO occurs, since elemental Si is not formed in the product. The SiO vapors deposited on the walls of the alumina boat react with the oxygen contained in the reaction system to form crystalline nanowires.

66

Such oxidation reactions are well documented [31,62]. The growth of the nanowires is likely to occur by the vapor-solid mechanism [21,22] since no metal catalyst has been used in the synthesis. Accordingly, microscopic investigations do not reveal the presence of catalyst/liquid droplets at the ends of the nanowires.

In conclusion, we have, for the first time, synthesized good single-crystalline nanowires of silica in the α-cristobalite form by a simple carbothermal procedure. The nanowires might find useful applications. [‡]

(d) Silicon nanowires

Heating silicon powder at 1200 °C , in the absence of any activated carbon, yields a small proportion of silicon nanowires (SiNWs). In Figure 1.2.18(a), we show a typical SEM image of the product of such a reaction to illustrate the poor yield of SiNWs. When the reaction was carried out in the presence of activated carbon (Si:C = 1:1) by procedure (i), we obtained nanowires in a good yield, as can be visualized in the SEM image in Figure 1.2.18(b). These have diameters ranging from 75-350 nm, with lengths of a few microns. The XRD pattern of the product shown in Figure 1.2.19(a) matches with that of bulk silicon of cubic structure (JCPDS file: 27-1702). There is a minor peak (with asterisk) which is attributed to the surface silicon oxide, since SiNWs undergo oxidation upon exposure in air. Due to the high surface-to-volume ratio of the nanowires, a prominent surface oxide layer is generally present. We, however, see no reflections due to carbide and other impurity phases. Along with the nanowires, we also obtain Si nanojunctions, as shown in the low-magnification TEM image in Figure 1.2.20(a). The junction has a Y-shape, with arms of a uniform width of 200 nm, and a length of a few microns. Careful studies of the TEM images and electron diffraction data may unravel the nature of the junction.

In Figure 1.2.18(c), we show the SEM image of the SiNWs obtained by procedure (i) with Si:C ratio of 1:0.5. The nanowires have diameters between 75 and 600 nm with lengths up to tens of microns. The TEM image presented in Figure

---

[‡]A communication based on this study is appearing in J. Mater. Res., (2004).
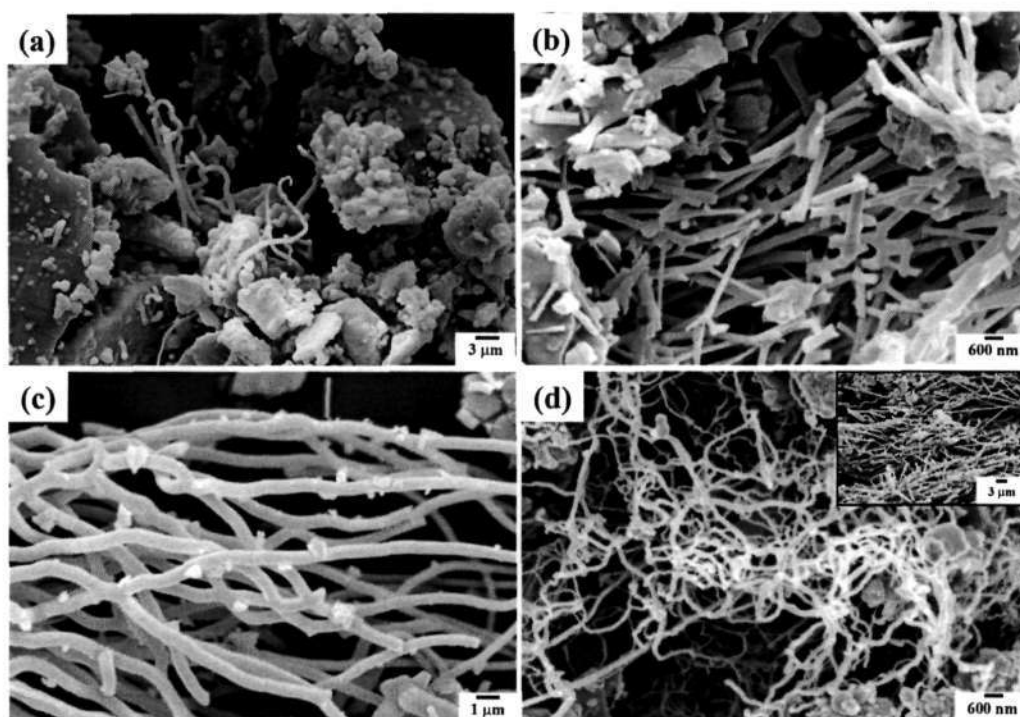
Figure 1.2.18: SEM images of (a) the product of the reaction of silicon powder obtained by procedure (i) in the absence of carbon, (b) SiNWs obtained by procedure (i) with a Si:C ratio of 1:1, (c) SiNWs obtained by procedure (i) with Si:C ratio of 1:0.5 and (d) SiNWs obtained in the grey portion of the sample synthesized by procedure (ii). Inset shows the nanowires obtained in the white portion.

1.2.20(b) reveals that the nanowires have a crystalline core and an amorphous sheath. The diameter of the crystalline core is 40 nm and the thickness of the sheath is around 17 nm. The amorphous sheath serves as a protective layer to the underlying crystalline silicon core. The amorphous sheath is of silica, formed by surface oxidation. The selected area electron diffraction, given in the inset of Figure 1.2.20(b), indicates the core to be of cubic silicon. The XRD pattern of the product, given in Figure 1.2.19(b), is characteristic of cubic silicon with a small impurity of silica.

Reaction of silicon powder with activated carbon in the absence of H_2, by procedure (ii), yielded abundant quantities of SiNWs. The product obtained consisted of grey and white portions. The grey portion comprised SiNWs with diameters of *ca.* 50 nm as shown in the SEM image in Figure 1.2.18(d). The
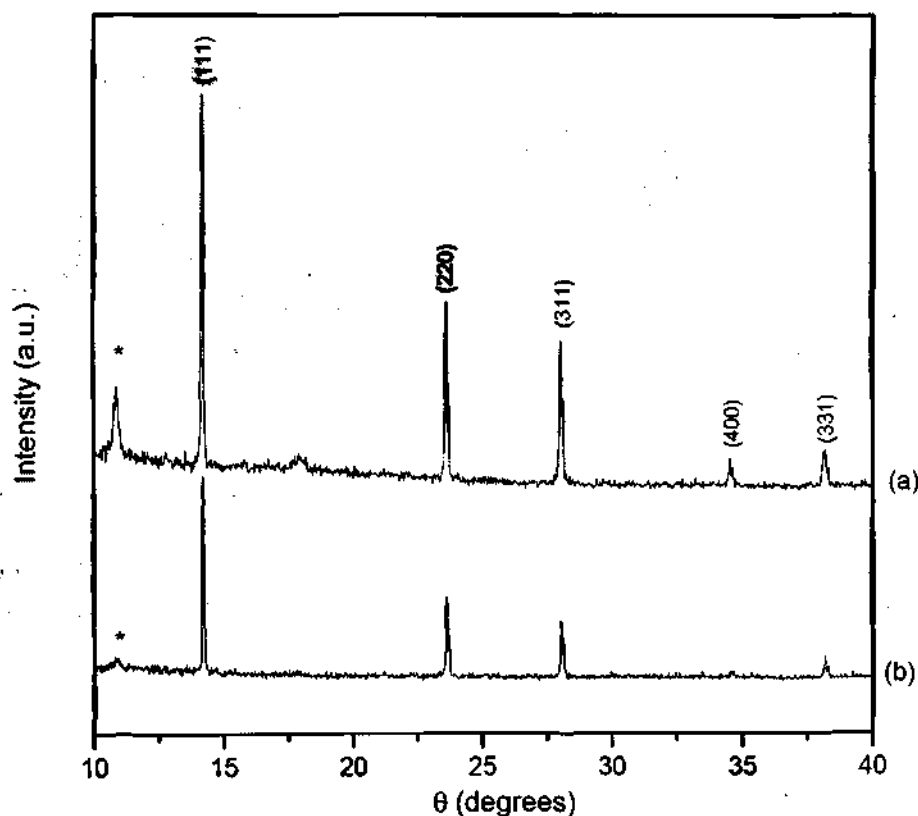
Figure 1.2.19: XRD patterns of SiNWs obtained by procedure (i) with a Si:C ratio of (a) 1:1 and (b) 1:0.5.

length of the nanowires was several tens of microns. Shown in the inset of Figure 1.2.18(d) is the SEM image of the white portion of the product. These nanowires have diameters ranging from 50 to 700 nm, with several tens of microns in length. A low-magnification TEM image of the nanowires is shown in Figure 1.2.20(c). The nanowires are highly crystalline as can be seen from the high-resolution transmission electron microscope (HREM) image in Figure 1.2.20(d). The lattice spacing between the fringes is 0.31 nm, corresponding to the (111) planes of silicon. The crystallinity of the nanowires is considerably higher when only argon was used instead of a mixture of argon and hydrogen. The role of hydrogen in promoting the amorphization of silicon is well-known [63,64].

In order to show the versatility of this method, we have investigated the formation of SiNWs by heating silicon substrates coated with carbon, by procedure (iii). A schematic illustration of the reaction is shown in Figure 1.2.21. In the absence
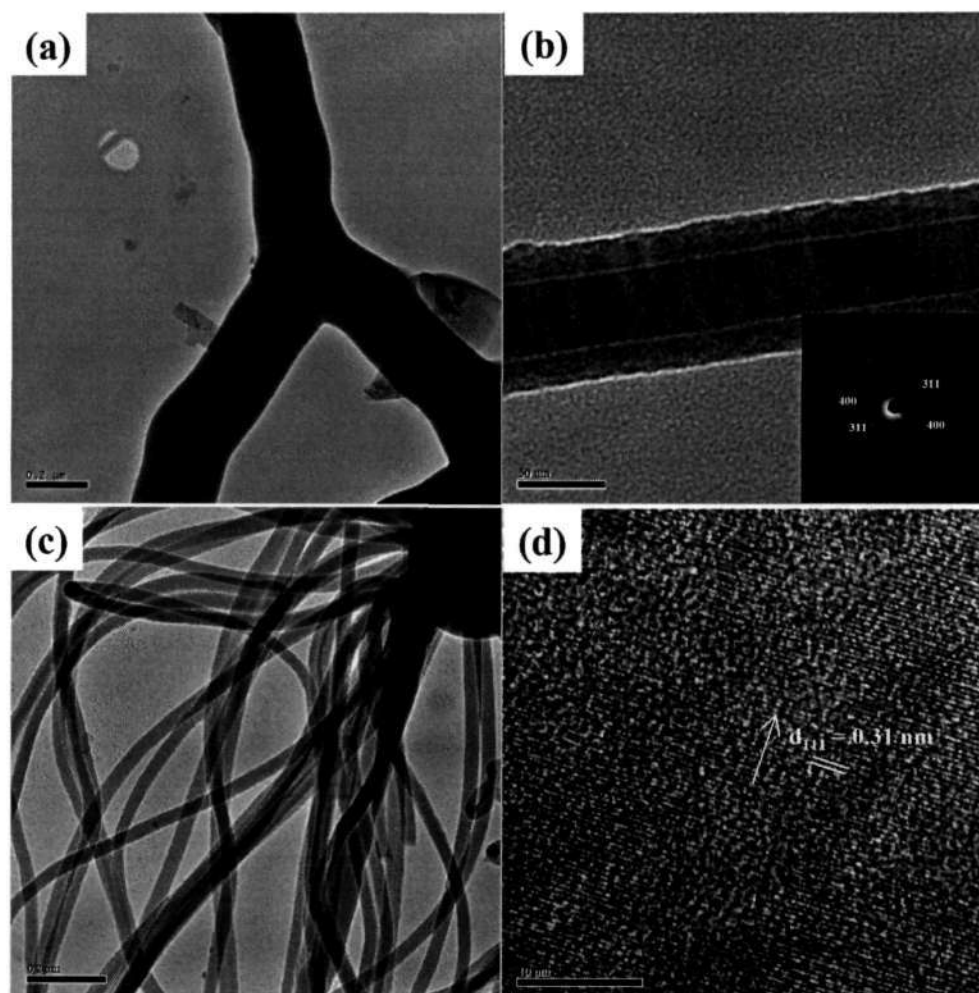
Figure 1.2.20: (a) TEM image of a Si nanojunction obtained by procedure (i) with Si:C ratio of 1:1. (b) TEM image of a nanowire obtained by procedure (i) with Si:C ratio of 1:0.5. Inset is the SAED pattern. (c) TEM image of the white portion of the sample obtained by procedure (ii). (d) HREM image of a single nanowire obtained in the white portion of the sample synthesized by procedure (ii). The white arrow indicates the direction of growth of the nanowire.
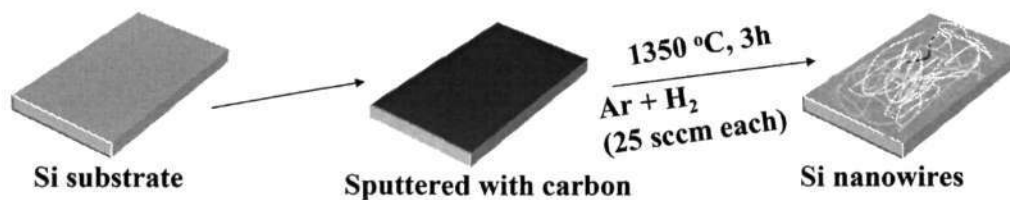
Figure 1.2.21: Schematic of the reaction for synthesizing Si nanowires using Si substrates.

of carbon, we obtained very few SiNWs, as shown in the SEM image in Figure 1.2.22(a). On carrying out the reaction with sputtered carbon, the yield of SiNWs improves considerably, as can be seen from the SEM image in Figure 1.2.22(b). The nanowires have diameters in the range of 50-300 nm.
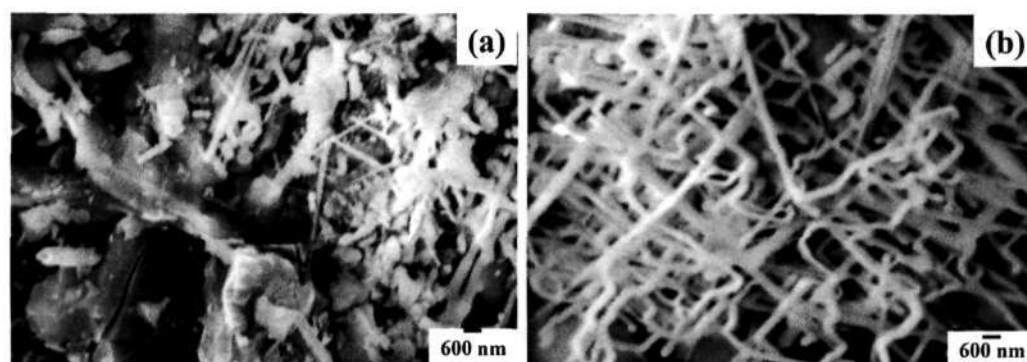
Figure 1.2.22: SEM images of SiNWs obtained with a Si substrate by procedure (iii) (a) in the absence of carbon and (b) with carbon sputtered on the surface.

We show the PL spectrum for the SiNWs (using 325 nm as the excitation wavelength) obtained by procedure (ii) in Figure 1.2.23. A broad blue emission centered at *ca.* 430 nm is observed. Similar observation were made by Yu *et al.* [31], who attributed the peak to the silicon oxide coating on the nanowires. Shown in the inset is the PL spectrum of the SiNWs using an excitation of 515 nm. There is a large band in the red region, which arises due to the quantum size effects of the Si core, which is below 10 nm [65].

The formation of SiNWs in the presence of carbon can be explained as follows. Silicon is generally covered by an oxide layer. The oxide layer gets reduced by carbon into silicon monoxide by the reaction

$$Si_xO_2 + C \longrightarrow Si_xO + CO \ (x > 1) \quad \cdots \quad (1)$$
$$Si_xO \longrightarrow Si_{x-1} + SiO \quad \cdots \quad (2)$$
$$2SiO \longrightarrow Si + SiO_2 \quad \cdots \quad (3)$$

Crystalline silicon, formed in step (3), nucleates and grows perpendicular to the (111) direction to form the nanowires. Similar reactions have been proposed for

71
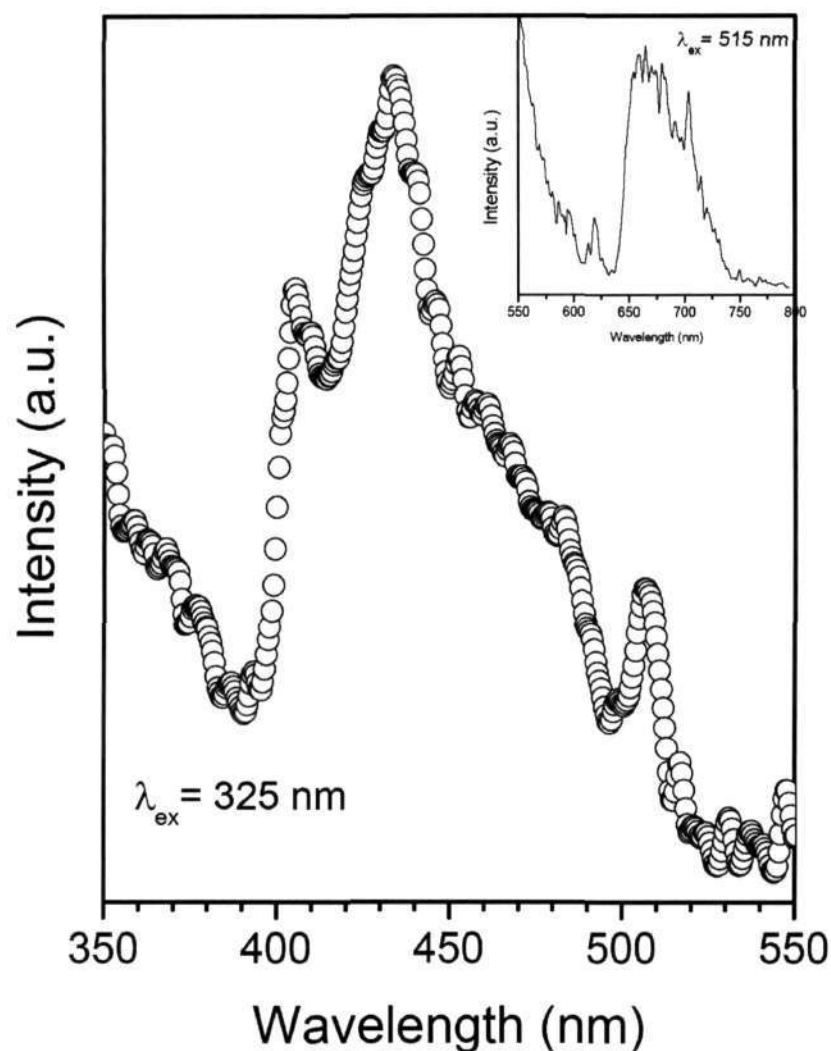
Figure 1.2.23: PL spectrum of Si nanowires obtained by procedure (ii). Inset shows the emission spectrum for the nanowires obtained by procedure (ii).

the oxide-assisted synthesis of SiNWs [34], although the monoxide type species is generated by other means.

In conclusion, SiNWs have been obtained by reacting silicon powder or silicon substrates with carbon in an inert atmosphere. Carbothermal reduction of the silica layer covering Si generates crystalline SiNWs with high aspect ratios. The method is convenient and inexpensive for the synthesis of Si nanowires, devoid of metallic impurities. §

---

§A paper based on this study has appeared in Chem. Phys. Lett., (2003).

72

(e) Silicon carbide, silicon oxynitride and silicon nitride nanowires

SiC nanowires

The reaction of activated carbon with silica gel at 1360 °C by procedure (i) gave a good yield of SiC nanowires after a period of 4 h. In Figure 1.2.24(a), we show SEM image of the nanowires obtained by this procedure. The diameter of the nanowires is around 350 nm and the length extends to several tens of microns. The XRD pattern of this sample shown in Figure 1.2.25(a) matches with that of cubic β-SiC with the unit cell parameters a = 4.3589 Å(JCPDS file: 29–1129). There are no reflections corresponding to α-SiC (hexagonal form) or SiO_2 in the diffraction pattern. We have carried out the same reaction for a period of 7 h (instead of 4 h) to improve the crystallinity of the SiC nanowires. The SEM image shown in Figure 1.2.24(b) indicates that the nanowires so obtained have a diameter of $\sim$40 nm with lengths of several tens of microns. The XRD pattern of this sample (Figure 1.2.25(b)) is characteristic of the β-SiC phase. The pattern also shows that the crystallinity of the sample is considerably improved. The SiC nanowires did not have a silica coating as evidenced from the XRD pattern and transmission electron microscope images. Low-magnification electron microscope images of the nanowires did not reveal the presence of any droplets at the ends of the nanowires. A bead-necklace morphology, similar to that reported by Wu et al. [66] was, however, present in the nanowires, suggesting that the growth of the nanowires probably occurs by the VLS mechanism [67, 68]. In this mechanism, the SiO_2 nanoparticles form droplets that are in contact with the activated carbon to give SiO vapour. The SiO vapour further reacts with carbon to form β-SiC particles, which act as the nuclei for the growth of the nanowires. Once the droplets are saturated with β-SiC, crystallization of the β-SiC occurs, followed by growth in one direction to yield nanowires.

We have carried out the reaction of silica gel with activated carbon in the presence of H_2 gas instead of NH_3 gas. This also gives excellent yields of nanowires of β-SiC. In Figure 1.2.26(a) we show the SEM image of β-SiC obtained by this method. The nanowires are thick with a uniform diameter of $\sim$325 nm and have

Figure 1.2.24: SEM images of the β-SiC nanowires obtained by procedure (i) (heating the gel containing the activated carbon and silica at 1360 °C in NH_3) for (a) 4 h and (b) 7 h.
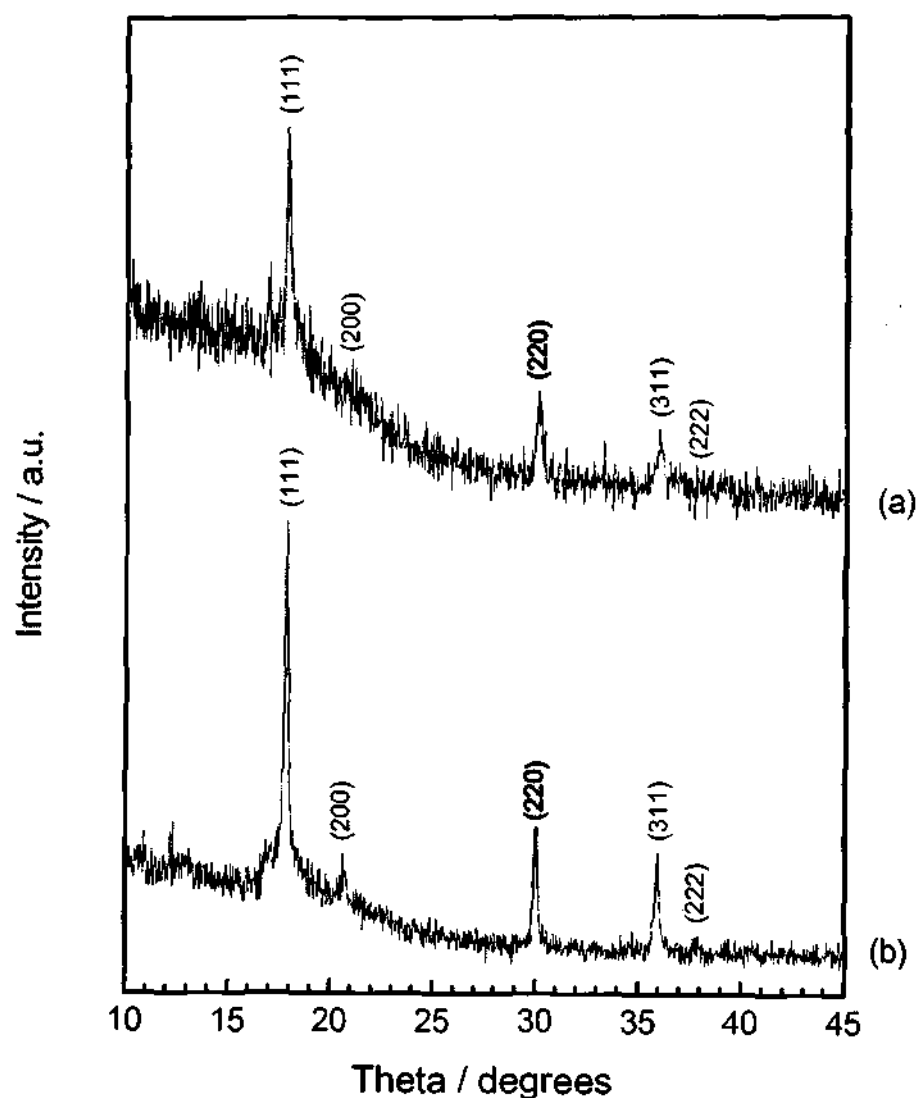
Figure 1.2.25: XRD patterns of the SiC nanowires obtained by procedure (i) (heating the gel containing the activated carbon and silica at 1360 °C in NH₃) for (a) 4 h and (b) 7 h.

lengths of several tens of microns.

The HREM image of a SiC nanowire presented in Figure 1.2.27, shows a spacing of 2.5 Å between the (111) planes. The normal to the (111) planes forms an angle of 35° with the growth direction of the nanowires. The selected area electron diffraction pattern (SAED) pattern showed Bragg spots corresponding to the (111) planes, with some streaking due to the presence of stacking faults.

The basic reactions involved in the formation of the SiC nanowires are given by,

Figure 1.2.26: SEM images of SiC nanowires obtained by (a) procedure (i) (heating the gel containing the activated carbon and silica for 7 h at 1360 °C) in the presence of H_2 gas and (b) procedure (iii) (heating the gel prepared by the reaction of ethylene glycol with citric acid in the presence of TEOS at 1360 °C for 7 h in NH_3).

$$SiO_2 + C \longrightarrow SiO + CO \qquad \cdots \quad (1)$$
$$SiO + 2C \longrightarrow SiC + CO \qquad \cdots \quad (2)$$
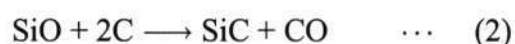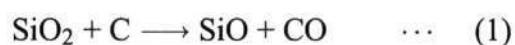
The NH_3 and H_2 in the gas stream favour the formation of SiO from SiO_2. The SiO reacts readily with carbon to form SiC.

In procedure (i), we have employed TEOS as the starting material since it gives fine particles of silica at low pH values. We have carried out the reaction of fumed silica (instead of a silica gel) with activated carbon by grinding the reactants in order to see if this procedure also gives us a good yield of SiC nanowires as in the case of the solgel route. Procedure (ii) yielded a grey, wool-like product, which had β-SiC as the major component. The diameter of the nanowires was $\sim$500 nm and with the lengths extending to tens of microns. The XRD pattern, however, showed the presence of some silica.

We could obtain β-SiC nanowires by procedure (iii) wherein the gel formed by ethylene glycol, citric acid and TEOS was heated in a reducing atmosphere at 1360 °C . The ethylene glycol initially reacts with citric acid (in the presence of silica gel) to form silica particles embedded in carbon precursors. On treatment with NH_3 or H_2, this composite generates active carbon *in situ* which reacts with the silica nanoparticles to yield SiC. The SEM image (Figure 1.2.26(b)) shows that the nanowires have large diameters ($\sim$750 nm) with lengths of up to tens of microns.
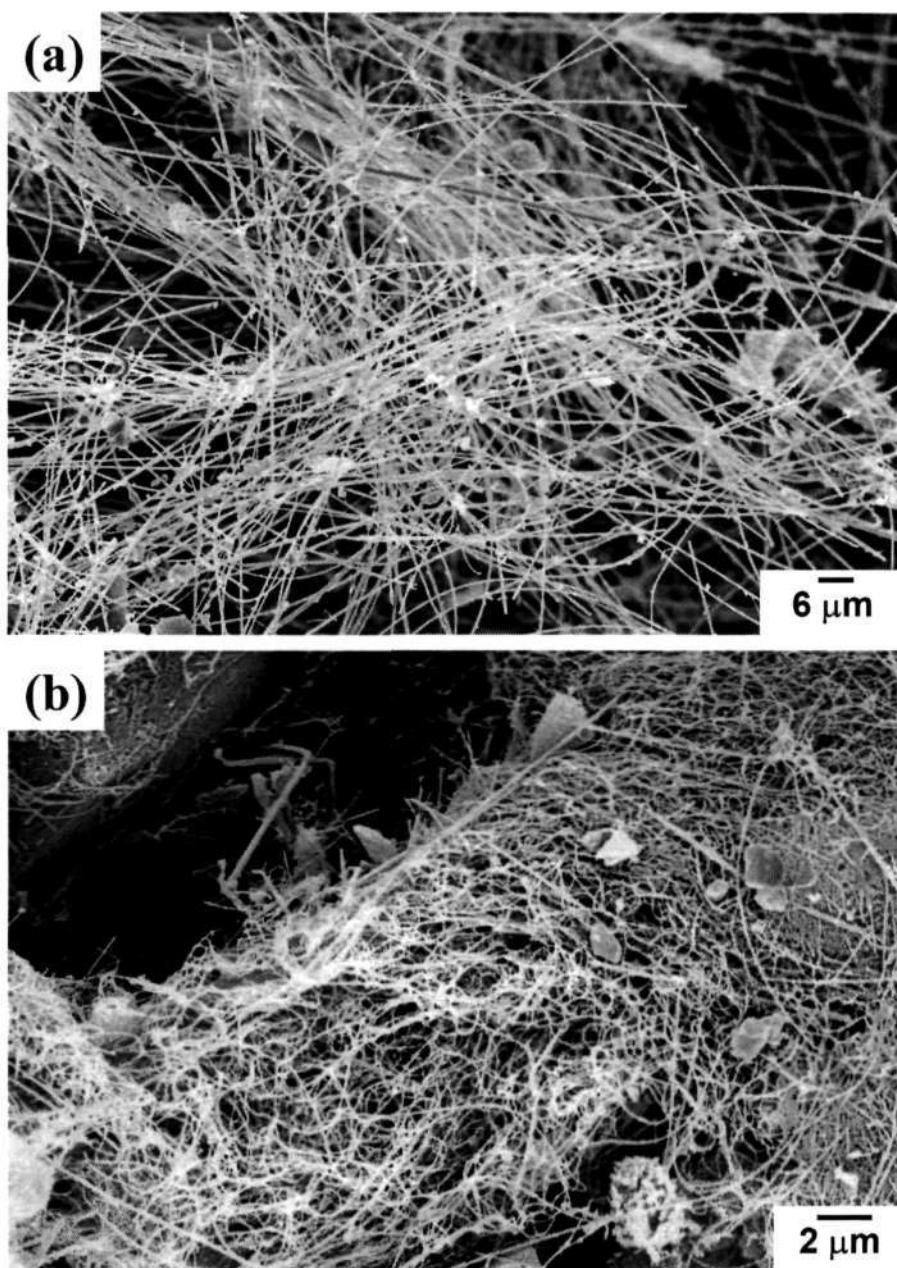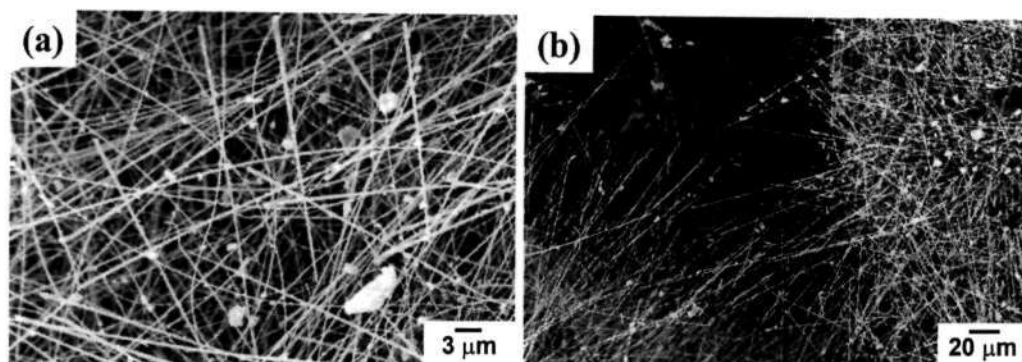
Figure 1.2.27: HREM image of a SiC nanowire prepared by procedure (i) (heating the gel containing activated carbon and silica for 7 h at 1360 °C in NH_3). The inset shows the SAED pattern. The arrow denotes the normal to the (111) planes and the direction of growth of the nanowire.

The nanowires appear to be straight, unlike the ones obtained earlier, and seem to grow out from the carbon-silica composite particles.

The photoluminescence (PL) spectrum of the β-SiC nanowires synthesized by procedure (i) is shown in Figure 1.2.28. The sample exhibits a single broad peak at 400 nm. Such a PL feature is characteristic of SiC, though there is a considerable blue shift as compared to the bulk sample [69]. The 3C form SiC shows a PL band maximum around 540 nm due to the presence of defect centres within the band gap.

Figure 1.2.28: Photoluminescence spectrum of SiC nanowires synthesized by procedure (i) (heating the gel containing activated carbon and silica for 7 h at 1360 °C in NH_3).

Infrared spectra of the β-SiC nanowires (Figure 1.2.29(a)) show a strong band at 810 cm^{-1} due to the Si-C stretching band. The Raman spectrum of the nanowires is more interesting. Figure 1.2.30 shows the room temperature Raman spectrum of the SiC nanowires with a quasi-backscattering geometry. We observe a broad band around 780 cm^{-1} corresponding to the TO phonon at the Γ point of cubic SiC. The absence of the folded modes that are related to the SiC polytypes (natural superlattices due to various stacking orders of SiC bilayers) in the Raman spectrum

78
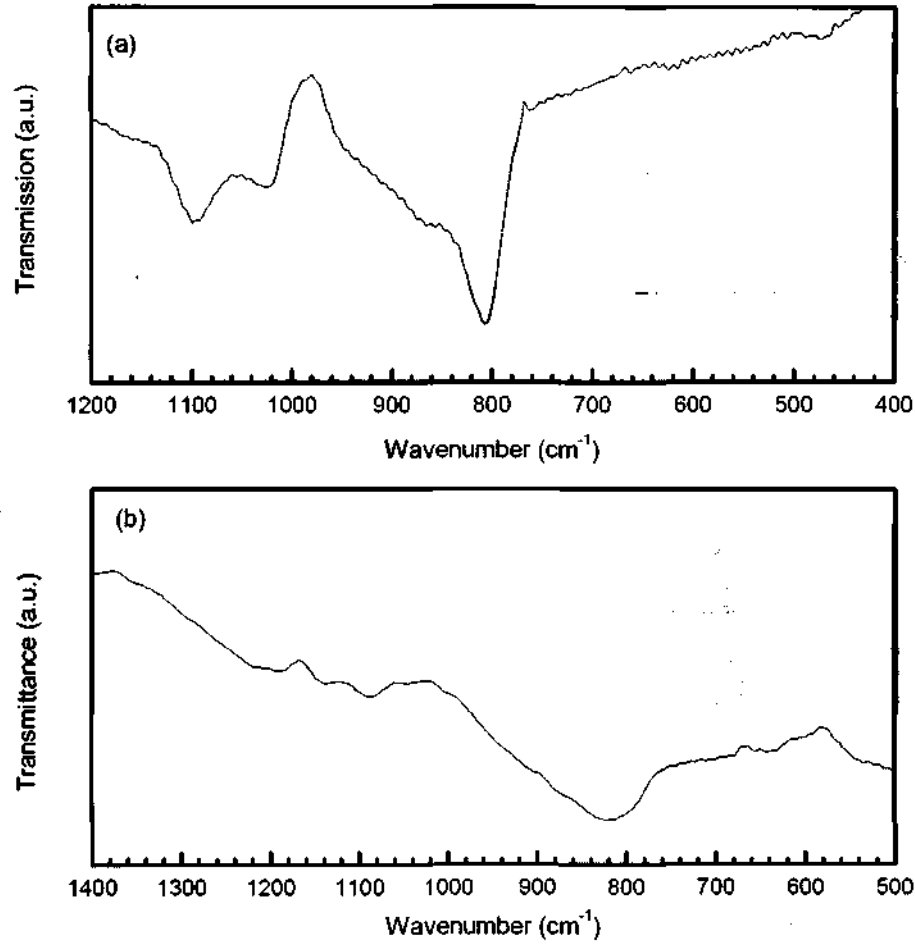
Figure 1.2.29: Infrared spectrum of (a) SiC nanowires and (b) Si_3N_4 nanowires.

is consistent with the X-ray data, and suggests the nanowires are only cubic SiC [70,71]. The TO phonon line is shifted by around 16 cm^{-1} from the bulk SiC [72] towards lower energy. This is due to the small grain size of SiC and the presence of growth faults of the nanowires.

In the zinc-blende structure (as in cubic SiC) the LO phonon has a higher energy than the TO phonon near the zone center. LO phonon is around 972 cm^{-1} in bulk at ambient conditions in the bulk 3C-SiC [72]. In the Raman spectrum recorded by us, we do not see the LO phonon. As shown in Figure 1.2.30, the LO phonon is absent even when different excitation wavelengths are used. Raman selection rules for the zinc-blende structure governs this observation as explained below. While preparing the SiC sample for Raman experiments, the nanowires are compressed to
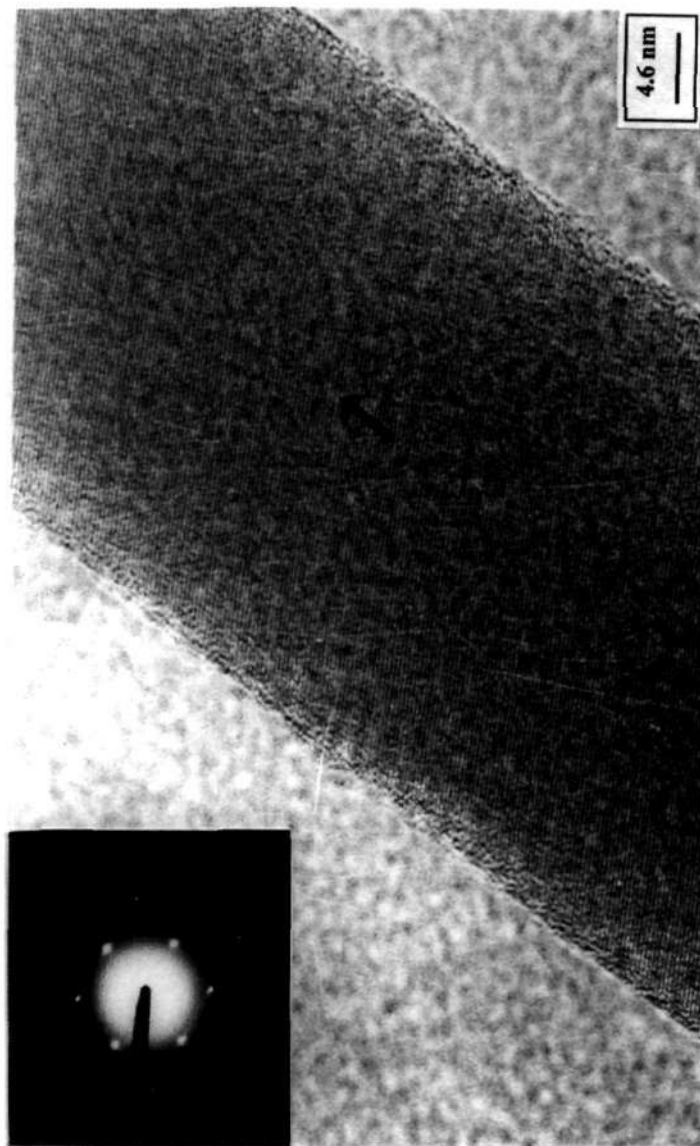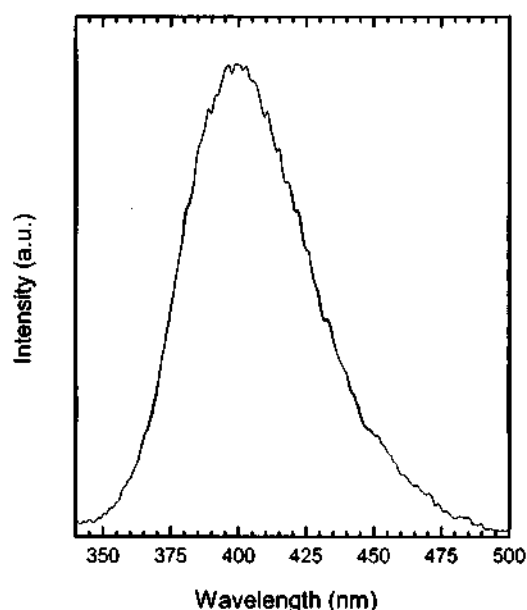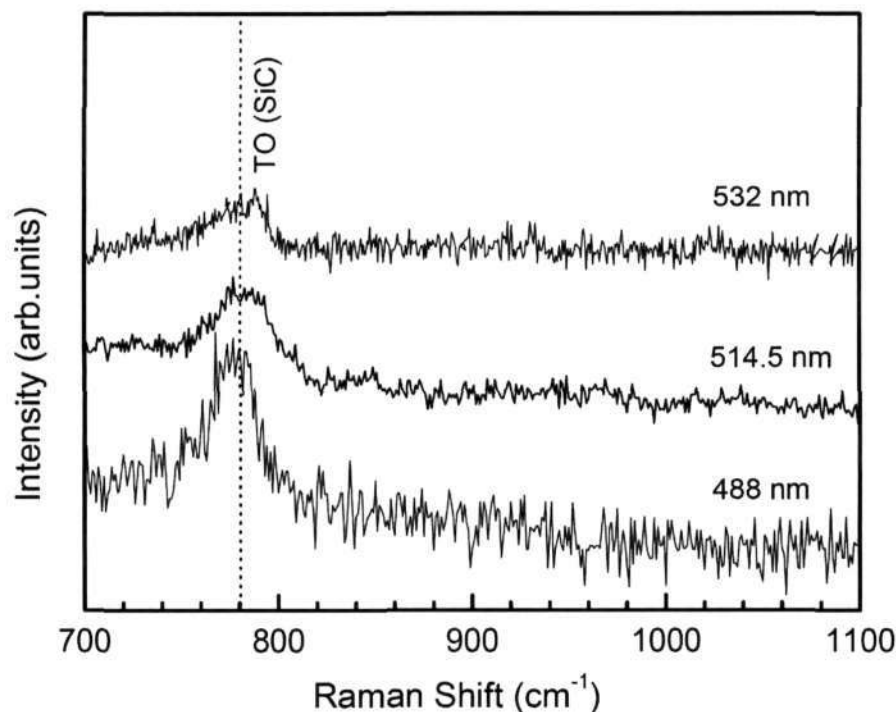
Figure 1.2.30: Raman spectra of SiC nanowires synthesized by procedure (i) (heating the gel containing activated carbon and silica for 7 h at 1360 °C in NH_3).

form a continuous surface. This orients the nanowires, such that the long cylindrical axes of the nanowires are parallel to the sample plane. From the TEM images it is clear that the cylindrical axis of the nanowires is [011] for the zinc-blende 3C-SiC. Raman experiments are carried out in the quasi-backscattering geometry on planes perpendicular to the (011) planes, such as ($0\bar{1}1$). In the case of such a backscattering geometry, the incident wave vector (k_i) and scattered wave vector (k_s) are along the [$0\bar{1}1$] direction and the polarization of the incident (e_i) and scattered (e_s) wave vectors are along the [011] direction. According to the Raman selection rules, the TO phonon is allowed whereas the LO phonon is forbidden for a zinc-blende structure [73]. This is the reason for the absence of the LO mode in the present experiment.

Si_3N_4 nanowires

The reaction of silica gel with ammonia alone or in the presence of activated carbon in the temperature range 1100–1360 °C did not yield Si_3N_4 nanowires.

80

However, when the reaction of silica gel was carried out with arc-generated multi-walled carbon nanotubes in an NH_3 atmosphere at 1360 °C for 4 h, we obtained a good yield of Si_2N_2O nanowires. The XRD pattern of the nanowires, shown in Figure 1.2.31(a), is characteristic of Si_2N_2O with unit cell parameters a = 8.868 Å, b = 5.497 Å, c = 4.854 Å, $\alpha = \beta = \gamma = 90°$ (JCPDS file: 47–1627). The SEM image of the Si_2N_2O nanowires shown in Figure 1.2.32(a) reveals the diameter of the nanowires to be $\sim$300 nm with lengths of up to tens of microns.

When the reaction of arc-generated multi-walled carbon nanotubes with silica gel was carried out at 1360 °C for longer periods ($\geq$7 h), the product contained mainly Si_3N_4 nanowires. The XRD pattern of the sample, shown in Figure 1.2.31(b), establishes the nanowires to be predominantly of the hexagonal α-Si_3N_4 phase with unit cell parameters a = 7.7541 Å, c = 5.6217 Å(JCPDS file: 41–0360), with a minor component of Si_2N_2O. The composition of the final product was dependent on the duration over which the reaction was carried out. Figure 1.2.32(b) shows an SEM image of these nanowires, which have diameters of between 150 and 175 nm. In the presence of catalytic Fe particles, the reaction of silica gel with carbon nanotubes occurs within 4 h giving a good yield of nanowires of pure Si_3N_4 with no Si_2N_2O. Figures 1.2.31(c) and (d) show the XRD patterns of the products obtained in the presence of 0.1% and 0.5% Fe catalysts. While the 0.1% Fe catalyst gives a mixture of the α-phase with the hexagonal β-phase with unit cell parameters a = 7.6044 Å, c = 2.9075 Å(JCPDS file: 33–1160), the 0.5% Fe catalyst yields almost monophasic α-Si_3N_4 nanowires, as can be seen from Figure 1.2.31(d). Figure 1.2.33(a) shows an SEM image of the Si_3N_4 nanowires obtained with 0.1% catalyst. The diameter is $\sim$400 nm and the length extends to hundreds of microns. The nanowires prepared with the 0.5% Fe catalyst however have larger diameters ($\sim$700 nm) as can be seen from Figure 1.2.33(b). It should be noted that both the length and diameter of the Si_3N_4 nanowires are generally larger than those of the carbon nanotubes.

The reaction involved in the formation of Si_3N_4 nanowires in the presence of carbon nanotubes can be represented as,

81
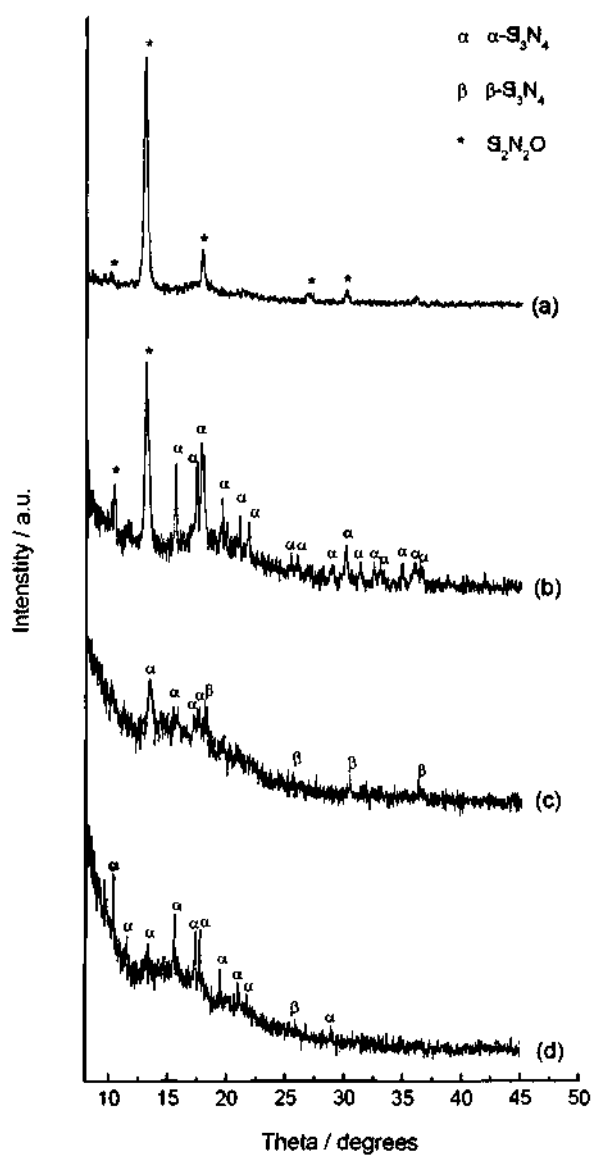
Figure 1.2.31: XRD patterns of the products obtained by the reaction of multiwalled carbon nanotubes with silica gel at 1360 °C in an NH_3 atmosphere: (a) for 4 h, (b) for 7 h, (c) for 4 h in the presence of 0.1 mol% Fe, and (d) for 4 h in the presence of 0.5 mol% Fe. Relative intensities of the α-Si$_3$N$_4$ peaks show variations due to the orientational effects.
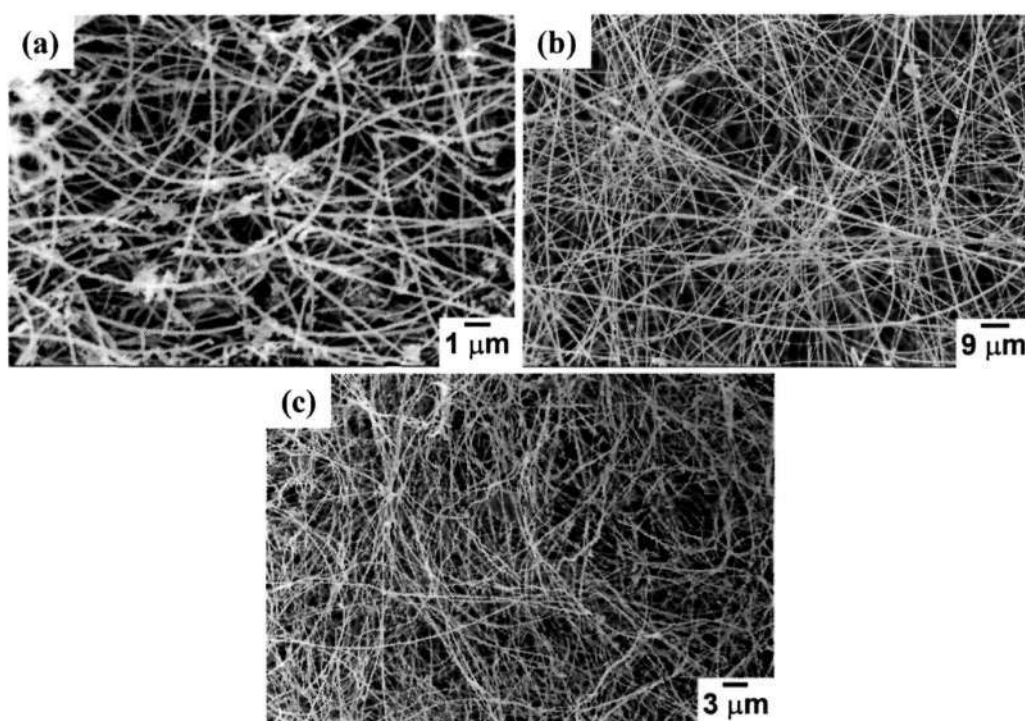
Figure 1.2.32: SEM images of (a) Si_2N_2O nanowires obtained by the reaction of silica with NH_3 in the presence of multi-walled carbon nanotubes with silica at 1360 °C for 4 h, (b) Si_3N_4 nanowires prepared by the reaction of silica with NH_3 in the presence of multi-walled carbon nanotubes with at 1360 °C for 7 h and (c) Si_2N_2O nanowires obtained by the reaction of silica with NH_3 at 1100 °C in the presence of activated carbon and 0.5% Fe catalyst.

$$3SiO_2 + 6C + 4NH_3 \longrightarrow Si_3N_4 + 6H_2 + 6CO$$

The role of the catalytic iron particles is likely to be in facilitating the removal of oxygen from the silica. The iron oxide formed in such a reaction would readily get reduced back to metal particles in the reducing atmosphere. The formation of Si_2N_2O is given by the reaction

$$2SiO_2 + 3C + 2NH_3 \longrightarrow Si_2N_2O + 3H_2 + 3CO$$

Carbon nanotubes prepared by precursor pyrolysis get oxidized at a relatively low temperature ($\sim$550 °C) compared to the nanotubes prepared by arc evaporation (which oxidize at around 700 °C). We have carried out the reaction of silica and NH_3 with multi-walled carbon nanotubes prepared by the decomposition of ferrocene.

83
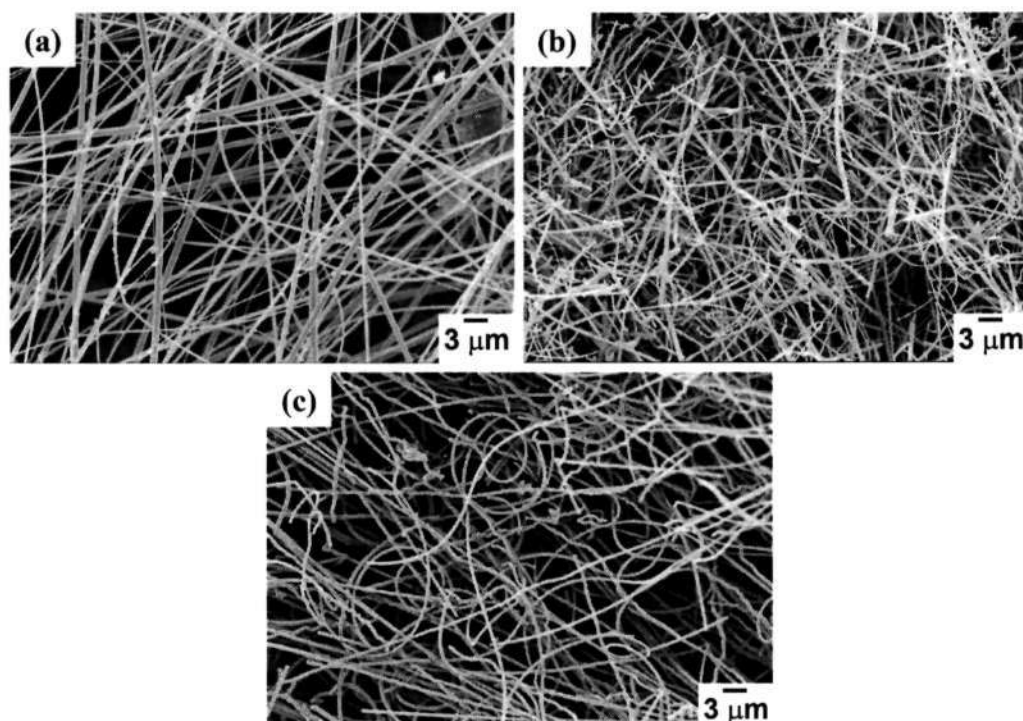
Figure 1.2.33: SEM images of the Si_3N_4 nanowires prepared by the reaction of multi-walled carbon nanotubes with silica at 1360 °C for 4 h in the presence of (a) 0.1% Fe and (b) 0.5% Fe catalysts, respectively. (c) SEM image of the Si_3N_4 nanowires prepared by the reaction of aligned multiwalled carbon nanotubes with silica at 1360 °C for 4 h.

The reaction of these nanotubes with silica gel and NH_3 at 1360 °C yields a mixture of α- and β-Si_3N_4. Figure 1.2.33(c) shows the SEM image of the product obtained by this reaction. The nanowires have a large diameter (5-7 μm), with lengths of the order of hundreds of microns. Activated carbon has a larger surface area than the nanotubes produced from hydrocarbon pyrolysis and gets oxidized at temperatures as low as 500 °C (compared to 800 °C for graphite). We would therefore expect activated carbon to yield Si_3N_4 by reacting with silica gel in the presence of NH_3 under milder conditions. However, as mentioned earlier, we did not obtain Si_3N_4 nanowires with activated carbon. In the presence of 0.5% Fe, however, the reaction of silica gel with activated carbon at 1200 °C for 8 h yielded α-Si_3N_4. The same reaction at 1360 °C for 4-7 h yields β-SiC nanowires. When the reaction was carried out at 1100 °C for 4 h, it gave Si_2N_2O nanowires. We show an SEM image of these nanowires in Figure 1.2.32(c).

Figure 1.2.34: TEM image of Si_3N_4 nanotubes obtained by the reaction of aligned multi-walled nanotubes with silica gel at 1360 °C .

Infrared spectra of the Si_3N_4 nanowires (Figure 1.2.29(b)) show a prominent band around 825 cm^{-1} due to the SiN stretching vibration. There were no bands due to SiO stretching.

In the synthesis of Si_3N_4 nanowires using aligned multi-walled nanotubes as the carbon source, we occasionally obtained nanotubes of α-Si_3N_4 along with the nanowires. The outer diameter of the nanotubes is $\sim$200 nm as seen in the low resolution TEM image in Figure 1.2.34.

The present study establishes that pure β-SiC (cubic) nanowires are easily obtained by reacting silica gel with activated carbon in a reducing atmosphere at 1360 °C . This procedure eliminates the need to use SiO as the starting material. Furthermore, carbon nanotubes are not necessary to produce SiC nanowires. The reaction of activated carbon with silica gel and NH_3 in the presence of catalytic iron particles yields α-Si_3N_4 nanowires at 1200 °C , and Si_2N_2O nanowires at 1100 °C . The reaction of multi-walled carbon nanotubes with silica at 1360 °C in an atmosphere of NH_3 also yields pure Si_3N_4 nanowires, while the same reaction at 1100 °C gives Si_2N_2O nanowires. The presence of catalytic iron particles favours the formation of nanowires of α-Si_3N_4. A summary of the results obtained by us
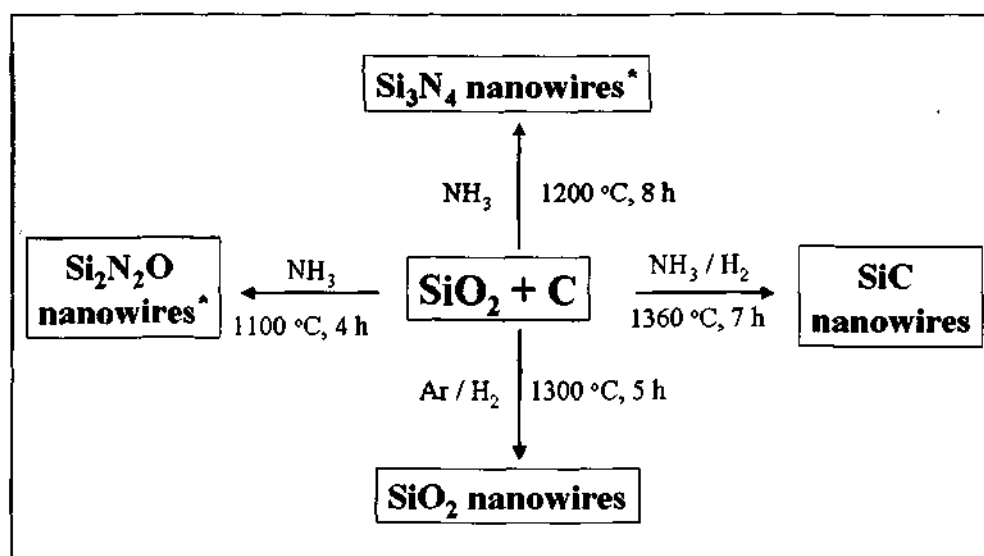
* 0.5 % of Fe catalyst used

Figure 1.2.35: Schematic showing the synthesis of silicon-based nanowires by the carbon-assisted synthesis route.

are presented in Table 1.2.1. ¶

1.2.5 Conclusions

We have employed the carbon-assisted synthesis route to obtain nanowires of various classes or nanowires such as elements (Si), oxides (SiO_2, Ga_2O_3 and ZnO), carbides (SiC) and nitrides (Si_3N_4). The method is a simple one and the nanowires obtained are generally single-crystalline. In the case of non-oxide nanowires, the presence of oxide coatings can be avoided by a suitable choice of reaction conditions and the relative proportion of carbon. The versatility of carbon-assisted synthesis is illustrated in Figure 1.2.35 using silicon-based nanowires as an example. By starting with a mixture of silica and carbon, it is possible to obtain nanowires of various materials by changing parameters such as temperature, concentrations, and source of carbon and silica. Clearly, nanowires of several other materials will be synthesized in the future by employing this strategy.

¶A paper based on this study has appeared in J. Mater. Chem., (2002).

Table 1.2.1: Synthesis of silicon carbide, nitride and oxynitride nanowires.

No.	Silica / carbon source	Fe catalyst	Temp. (°C)	Time (h)	Gas used	Product
1.	silica gel + act. C	-	1360	4-7	NH_3	β-SiC
2.	silica gel + act. C	-	1360	7	H_2	β-SiC
3.	fumed silica + act. C	-	1360	7	NH_3	β-SiC
4.	TEOS + ethylene glycol + citric acid	-	1360	7	NH_3	β-SiC
5.	silica gel + MWNT (arc)	-	1360	7	NH_3	α-Si_3N_4 + Si_2N_2O
6.	silica gel + MWNT (arc)	0.1%	1360	4	NH_3	$(\alpha + \beta)$-Si_3N_4
7.	silica gel + MWNT (arc)	0.5%	1360	4	NH_3	α-Si_3N_4
8.	silica gel + MWNT (arc)	-	1360	4	NH_3	Si_2N_2O
9.	silica gel + AlCNT	-	1360	7	NH_3	$(\alpha + \beta)$-Si_3N_4
10.	silica gel + act. C	0.5%	1200	8	NH_3	α-Si_3N_4
11.	silica gel + act. C	0.5%	1100	4	NH_3	Si_2N_2O

87

References

[1] T. Harwig and F. Kellendonk, *J. Solid State Chem.*, 1978, **24**, 255.

[2] H. Z. Zhang, Y. C. Kong, Y. Z. Wang, X. Du, Z. G. Bai, J. J. Wang, D. P. Yu, Y. Ding, Q. L. Hang and S. Q. Feng, *Solid State Commun.*, 1999, **109**, 677.

[3] Y. C. Choi, W. S. Kim, Y. S. Park, S. M. Lee, D. J. Bae, Y. H. Lee, G. S. Park, W. B. Choi, N. S. Lee and J. M. Kim, *Adv. Mater.*, 2000, **12**, 746.

[4] X. C. Wu, W. H. Song, W. D. Huang, M. H. Pu, B. Zhao, Y. P. Sun and J. J. Du, *Chem. Phys. Lett.*, 2000, **328**, 5.

[5] C. H. Liang, G. W. Meng, G. Z. Wang, Y. W. Wang, L. D. Zhang and S. Y. Zhang, *Appl. Phys. Lett.*, 2001, **78**, 3202.

[6] M. H. Huang, S. Mao, H. Feick, H. Yan, Y. Wu, H. Kind, E. Weber, R. Russo and P. Yang, *Science*, 2001, **292**, 1897.

[7] M. H. Huang, Y. Wu, H. Feick, N. Tran, E. Weber and P. Yang, *Adv. Mater.*, 2001, **13**, 113.

[8] S. C. Lyu, Y. Zhang, H. Ruh, H.-J. Lee, H.-W. Skim, E.-K. Suh and C. J. Lee, *Chem. Phys. Lett.*, 2002, **363**, 134.

[9] S. Y. Li, C. Y. Lee and T. Y. Tseng, *J. Cryst. Growth*, 2003, **247**, 357.

[10] C. J. Lee, T. J. Lee, S. C. Lyu, Y. Zhang, H. Ruh and H. J. Lee, *Appl. Phys. Lett.*, 2001, **81**, 3648.

[11] J. S. Lee, M. I. Kang, S. Kim, M. S. Lee and Y. K. Lee, *J. Cryst. Growth*, 2003, **249**, 201.

[12] M. J. Zheng, L. D. Zhang, G. H. Li and W. Z. Shen, *Chem. Phys. Lett.*, 2002, **363**, 123.

[13] Y. Li, G. W. Meng, L. D. Zhang and F. Phillipp, *Appl. Phys. Lett.*, 2000, **76**, 2011.

[14] L. Vayssieres, *Adv. Mater.*, 2003, **15**, 464.

[15] J. Zhang, L. Sun, H. Pan, C. Liao and C. Yan, *New J. Chem.*, 2002, **26**, 33.

[16] J. J. Wu and S. C. Liu, *Adv. Mater.*, 2002, **14**, 215.

[17] W. I. Park, D. H. Kim, S. W. Jung and G. C. Yi, *Appl. Phys. Lett.*, 2002, **80**, 4232.

[18] J. Zygmunt, F. Krumeich and R. Nesper, *Adv. Mater.*, 2003, **15**, 1538.

[19] C. N. R. Rao and M. Nath, *Dalton Trans.*, 2003, 1.

[20] Z. L. Wang, *Adv. Mater.*, 2003, **15**, 432.

[21] C. N. R. Rao, F. L. Deepak, G. Gundiah and A. Govindaraj, *Progress in Solid State Chem.*, 2003, **31**, 5.

[22] B. Zheng, Y. Wu, P. Yang and J. Liu, *Adv. Mater.*, 2002, **14**, 122.

[23] Z. W. Pan, Z. R. Dai, C. Ma and Z. L. Wang, *J. Am. Chem. Soc.*, 2002, **124**, 1817.

[24] S. Sun, G. Meng, M. Zhang, Y. Hao, X. Zhang and L. Zhang, *J. Phys. Chem. B*, 2003, **107**, 13029.

[25] D. P. Yu, Q. L. Hang, Y. Ding, H. Z. Zhang, Z. G. Bai, J. J. Wang, Y. H. Zou, W. Qian, G. C. Xiong and S. Q. Feng, *Appl. Phys. Lett.*, 1998, **73**, 3076.

[26] J. Q. Hu, Y. Ziang, X. M. Meng, C. S. Lee and S. T. Lee, *Chem. Phys. Lett.*, 2003, **367**, 339.

[27] Y. W. Wang, C. H. Liang, G. W. Meng, X. S. Peng and L. D. Zhang, *J. Mater. Chem.*, 2002, **12**, 651.

[28] K. S. Wenger, D. Cornu, F. Chassagneux, T. Epicier and P. Miele, *J. Mater. Chem.*, 2003, **13**, 3058.

[29] K.H. Lee, H. S. Yang, K. H. Baik, J. Bang, R. R. Vanfleet, W. Sigmund, *Chem. Phys. Lett.*, 2004, **383**, 380.

[30] R. Fan, Y. Wu, D. Li, M. Yue, A. Majumdar and P. Yang, *J. Am. Chem. Soc.*, 2003, **125**, 5254.

[31] D.P. Yu, Z.G. Bai, Y. Ding, Q.L. Hang, H.Z. Zhang, J.J. Wang, Y.H. Zou, W. Qian, G.C. Xiong, H.T. Zhou, S.Q. Feng, *Appl. Phys. Lett.*, 1998, **72**, 3458.

[32] M.K. Sunkara, S. Sharma, R. Miranda, G. Lian, E.C. Dickey, *Appl. Phys. Lett.*, 2001, **79**, 1546.

[33] A.M. Morales, C.M. Lieber, *Science*, 1998, **279**, 208.

[34] N. Wang, Y.H. Tang, Y.F. Zhang, C.S. Lee, S.T. Lee, *Phys. Rev. B*, 1998, **58**, R16024.

[35] N. Wang, Y.F. Zhang, Y.H. Tang, C.S. Lee, S.T. Lee, *Appl. Phys. Lett.*, 1998, **73**, 3902.

[36] Y.F. Zhang, Y.H. Tang, N. Wang, C.S. Lee, I. Bello, S.T. Lee, *J. Cryst. Growth*, 1999, **197**, 136.

[37] J.L. Gole, J.D. Stout, W.L. Rauch, Z.L. Wang, *Appl. Phys. Lett.* 2000, **76**, 2346.

[38] S. Botti, R. Gardi, R. Larciprete, A. Goldoni, L. Gregoratti, B. Kaulich, M. Kiskinova, *Chem. Phys. Lett.*, 2003, **371**, 394.

[39] H. Dai, E. W. Wong, Y. Z. Lu, S. Fan and C. M. Lieber, *Nature (London)*, 1995, **375**, 769.

[40] W. Han, S. Fan, Q. Li, W. Liang, B. Gu and D. Yu, *Chem. Phys. Lett.*, 1997, **265**, 374.

[41] G. W. Meng, L. D. Zhang, C. M. Mo, S. Y. Zhang, Y. Qin, S. P. Feng and H. J. Li, *J. Mater. Res.*, 1998, **13**, 2533.

[42] X. T. Zhou, N. Wang, H. L. Lai, H. Y. Peng, I. Bello, N. B. Wong, C. S. Lee and S. T. Lee, *Appl. Phys. Lett.*, 1999, **74**, 3942.

[43] C. H. Liang, G. W. Meng, L. D. Zhang, Y. C. Wu and Z. Cui, *Chem. Phys. Lett.*, 2000, **329**, 323.

[44] J. Q. Hu, Q. Y. Lu, K. B. Tang, B. Deng, R. R. Jiang, Y. T. Qian, W. C. Yu, G. E. Zhou, X. M. Liu and J. X. Wu, *J. Phys. Chem. B*, 2000, **104**, 5251.

[45] Y. Zhang, N. Wang, R. He, X. Chen and J. Zhu, *Solid State Commun.*, 2001, **118**, 595.

[46] Z. Pan, H. L. Lai, F. C. K. Au, X. Duan, W. Zhou, W. Shi, N. Wang, C. S. Lee, N. B. Wong, S. T. Lee and S. Xie, *Adv. Mater.*, 2000, **12**, 1186.

[47] W. Han, S. Fan, Q. Li, B. Gu, X. Zhang and D. Yu, *Appl. Phys. Lett.*, 1997, **71**, 2271.

[48] M. J. Wang and H. Wada, *J. Mater. Sci.*, 1990, **25**, 1690.

[49] X. C. Wu, W. H. Song, B. Zhao, W. D. Huang, M. H. Pu, Y. P. Sun and J. J. Du, *Solid State Commun.*, 2000, **115**, 683.

[50] R. Seshadri, A. Govindaraj, H. N. Aiyer, R. Sen, G. N. Subbanna, A. R. Raju, C. N. R. Rao, *Current Sci.*, 1994, **66**, 839.

[51] M. Nath, B. C. Satishkumar, A. Govindaraj, C. P. Vinod and C. N. R. Rao, *Chem. Phys. Lett.*, 2000, **322**, 333.

[52] C. N. R. Rao, R. Sen, B. C. Satishkumar and A. Govindaraj, *Chem. Commun.*, 1998, 1525.

[53] Z. W. Pan, Z. R. Dai and Z. L. Wang, *Science*, 2001, **291**, 1947.

[54] L. Binet and D. Gourier, *J. Phys. Chem. Solids*, 1998, **59**, 1241.

[55] V. I. Vasil'tsiv, Ya. M. Zakharko and Ya. I. Prim, *Ukr. Fiz. Zh.*, 1988, **33**, 1320.

[56] H. Iwanga, N. Shibata, O. Nittono and M. Kasuga, *J. Cryst. Growth*, 1978, **45**, 228.

[57] K. Vanheusdan, W. L. Warren, C. H. Seager, D. R. Tallant, J. A. Voigt and B. E. Gnade, *J. Appl. Phys.*, 1996, **79**, 7983.

[58] I. P. Swainson, M. T. Dove and D. C. Palmer, *Phys. Chem. Minerals*, 2003, **30**, 353.

[59] V. N. Sigaev, E. N. Smelyanskaya, V. G. Plotnichenko, V. V. Koltashev, A. A. Volkov and P. Pernice, *J. Non-Cryst. Solids*, 1999, **248**, 141.

[60] N. N. Greenwood and A. Earnshaw, *Chemistry of the Elements*, 2nd ed. (Butterworth Heinemannm), pp. 343.

[61] Y. Yin and Y. Xia, *Adv. Funct. Mater.*, 2000, **12**, 293.

[62] Z. W. Pan, Z. R. Dai, C. Ma and Z. L. Wang, *J. Am. Chem. Soc.*, 2002, **124**, 1817.

[63] Y. J. Xing, D.P. Yu, Z.H. Xi and Z.Q. Xue, *Appl. Phys. A*, 2003, **76**, 551.

[64] H. Fritzsche (Ed.), *Amorphous Silicon and Related Materials*, World Scienti.c, Singapore, 1989.

[65] Y. F. Zhang, Y. H. Tang, H. Y. Peng, N. Wang, C. S. Lee, I. Bello, and S. T. Lee, *Appl. Phys. Lett.*, 1999, **75**, 1842.

[66] X. C. Wu, W. H. Song, W. D. Huang, M. H. Pu, B. Zhao, Y. P. Sun and J. J. Du, *Mater. Res. Bull.*, 2001, **36**, 847 and references therein.

[67] E. I. Givargizov, *J. Cryst. Growth*, 1975, **31**, 20.

[68] R. S. Wagner and W. C. Ellis, *Appl. Phys. Lett.*, 1964, **4**, 89.

[69] A. O. Konstantinov, A. Henry, C. I. Harris and E. Jansén, *Appl. Phys. Lett.*, 1995, **66**, 2250.

[70] (a) T. Tomita, S. Saito, M. Baba, M. Hundhausen, T. Suemoto and S. Nakashima, *Phys. Rev. B*, 2000, **62**, 12896

[71] S. Nakashima, H. Katashama, Y. Nakamura and A. Mitsuishi, *Phys. Rev. B*, 1986, **33**, 5721.

[72] D. Olego and M. Cardona, *Phys. Rev. B*, 1982, **25**, 3889.

[73] P. Y. Yu and M. Cardona, *Fundamentals of Semiconductors*, Springer-Verlag, Berlin, 1996, p. 366.

1.3 Hydrogel route to inorganic nanotubes

1.3.1 Introduction

Nanotubes of metal oxides have been synthesized by employing different strategies [1]. Sol-gel chemistry has been used by a few workers in the synthesis of nanotubes of metal oxides such as silica [2] and titania [3]. Oxide gels in the presence of surfactants or suitable templates form nanotubes. For example, by coating carbon nanotubes (CNTs) with oxide gels and then burning off the CNTs, one obtains nanotubes and nanowires of metal oxides such as ZrO_2, SiO_2, Al_2O_3, V_2O_5, IrO_2, RuO_2, WO_3 and MoO_3 [4–6]. Sol-gel synthesis of oxide nanotubes has also been accomplished in the pores of alumina membranes [7].

One of the novel methods for the synthesis of metal oxide nanotubes employs gels derived from low molecular weight organic compounds. Organic supramolocular assemblies have been extensively used as templates to obtain inorganic materials with morphologies and properties, which are difficult to obtain by conventional chemical and physical techniques. Examples of these include micelles which act as templates for the synthesis of mesoporous materials, polymer beads for synthesizing macroporous materials and organogelators for the synthesis of oxide nanotubes. Organogelators gel solvent at low concentrations due to the formation of a three-dimensional network based on fibrous aggregates in organic fluids [8,9]. The self-assembled organogelators act as templates in the sol-gel polymerization process [10]. The gel fibers are coated with oxidic materials followed by the dissolution on the gel in a suitable solvent and by calcination. This strategy has been employed to synthesize silica nanotubes [11, 12]. Shinkai and co-workers have shown that certain cholesterol derivatives can gelate tetraethylorthosilicate (TEOS), causing silica polymerization [11,13–16], giving rise to hollow lamellar [13,14], helical [12], linear fiber [8, 15] or chiral spiral [16, 17] structures. Hollow silica tubes have

also been synthesized using organic gelators based on chiral diaminocyclohexane derivatives [18], 2,3-di-n-decycloxyanthracene [19], cyclohexane [20] and sugar-appended porphyrin [21]. Jung *et al.* [22] have thus prepared ultrastable mesoporous silica using a phenanothroline-appended cholesterol organogelator as the template. TiO_2 hollow fibers have been obtained by Kobayashi *et al.* [23] using titanium alkoxide as the precursor along with the supramolocular assemblies of *trans*-(1R, 2R)-1,2-cyclohexanedi(11-aminecarbonylundecylpyridinium) hexafluorophate as templates. Helical ribbon and double-layered TiO_2 nanotubes have been prepared using a cholesterol-based gelator [24]. Nanotubes of transition metal (Ta, V) oxides have also been prepared by this templating method [25]. The above nanotube syntheses have generally made use of organogels as templates.

In all the syntheses listed above, organogelators have been used as templates due to which metal alkoxides become necessary precursors. Due to the difficulties in synthesizing as well as handling metal alkoxides, most of them being moisture sensitive, the number of metal oxides that can be synthesized using organogelators gets limited. In order to use simple metal salts as precursors, the reactions have to be carried out in an aqueous medium in which these salts are soluble. This prompted us to use hydrogels as instead of organogels as templates. Gelation of aqueous fluids is different from that in organic solvents in that the aggregation process in aqueous environments is predominantly driven by the hydrophobic effect. It had been previously reported that a tripodal cholamide (1), shown in Figure 1.3.1 having hydrophobic surfaces (coming from the β-face of the bile acid backbone), spontaneously aggregates into gel fibers in predominantly aqueous media [26].

We considered it might be of value to use this hydrogelator to synthesize nanotubes of metal oxides. It has been possible to prepare nanotubes of SiO_2, TiO_2, ZrO_2, ZnO and WO_3 as well as of $ZnSO_4$ and $BaSO_4$ by employing this hydrogel.

1.3.2 Experimental

The gelator 1 was synthesized by the procedure reported elsewhere [26]. In a typical reaction for the synthesis of silica nanotubes, 20 mg (0.03 mmol) of the
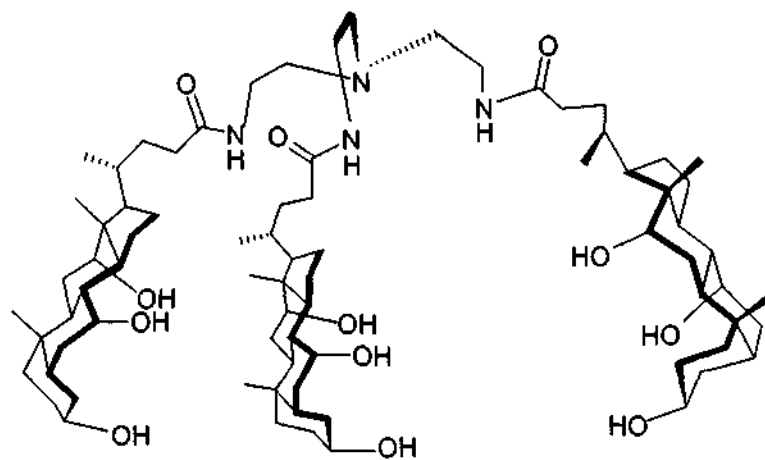
1

Figure 1.3.1: Schematic of the tripodal cholamide gelator

gelator was dissolved in 0.4 ml CH_3COOH and 1.6 ml H_2O was added to induce gelation. This was thoroughly mixed by shaking and warmed slightly to form a sol. To this sol, 0.1 ml (0.45 mmol) of tetraethylorthosilicate (TEOS, Merck, > 98%) was added and the mixture allowed to stand at room temperature. Gel fibers soon formed, simultaneously accompanied by the hydrolysis of TEOS around them. The gel was dried after 24 h in vacuum to obtain gel fibers coated with silica.

In order to prepare titania nanotubes, tetrabutyl orthotitanate (TBOT, Fluka) was used as the starting material. 0.1 ml (0.29 mmol) of TBOT was added to 0.5 ml of distilled C_2H_5OH and 0.1 ml CH_3COOH to obtain a gel. This was added to a sol containing 20 mg gelator with 0.3 ml CH_3COOH and 1.6 ml H_2O to obtain a white gel. The gel was allowed to stand for a day at room temperature and then dried under vacuum. We thus obtained gel fibers coated with titania. For the synthesis of zirconia nanotubes, 50 mg $ZrOCl_2$ (0.16 mmol, S. D. Fine, 96%) was dissolved in 1 ml H_2O and a drop of NH_3 was added to form a gel. This was mixed with a solution containing 20 mg gelator with 0.4 ml CH_3COOH and 0.6 ml H_2O. A white gel was obtained, which on drying gave gel fibers coated with zirconia. $ZrOCl_2$ was chosen as the source of Zr since it is possible to control the rate of hydrolysis of this as compared to other sources of Zr such as zirconium isopropoxide, which are

difficult to handle due to their extremely fast hydrolysis in aqueous media.

In order to prepare ZnO nanotubes, a gel was formed initially by taking 35 mg zinc acetate (0.16 mmol, Merck, 98%) in ethanol and mixing with 10 mg KOH in 1 ml ethanol. This was added to a sol containing 20 mg gelator with 1.6 ml H_2O and 0.4 ml CH_3COOH. A white gel was obtained that was allowed to stand for a day at ambient temperature and then dried in vacuum. For the synthesis of WO_3 nanotubes, tungstic acid prepared by passing sodium tungstate (S. D. Fine, 99%) through a cation exchange column was used. 2 ml of the above solution was added to a solution containing 20 mg gelator and 0.4 ml CH_3COOH to obtain a gel. This was allowed to stand for a day at room temperature and then dried in vacuum.

Nanotubes of $ZnSO_4$ were prepared by starting from an ammonical solution of $ZnSO_4$ (30 mg $ZnSO_4$ (0.19 mmol, Qualigens, 99%) in 1.6 ml H_2O with a drop of NH_3) to which a solution containing 20 mg gelator in 0.4 ml CH_3COOH was added. A white gel was obtained immediately which was dried in vacuum. In order to synthesize nanotubes of $BaSO_4$, 55 mg of $BaCl_2$ (0.23 mmol, Aldrich, 99%) taken in 0.5 ml water was added to a solution containing 20 mg gelator in 0.1 ml CH_3COOH to form a gel. To this gel, a solution containing 30 mg ammonium sulfate in 0.5 ml water was added to obtain $BaSO_4$. This was further dried in vacuum.

Thermogravimetric analysis (TGA) of the samples was carried out on a Mettler-Toledo-TG-850 instrument to verify the removal of the gelator. In Figure 1.3.2, we show a representative TGA curve for the as-synthesized and calcined ZrO_2 nanotubes. In the as-synthesized sample, there is a weight loss of 64% corresponding to the removal of the gelator, which is completely done at a temperature of 475 °C. There was no weight loss in the calcined samples indicating the complete removal of the gelator. In order to remove the template, the samples were generally washed 2–3 times with 10 ml distilled ethanol and then heated to 500 °C for 1 h (1 °C min^{-1}) in flowing O_2 gas.

After obtaining the gel fibers coated with the inorganic precursors, they were observed by transmission electron microscopy (TEM) using a JEOL JEM 3010 microscope, operating with an accelerating voltage of 300 kV. Samples for TEM
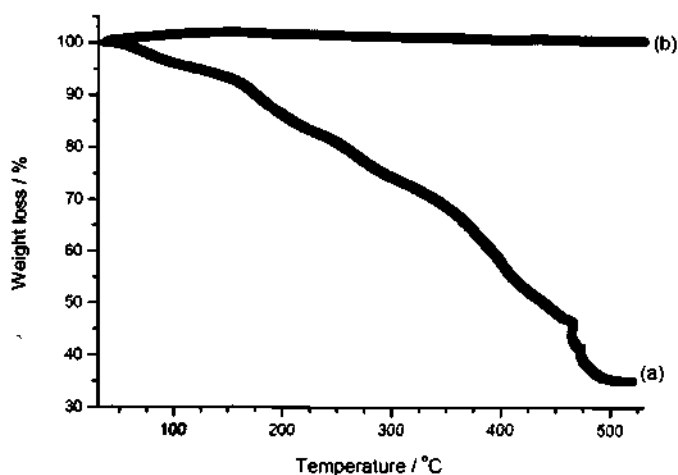
Figure 1.3.2: TGA curves for the ZrO_2 nanotubes (a) as–synthesized and (b) after removal of the gel by calcination.

studies were prepared by dispersing the nanotubes by sonication in CCl_4. A drop of the suspension was put on a holey carbon coated Cu grid and allowed to evaporate slowly. Scanning electron microscopy (SEM) images were obtained on a LEICA S440i scanning electron microscope. Powder X-ray diffraction (XRD) patterns were recorded using $CuK\alpha$ radiation on a Rich-Siefert, XRD3000-TT diffractometer. XRD patterns revealed the samples to be amorphous before removal of the template. Photoluminescence (PL) measurements were carried out at room temperature with a Perkin- Elmer model LS50B luminescence spectrometer using 325 nm as the excitation wavelength (λ_{ex}).

1.3.3 Results and discussion

The hydrogel contains well-defined fibers with diameters between 8 and 10 nm and lengths extending to a few hundred nanometers as revealed by the TEM images in Figure 1.3.3(a). In Figure 1.3.3(b), we show a TEM image of the silica nanotubes obtained after removal of the gel template. The image clearly indicates the hollow nature of the tubes, which have an outer diameter of 30–40 nm and an inner diameter of 4–5 nm. The nanotubes have lengths extending to a few hundred nanometers. Although silica shrinks to some extent during the calcination, the size of the nanotubes is comparable with that of the gelator fibers (8–10 nm). The

99
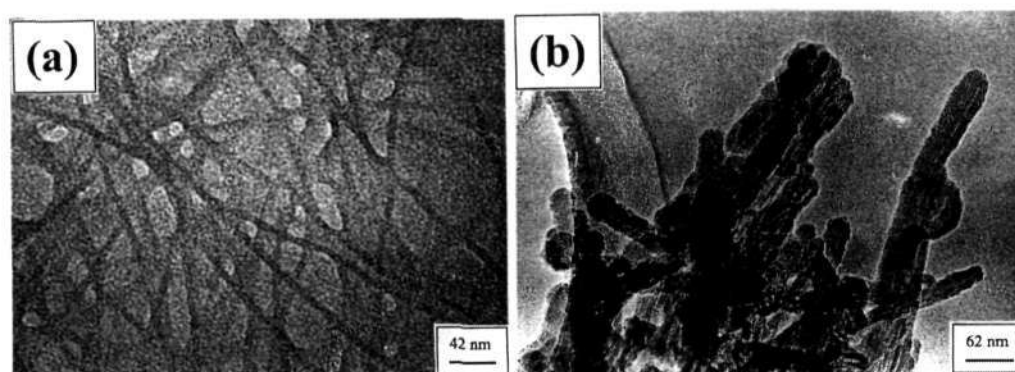
Figure 1.3.3: Low-magnification TEM images of (a) the hydrogel fibers and (b) the silica nanotubes obtained after removal of the gel fibers

distribution of the diameters is quite narrow as evidenced from Figure 1.3.3(b). The SiO_2 nanotubes were X-ray amorphous.

We could obtain good yields of the TiO_2 nanotubes by the hydrogel method. In Figure 1.3.4(a), we show a low- magnification TEM image of the titania coated gel fibers. After removal of the template with ethanol, followed by calcination, we obtained hollow TiO_2 nanotubes as shown in Figures 1.3.4(b)-(d). These have inner diameters between 4 and 7 nm and an outer diameter between 10 and 20 nm with a narrow size distribution. The lengths go up to a few hundred nanometers. The XRD pattern of the TiO_2 nanotubes (Figure 1.3.5(a)) showed them to be in the anatase phase (JCPDS file: 21–1272), as also confirmed by the selected area electron diffraction (SAED) pattern (see inset of Figure 1.3.4(b)). The TiO_2 nanotubes obtained by using organogelators are reported to have diameters in the range of 150 to 600 nm. The nanotubes obtained by us in the present study are therefore considerably thinner and may be useful for carrying out photocatalytic reactions and other purposes.

There have been no reports on the synthesis of zirconia nanotubes using gelators as templates and in Figure 1.3.6, we show TEM images of the zirconia nanotubes synthesized. These have outer diameters of *ca.*25 nm and inner diameters between 4 and 7 nm. The length extends to a few hundreds of nanometers. Figure 1.3.6(a) shows a nanotube with smooth walls. Also seen in Figure 1.3.6(b) are sphere-like particles along with the nanotubes. These may be formed when the hydrolysis
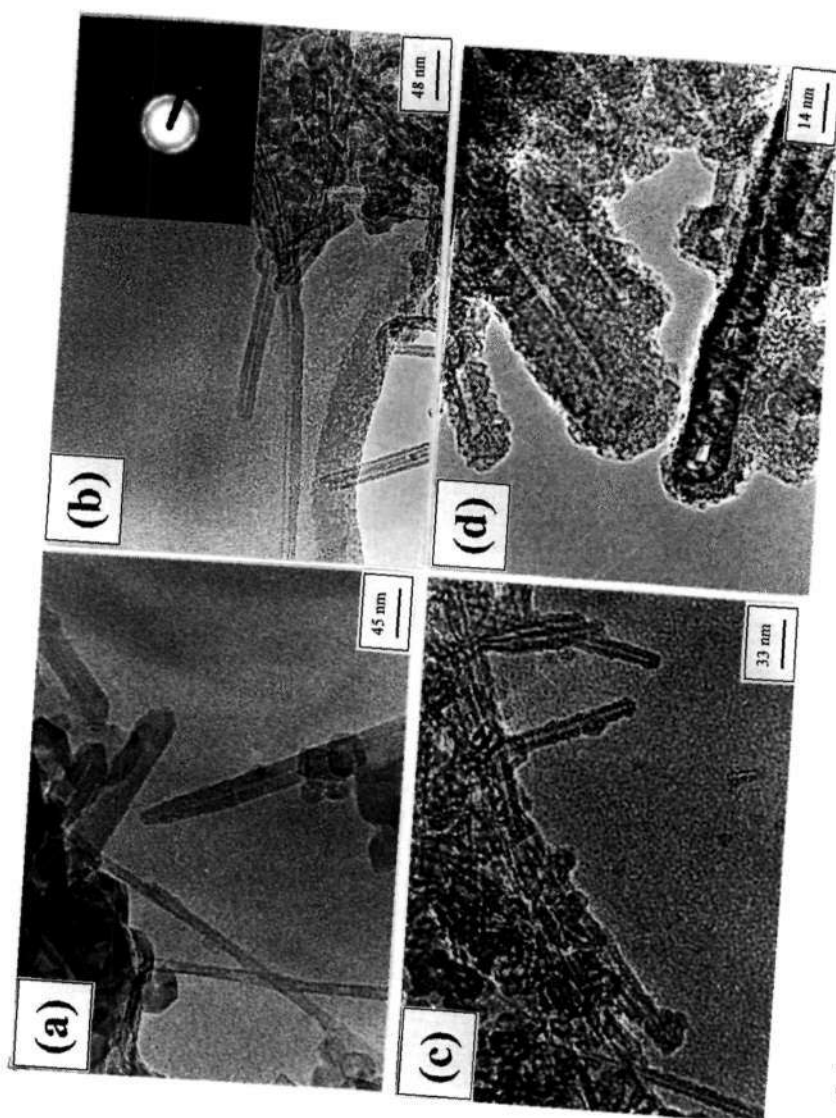
Figure 1.3.4: TEM images of titania nanotubes (a) as-synthesized and (b)-(d) after removal of the gel fibers. Inset shows the SAED pattern taken on a single nanotube.
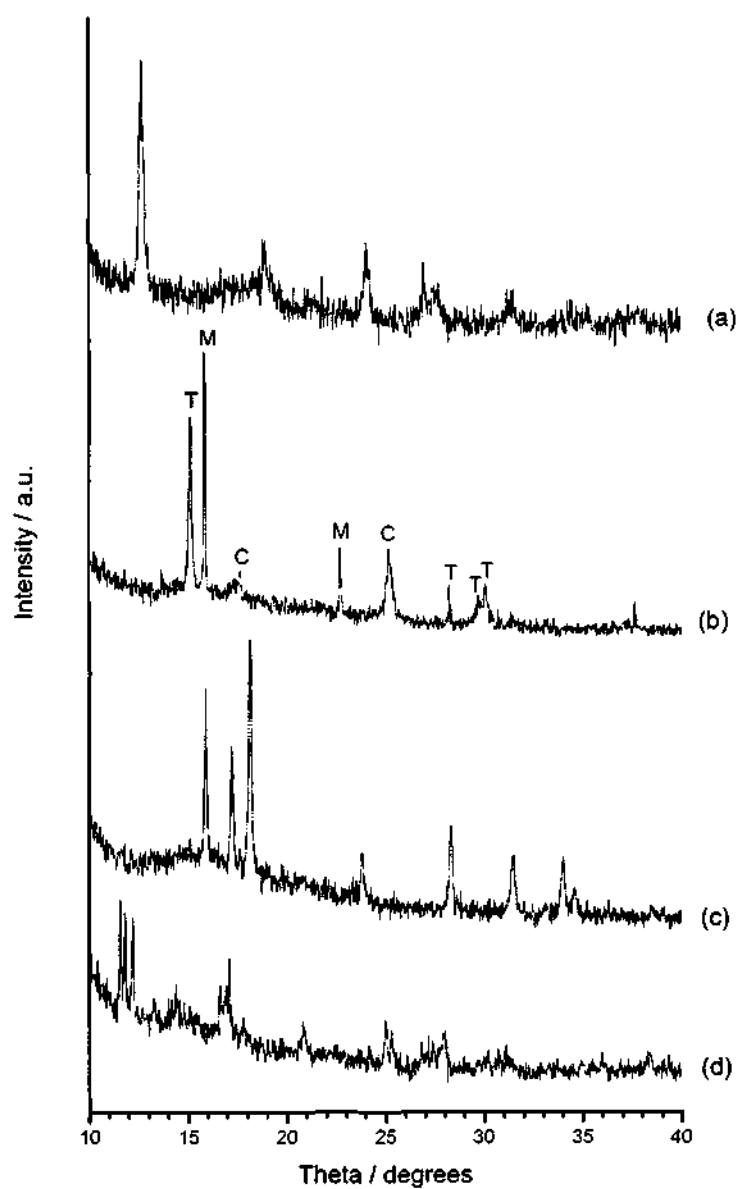
Figure 1.3.5: XRD patterns of (a) TiO_2, (b) ZrO_2 (where C, M and T denote the cubic, monoclinic and tetragonal phases respectively), (c) ZnO and (d) WO_3 nanotubes.

102
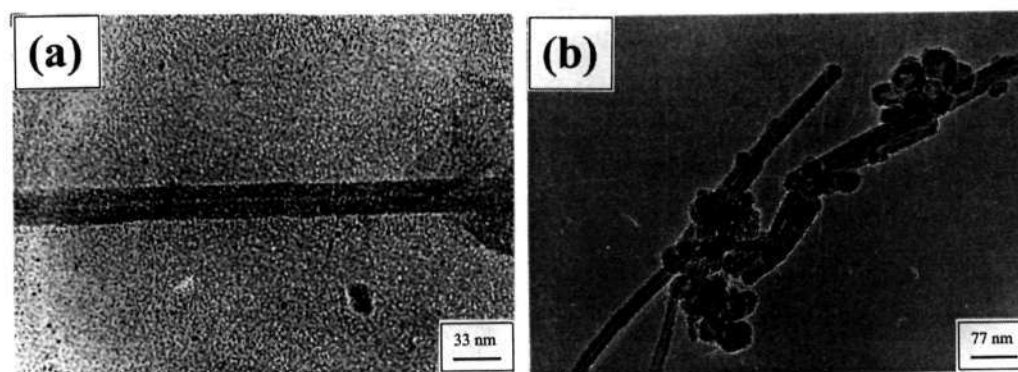
Figure 1.3.6: Low magnification TEM images of the zirconia nanotubes obtained after removal of the gel fibers.
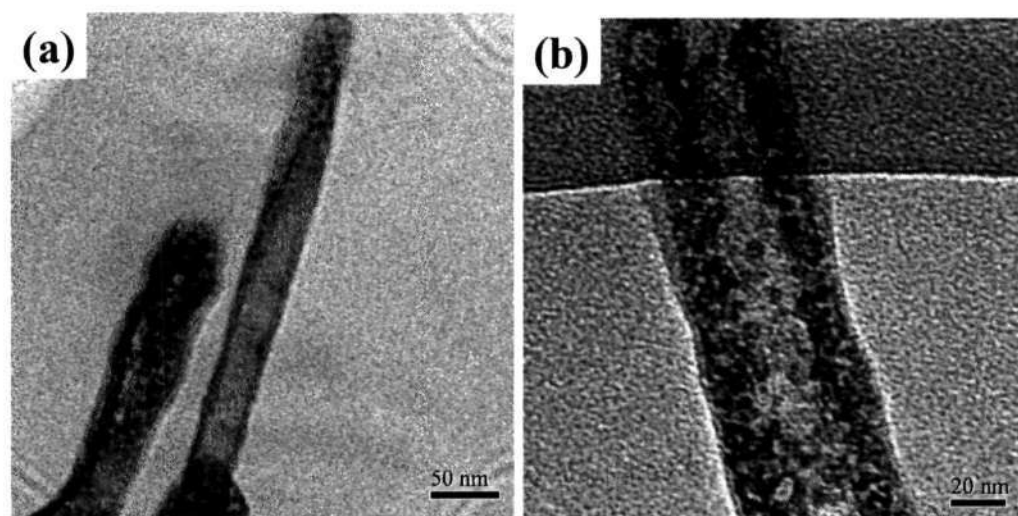
Figure 1.3.7: Low magnification TEM images of ZnO nanotubes obtained after removal of the gel fibers.

of the inorganic species occurs at a faster rate that the formation of the gel fibers from the gelator. As a result, the inorganic species encapsulate a part of the gelator that leads to hollow, spherical particles after heat treatment. The XRD pattern of the calcined sample (Figure 1.3.5(b)) shows the nanotubes to be composed of a mixture of the stable monoclinic phase (JCPDS file: 37-1484) with the metastable cubic and tetragonal phases (JCPDS files: 27-0997 and 42-1164 respectively).

We have been successful in preparing ZnO nanotubes as shown in the low-magnification TEM images in Figure 1.3.7. The SEM images in 1.3.8(a) and (b) reveal the yields of the nanotubes to be excellent. The nanotubes have outer

103

diameters in the range of 30–60 nm and inner diameters of $ca.20$ nm, with lengths extending into several hundred nanometers. The XRD pattern, shown in Figure 1.3.5(c), could be indexed on the basis of the hexagonal structure of ZnO (JCPDS file: 36–1451). ZnO is a wide bandgap (3.37 eV) and has been extensively investigated as a short-wavelength light-emitting, transparent conducting and piezoelectric material. There are several reports on the synthesis of ZnO nanowires [27, 28] and nanorods [29] but just one on the synthesis of ZnO nanotubes [30] synthesized hydrothermally. These nanotubes had inner diameters in the range of 250 nm. The nanotubes obtained by us are much thinner in diameters, therefore, we considered it worthwhile to investigate the photoluminescence. The photoluminescence spectrum of the ZnO nanotubes obtained by us (Figure 1.3.8(c)) shows peaks centered around 385 nm and 440 nm, the former being the major one corresponding to the near band-edge emission of ZnO. The origin of the 440 nm band is not clear [31]. We do not see the PL band around 520 nm due to the single ionized oxygen vacancy in ZnO.

In Figure 1.3.9, we show TEM images of the WO_3 nanotubes obtained after removal of the gel fibers. Shown in Figure 1.3.9(a) is a single nanotube having an outer diameter of $ca.40$ nm and an inner diameter of $ca.5$ nm. The nanotubes have lengths that go to a few hundred nanometers. A bundle of the WO_3 nanotubes is shown in Figure 1.3.9(b). The XRD pattern shown in Figure 1.3.5(d), confirms the monoclinic structure of WO_3 (JCPDS file: 43-1035).

We could obtain good yields of $ZnSO_4$ nanotubes as evidenced from the TEM image shown in Figure 1.3.10(a). The nanotubes have an inner diameter of $ca.4$ nm and an outer diameter in the 10–12 nm range. Most of the nanotubes were 200–300 nm long, but a few had lengths going up to several hundreds of nanometers (Figure 1.3.10(b)). The XRD pattern of the nanotubes confirmed the orthorhombic structure (JCPDS file: 080491). These nanotubes are readily soluble in water.

The $BaSO_4$ nanotubes obtained by us are shown in the low magnification TEM images in Figure 1.3.11. The nanotubes have small aspect ratios, with the outer diameters being in the range of 100 nm and length between 250 and 350 nm. The
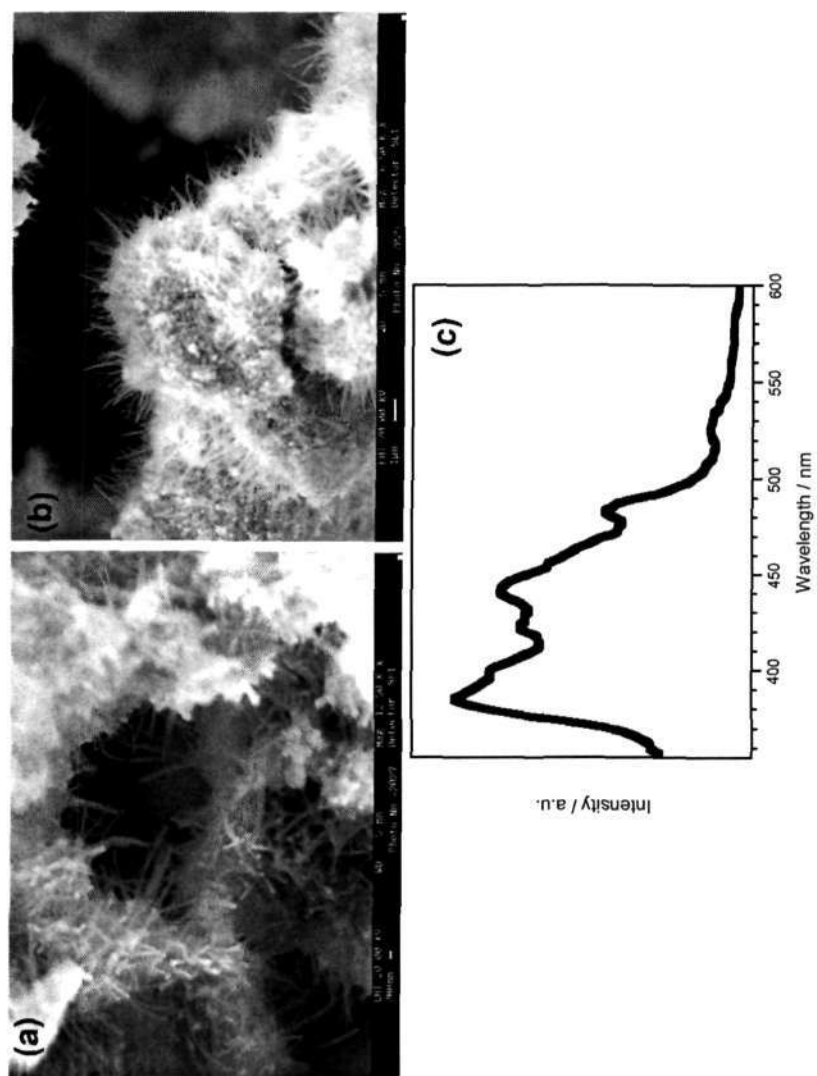
Figure 1.3.8: (a) and (b) SEM images and (c) PL spectrum of ZnO nanotubes obtained after removal of the gel fibers.
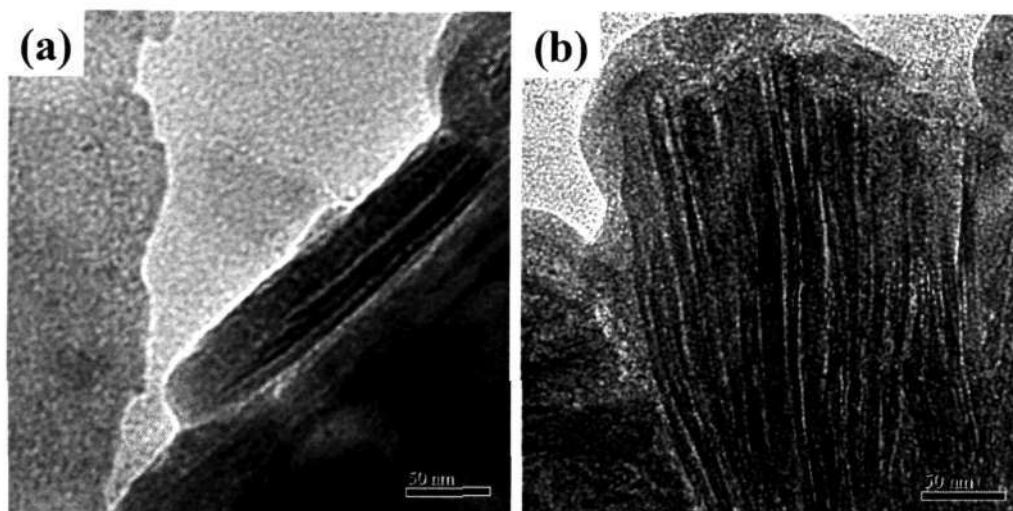
Figure 1.3.9: Low-magnification TEM images of WO$_3$ nanotubes: (a) a single nanotube and (b) a bundle of nanotubes.

nanotubes have an inner diameter of *ca.* 9 nm indicating that the gel fibers indeed act as templates. The rate at which BaSO$_4$ precipitated was fast compared to the rate of formation of the gel fibers, resulting in the small aspect ratios.

The formation of the nanotubes may be explained by the mechanism shown in Figure 1.3.12. In the first step, positively charged gelator molecules are formed in the acidic solution, which polymerize to form the gel fibers. The rate of polymerization is determined by the pH of the solution as well as the amount of water added for the gelation process. To this solution, we add a salt in which the negatively charged inorganic precursors interact with the positively charged gelator species as shown in the figure. If the rate of formation of the gel fibers is greater than that of the formation of the coating inorganic species, then we obtain nanotubes on calcination. On the other hand, if the hydrolysis and condensation of the inorganic species is faster as compared to the formation of the gel fibers, we obtain hollow spheres on removal of the organic gelator. This mechanism can explain the reason why we obtain nanotubes of similar inner diameters but contrasting lengths.
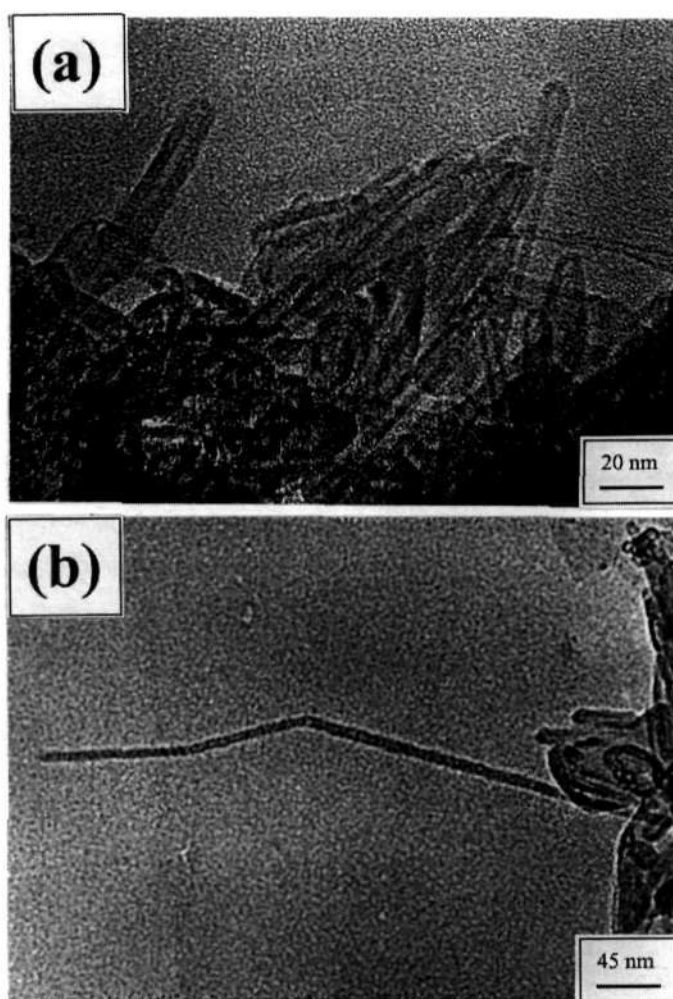
Figure 1.3.10: Low-magnification TEM images of the ZnSO$_4$ nanotubes obtained after removal of the gel fibers.

1.3.4 Conclusions

In conclusion, by using a hydrogelator (**1**), we have successfully prepared a wide range of nanotubes of oxides, which includes SiO$_2$, TiO$_2$, ZrO$_2$, ZnO and WO$_3$ as well as of metal sulfates such as ZnSO$_4$ and BaSO$_4$. The synthesis of the oxide nanotubes is not restricted to the use of inorganic alkoxides as precursors. Nanotubes of a desired diameter can easily be made by a suitable choice of the hydrogelator or by slightly modifying the conditions of gelation. This opens up new avenues to synthesize nanotubes that were previously difficult to synthesize using traditional methods. The surface areas of the nanotubes prepared by us are likely

107
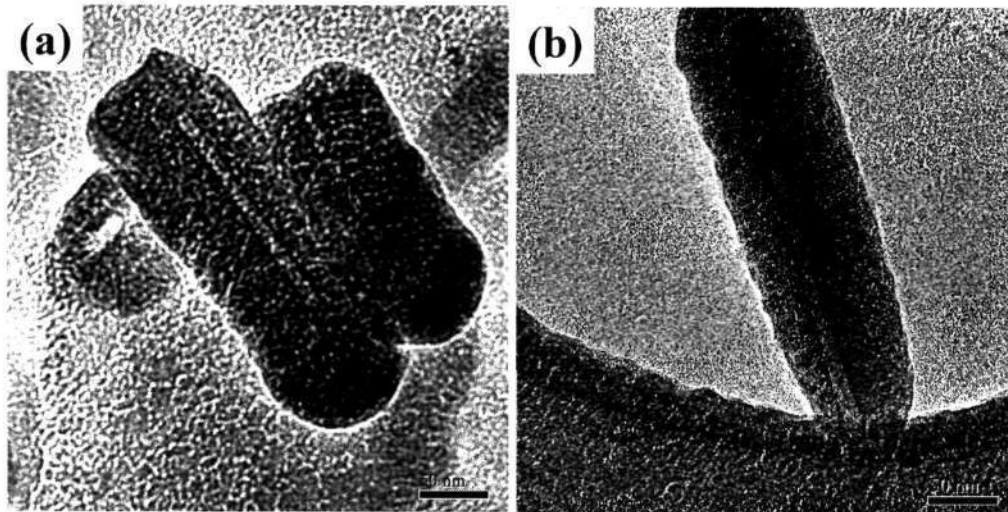
Figure 1.3.11: Low-magnification TEM images of the BaSO$_4$ nanotubes obtained after removal of the gel fibers.
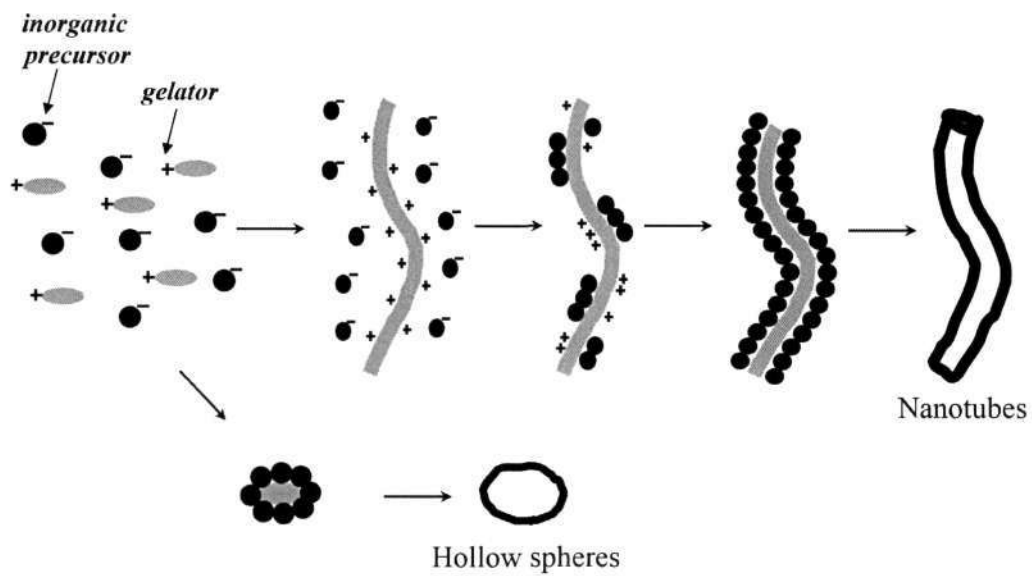
Figure 1.3.12: Mechanism for the formation of nanotubes.

to be appreciable, although we have not actually carried out the measurements. It would be useful to pursue such studies. *

*A paper based on this study has appeared in J. Mater. Chem., (2003).

References

[1]   C. N. R. Rao and M. Nath, *Dalton Trans.*, 2003, 1 and references therein.

[2]   M. Nakamura and Y. Matsui, *J. Am. Chem. Soc.*, 1995, **117**, 2651.

[3]   T. Kasuga, M. Hiramatsum, A. Hason, T. Sekino and K. Niihara, *Langmuir*, 1998, **14**, 3160.

[4]   B. C. Satishkumar, A. Govindaraj, E. M. Vogl, L. Basumallick and C. N. R. Rao, *J. Mater. Res.*, 1997, **12**, 604.

[5]   B. C. Satishkumar, A. Govindaraj, M. Nath and C. N. R. Rao, *J. Mater. Chem.*, 2000, **10**, 2115.

[6]   C. N. R. Rao, B. C. Satishkumar and A. Govindaraj, *Chem. Commun.*, 1997, 1581.

[7]   B. B. Lakshmi, C. J. Patrissi and C. R. Martin, *Chem. Mater.*, 1997, **9**, 2544.

[8]   P. Terech and R. G. Weiss, *Chem. Rev.*, 1997, **97**, 3133.

[9]   K. Hanabusa, K. Hiratsuka, M. Kimura and H. Shirai, *Chem. Mater.*, 1999, **11**, 649.

[10] S. Kobayashi, K. Hanabusa, M. Suzuki, M. Kimura and H. Shirai, *Chem. Lett.*, 1999, 1077.

[11] Y. Ono, K. Nakashmia, M. Sano, Y. Kanekiyo, K. Inoue, J. Hojo and S. Shinkai, *Chem. Commun.*, 1998, 1477.

[12] Y. Ono, K. Nakashmia, M. Sano, J. Hojo and S. Shinkai, *Chem. Lett.*, 1999, 1119.

[13] J. H. Jung, Y. Ono and S. Shinkai, *Langmuir*, 2000, **16**, 1643.

[14] J. H. Jung, Y. Ono and S. Shinkai, *J. Chem. Soc. Perkin Trans. 2*, 1999, 1289.

[15] Y. Ono, Y. Kanekiyo, K. Inoue, J. Hojo and S. Shinkai, *Chem. Lett.*, 1999, 23.

[16] J. H. Jung, Y. Ono and S. Shinkai, *Angew. Chem. Int. Ed.*, 2000, **39**, 1862.

[17] J. H. Jung, H. Kobayashi, M. Masuda, T. Shimizu and S. Shinkai, *J. Am. Chem. Soc.*, 2001, **123**, 8785.

[18] J. H. Jung, Y. Ono, K. Hanabusa and S. Shinkai, *J. Am. Chem. Soc.*, 2000, **122**, 5008.

[19] G. M. Clavier, J. L. Pozzo, H. Bouas-Laurent, C. Liere, C. Roux and C. Sanchez, *J. Mater. Chem.*, 2000, **10**, 1725.

[20] J. H. Jung, Y. Ono and S. Shinkai, *Eur. J. Chem.*, 2000, **6**, 4552.

[21] S. Tamaru, M. Takeuchi, M. Sano and S. Shinkai, *Angew. Chem. Int. Ed.*, 2002, **41**, 853.

[22] J. H. Jung, K. Nakashima and S. Shinkai, *NanoLett.*, 2001, **1**, 145.

[23] S. Kobayashi, K. Hanabusa, N. Hamasaki, M. Kimura, H. Shirai and S. Shinkai, *Chem. Mater.*, 2000, **12**, 1523.

[24] J. H. Jung, H. Kobayashi, K. J. C. van Bommel, S. Shinkai and T. Shimizu, *Chem. Mater.*, 2002, **14**, 1445.

[25] S. Kobayashi, N. Hamasaki, M. Suzuki, M. Kimura, H. Shirai and K. Hanabusa, *J. Am. Chem. Soc.*, 2002, **124**, 6550.

[26] U. Maitra, S. Mukhopadhyay, A. Sarkar, P. Rao and S. S. Indi, *Angew. Chem. Int. Ed.*, 2001, **40**, 2281.

[27] M. H. Huang, Y. Wu, H. Feick, N. Tran, E. Weber and P. Yang, *Adv. Mater.*, 2001, **13**, 113.

[28] Y. C. Kong, D. P. Yu, B. Zhang, W. Fang and S. Q. Feng, *Appl. Phys. Lett.*, 2001, **78**, 407.

[29] C. Xu, G. Xu, Y. Liu and G. Wang, *Solid State Commun.*, 2002, **122**, 175.

[30] J. Zhang, L. Sun, C. Liao and C. Yan, *Chem. Commun.*, 2002, 262.

[31] Z. Fu, B. Lin, G. Liao and Z. Wu, *J. Cryst. Growth*, 1998, **193**, 316.

1.4 Hydrogen storage in carbon nanotubes and related materials

1.4.1 Introduction

The early report of Dillon *et al.* [1] that carbon nanotubes can be used to store considerable amounts of hydrogen created high expectations [2]. Dillon *et al.* used unpurified soot containing 0.1–0.2 wt% of single-walled carbon nanotubes (SWNTs) and obtained 0.01 wt% of H_2 storage at 0 °C. They extrapolated that SWNTs had 5 wt% H_2 storage capacity assuming that only the nanotubes were responsible for the H_2 uptake. Since then, several workers have examined H_2 adsorption with carbon fibres as well as nanotubes produced by different methods [3–7]. While Liu *et al.* [8] reported a H_2 storage capacity of 4.2 wt% in SWNTs generated by a semicontinuous hydrogen arc-discharge method, Ye *et al.* [9] found a gravimetric H_2 storage capacity as high as 8.25 wt% in high purity cut-SWNTs at 80 K under a pressure of *ca.* 7 MPa. Chen *et al.* [10] have reported a hydrogen storage capacity upto 13 wt% with aligned multiwalled carbon nanotubes (MWNTs). These workers employed quadrupole mass spectrometry and thermogravimetric analysis to study H_2 desorption properties. Interesting results on hydrogen storage have been reported with alkali-doped carbon nanotubes [11]. Li- and K-doped carbon nanotubes are reported to adsorb 20 and 14 wt% of H_2, respectively, at 1 atm. pressure, at 200 − 400 °C in the case of Li-doped nanotubes and near room temperature for the K-doped nanotubes. A lower, but substantial, H_2 adsorption was also reported for alkali-doped graphite. The highest capacity for H_2 storage (up to 67 wt%) reported to date is that by Chambers *et al.* [12] for graphite nanofibres at ambient temperatures and at a pressure of 11.35 MPa. Electrochemical hydrogen storage in carbon nanotube materials was carried out by Nützenadel *et al.* [13] on as-prepared SWNTs and MWNTs. For the SWNT samples, the measured discharge capacities indicated a storage capacity of 0.39 wt%

(110 mA h g^{-1}). SWNTs are also reported to show reversible charging capacities of up to 800 mA h g^{-1} corresponding to a capacity of 2.9 wt% [14].

In spite of several of the favorable reports listed above, the scenario is not encouraging. Some of the recent papers report hardly any adsorption in the different carbon nanostructures, the maximum adsorption in some cases being lower than 1 wt% [15, 16]. In view of the importance of the subject and also the wide *differences amongst the various findings, we considered it important to carry out* H_2 adsorption measurements systematically on well-characterized samples of carbon nanotubes and fibres prepared by different methods. We have, therefore, carried out measurements on SWNTs produced by the arc-discharge method, on MWNTs synthesized by arc-discharge and by the pyrolysis of acetylene over catalysts, on aligned multi-walled nanotubes obtained by the pyrolysis of organometallic precursors as well as carbon fibres. The measurements have been carried out on as-synthesized samples as well as samples subjected to acid treatment to remove catalyst particles. In addition to carrying out adsorption measurements, electrochemical studies of hydrogen storage have also been performed on these materials.

1.4.2 Experimental

Synthesis and characterization of the samples

The carbon samples that we studied for hydrogen storage are as follows: SWNTs synthesized by the arc-discharge method (as-synthesized), **I**; SWNTs synthesized by the arc-discharge method (treated with conc. HNO_3), **II**; MWNTs synthesized by the pyrolysis of acetylene (as-synthesized), **III**; MWNTs synthesized by the pyrolysis of acetylene (treated with conc. HNO_3), **IV**; MWNTs synthesized by the arc-discharge method, **V**; aligned MWNT bundles synthesized by the pyrolysis of ferrocene (as-synthesized), **VI**; aligned MWNT bundles synthesized by the pyrolysis of ferrocene (treated with acid), **VII**; aligned MWNT bundles synthesized by the pyrolysis of ferrocene and acetylene (as-synthesized), **VIII**; and aligned MWNT bundles synthesized by the pyrolysis of ferrocene and acetylene (treated

116
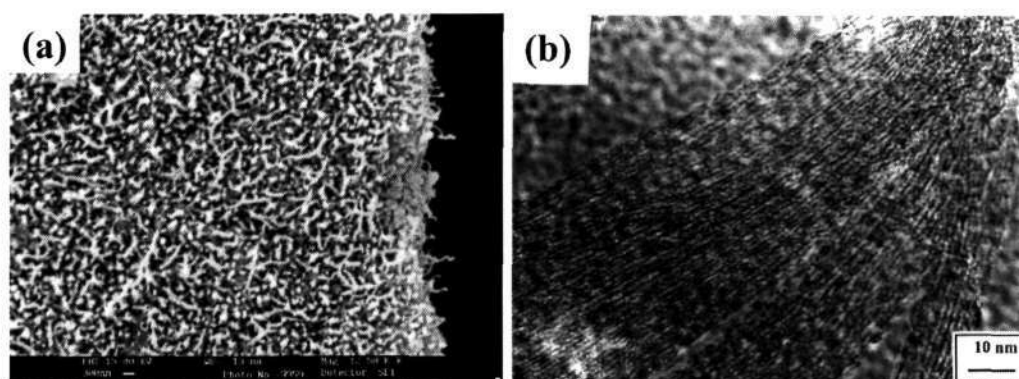
Figure 1.4.1: (a) SEM and (b) HREM images of SWNTs, II.

with acid), IX.

Scanning electron microscopy (SEM) images for all the samples were obtained on a LEICA S440i scanning electron microscope. Transmission electron microscopy (TEM) images were obtained with a JEOL JEM 3010 operating with an accelerating voltage of 300 kV. In order to find out the percentage of catalyst particles, thermogravimetric analysis (TGA) was performed on the samples.

SWNTs, I, were produced by the dc arc-discharge method using a composite graphite rod containing Y_2O_3 (1 at%) and Ni (4.2 at%) as anode and a graphite rod as cathode under a helium pressure of 660 Torr with a current of 100 A and 30 V as reported earlier [17]. The web-like product obtained was heated at 300 °C in air for $ca.$ 24 h to remove amorphous carbonaceous materials. In order to remove the catalyst particles and open the ends of the nanotubes, the sample was stirred with concentrated nitric acid at 60 °C for $ca.$ 12 h and washed with distilled water in order to remove the dissolved metal particles [18]. We denote the acid-treated SWNTs as II. We show a typical SEM image of the SWNT bundles in Figure 1.4.1(a). The diameter of the bundles varied between 50 and 75 nm and there seems to be hardly any amorphous carbon or catalyst impurity. The SWNTs in II had bundles of 5–50 nanotubes as revealed by high-resolution electron microscopy (HREM). The diameter of the individual nanotubes is in the range 1.2–1.4 nm. We show a typical HREM image of sample II in Figure 1.4.1(b). There is a negligible amount of amorphous carbon and of metal particles adhering to the nanotubes.

MWNTs, **III**, were prepared by the decomposition of acetylene at a flow rate of 50 standard cubic centimeters per minute (sccm) at 730 °C over an iron/silica catalyst in flowing hydrogen (75 sccm) according to a previously reported method [19]. The silica was removed by treatment with aqueous hydrofluoric acid (HF) for 12 h. The metal catalyst particles in **III** were removed by treatment with concentrated nitric acid at 60 °C for *ca.* 12 h and washing with distilled water. The acid-treated sample was heated at 350 °C to obtain **IV**. Nanotubes **III** had diameters of between 25 and 75 nm with lengths up to tens of microns [see SEM image in the inset of Figure 1.4.2(a)]. The TEM image, shown in Figure 1.4.2(a), showed the presence of extraneous carbonaceous material and catalyst particles. HREM images showed that they were not very well graphitized, presumably due to the low temperatures at which they were prepared. Upon treatment with conc. HNO_3, we found that we were able to remove a majority of the catalyst particles, which was also verified by TGA. Furthermore, the nanotubes had open ends as revealed by TEM images.

MWNTs were also prepared by striking an arc between graphite electrodes in 500 Torr of helium by a previously published method [20]. A current of 60-100 A across a potential drop of *ca.* 25 V gives high yields of carbon nanotubes. The nanotubes thus obtained were opened by heating to 600 °C in air. This sample, denoted by **V**, had nanotubes with diameters in the 300 nm range with lengths of several microns, as revealed by the SEM image in Figure 1.4.2(b). They had open ends but were well graphitized as revealed by the HREM images.

Aligned bundles of MWNTs, **VI**, were synthesized by the pyrolysis of ferrocene in an Ar atmosphere by a previously reported method [20]. The sample was scraped out from the walls of the quartz tube. We show an SEM image of the aligned MWNTs, **VI**, in Figure 1.4.2(c). The nanotubes are well aligned with lengths extending to tens of microns. In order to remove the catalyst particles, a sample of **VI** was treated with concentrated nitric acid for 4 h, followed by washing thoroughly with distilled water and drying. This acid-treated sample, denoted by **VII**, had open ends, but the alignment was retained. In order to synthesize dense bundles of aligned nanotubes (**VIII**), a mixture of acetylene (85 sccm) and ferrocene was sublimed. In
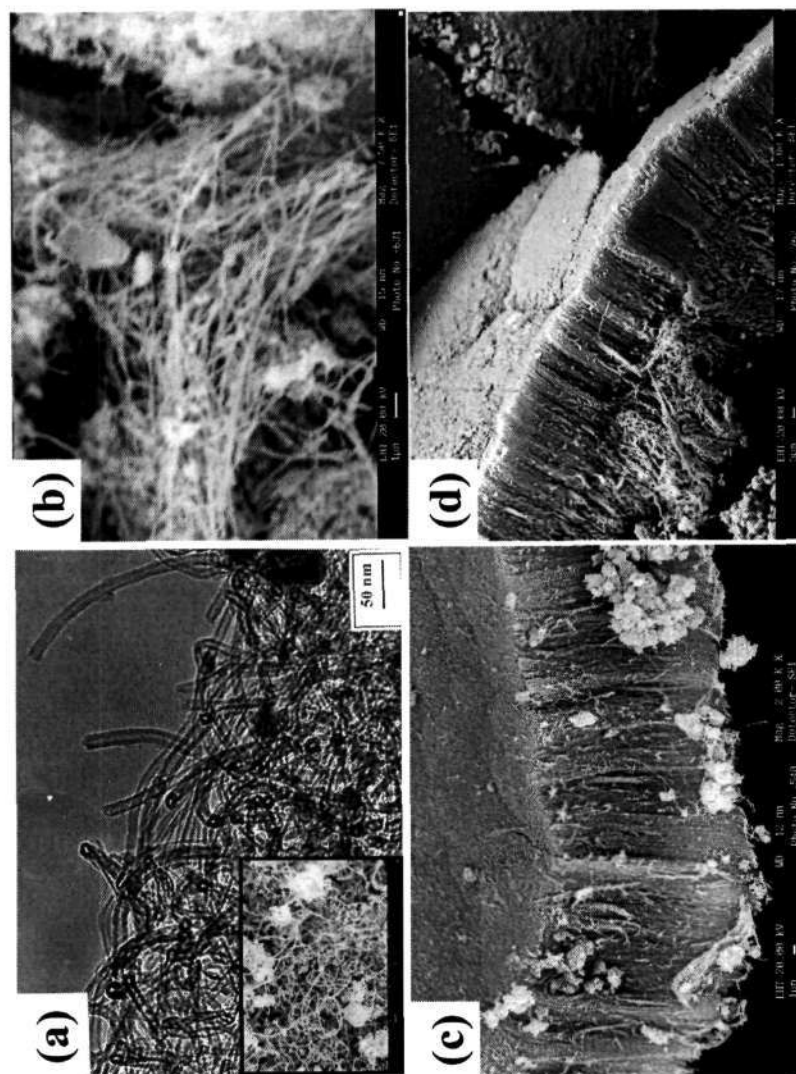
118

Figure 1.4.2: (a) Low-magnification TEM image of **III**. Inset shows the SEM image, (b) SEM image of **V**, (c) SEM image of **VI** and (d) SEM image of **VII**

119

Figure 1.4.2(d) we show a SEM image of this sample. The catalyst particles in **VIII** were removed by treating the aligned bundles with concentrated nitric acid for 4 h and then washing thoroughly with distilled water. The acid-treated sample, **IX**, was dried at 100 °C.

Carbon fibres were synthesized by the decomposition of acetylene at a flow rate of 20 sccm at 750°C over a nickel/silica catalyst in flowing argon (80 sccm). The silica was removed by treatment with aqueous HF for 12 h. We show a low magnification SEM image of the carbon fibres prepared by us in Figure 1.4.3(a). The yield of the fibres was good, with the fibres having diameters of *ca.* 200 nm and lengths up to tens of μm. The HREM image of this sample in Figure 1.4.3(b) shows that the fibres are not well graphitized, with the planes inclined at an angle of *ca.* 32° with respect to the fibre axis.

Hydrogen storage studies

The apparatus used for hydrogen adsorption experiments was custom-built and similar to that described elsewhere [12]. A schematic of the apparatus is shown in Figure 1.4.4. It consists of a high-pressure stainless steel sample cell that is connected to a high-pressure reservoir via a high-pressure bellow valve. The pressure is monitored using a pressure gauge that is connected in the system. Experiments were conducted to verify that the system was leak-free. This was done by pressurizing the unit, and verifying that the pressure remained constant over a period of 10 h. Calibration of the system to account for the pressure drop brought about by the increase in volume upon opening of the valve between the reservoir and the evacuated sample cell at various pressures was also carried out. The volume of gas contained in the system at various pressures in the absence of the carbon samples was determined by allowing it to exit the system and then measuring by the displacement of water. Shown in Figure 1.4.5 is a plot of the volumes accommodated in the system at various pressures. The points represent data points at various pressures while the straight line is the linear fit for the same.

Hydrogen adsorption experiments were performed at 300 K. The hydrogen that

120
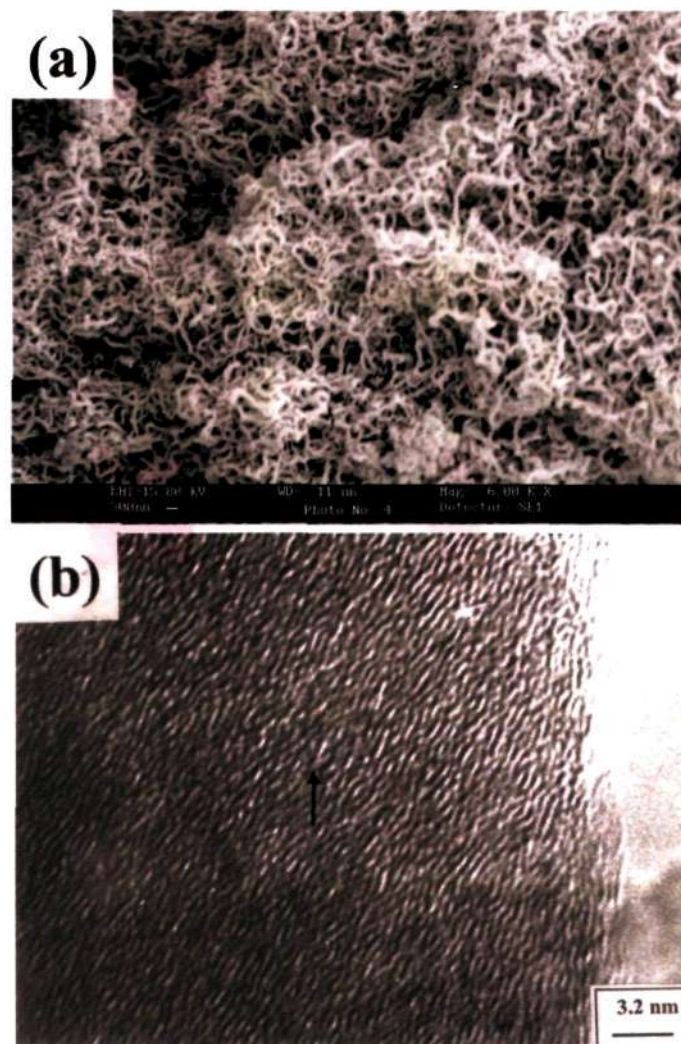
Figure 1.4.3: (a) SEM image of as-synthesized carbon fibers; (b) HREM image of carbon fibers showing the stacking of graphitic planes. The arrow denotes the direction of growth of the fiber.

was used was of ultra high purity ($>$ 99.99%), with an impurity (*e.g.* moisture and nitrogen) content of less than 10 ppm. The carbon samples were accurately weighed and taken in the sample cell. The sample cell was evacuated to 10^{-5} Torr and heated for 12 h at 125 °C in order to degas the sample. This vacuum is sufficient as per the IUPAC recommendations on adsorption measurements [21]. Hydrogen was then introduced into the reservoir container and subsequently let into the sample cell. The drop in pressure from the initial value, of *ca.* 145 bar, was measured at regular intervals. The amount of hydrogen stored in the samples was calculated from the

121
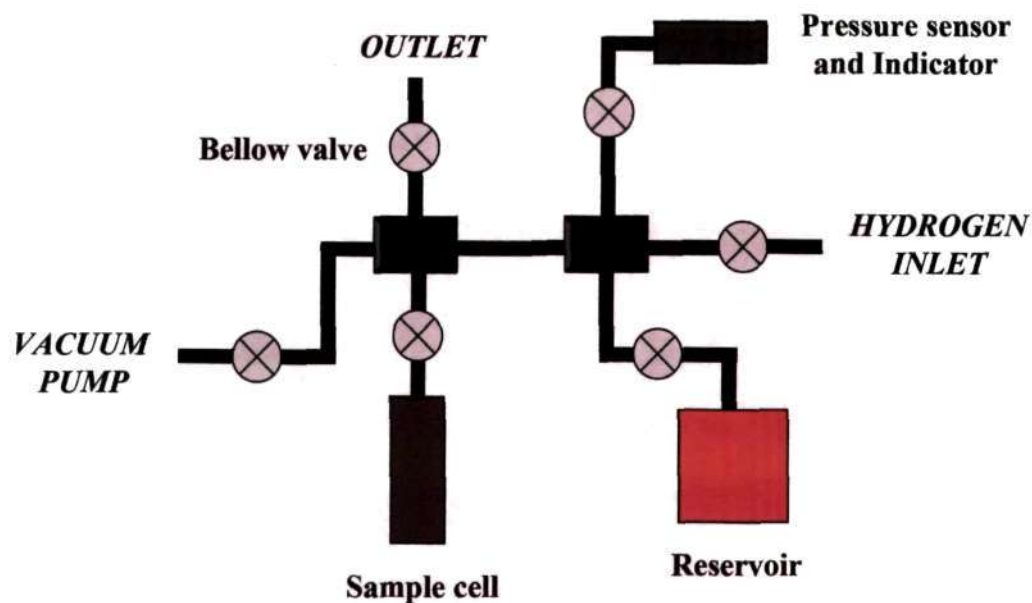
Figure 1.4.4: Schematic of the high-pressure hydrogen apparatus
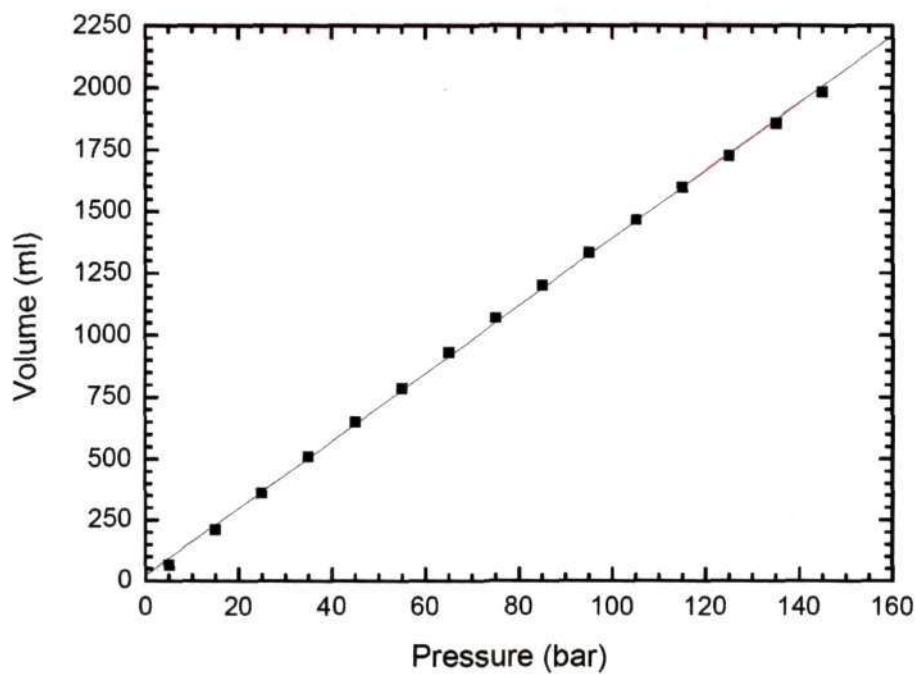
Figure 1.4.5: Calibration of the high-pressure hydrogen apparatus carried out in the absence of sample.

changes in pressure following the interaction of the material with the gas. Blank tests were repeated at regular intervals to verify that the system was free of leaks and that the pressure drop observed was only due to the uptake of hydrogen by the samples. In order to minimize errors, more than 125 mg of the sample was used for each measurement. All of the adsorbed hydrogen could be desorbed, as established by adsorption-desorption experiments, the only desorbed gas being hydrogen.

1.4.3 Results and discussion

Unlike metal alloys that adsorb hydrogen after a short period of incubation, hydrogen is adsorbed soon after it is admitted in the carbon samples studied by us. The entire adsorption was over within 100-150 min. Similar observations have been made by other workers [8, 12].

In Figure 1.4.6, we show plots of hydrogen adsorption versus time for the various carbon nanostructured samples studied by us. The broken curve representing the blank run with an adsorption of 0.0 wt% was obtained when the system was evacuated and then pressurized with hydrogen gas in the absence of a carbon sample. This indicates that there is no adsorption by the system itself in the absence of the carbon sample. Similar blank runs, performed after each adsorption experiment with a carbon sample, showed identical curves. The SWNT sample I showed a storage capacity of 0.2 wt%. On removal of the catalyst particles, the storage capacity for the sample (II) increased only slightly to 0.4 wt%. This indicates that the catalyst particles are probably inert with regard to H_2 adsorption. The H_2 storage that we have obtained for SWNTs is considerably lower than that reported by others [1,8]. We further cleaned the surface of the tubes by treatment with a mixture of conc. HCl and H_2O_2 and were able to obtain a storage capacity of 1.2 wt%. This treatment would remove any extra carbonaceous materials that may block the pores and hinder the entry of the hydrogen molecules, as evidenced by the HREM images (not shown).

The hydrogen storage capacity for the MWNT sample III was 0.2 wt% as shown in Figure 1.4.6. These results are consistent with the values obtained by
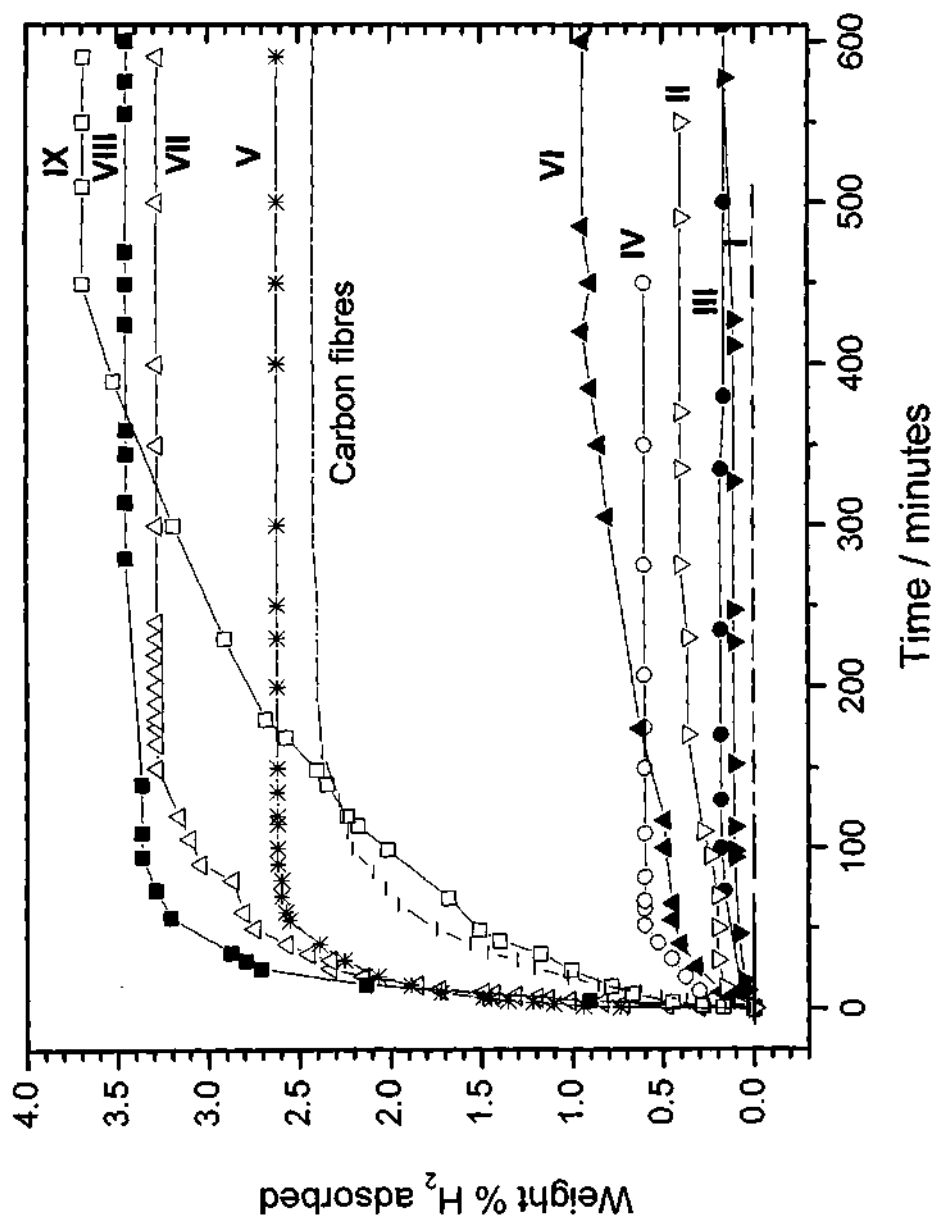
123

Figure 1.4.6: Amount of hydrogen adsorbed in wt% as a function of time for the various carbon nanostructures. The broken curve represents the blank data obtained in the absence of a carbon sample.

Cao *et al.* [22] who obtained low H_2 storage for random MWNTs. Opening of the tubes (**IV**) increased the hydrogen storage capacity to 0.6 wt% (Figure 1.4.6). The low values for adsorption may by due to the fact that the nanotubes are not well graphitized since the temperatures we used in their synthesis were low. Well-graphitized MWNTs have been reported to show higher percentages of hydrogen adsorption [23]

We find the MWNTs, **V**, which were well graphitized, show an increased hydrogen storage capacity of 2.6 wt% as shown in Figure 1.4.6. It appears that opened nanotubes show slightly higher storage as shown by samples **IV** and **V**.

The hydrogen storage capacity for sample **VI** is 1.0 wt%, which is considerably higher than that shown for the random MWNTs prepared by the pyrolysis route. This value is considerably less than that reported by Chen *et al.* [10] who studied the desorption of hydrogen using thermogravimetric analysis and reported a value of 5–7 wt% at around 10 atm. The present value is to be compared to that of Cao et al. [22] who reported a hydrogen storage of 2.4 wt% at slightly lower pressures of around 100 bar. Hydrogen is expected to be stored between the graphite layers as well as in the pores formed by the internanotube space between adjacent parallel nanotubes [10, 22]. We expect that if the catalyst can be removed, hydrogen would also be stored in the hollow center of the tubes, which is the storage mechanism for SWNTs [1,8]. Accordingly, we could reproducibly achieve a H_2 storage capacity of 3.3 wt% for sample **VII**, as shown in Figure 1.4.6. On increasing the packing density of the aligned nanotubes (sample **VIII**), we found only a marginal increase in the storage capacity (Figure 1.4.6), the value being 3.5 wt%. On acid treatment and removal of metal particles, the sample, **IX**, showed even a higher storage capacity of 3.7 wt%. This is the highest storage capacity obtained by us in the present study.

In order to ensure the validity of the results in Figure 1.4.6, we carried out independent adsorption experiments at different pressures of hydrogen. At first, measurements were performed at a high pressure followed by desorption at 300 °C in a vacuum (10^{-5} Torr) and readsorption and a lower pressure. We show the results of such studies on sample **IX** in Figure 1.4.7, where the wt% of H_2 (after desorption
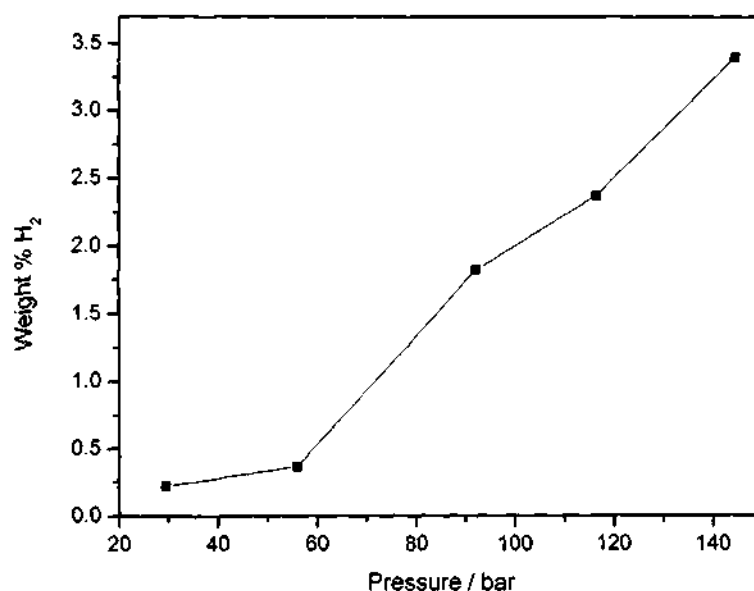
Figure 1.4.7: Hydrogen storage in aligned MWNTs (acid-treated), sample **IX**, at different pressures.

and readsorption) is plotted against pressure. The results show the expected trend with a decrease in storage with any decrease in pressure.

The adsorption curve for the carbon fibres is also shown in Figure 1.4.6. We see that the storage is 2.4 wt%, higher than in some of the nanotube samples, but lower than the 3.7 wt% storage found with **IX**. It appears that hydrogen is between graphite planes of the fibres [12]. The storage capacity found by us is considerably lower than that reported in the literature [12, 24]. The low storage capacity may partly be due to incomplete crystallization. Furthermore, the fibres do not distinctly have a herringbone structure present in the samples employed by Chambers *et al.* [12]. In order to remove the catalyst particles from the fibres, we treated the sample with conc. HNO_3 but found that the morphology was disrupted badly, resulting in a very low storage capacity (0.8 wt%).

It has been pointed out by Tibbetts *et al.* [16] that erroneous H_2 adsorption data can result from the small sample weights. We therefore performed adsorption studies using different weights of **VII**. The results of the adsorption are shown in Figure 1.4.8. Thus, with sample weights of 138.5 and 200 mg, the shape of the adsorption curve remained the same as did the storage capacity (3.3 wt%).
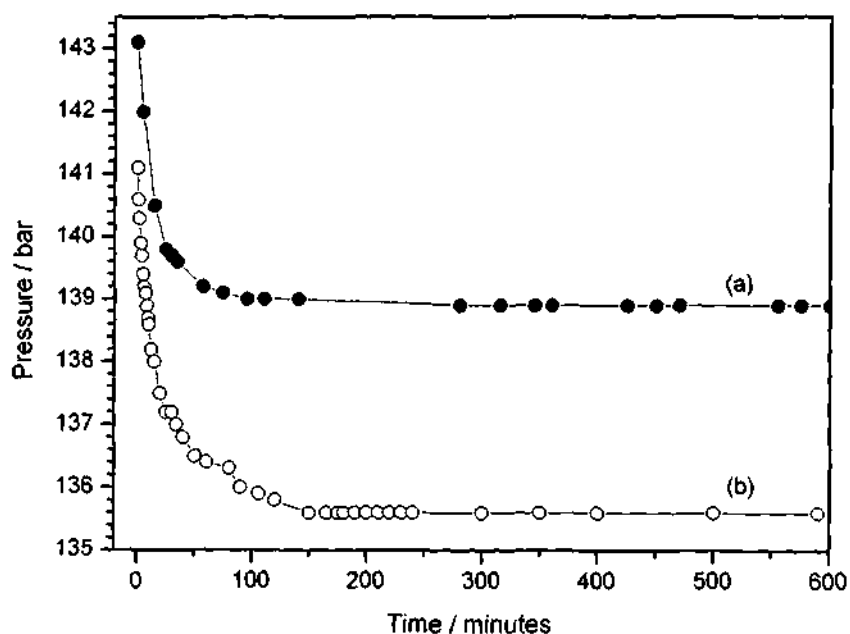
Figure 1.4.8: Plots of pressure versus time for the MWNT bundles, **VII**, obtained with (a) 138.5 mg, and (b) 200 mg of the sample.

Electrochemical measurements of hydrogen storage were also carried out on the various nanotube samples as well as on the carbon fibres to verify the values obtained by the gas storage method.

1.4.4 Conclusions

The maximum H_2 storage capacity achieved by us is obtained with densely aligned bundles of MNWTs that have been treated with acid. We find that carbon fibres do not show the exceptional storage capacities reported by others. Though the maximum capacity we have achieved in our studies with the nanotubes is 3.7 wt%, we are well below the 6.5 wt% benchmark set by the US Department of Energy (DOE). We have verified that the results obtained by us are reproducible as confirmed by experiments at lower pressures and with different weights of samples. The hydrogen storage in the samples has been studied electrochemically to obtain values that are similar to the gas storage values. Though there have been a few recent reports of very low percentages of hydrogen storage in carbon nanotubes [15, 16], there have also been reports giving detailed procedures for the

synthesis and purification along with good H_2 storage capacities [22, 23]. What is noteworthy in the present study is that we have avoided many of the pitfalls by using different sample weights as well as by doing experiments at lower pressures. It is also significant that the hydrogen storage capacities obtained by the gas adsorption method are similar to those obtained electrochemically. *

---

*A paper based on this study has appeared in J. Mater. Chem., (2003).

References

[1] A. C. Dillon, K. M. Jones, T. A. Bekkedahl, C. H. Kiang, D. S. Bethune and M. J. Heben, *Nature*, 1997, **386**, 377.

[2] C. Zandonella, *Nature*, 2001, **410**, 734.

[3] R. G Ding, G. Q. Lu, Z. F. Yan and M. A. Wilson, *J. Nanosci. Nanotechnol.*, 2001, **1**, 7.

[4] H. M. Cheng, Q. H. Yang and C. Liu, *Carbon*, 2001, **39**, 1447.

[5] M. S. Dresselhaus, K. A. Williams and P. C. Eklund, *MRS Bull.*, 1999, **24**, 45.

[6] J. E. Fischer, *Chem. Innov.*, 2000, **30**, 21.

[7] A. C. Dillon and M. J. Heben, *Appl. Phys. A*, 2001, **72**, 133.

[8] C. Liu, Y. Y. Fan, M. Liu, H. T. Cong, H. M. Cheng and M. S. Dresselhaus, *Science*, 1999, **286**, 1127.

[9] Y. Ye, C. C. Ahn, C. Witham, B. Fultz, J. Lui, A. G. Rinzler, D. Colbert, K. A. Smith and R. E. Smalley, *Appl. Phys. Lett.*, 1999, **74**, 2307.

[10] Y. Chen, D. T. Shaw, X. D. Bai, E. G. Wang, C. Lund, W. M. Lu and D. D. L. Chung, *Appl. Phys. Lett.*, 2001, **78**, 2128.

[11] P. Chen, X. Wu, J. Lin and K. L. Tan, *Science*, 1999, **285**, 91.

[12] A. Chambers, C. Park, R. T. K. Baker and N. M. Rodriguez, *J. Phys. Chem. B*, 1998, **102**, 4253.

[13] C. Nützenadel, A. Zuüttel, D. Chartouni and L. Schlapbach, *Electrochem. Solid State Lett.*, 1999, **2**, 30.

[14] N. Rajalakshmi, K. S. Dhathathreyan, A. Govindaraj and B. C. Satishkumar, *Electrochem. Acta.*, 2000, **45**, 4511.

129

[15] M. Ritschel, M. Uhlemann, O. Gutfleisch, A. Leonhardt, A. Graff, Ch. Täschner and J. Fink, *Appl. Phys. Lett.*, 2002, **80**, 2985.

[16] G. G. Tibbetts, G. P. Meisner and C. H. Olk, *Carbon*, 2001, **39**, 2291.

[17] C. Journet, W. K. Maser, P. Bernier, A. Loiseau, M. Lamy de la Chapelle, S. Lefrabt, P. Denierd, R. Lee and J. E. Fischer, *Nature*, 1997, **388**, 756.

[18] C. N. R. Rao, A. Govindaraj, R. Sen and B. C. Satishkumar, *Mater. Res. Innov.*, 1998, **2**, 128.

[19] K. Hernadi, A. Fonseca, J. B. Nagy, D. Bernaerts, J. Riga and A. Lucas, *Synth. Met.*, 1996, **77**, 31.

[20] R. Seshadri, A. Govindaraj, H. N. Aiyer, R. Sen, G. N. Subbanna, A. R. Raju and C. N. R. Rao, *Curr. Sci. (India)*, 1994, **66**, 839; C. N. R. Rao, R. Sen, B. C. Satishkumar and A. Govindaraj, *Chem. Commun.*, 1998, 1525.

[21] K. S. W. Sing, D. H. Everett, R. A. W. Haul, L. Moscou, R. A. Pierotti, J. Rouquerol and T. Siemieniewska, *Pure Appl. Chem.*, 1985, **57**, 603.

[22] A. Cao, H. Zhu, X. Zhang, X. Li, D. Ruan, C. Xu, B. Wei, J. Liang and D. Wu, *Chem. Phys. Lett.*, 2001, **342**, 510.

[23] P. X. Hou, Q. H. Yang, S. Bai, S. T. Xu, M. Liu and H. M. Cheng, *J. Phys. Chem. B*, 2002, **106**, 963.

[24] Y. Y. Fan, B. Liao, M. Liu, Y. L. Wei, M. Q. Lu and H. M. Cheng, *Carbon*, 1999, **37**, 1649.

1.5 Dip-pen Nanolithography with magnetic Fe$_2$O$_3$ nanocrystals

1.5.1 Introduction

The ability to tailor the chemical composition and structure of a surface on the 1–100 nm length scale is important for the development of various fields. Lithographic methods have been extensively used in modern-day microfabrication. The dip-pen technology, in which the ink on a sharp object is transported to a paper substrate via capillary forces is several centuries old and has been used to transport molecules on macroscale dimensions. Mirkin and co-workers have recently merged the two processes and developed an atomic force microscopy (AFM) based dip-pen nanolithographic (DPN) technique to create patterns of nanoscopic dimensions [1]. The method exploits the water meniscus formed between a slowly scanning AFM tip and a substrate to transfer the species on the tip to the substrate by diffusion. A schematic of the entire process is shown in Figure 1.5.1. Inspiration for this process was drawn from a problem that has plagued the AFM since its invention. The narrow gap capillary formed between the AFM tip and the sample, when an experiment is conducted in air, condenses water from the ambient and substantially influences imaging experiments [2]. Depending on the relative humidity and substrate wetting properties, the water will be transported onto the substrate. Initial studies employed gold-thiol interaction to create robust patterns, with the dimensions being determined by the preset scan area [3]. Though the thiols formed chemical bonds with the gold substrates, the patterns obtained were not functional due to the non-reactive alkyl chains. The use of bifunctional thiols as inks permits tethering of colloids, proteins and other macromolecules at specific regions on a given surface [4–6]. Ali *et al.* [7] have reported a DPN-based procedure to deposit small volumes of an Au sol on a substrate, which, on evaporation of the solvent, leads to circular nanocrystal patterns. Garno *et al.* [8] have suggested methods to

131
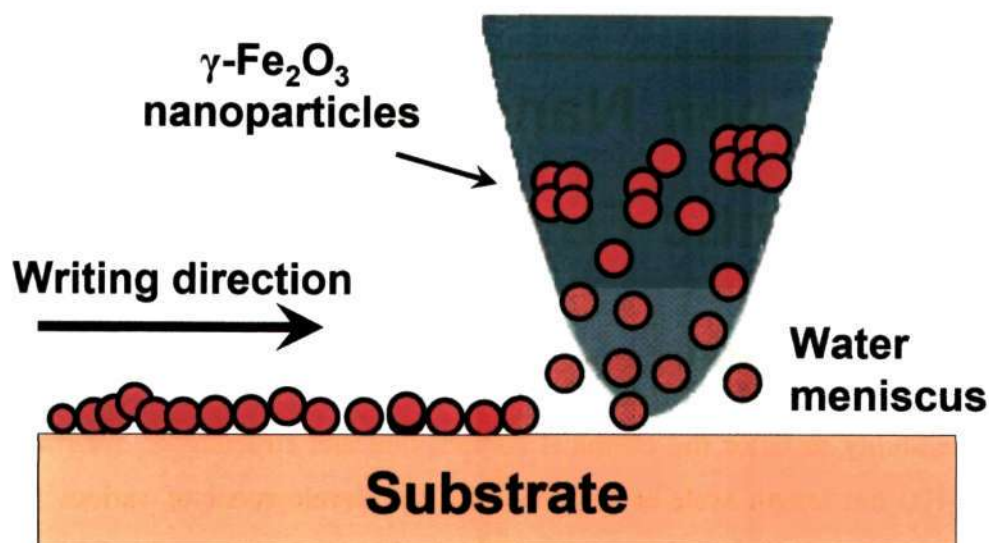
Figure 1.5.1: Schematic representation of the DPN process

obtain linear patterns of Au nanocrystals on Au substrates. DPN patterning of Au and Pd nanocrystals has been accomplished on different substrates starting from hydrosols [9]. Magnetic barium hexaferrite nanostructures have been patterned by coating the AFM cantilever tip with a precursor followed by its deposition on silicon substrates and heating [10]. Based on DPN experiments on organic dyes, Su and Dravid [11] suggest that weak interactions between the substrate and the molecular ink suffice to form DPN patterns. In spite of the progress made with DPN, there is a clear need to develop new and better inks for different surfaces and fully characterize the nanopatterns by appropriate spectroscopic and microscopic tools [12].

We have sought to pattern nanoparticles of γ-Fe$_2$O$_3$ by the DPN method on different substrates. It may be interesting to recall that hematite has been traditionally employed as a dye, the prehistoric cave paintings of Lascaux, being a well-known example. Since γ-Fe$_2$O$_3$ is magnetic, the nanopatterns also lend themselves to a magnetic force microscopy (MFM) study. In this study, we report DPN with γ-Fe$_2$O$_3$ nanoparticles wherein MFM as well as low energy electron microscopy (LEEM) and X-ray photoemission electron microscopy (XPEEM) [13] have been employed to independently characterize the patterns.

1.5.2 Experimental

The experiment consists of four parts: (i) the synthesis and suitable characterization of the nanocrystals, (ii) designing suitable markers on the substrate in order to relocate the patterns for their characterizaion, (iii) patterning the nanocrystals on the substrate and (iv) relocation and characterization of the nanopatterns.

(a) Synthesis and characterization of nanocrystals γ-Fe_2O_3

Citrate-capped γ-Fe_2O_3 nanocrystals were prepared by wet-chemical means, by modifying the procedure of Ngo and Pileni [14]. The preparation yields a sol, which can be precipitated and redispersed readily in water. The nanocrystals were characterized using TEM and magnetic measurements were carried out using a Quantum design superconducting quantum interference device (SQUID). Redispersibility is crucial for a colloidal sol to be used as an ink in DPN experiments. The TEM image (see Figure 1.5.2(a)), revealed the nanocrystals to be of an average diameter of 11 nm and a log-normal diameter distribution (see inset in Figure 1.5.2(a)). The nanocrystals in the powder form were superparamagnetic at room temperature, exhibiting hysteresis at low temperatures (see Figure 1.5.2(b)). The observed squareness ratio of 0.42 is close to that expected (0.5) for randomly oriented single domain magnetic particles with uniaxial anisotropy [15].

(b) Designing of markers

This is a very important step in order to further characterize the nanocrystal patterns. Freshly cleaved mica and silicon were used as substrates with and without the native SiO_x layer (the latter by treating with a solution of aq. HF). A copper TEM grid containing a fine mesh was used as the mask. A portion of the TEM grid was placed on the substrate and sputtered with gold for 1-2 minutes. The grid was carefully removed, which yielded the inverse of the mask as shown in the photograph as well as the low-magnification SEM image in Figure 1.5.3. A suitable location was chosen (by means of a CCD camera) for patterning the nanocrystals. Shown in Figure 1.5.3 (a) is the top view of the AFM cantilever positioned above

133

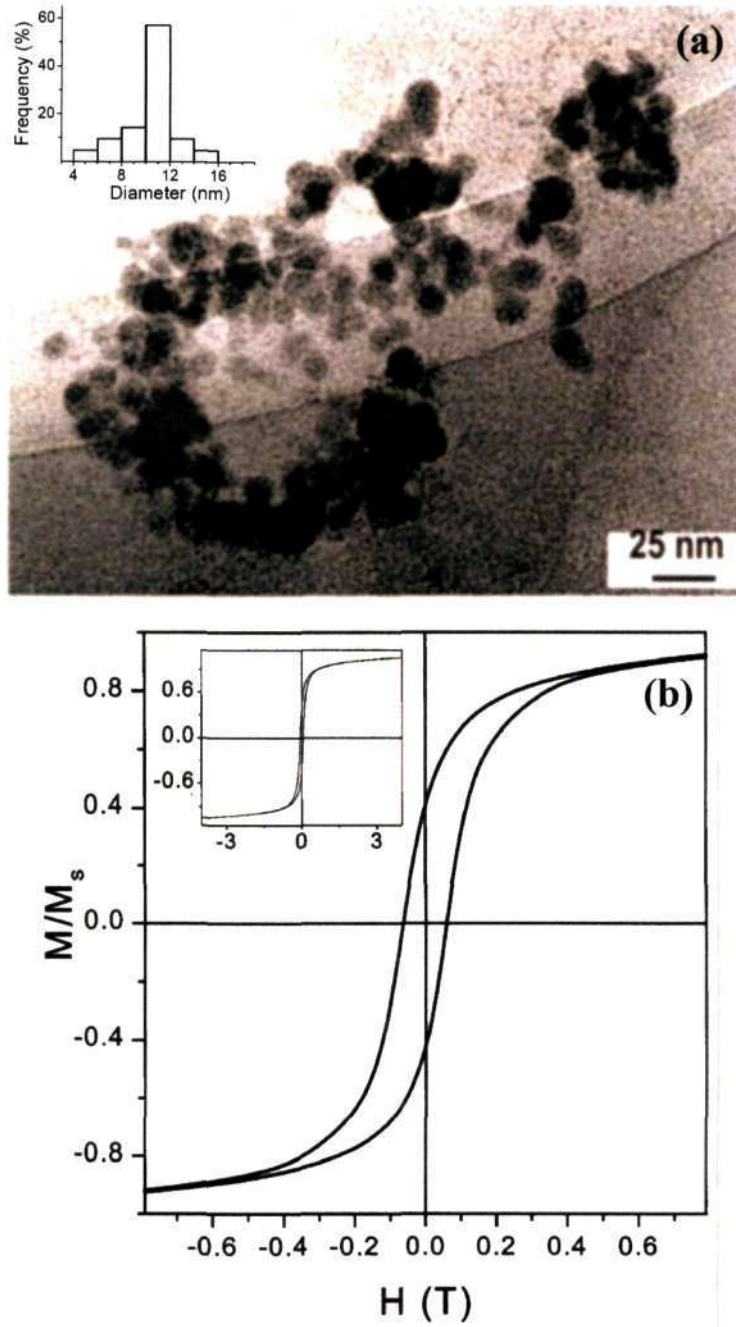**Figure 1.5.2:** Citrate-capped γ-Fe_2O_3 nanocrystals: (a) TEM image along with a histogram showing the distribution in particle size (in the inset) and (b) Hysteresis loop at 2K (H = 4 T). The inset shows the hysteresis loop in the full range of the magnetic field.
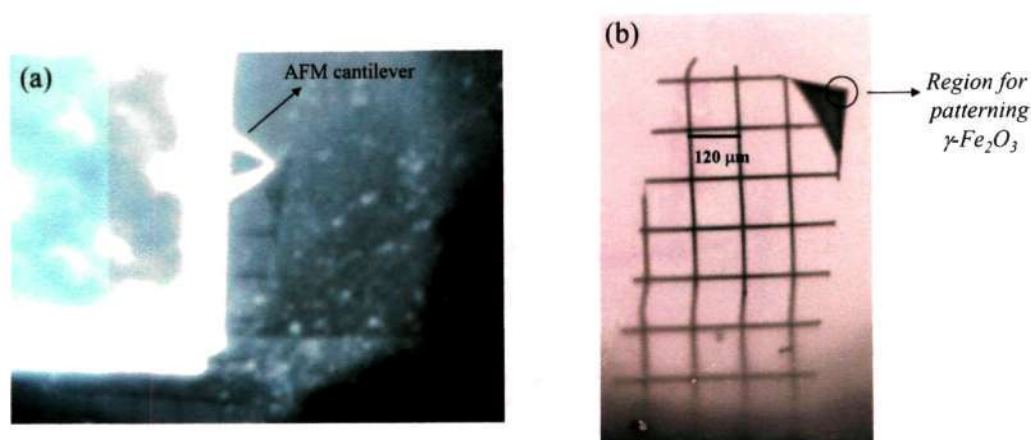
Figure 1.5.3: (a) Photograph and (b) SEM image of the substrate with suitable markers

the patterned substrate, where the nanocrystals were deposited.

(c) Patterning of the γ-Fe$_2$O$_3$ nanocrystals

DPN experiments were carried out under ambient conditions (humidity of 35–45 %) by employing a Digital Instruments Multimode head attached to a Nanoscope-IV controller. A photograph of the Atomic Force Microscope (AFM) is shown in Figure 1.5.4. Contact mode imaging was carried out in both normal and lateral force modes. Standard Si$_3$Ni$_4$ cantilevers were coated with γ-Fe$_2$O$_3$ nanocrystals by immersing them in a dispersion for 5–10 min followed by drying using a hot air blower. Deposition of the nanocrystals was achieved by scanning an area in the contact mode with scan speeds of *ca.* 1 μm.s^{-1} for a period of 30 minutes. Subsequently, imaging was carried out using the same cantilever and scanning a larger area with higher scan rates (10 μm.s^{-1}).

(d) Characterization of the nanopatterns

The magnetic behavior of the nanopatterns was probed by magnetic cantilever tips, the magnetic nature of the γ-Fe$_2$O$_3$ nanocrystals being exploited to obtain MFM contrast. In this method, a magnetic tip is scanned in the lift-mode [16], at various z-values, wherein the magnetic interaction emerges as a difference in the phase-shift.

135

Figure 1.5.4: Photograph of the atomic force microscope (Digital Instruments Multimode head)

In order to characterize the DPN patterns by an independent method, we have employed the Nanospectroscopy Beamline at the synchrotron radiation facility Elettra in Trieste [17]. Electron beam-based techniques are ideal for such studies [18] in that they have a lateral resolution of 10 nm and atomic depth resolution. In LEEM, a low energy electron beam (1–100 eV) is incident on the sample and the backscattered beam is used for imaging in the dark or bright field. In the XPEEM mode the sample is illuminated by monochromatic soft X-rays (20–1000 eV). This leads to the emission of a whole spectrum of photoelectrons with kinetic energies, from which electrons with a certain kinetic energy, for example, characteristic core or valence electrons, are used for imaging.
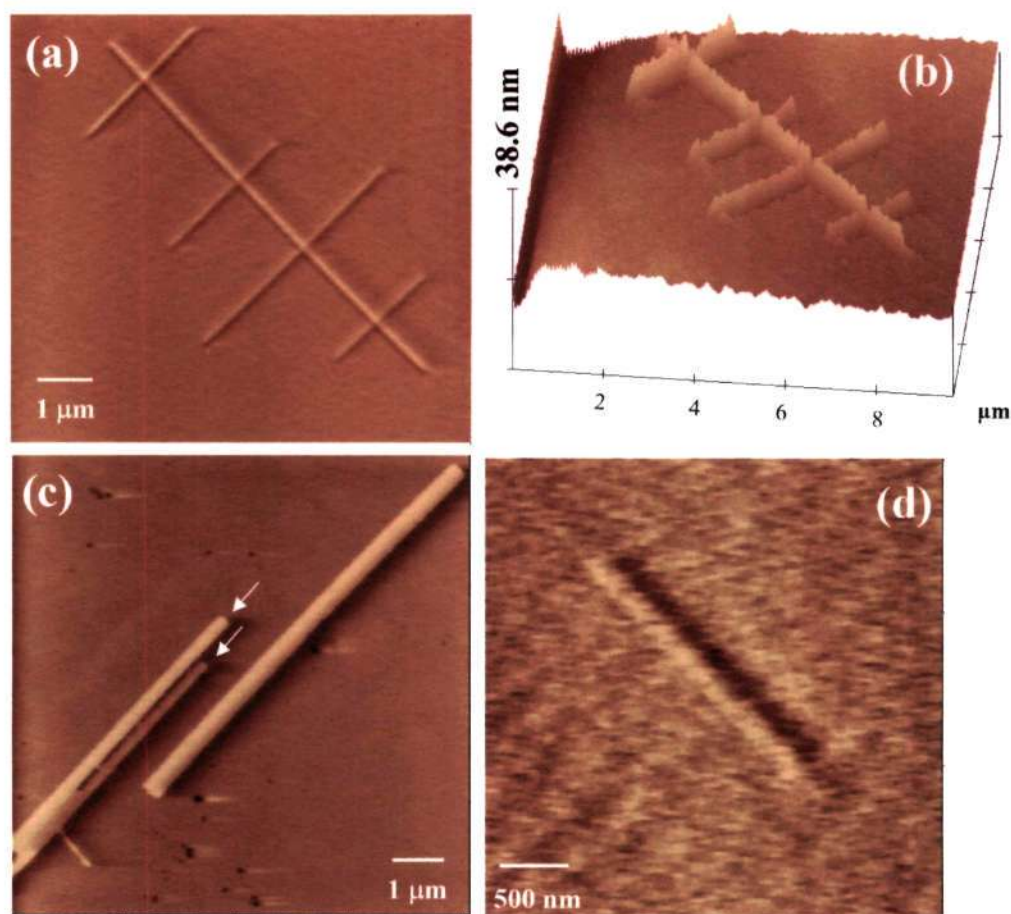
Figure 1.5.5: Contact AFM images of γ-Fe$_2$O$_3$ nanocrystal patterns drawn (a) on mica along with (b) its surface plot, (c) on silicon with the native SiOx layer (arrows point to closely-drawn patterns) and (d) on etched silicon.

1.5.3   Results and discussion

AFM images of γ-Fe$_2$O$_3$ nanocrystals patterns drawn on different substrates are shown in Figure 1.5.5. The images clearly reveal that the nanocrystals can be fabricated satisfactorily on different substrates. In each case, high aspect ratio lines, corresponding to the desired scan area are obtained with sharp edges. For example, by scanning an area of 9000 nm by 230 nm during deposition produced a pattern of dimensions 9010 nm by 226 nm (Figure 1.5.5(a), central line). Typical line widths are in the range of 140–200 nm with lengths extending to 10 μm. It is gratifying that there is no sign of lateral diffusion of the ink in any of the cases. These patterns are therefore distinct from water droplets that are deposited from undipped tips [2]. The

Figure 1.5.6: (a) Tapping mode AFM image of a γ-Fe$_2$O$_3$ nanopattern, (b) the corresponding MFM image at a lift-height of 5 nm and (c) plot of the phase shift versus the lift height.

water droplets evaporate readily and exhibit non-continuous structures with diffuse boundaries. The surface plot shown in Figure 1.5.5(b) confirms the observations made in Figure 1.5.5(a). We also see corrugations along the edges corresponding to the particle size. The individual particles are not visible in the patterns, possibly due to the blunt nature of the cantilever 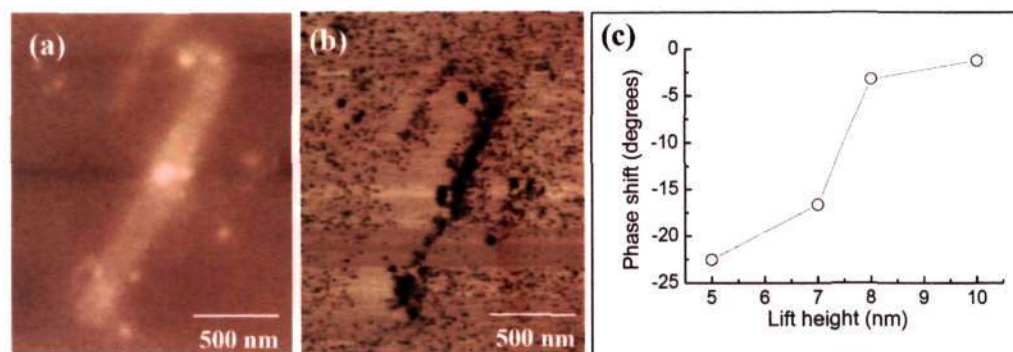coated with the nanocrystals and also due to the mild contact forces employed. The observed height of around 10 nm reveals that the patterns are made of a single layer of γ-Fe$_2$O$_3$ nanocrystals. It is noteworthy that similar lines are obtained on Si with and without the native oxide layer, although the latter is not ideal for good imaging (see Figures 1.5.5(c) and (d)).

The magnetic behavior of the nanopatterns was probed by magnetic cantilever tips, the magnetic nature of the γ-Fe$_2$O$_3$ nanocrystals being exploited to obtain MFM contrast. Typical tapping mode topography and MFM images are shown in Figures 1.5.6(a) and (b). The tapping mode reveals rougher edges arising from the nanocrystals. The change in the phase-shift as function of the lift-height is shown in Figure 1.5.6(c), to show that the superparamagnetic nanocystals in the pattern are susceptible to magnetization by the stray field emanating from the magnetic tip. The loss of contrast on changing the lift height to 10 nm is consistent with the rather weak magnetic nature of the nanocrystals (see Figure 1.5.2(b)).

The nanopatterns were further characterized using the Nanospectroscopy Beam-line at Trieste and the correspodning images are shown in Figure 1.5.7. The LEEM

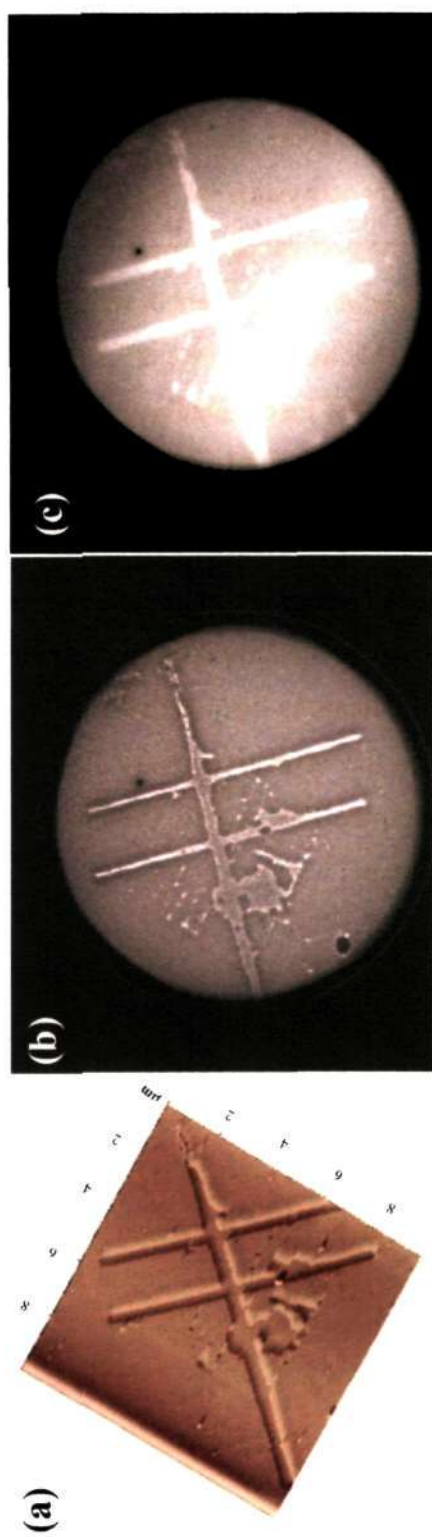**Figure 1.5.7:** (a) Tapping mode topographic AFM image of a γ-Fe_2O_3 nanocrystal pattern along with (b) the corresponding MEM image collected with electron beam of energy 0.8 eV and (c) XPEEM image obtained by collecting the secondary electrons (energy 0.6 eV) following excitation with 712 eV (Fe L_3 edge). The field of view in both cases is 10 μm.

139

image of Figure 1.5.7(b) was acquired in the mirror electron microscopy (MEM) mode wherein the sample potential is negative with respect to the filament so that the electrons are reflected by the surface potential in front of the sample, causing minimal damage to the nanocrystals. The contrast itself arises from variation in the surface potential and topography. These studies were carried out typically a few weeks after patterning of the nanocrystals on Si surfaces with native oxide layers, demonstrating thereby that the patterns are robust. The patterns were located on the substrates by using the micron-sized markers described in the experimental procedure. In Figure 1.5.7 (a) and (b), we compare the LEEM image in the MEM mode along with the corresponding AFM image obtained right after patterning. The LEEM image corresponds exactly with the AFM image.

We have ascertained the chemical nature of the species by imaging the nanopattern by an independent method, we have recorded XPEEM images. The image in Figure 1.5.7(c) was obtained in X-ray absorption spectroscopy mode with a photon energy of 712 eV using secondary electrons for imaging (electron energy 0.6 eV). The photon energy corresponds to the excitation of the Fe L_3 edge in Fe_2O_3 as verified with a bulk reference sample. The image obtained with photoelectrons corresponds exactly to the AFM image.

1.5.4 Conclusions

In conclusion, we have demonstrated a versatile DPN method for nanopatterning γ-Fe_2O_3 nanocrystals on different substrates. The patterns are well-defined with minimal lateral diffusion of the ink as well as robust for several weeks after their creation. The patterns are also magnetic and yields well-resolved LEEM and XPEEM images. *

---

*A paper based on this study has appeared in Appl. Phys. Lett. (2004).

References

[1] D. S. Ginger, H. Zhang and C. A. Mirkin, *Angew. Chem. Int. Ed.*, 2004, **43**, 30 and references therein.

[2] J. Hu, X. -d. Xiao, D. F. Ogletree and M. Salmeron, *Surf. Sci.*, 1995, **344**, 221.

[3] R. D. Piner, J. Zhu, F. Xu, S. Hong and C. A. Mirkin, *Science*, 1999, **283**, 661.

[4] R. Mckendry, W. T. S. Huck, B. Weeks, M. Fiorini, C. Abell and T. Rayment, *Nano Lett.*, 2002, **2**, 713.

[5] L. M. Demers and C. A. Mirkin, *Angew. Chem. Int. Ed.*, 2001, **40**, 3069.

[6] X. Liu, L. Fu, S. Hong, V. P. Dravid and C. A. Mirkin, *Adv. Mater.*, 2002, **14**, 231.

[7] M. B. Ali, T. Ondarcuhu, M. Brust and C. Joachim, *Langmuir*, 2002, **18**, 872.

[8] J. C. Garno, Y. Yang, N. A. Amro, S. Cruchon-Dupeyrat, S. Chen and G. Y. Liu, *Nano Lett.*, 2002, **389**, 3.

[9] P. J. Thomas, G. U. Kulkarni and C. N. R. Rao, *J. Mater. Chem.*, 2004, **14**, 625.

[10] L. Fu, X. Liu, Y. Zhang, V. P. Dravid and C. M. Mirkin, *Nano Lett.*, 2003, **3**, 757.

[11] M. Su and V. P. Dravid, *Appl. Phys. Lett.*, 2002, **80**, 4434.

[12] C. A. Mirkin, *MRS Bull.*, 2001, **26**, 535.

[13] Th. Schmidt, S. Heun, J. Slezak, J. Diaz, K. C. Prince, G. Lilienkamp, and E. Bauer, *Surf. Rev. Lett.*, 1998, **5**, 1287.

[14] A. T. Ngo and M. P. Pileni, *J. Phys. Chem. B*, 2001, **105**, 53.

[15] S. Chikuzumi and S. H. Charap, *Physics of Magnetism*, John Wiley New York, 1964.

[16] Digital Instruments, Santa Barbara, CA.

[17] A. Locatelli, A. Bianco, D. Cocco, S. Cherifi, S. Heun, M. Marsi, A. Pasqualetto, and E. Bauer, *J. Phys. IV*, 2003, **104**, 99.

[18] M. Lazzarino, S. Heun, B. Ressel, K. C. Prince, P. Pingue and C. Ascoli, *Appl. Phys. Lett.*, 2002, **81**, 2842.

Part 2

INVESTIGATIONS OF

MACROPOROUS AND

MESOPOROUS MATERIALS

SUMMARY

This part of the thesis contains studies of macroporous networks of oxidic materials and carbon as well as of mesoporous spheres of aluminosilicates.

Ordered mesoscale hollow spheres (1000 nm diameter) of binary oxides such as TiO_2 and ZrO_2 as well as of ternary oxides such as ferroelectric $PbTiO_3$ and $Pb(ZrTi)O_3$ have been prepared by templating against colloidal crystals of polystyrene, by adopting different procedures.

Macroporous carbons of different pore sizes, containing three-dimensionally connected voids, have been prepared by an elegant method. The method involves the coating of ordered silica spheres with sucrose, followed by carbonization using sulfuric acid, and the removal of silica with aqueous hydrofluoric acid. The carbon samples show the expected optical properties. The surface area of the macroporous carbon samples varies between 120 to 550 m^2g^{-1} depending on whether non-porous or mesoporous silica spheres were used as templates.

Macroporous silica-alumina composites with mesopores have been prepared by employing polymethylmethacrylate (PMMA) beads as templates in the presence of the cationic surfactant, N-Cetyl-N,N,N-trimethylammonium bromide (CTAB). The Si/Al ratio in the composites has been varied between 4.5 and 48 and the occurrence of mesopores has been verified by X-ray diffraction. The surface areas of the samples vary between 676 and 1038 m^2g^{-1}, with the highest value in the sample with Si/Al = 48.0.

Mesoporous aluminosilicate spheres of 0.3-0.4 μm diameter, with different Si/Al ratios, have been prepared by surfactant templating. The surface area of these materials is in the 510-970 m^2g^{-1} range and the pore diameter in the 15-20 Å range. [†]

2.1 Introduction

The design of inorganic materials with novel structures and properties has long been a prime objective of materials research. Chemists have been able to make a variety of materials based on their understanding of structure-property relations. Porous solids form a major part of materials research due to their wide range of applications: for example as membranes for separation and purification [1], as high surface area adsorbents [2], as solid supports for sensors and catalysts [3] and photonic band gap materials for use in optoelectronics [4]. According to their pore sizes, the International Union for Pure and Applied Chemistry (IUPAC) has recommended a specific nomenclature for porous materials: microporous (pore diameter < 2 nm), mesoporous (2 nm < pore diameter < 50 nm) and macroporous materials (pore diameter > 50 nm) [5]. These classes of porous materials are prepared by different methods and have different properties and uses.

2.1.1 Microporous materials

Microporous materials with three-dimensional frameworks are synthesized using molecular units or hydrated alkali or alkaline earth cations as templates. The pore structure and size in these materials are well defined. Zeolites belong to this class of porous materials. First discovered in mid-1700's, zeolites are hydrated, crystalline aluminosilicates that organize into stable, discrete frameworks [6]. Basic structures employ tetrahedral atoms (silicon or aluminium) bridged by oxygen atoms, where each oxygen atom is shared between two metalloid tetrahedra. Resulting covalent lattices can be neutral or negatively charged and often employ alkali metal or alkaline earth counterions to balance the charges. Synthetic zeolites are generally prepared hydrothermally.

More recently, compounds that exhibit similar framework structures have been synthesized in which Al and/or Si are substituted by other elements such as Be, B, Ga, Ge, Zn and P. This has given rise to a new family of microporous materials called

147

open-framework materials which use structure directing agents such as organic amines, etc. to help nucleate and direct the formation of microporous structures [7,8]. They find applications in the field of ion-exchange (use of Zeolite A as water softener in detergents), sorption and catalysis.

2.1.2 Mesoporous materials

The limitation of pore size in microporous materials had been a matter of concern for chemists, and they were constantly exploring synthetic methods to break the pore size barrier and crossover to materials with mesoscopic dimensions having crystallinity similar to that of microporous materials. In 1992, scientists at Mobil Oil Research and Development got over this limitation by the direct synthesis of the first broad family of mesoporous solids (denoted M41S) [9,10]. Three members of the M41S family were distinguished: hexagonal MCM-41, cubic MCM-48 and lamellar MCM-50. There are several reviews that deal with the synthesis and characterization of mesoporous solids [11].

Various mesoporous metal oxides such as alumina [12], titania [13], chromia [14], tin oxide [15] and zirconia [16] have been prepared. Other mesoporous materials that have been synthesized include silicophosphates [17], silicoaluminophosphates [18] and aluminophosphates [19].

The initial reports on mesoporous materials dealt with the synthesis of new systems and in understanding their formation mechanism. Later on, people began trying to control the morphology of the materials and make them organize into desired shapes. Using oil/solution emulsion as templates, Schacht *et al.* showed that mesoporous silica can form hollow spheres, fibres or thin sheets [20]. Ozin and co-workers described the synthesis of oriented mesoporous silica films grown on the mica-water or air-water interface [21]. They further obtained a rich diversity of morphology of mesoporous silica, namely spheres and gyroids [22]. Schaumacher *et al.* [23] developed a novel synthetic method for preparing spheres of MCM-48 silicate doped with different elements like Al, Cr, V, Ga, and Nb. Using NMR they verified that the elements were indeed a part of the silica framework and not in the

148

pores.

Formation of MCM-41 form of silica involves liquid crystalline templating. One pathway proposed by Chan *et al.* [24] involves the independent organization of surfactant molecules in the form of randomly ordered rod like micelles prior to interaction with inorganic species. Due to the charge interaction between the cationic headgroup and anionic inorganic species or between the anionic headgroup and cationic inorganic species or via hydrogen bonding between neutral amine with hydrophilic inorganic silicate, the inorganic species get attracted to the surface of the micellar rods. The second pathway proposed by Huo *et al.* [25] states that the silicate anions in solution, by virtue of their charge balance with the cationic surfactant, force the surfactant molecules to form supramolecular arrays.

Mesoporous solids have very large surface areas (700 to 1200 m^2g^{-1}) and are useful as catalysts.

2.1.3   An Overview of Macroporous Materials

Macroporous materials contain pores with pore diameters greater than 50 nm. Such materials occur in Nature and have been put to use. These include materials such as charcoal that are macroporous carbon in the amorphous form and used as catalyst supports. It is a great challenge for materials scientists to prepare macroporous solids that contain three dimensionally ordered pores.

"Nature abhors voids", but these solids contain voids of diameters larger than 50 nm. They have over 70% air and have surface areas of several square meters. They are still sturdy enough to withstand routine handling. The voids of these samples are highly ordered over large length scales and are interconnected by small windows that give solvents and gases ready access to the internal surface. Since the porous structure is ordered and the surface is relatively flat, the materials possess striking optical properties.

149

(a) Synthesis of Macroporous Materials

A number of methods have been developed for producing macroporous membranes including those based on selective etching (electrochemical etching of alumina or silicon [26], chemical etching of glasses [27], and ion-track etching of polymers [28]), those based on the self assembly of block copolymers [29], and those based on replica moulding against various kinds of templates [30]. Methods based on the selective etching usually generate straight, one dimensional channel structures and have been very successful in the manufacture of many commercial membrane films [26–28]. Methods based on the assembly of block copolymers are very elegant but only form arrays of spherical pores that are isolated from each other. Template-directed synthesis is a convenient and versatile method for generating porous materials. It is also a cost-effective and high-throughput procedure.

The term templating refers to a technique that initially involves the formation of a temporary medium, the template, whose interstices are then filled with another material. The template is subsequently removed chemically or thermally, leaving behind a porous material that is and inverse replica of the template microstructure. The architecture and form of the resulting porous sample thus depends directly on the characteristics of the starting template. In particular, templating against opaline arrays of colloidal spheres offers a generic route to macroporous materials that exhibit precisely controlled pore sizes and highly ordered three dimensional porous structures. Figure 2.1.1 illustrates the schematic procedure for this approach. After the opaline array of colloidal spheres has been dried, the void spaces (26% by volume) among the colloidal spheres are fully infiltrated with a suitable liquid precursor. Subsequent solidification of the precursor and removal of the colloidal spheres gives a three dimensional porous structure that has a highly ordered architecture of uniform air balls (interconnected to each other by small circular "windows").

The fidelity of this procedure is mainly determined by Van der Waals interaction between the templating spheres and the precursor, the wetting of the template surface, kinetic factors such as the filling of the void spaces in the template, and the
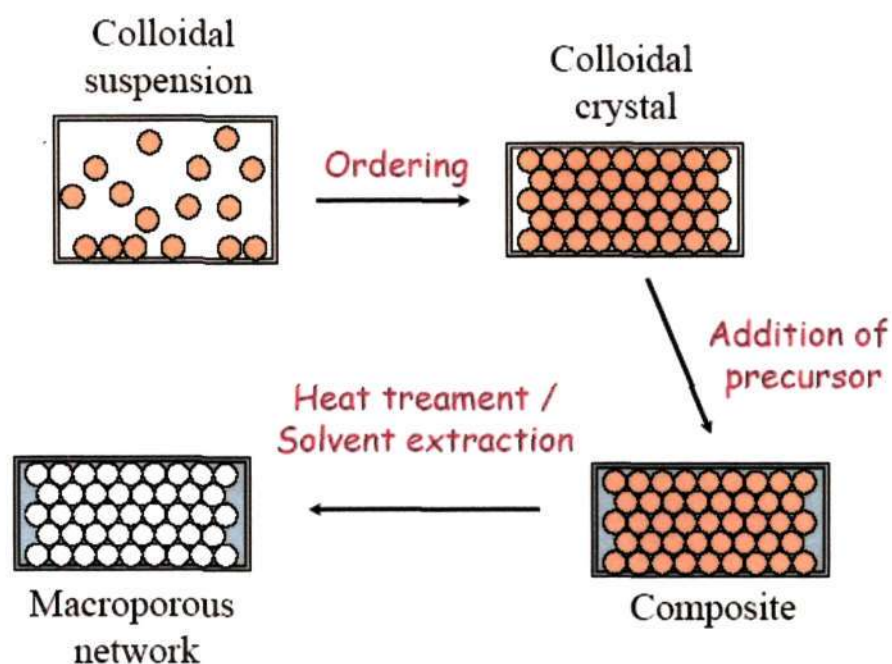
Figure 2.1.1: General scheme for synthesizing macroporous materials

volume shrinkage of the precursors during the solidification process. The porous material obtained by this approach have also been referred to as "inverse opals" or "inverted opals" because they have an open, periodic three dimensional framework complementary to that of an opaline structure. This approach is remarkably simple and the size of the pores and the periodicity of the porous structure can be precisely controlled and readily tuned by changing the size of the colloidal spheres. The only requirement seems to be the availability of a precursor that can infiltrate into the void spaces among the colloidal spheres without the significant swelling or dissolving the template.

The templating spheres

A very important step that ensures the long-range ordering and the interconnectivity of the final porous structure is the synthesis and ordering of the templating colloidal spheres.

The templating spheres that are used are either inorganic, like silica, which is used to template organic materials like polymers [31, 32] or carbon [33], or the

spheres may be polymers like polystyrene (PS), which are used to make inorganic oxides [34–37] or PMMA, which are used to make macroporous alloys [38].

A wide variety of chemical approaches are available for producing colloidal spheres that are monodispersed in size [39]. The best established and most commonly used methods seems to be controlled precipitation for inorganic oxides and emulsion polymerization for polymer latex spheres, respectively. Using these methods, inorganic oxides such as amorphous silica have been readily prepared as uniform spheres with diameters ranging from few nm to 1 μm; polymer latexes of 20 nm to 20 μm in size have also been routinely produced as uniform beads.

Inorganic colloids are usually prepared via precipitation reactions, a process that often involves two sequential steps: nucleation and growth of the nuclei. To achieve monodispersity, these two stages must be strictly separated and nucleation should be avoided during the period of growth. In a closed system, the monomer (usually exists as a complex or solid precursor) must be added or released slowly at a well-controlled rate in order to keep it from passing the critical supersaturation levels during the growth period. In 1968, Stöber and Fink applied this strategy to other systems and demonstrated an extremely useful procedure for preparing monodisperse silica colloids [40]. They hydrolyzed a dilute solution of tetraethylorthosilicate (TEOS) in ethanol at a high pH and obtained uniform spheres of amorphous silica whose sizes could be varied from 50 nm to 2 μm simply by changing the concentration of the reactants. This method was later improved by many others, and now seems to be the simplest and most effective route to monodisperse silica spheres [41].

Polymer colloids of different chemical compositions can be produced as exceedingly spheres by the process of emulsion polymerization. Using this technique, monodisperse polymer colloids such as PMMA and PS have been obtained.

Formation of Colloid Crystals

There are many ways in which the templating colloidal spheres can be ordered into three-dimensional arrays. Figure 2.1.2 illustrates two methods using which
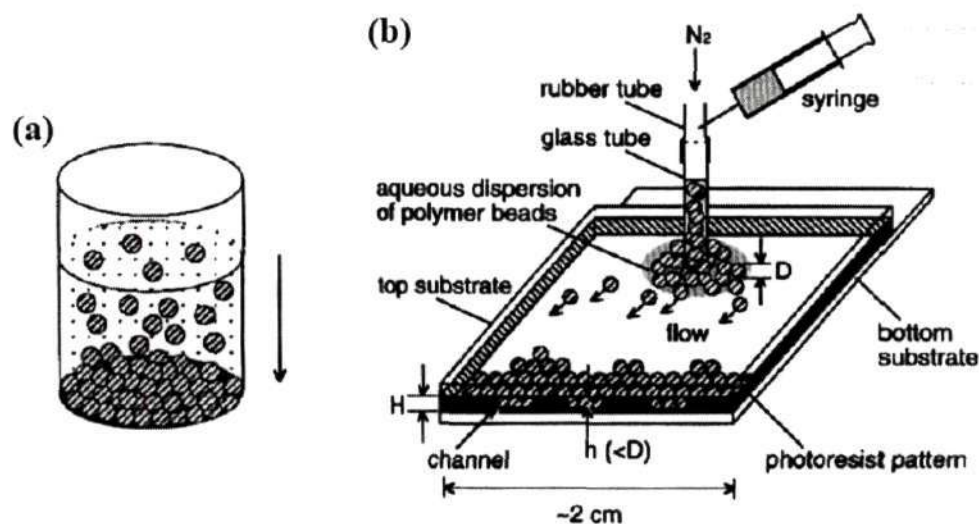
Figure 2.1.2: Methods used to assemble colloidal spheres into 3D lattices: (a) Sedimentation and (b) Crystallization through physical confinement

colloidal spheres have been successfully assembled into arrays.

Sedimentation in a gravitational field (Figure 2.1.2(a)) seems to be the simplest approach to the formation of 3D crystalline spheres from colloidal spheres [42]. Even though it looks simple, this method involves a strong coupling of several complex processes such as gravity settling, translational diffusion (or Brownian motion), and crystallization (nucleation and growth). The parameters that we must control in order to get good crystals are the size and density of the colloidal spheres, as well as the rate of sedimentation. Silica spheres have been successfully used to make 3D ordered arrays using this method to form artificial or synthetic opals [43, 44].

Monodisperse colloidal spheres often organize themselves into a highly ordered 3D structure when they are subjected to a physical confinement [45]. Xia and co-workers recently demonstrated such a method, which is schematically shown Figure 2.1.2(b). Using this method, they were able to assemble spheres with diameters ranging from 50 nm to 1 μm. The 3D crystalline array was found to be ccp structure with a packing density very close to 74%, and the (111) face was parallel to the glass substrate. They were able to assemble polystyrene as well as silica colloids to get 3D ordering that extended into the centimeter scale [46].

153

Synthesis of Macroporous Networks

Using the colloidal crystals, macroporous networks of inorganic materials as well as carbon have been obtained. The colloidal crystals are treated with solutions that permeate the cavities where they polymerize. In some cases, presence of a surfactant is found to be essential for the wetting of the spheres [35].

For the synthesis of metal oxide networks, metal alkoxides have generally been used as precursors. These hydrolyze and condense readily to form the oxide coating. Three-dimensionally ordered macroporous metal alloys of Ni_xCo_{1-x} (a solid solution) and Mn_3Co_7 (an intermetallic compound) have been prepared by templated precipitation of mixed metal salts within colloidal crystals of PMMA spheres and subsequent conversion of the inorganic precursors [47]. Colvin and coworkers also prepared macroporous films by templating silica films with polymer precursors like methyl methacrylate, styrene, etc. and studied the optical properties of the iridescent samples [32]. Porous carbons with 3D periodicity were prepared by using silica spheres as templates [33]. The templating spheres in each case have been obtained by calcination or by treatment with an appropriate solvent.

Silicon photonic crystals with complete three-dimensional bandgap near 1.5 μm were recently produced by growing silicon inside the voids of an opal template of closely-packed silica spheres followed by the removal of the silica spheres [48]. The reflectance spectrum clearly indicates the bandgap at a wavelength of 1.5 μm which is also the wavelength used by for the fibre optic telecommunication.

(b) Application as photonic crystals

Due to their long-range ordering, three-dimensionally periodic macroporous structures are promising candidates for photonic bandgap applications. A photonic band gap crystal (or photonic crystal) is a spatially periodic structure fabricated from materials having different dielectric constants [49]. These materials affect the properties of photons, in much the same way that ordinary semiconductor crystals affect the properties of electrons. We see many examples of these in Nature - the bright colours of opals is due to closely packed silica spheres and the bright

colours of a butterfly's wings are also due to this phenomenon. These ideas had been proposed independently by John [50] and Yablonovitch [51] in 1987 and since then have opened up a new, exciting field of research.

In a semiconductor, the atomic lattice presents a periodic potential to an electron propagating through the crystal. Due to the geometry of the lattice and the strength of the potential, Bragg-like diffraction occurs from the atoms, that opens up a gap in the allowed energy levels for which an electron is forbidden to propagate in any direction. In a photonic crystal, the periodic "potential" is due to a lattice of macroscopic dielectric media instead of atoms. If the dielectric constants of the constituent media are different enough, Bragg scattering of the dielectric interfaces can provide many of the same phenomena for photons as an atomic potential does for electrons. The aim is to produce photonic structures with a bandgap that extends over the entire Brillouin Zone - a range of frequencies for which light is forbidden to exist within the crystal. Creating a defect in the periodicity is also used to our advantage - a point defect could act as a microcavity, a line defect as a waveguide and a planar defect as a perfect mirror. Thus, it should be possible to fabricate materials that can guide light along narrow channels and tight corners with as little loss in power as possible.

The periodic array of atoms occurs naturally in crystals but these photonic crystals need to be fabricated artificially. It should be noted that the lattice constant in these photonic crystals should be comparable to the wavelength of light. For the optoelectronic industry, where the operating frequency used is 1.5 μm, the lattice constant of a photonic crystal should be of the order of 0.5 μm.

Yablonovitch fabricated the first three-dimensional photonic crystal possessing a complete bandgap in 1991 in the microwave regime [52]. Since then, several groups have tried to make photonic crystals of different colloids assembled into array and measured their optical properties. Colvin and coworkers [53] investigated the photonic properties of artificial opals. They have also measured the dependence of the stop band attenuation on the number of layers along the [111] direction. Xia and coworkers [54] studied the photonic properties of opaline structures assembled

155

from PS beads. The position of the stop band could be shifted by changing the size of the colloid particles. Colloidal systems do not have a high effective refractive index and hence are not good candidates to exhibit full bandgap. Inverse opal structures are ideal for this purpose.

All the photonic properties are technologically important because they can be exploited, in principle, to produce light-emitting diodes (LEDs) that display coherence properties, to fabricate thresholdless semiconductor diode lasers, and to significantly enhance the performance of many other types of optical, electro-optical, and quantum electronic devices. The future research will be directed at producing different materials possessing 3D photonic bandgap, which can be manufactured cost-effectively and in a large scale.

2.2 Scope of the present investigations

2.2.1 Macroporous oxide materials with three-dimensionally interconnected pores

Macroporous networks of various oxides have been synthesized using spheres of polystyrene or PMMA as templates. Velev *et al.* [35] obtained ordered macroporous silica by templating colloidal crystals of polystyrene while Imhof and Pine [37] obtained macroporous titania by using surfactants. The preparation of a few ceramic oxides with periodic three-dimensional arrays of macropores by using polystyrene spheres as templates has been reported [31, 36, 55]. Macroporous TiO_2 with diameters between 240 and 2000 nm has also been prepared by filling voids in opals by a liquid phase chemical reaction [34]. While some of the workers have removed the organic template by dissolution in an appropriate solvent [31], others have burnt off the polymer template [37] or extracted it by refluxing in a solvent [31,36].

In our study, we have prepared ordered mesoscale hollow spheres of $\sim$1000 nm diameter of binary as well as ternary oxides by employing crystalline arrays of polystyrene beads as templates. Typical of the ordered macroporous ternary oxides obtained by us is ferroelectric $PbTiO_3$ and $Pb(ZrTi)O_3$. In preparing these ordered porous networks, we have employed calcination as well as washing with a solvent as the means of removing the template.

2.2.2 Macroporous carbons obtained by templating with silica spheres

Macroporous membranes of various polymers have been prepared by templating silica spheres [32]. Porous carbons with similar features have been prepared by infiltrating silica opal plates with a phenolic resin or by chemical vapor deposition

157

using propylene, and then dissolving the silica [33]. We have prepared macroporous carbon with three dimensionally interconnected voids by a novel method, involving the coating of close-packed monodisperse silica spheres with sucrose, converting sucrose into carbon by mild carbonization using sulfuric acid as the catalyst [56], and then dissolving the silica with aqueous hydrofluoric acid. Excellent results have been obtained using this technique in preparing three-dimensionally ordered macroporous carbon networks. Carbon samples with macropores were also obtained by using mesoporous silica spheres instead of the non-porous silica spheres. Also present are the adsorptive properties of the various macroporous carbon samples.

2.2.3 Macroporous silica-alumina composites with meso-porous walls

Macroporous materials of oxides such as TiO_2, SiO_2 [34–37] are attracting much attention. Macroporous solids with micropores or mesopores would make useful adsorbents or catalyst supports. Recently, Stein and coworkers have reported the synthesis of macroporous silica containing mesoporous walls by treating a solution containing the silica precursor with an aqueous mixture of cetyltrimethylammonium hydroxide and tetrapropylammonium hydroxide and pouring the solution over an ordered array of polystyrene beads [36]. Macroporous silicates with zeolitic microporous frameworks were made hydrothermally by Stein and coworkers [57].

We have attempted to make macroporous aluminosilicates containing meso-porous walls. For this purpose, an ordered array of polymethylmethacrylate (PMMA) spheres has been employed in the presence of the cationic surfactant N-Cetyl-N,N,N-trimethylammonium bromide (CTAB). The macroporous-mesoporous silica-alumina composites with satisfactory/high surface areas has been described.

2.2.4 Submicron-sized mesoporous aluminosilicate spheres

The discovery of mesoporous silica marks a major event in areas related to catalysis, sorption and separation processes [9, 10]. Amongst the criteria for the use of such mesoporous materials for various purposes, the morphology and particle size

are important ones. In this context, several workers have attempted to prepare sub-micron sized mesoporous silica spheres. The synthetic procedure generally makes use of Stöber's reaction involving base hydrolysis and subsequent condensation of the silicon ester in an appropriate solvent [40]. One of the first efforts to make spherical silica is due to Unger *et al.* [58], who obtained non-porous silica beads with a particle size of ∼3 mm. Kaiser and Unger [59], however, obtained completely porous silica spheres by a similar procedure. Büchel *et al.* [60] have described a novel pathway for obtaining monodisperse silica spheres composed of a non-porous solid silica core and a thin mesoporous silica shell by taking advantage of the methods described by Unger *et al.* [58] and Kaiser and Unger [59]. By employing surfactant-stabilized emulsions as in the synthesis of MCM-41, Huo *et al.* [61] obtained large, monodisperse mesoporous silica spheres with high surface areas. The spheres had diameters between 0.1 to 2 mm and pore diameters of 1 to 5 nm. Mesoporous silica spheres ranging from 2 to 6 mm (pore diameter ∼2.5 nm) have been synthesized under static acidic conditions by mixed cationic-nonionic surfactant templating as well [62]. Spheres of ordered MCM-41 and MCM-48 have also been prepared by employing appropriate surfactants [23,63].

It was our interest to prepare monodisperse aluminosilicate spheres with meso-porous properties. We have been able to prepare such spherical aluminosilicates with Si/Al ratios between 14 and 40 by employing a cationic surfactant. For purpose of comparison, we have also prepared mesoporous silica spheres by the same procedure.

2.3 Experimental and related aspects

2.3.1 Macroporous oxide networks

Polystyrene beads of 1000 nm diameter, prepared by emulsifier-free polymerization of styrene, were centrifuged at 1100 rpm for six hours and dried in air. These beads yielded satisfactory colloidal crystals, as can be seen from a scanning electron microscopy (SEM) image (obtained with a Leica microscope) of a dispersion shown in Figure 2.3.1. We prepared macroporous networks of SiO_2, TiO_2 and ZrO_2 by using tetraethylorthosilicate (TEOS), tetrabutylorthotitanate (TBOT) and zirconium i-propoxide (ZIP) respectively as the precursors. Macroporous SiO_2, TiO_2 and ZrO_2 networks were prepared from using alkoxide precursors by the following procedure - Polystyrene spheres were taken on a Büchner funnel connected to a vacuum pump. The ratio of the weights of the metal precursors (TEOS, TBOT, ZIP) to the template was 10.0, 5.0 and 2.5 for SiO_2, TiO_2 and ZrO_2 respectively. The pure precursors were poured on the template to wet it completely. The precursors hydrolyzed on exposure to air. The composites were left to dry for 12 h at room temperature. The template was removed by calcination at 575 °C for 7 h.

Macroporous TiO_2 was prepared by an alternative route as well. $TiCl_4$ was taken in a 3-necked round bottom flask and kept in salt-ice mixture. Distilled water ice pieces were added to it slowly to form a yellow colored solution. Distilled water was finally added to get a transparent solution. This was poured on polystyrene beads kept in a glass vial and allowed to dry at room temperature. The template was removed by treatment with toluene.

Macroporous $PbTiO_3$ and $Pb(ZrTi)O_3$ (PZT) were prepared by the following procedure - 0.1 M solution of lead acetate, 0.1 M TBOT and 0.1 M ZIP (all in methanol) were prepared. In order to prepare $PbTiO_3$, stoichiometric amounts of
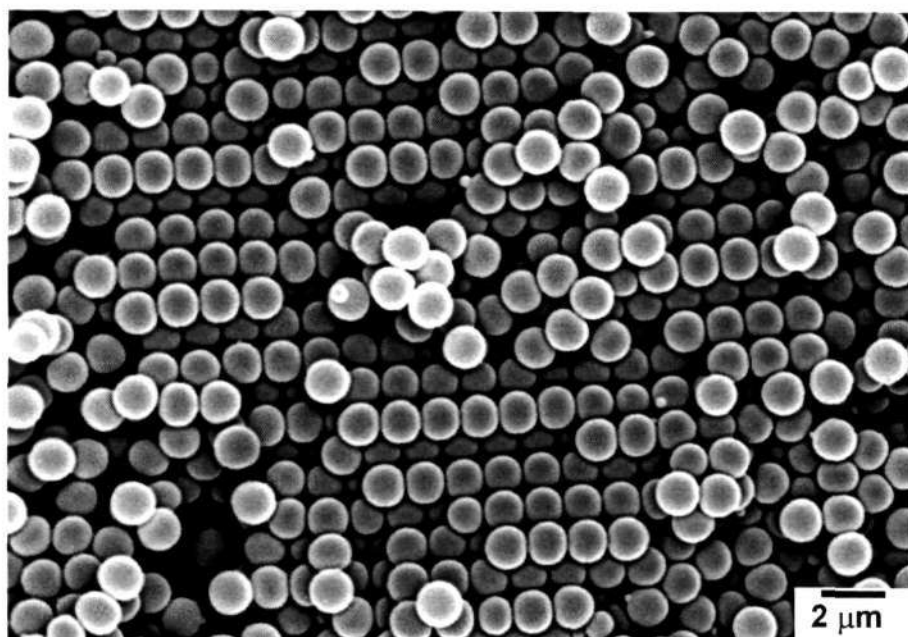
161

Figure 2.3.1: SEM image of an array of polystyrene beads

the Pb and Ti precursor solutions were taken in a beaker. The solution was stirred for 15 minutes after which it the temperature was increased to 60 °C . A few drops of water were added to the solution, which resulting in gel. This was poured on the polystyrene spheres and allowed to dry at room temperature for 12 h. The template was removed by treatment with toluene. The sample was crystallized by heating to 400 °C for 60 minutes. $Pb(Zr_{0.5},Ti_{0.5})O_3$ was obtained by a similar procedure (starting with Pb, Zr, Ti precursor solutions).

2.3.2 Macroporous carbon networks

The procedure employed for the synthesis of macroporous carbon is as follows. Monodisperse silica spheres were synthesized following the method of Stöber *et al.* [40]. Spheres of different sizes could be prepared by the hydrolysis of tetraethylorthosilicate (TEOS) in an alcohol medium with aqueous ammonia (25% solution) as the base. Evaporation of the alcohol solvent from between the spheres packs them into arrays. In Figures 2.3.2(a) and (b) we show a SEM image of ordered silica beads of diameter $\sim$625 and $\sim$200 nm respectively. The spheres have a narrow size distribution and are reasonably ordered. In order to template the silica spheres
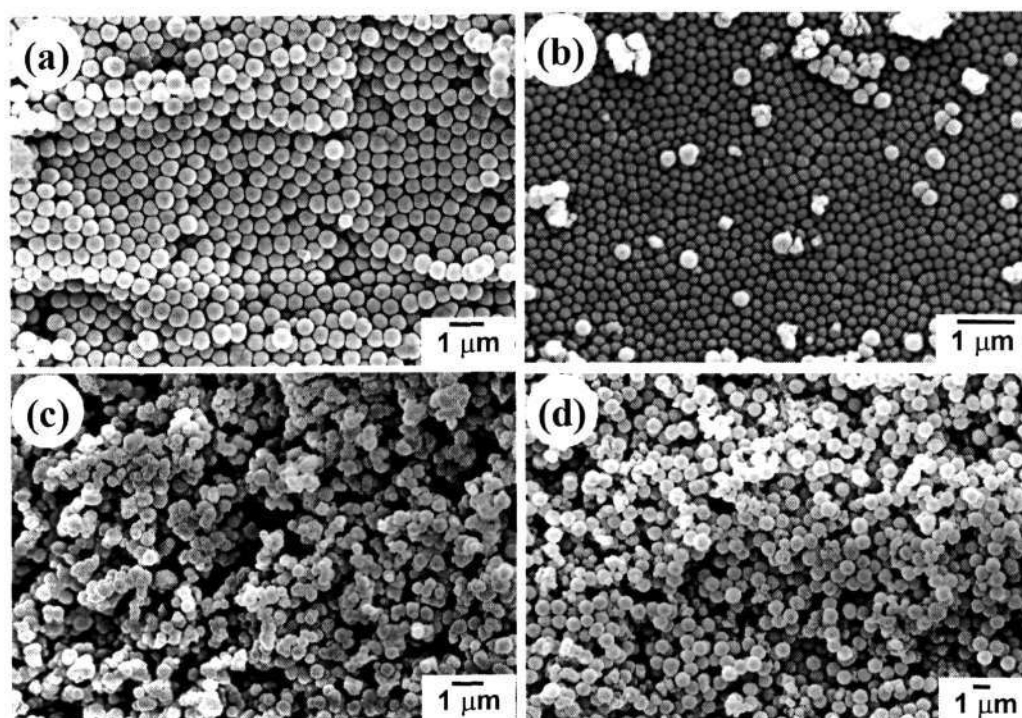
Figure 2.3.2: SEM images of (a) non-porous ordered silica spheres of diameter ∼625 nm; (b) non-porous ordered silica spheres of diameter ∼200 nm; (c) mesoporous silica spheres of ∼450 nm diameter and (d) a mixture of mesoporous (25%) and non-porous (75%) silica spheres.

with carbon, 0.245 g of the spheres was treated with a solution containing 0.2 g sucrose along with 4 mL H_2O and 0.5 mL H_2SO_4. The resulting mixture was kept in a drying oven at 60 °C for 6 h, and the temperature gradually raised to 100 °C to allow complete drying. The temperature was then increased to 150 °C at a rate of 2 °/min. Carbonization was carried out by heating the sample to 800 °C under vacuum (10^{-6} Torr). The composite thus formed was treated with an aqueous solution of HF (48%) for 24 h in order to dissolve the templating silica spheres. Aqueous HF was found to be better than aqueous NaOH for the dissolution. The product was washed several times with water and dried at 60 °C . Macroporous carbon samples were prepared by this procedure by employing non-porous silica spheres of diameters ∼625 and ∼200 nm.

We also prepared macroporous carbon by templating mesoporous silica spheres with sucrose. For this purpose, monodisperse silica spheres containing mesopores

163

(diameter ~450 nm) were prepared by a method similar to Schumacher *et al.* [23] In a typical synthesis, 0.667 g of N-cetyl-N,N,N-tetramethylammonium bromide was dissolved in a solution containing 14 mL H_2O and 14 mL C_2H_5OH. To the above solution, 3.5 mL ammonia (25% solution) was added under stirring. After 10 minutes, 1 mL of TEOS was added dropwise and stirred for a period of 2 h. The mixture was aged at room temperature (25 °C) for 2 h, filtered, washed with deionized water and dried at ambient temperature. The dried product was calcined at 400 °C for 2 h. Powder XRD patterns that was recorded established the mesoporous nature of the sample. Thermogravimetric analysis (TGA) showed that ~95% of the surfactant could be removed by calcination at 400 °C . SEM images showed the particles to be spherical, but there was a distribution of sizes. These spheres were taken along with water and sonicated for 30 minutes in order to disperse the spheres. This was left undisturbed at room temperature until a major part of the water had evaporated. The rest of the water was then evaporated at 60 °C . In Figure 2.3.2(c) we show an SEM image of the mesoporous silica spheres. Due to the variation in the sizes of the spheres, it was found difficult to order them into arrays. Using these spheres, macroporous carbon networks were prepared by a procedure similar to the one used for templating the non-porous silica spheres.

We also employed an array of silica spheres containing 25% mesoporous spheres (~450 nm diameter) and 75% non-porous spheres (~625 nm diameter) for preparing porous carbon samples. This was done by taking the spheres in water, followed by sonicating for 30 minutes. The spheres settled down under the influence of gravity. The SEM image of the dried spheres is shown in Figure 2.3.2(d). The ordering is considerably improved due to the presence of a larger percentage of uniform sized non-porous spheres. Employing these arrays, we repeated the synthesis of macroporous carbon.

The application of porous carbons as catalyst supports is widely recognized and we therefore carried out nitrogen adsorption studies at liquid nitrogen temperature on these samples. Reflectance spectra of the macroporous carbons were recorded in the visible region for the samples prepared with non-porous silica spheres (~200 nm diameter).

2.3.3 Macroporous silica-alumina composites with meso-porous walls

Polymethylmethacrylate (PMMA) spheres of diameter 275 nm were obtained from Soken Chemicals, Japan. These were taken as 1 % wt:wt in distilled water and sonicated for 30 minutes to disperse the spheres. This sol was centrifuged at 1000 rpm for 6–8 h. The water above the spheres was removed with a pipette carefully and the spheres were left to dry under ambient conditions. These formed millimeter-sized colloidal crystals which were used for further reactions.

The silica-alumina gel was synthesized in the following manner. To a solution of 0.5 g of CTAB in 10 mL H_2O, 0.1 g of $Al_2(SO_4)_3.16H_2O$ was added and stirred until a homogenous solution was obtained. 1 mL of tetraethylorthosilicate (TEOS) was added to this mixture and the stirring continued. Finally, a few drops of NH_3 (25% solution) were added to make the pH ~8. The turbid solution was poured on the colloidal crystals to allow it to percolate through the voids between the spheres. This was left to dry at room temperature. The dried products were calcined at 400 °C for 2 hours, which resulted in sample A shown in Table 2.4.1. By a similar procedure, we prepared two other silica-alumina samples (B and C) with different Si/Al ratios.

2.3.4 Mesoporous aluminosilicate spheres

We have prepared mesoporous aluminosilicate spheres with Si/Al ratios in the range 14 to 40 in addition to preparing pure silica mesoporous spheres by the following procedure. In a typical synthesis, 0.667 g N-cetyl-N,N,N-trimethylammonium bromide (CTAB) was dissolved in a solution containing 14 mL deionised water (H_2O) and 14 mL ethanol (C_2H_5OH). To the above solution, 3.5 mL ammonia (NH_3) solution (25%) was added under stirring, followed by the addition of a solution of 15 mL water of an aqueous solution containing 0.1 g $Al_2(SO_4)_3$. The final composition of the mixture was 0.4 M CTAB/360 M H_2O/53 M C_2H_5OH/42 M NH_3/1 M TEOS/0.04 M $Al_2(SO_4)_3$. After 10 min, 1 mL of tetraethylorthosilicate (TEOS) was added dropwise over a

period of 2 h under stirring to obtain a gel. The gel was aged at room temperature (298 K) for 16 h, filtered, washed with deionised water and dried at ambient temperature. The dried product was calcined at 200 °C for 4 h, which resulted in sample C. By a similar procedure, we prepared two other aluminosilicate samples (A and B) with different Si/Al ratios.

2.3.5 Characterization techniques

Powder X-ray diffraction (XRD) patterns were recorded using CuKa radiation on a Rich-Siefert, XRD-3000-TT diffractometer. To verify the removal of the surfactant, thermogravimetric analysis (TGA) was carried out on a Mettler-Toledo-TG-850 instrument. Energy dispersive analysis of X-rays (EDAX) and Scanning Electron Microscopy (SEM) images were obtained on a Leica scanning electron microscope fitted with a Link ISIS spectrometer. Surface areas and adsorption isotherm of the samples were measured using the Brunauer-Emmett-Teller (BET) method with the help of the adsorption setup fitted with a Cahn-2000 microbalance. In the case of the aluminosilicate samples, magic angle spinning nuclear magnetic resonance (MAS-NMR) were recorded on a Bruker DX-300 spectrometer.

2.4 Results and discussion

2.4.1 Macroporous oxide materials with three-dimensionally interconnected pores

In Figure 2.4.1(a) we show a SEM image of the ordered macroporous SiO_2. The pore diameter is slightly smaller ($\sim$ 850 nm) than that of the template beads because of shrinkage occurring during calcination. What is interesting is that we see lower layers in the SEM image due to the three-dimensional ordering in the material, although it is X-ray amorphous.

The SEM image of macroporous TiO_2 prepared by the TBOT route is shown in Figure 2.4.1(c). The pores are highly ordered and there is some shrinkage due to calcination. The pore diameter is approximately 800 nm. The material is crystalline as revealed by the X-ray diffraction (XRD) pattern (Figure 2.4.2). TiO_2 in this porous structure is in the anatase phase (JCPDS file: 21–1272). Macroporous TiO_2 obtained by the $TiCl_4$ route gave an ordered structure as well, as can be seen from the SEM image in Figure 2.4.1(d), but the material was X-ray amorphous. There was little shrinkage of the pores in this case. By carrying out the hydrolysis around 65 °C , one obtains the rutile phase [64]. A SEM image of ordered macroporous zirconia is shown in Figure 2.4.1(b). The material is crystalline as evidenced by the XRD pattern (Figure 2.4.2). ZrO_2 has the monoclinic structure (JCPDS file: 37–1484). The image in Figure 2.4.1(b) shows small circular windows approximately one-quarter the diameter of the big pores. The windows connect the spherical voids and are formed when the close packed spheres are in contact.

The as-prepared macroporous network of $PbTiO_3$ was amorphous. However, on heating at 400 °C for 2 hours it became crystalline as evidenced by the XRD pattern shown in Figure 2.4.2 (tetragonal: JCPDS file: 06–0452). The stoichiometry was verified by EDX analysis. There was no shrinkage of the pores in the network and we show the porous structure in Figure 2.4.3(a).
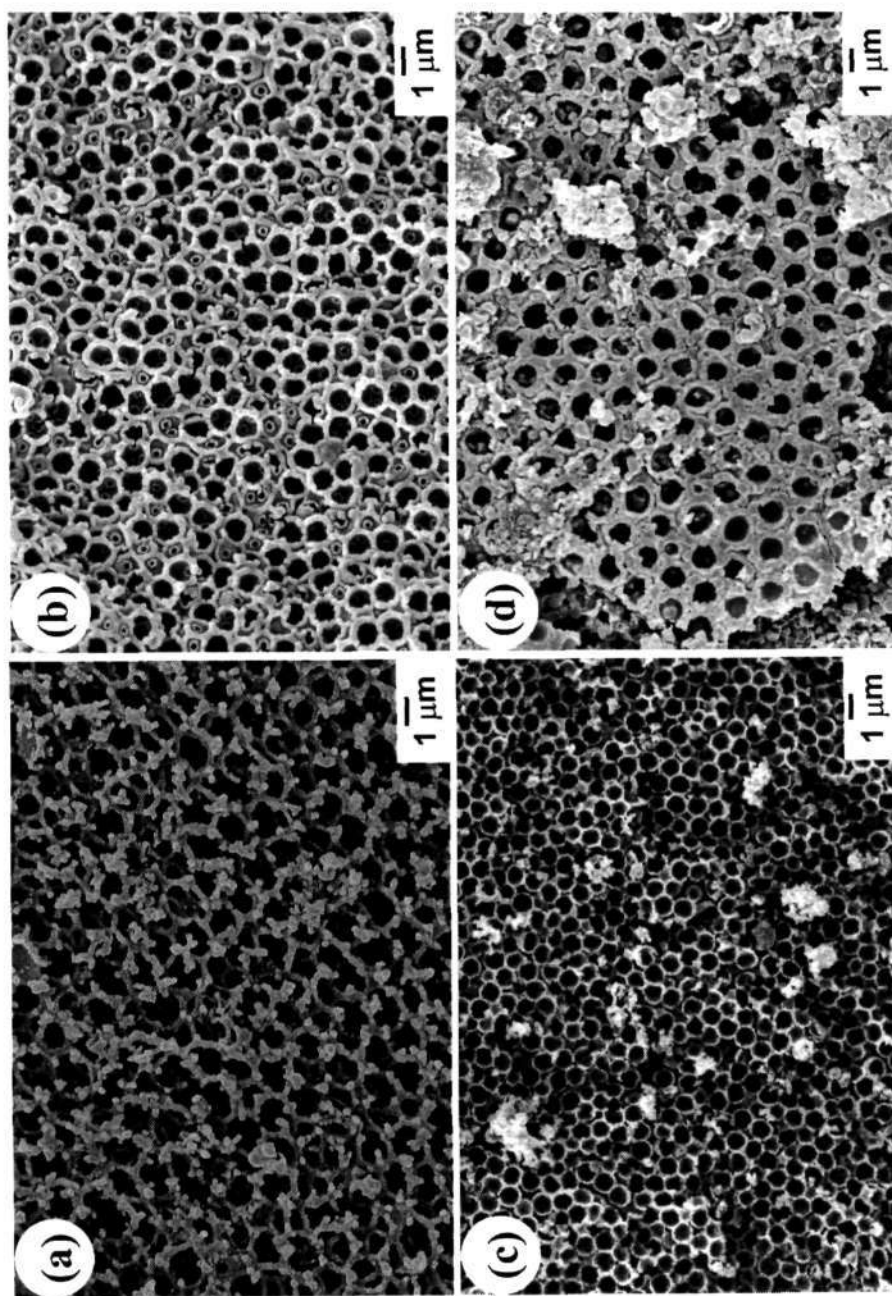
Figure 2.4.1: SEM images of ordered, macroporous networks of (a) SiO_2, (b) ZrO_2, (c) and (d) TiO_2 obtained by two different routes
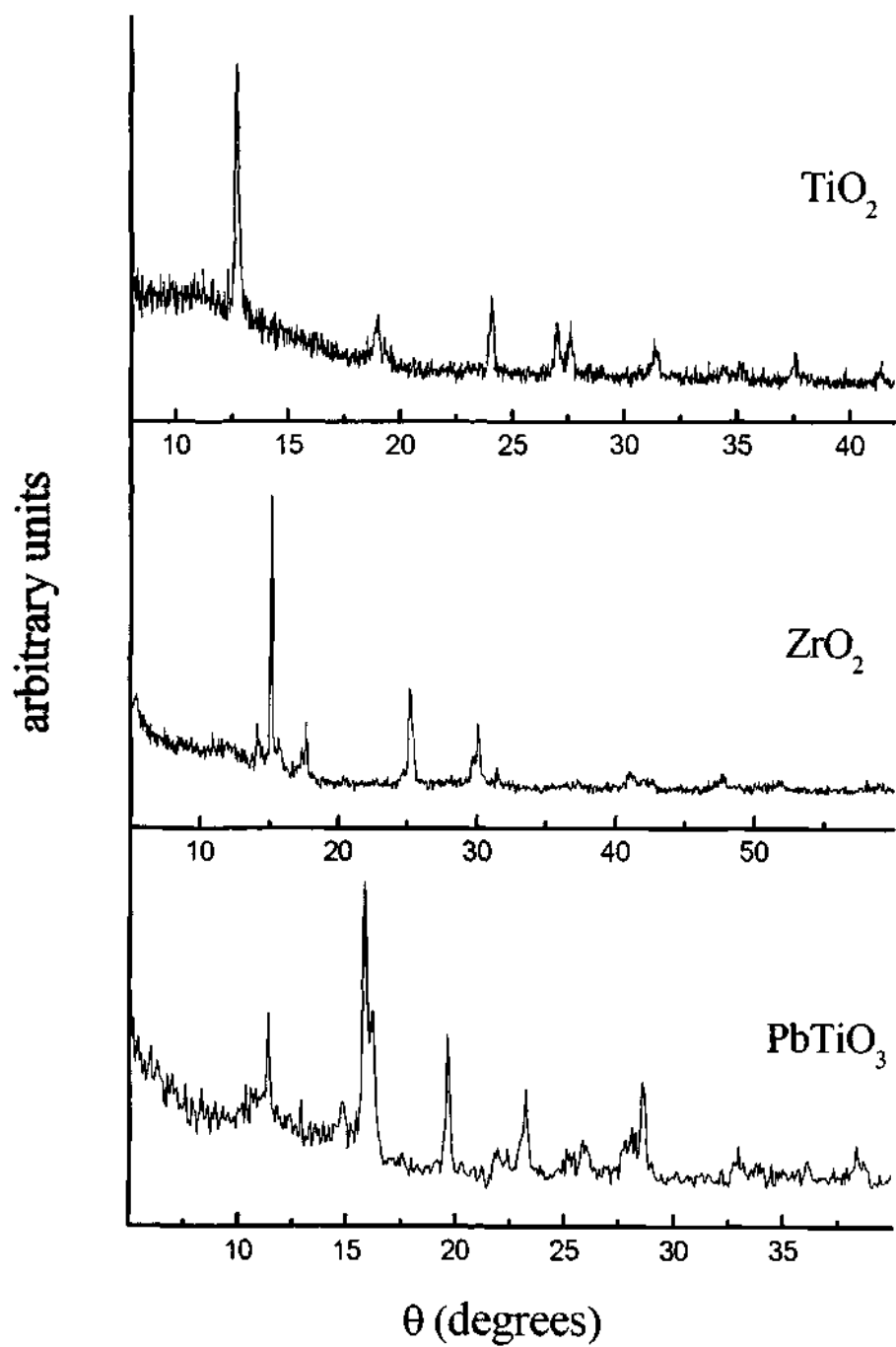
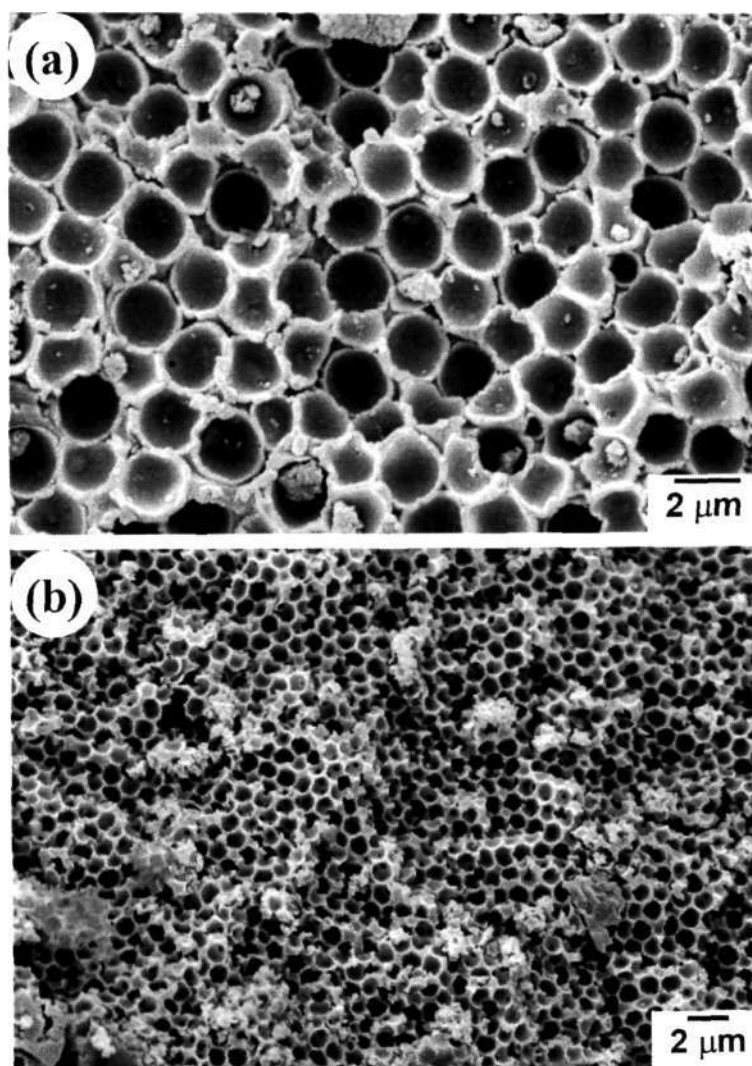Figure 2.4.2: XRD patterns of macroporous TiO_2, ZrO_2 and $PbTiO_3$

Figure 2.4.3: SEM images of ordered, macroporous (a) $PbTiO_3$ and (b) $Pb(ZrTi)O_3$.

The SEM image of the macroporous structure of $Pb(ZrTi)O_3$ obtained by us is shown in Figure 2.4.3(b). The material was however X-ray amorphous. Heating the material for purpose of crystallization destroyed the porous structure.

In summary, we have prepared three-dimensional ordered macroporous structures, with pore diameters of 1000 nm, of not only binary oxides, but also of ternary oxides such as ferroelectric $PbTiO_3$. *

* A paper based on this study has appeared in Solid State Sciences, (2000).
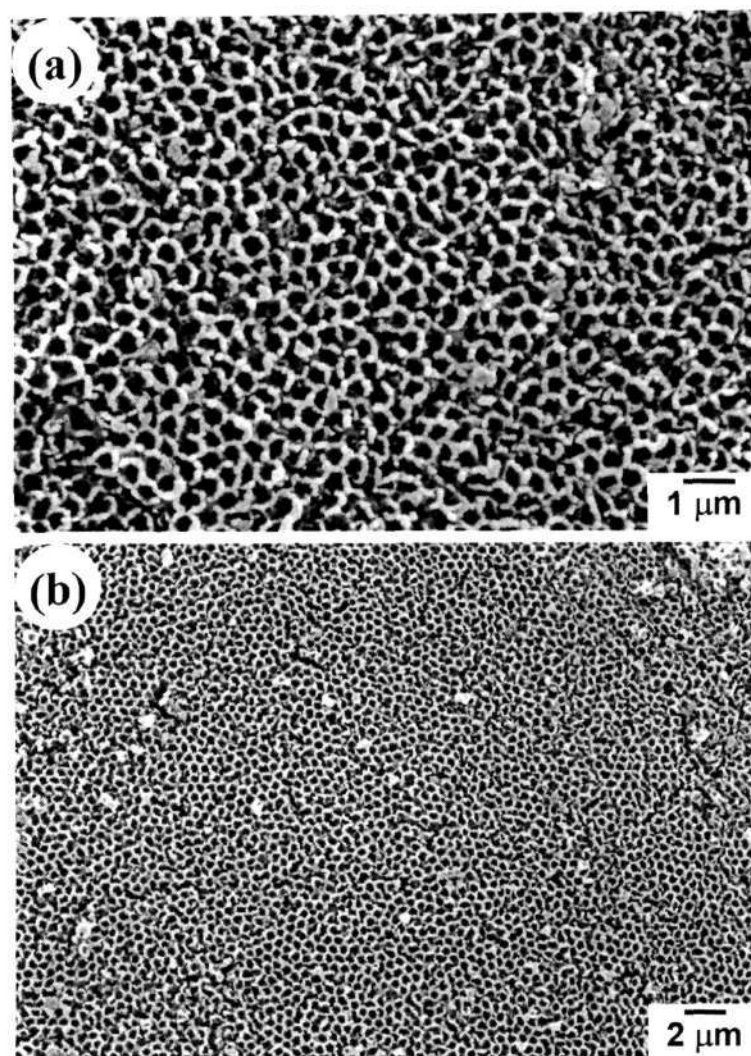
Figure 2.4.4: SEM images of macroporous carbon obtained by templating non-porous silica spheres of 625 nm diameter

2.4.2   Macroporous carbons

In Figure 2.4.4(a) we show the SEM images of the macroporous carbon obtained by templating non-porous silica spheres of ∼625 nm diameter. Figure 2.4.4(b) reveals long-range ordering extending to several tens of microns. Thus, the ordering of the templating silica spheres is maintained even after treatment with sucrose, carbonization followed by treatment with aqueous HF. There is considerable shrinkage on removal of the template as seen from Figure 2.4.4(a) which shows pores of ∼400 nm diameter. Similarly, the pores of the carbon sample prepared
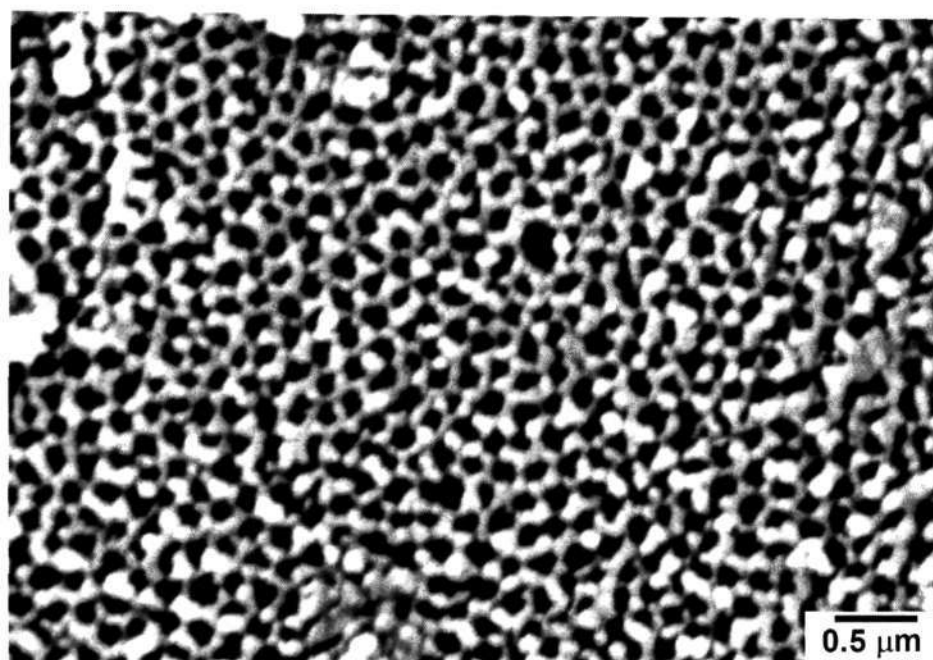
171

Figure 2.4.5: SEM images of macroporous carbon obtained by templating non-porous silica spheres of 200 nm diameter

from silica spheres of ~200 nm diameter, have a diameter of ~125 nm as shown in Figure 2.4.5. Three-dimensional (3D) ordering is indicated by the circular windows connecting the spheroidal voids, formed when the spheres in the array are in contact with one another. Due to extensive 3D ordering and interconnected voids, these carbon materials are ideal for photonic bandgap applications.

In Figure 2.4.6 we show the reflectance spectra of the silica spheres (~200 nm) coated with carbon as well as the macroporous carbon sample obtained after removal of the silica template. We see a clear maximum at 434 nm for the silica coated with carbon and a maximum at 465 nm for the macroporous carbon sample. These observations are similar to those of Zakhidov and co-workers who observed intense opalescence for their carbon inverse opals prepared by the phenolic and CVD routes [33]. There is a red shift in the wavelength of absorption for the carbon sample due to the increase in the effective refractive index after the silica spheres are removed. The inset in Figure 2.4.6 is a photograph of the sample taken under the optical microscope. The colour of the sample was bluish green.
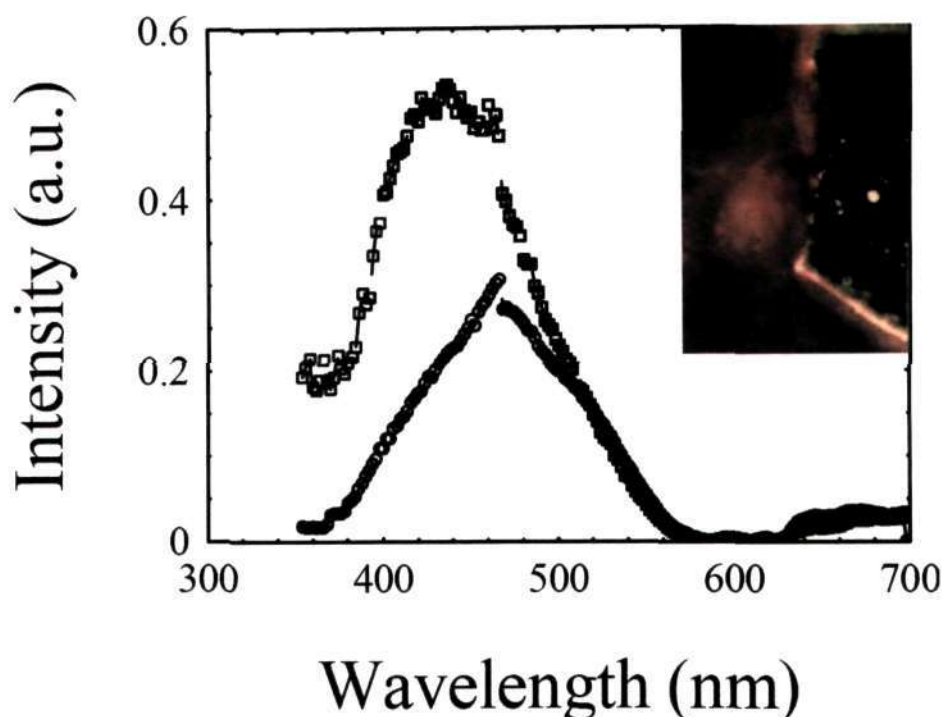
Figure 2.4.6: Reflectance spectra of silica spheres (200 nm) coated with carbon and of the carbon network obtained after removal of the silica spheres. Inset shows the photograph of the sample taken in an optical microscope.

The N_2 adsorption isotherm for the macroporous carbon with $\sim$400 nm diameter pores (prepared by starting with $\sim$625 nm non-porous silica spheres) is shown in Figure 2.4.7(a). It is a typical Type I isotherm, similar to that exhibited by microporous carbons [65]. The slope is high initially, indicating that the micropores get filled at low partial pressures. At higher partial pressures, there is saturation. The surface area calculated by the BET method is 119 m^2g^{-1}. The surface area of the macroporous carbon sample with 125 nm diameter pores (prepared by starting with 200 nm non-porous silica spheres) was 226 m^2g^{-1}. Although these values of the surface area are somewhat lower that those of other porous carbons [65], the presence of ordered macropores may provide certain advantage to macroporous carbons as potential catalyst supports.

The network prepared by templating mesoporous silica spheres ($\sim$450 nm diameter) did not show good ordering as the networks obtained with non-porous
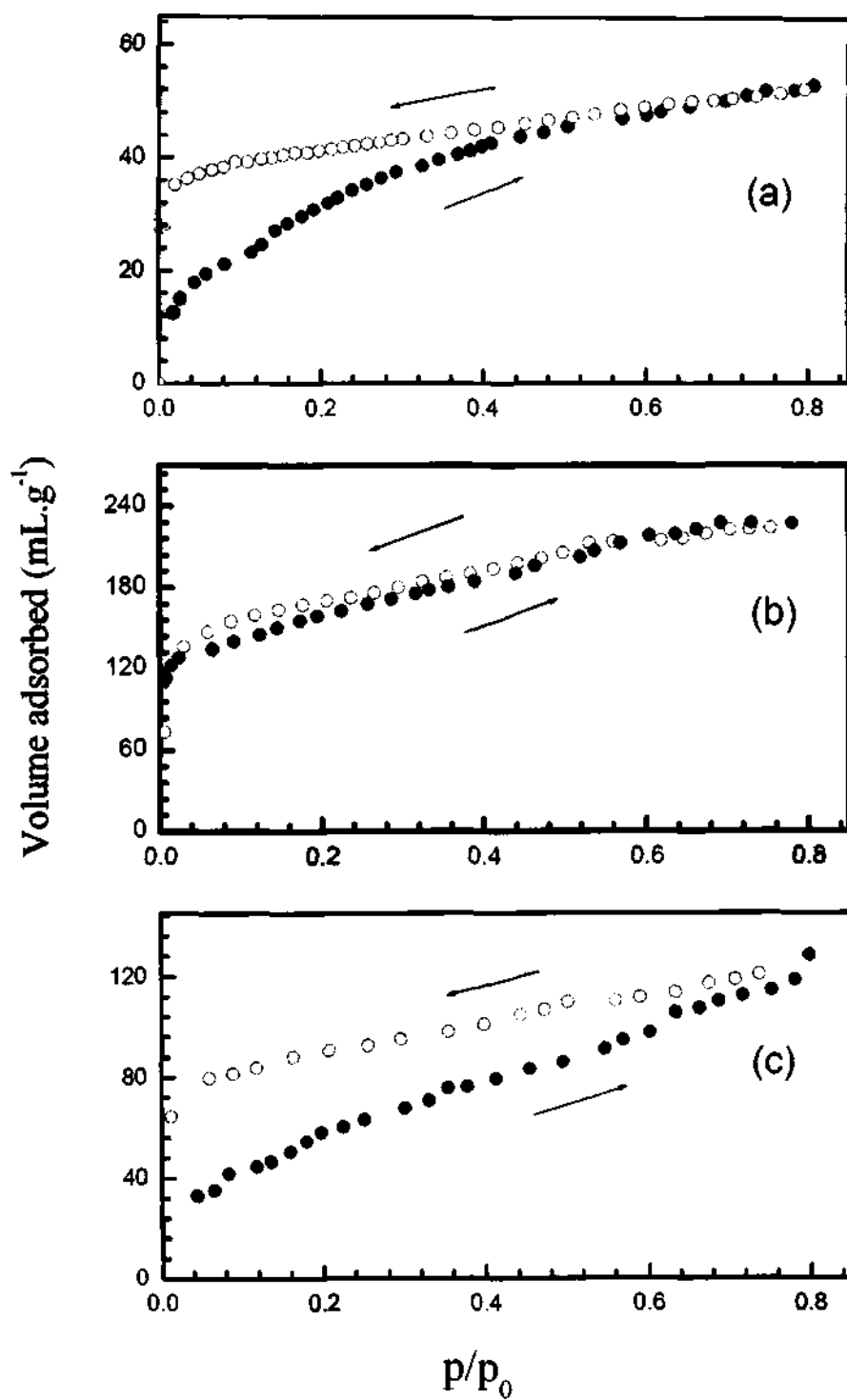
173

Figure 2.4.7: N_2 adsorption isotherms for macroporous carbons prepared by templating (a) non-porous silica spheres ($\sim$625 nm diameter), (b) mesoporous silica spheres ($\sim$450 nm diameter) and (c) mixture of 25% mesoporous and 75% non-porous silica spheres.
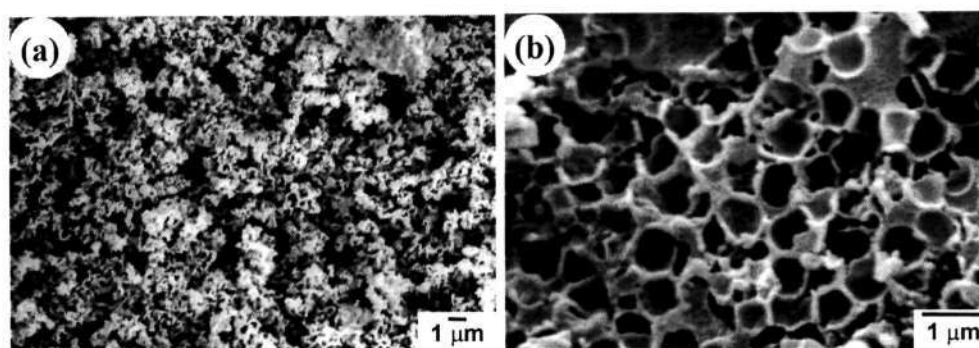
174

Figure 2.4.8: SEM images of carbon networks prepared by templating (a) mesoporous silica spheres and (b) mixture of 25% mesoporous and 75% non-porous silica spheres.

silica spheres (Figure 2.4.8(a)). This is mainly because the initial silica arrays themselves are not well ordered. The N_2 adsorption isotherm of the carbon network prepared by templating mesoporous silica spheres was of Type II and gave a surface area of 230 m^2g^{-1}. Since we had started with mesoporous silica spheres, it was expected that the macroporous carbon would have mesoporous walls. However, the mesopores seemed to have been blocked. In order to get a better porous structure, we reduced the sucrose content of the initial reaction mixture to 0.1 g. By this means we obtained a macroporous carbon sample exhibiting a N_2 adsorption isotherm of Type I as shown in Figure 2.4.7(b). The surface area calculated by the BET method was 551 m^2g^{-1}. This value of the surface area is the largest that we have obtained amongst the macroporous carbon samples prepared by us.

In Figure 2.4.8(b), we show the SEM image of the macroporous carbon obtained by templating a mixture of 25% mesoporous (~450 nm diameter) and 75% non-porous (~625 nm diameter) silica spheres. Accordingly, we see smaller pores in the SEM image along with the large pores. There is reasonable ordering in this sample, although not as good as in the images shown in Figure 2.4.4. The N_2 adsorption isotherm of this sample shown in Figure 2.4.7(c) is of Type II, with a large hysteresis. The BET surface area was 207 m^2g^{-1}, which is in between the values obtained with the samples prepared using non-porous and mesoporous silica spheres.

In summary, we have demonstrated a method for fabricating three-dimensionally ordered macroporous carbon networks. The method can be used to template silica

Table 2.4.1: Properties of macroporous SiO_2-Al_2O_3 with mesoporous walls

	Si/Al		d (Å)		Surface area (m^2g^{-1})
	gel	product	as-synth.	calcined	
A	18.5	48.0	38.94	35.6	1038
B	12.4	15.3	35.26	32.64	804
C	9.3	4.5	38.15	33.52	676

spheres of different sizes with good results, but the surface area of these carbon samples is relatively small. We have templated mesoporous silica spheres by the same method to obtain different porous carbons with somewhat higher surface areas. Although the surface areas of all these macroporous carbons are in the 120–550 m^2g^{-1} range, they could be useful as supports for metal catalysts. The presence of macropores may aid the diffusion of the reacting species to the active sites or of the product to leave the catalyst surface. The 3D ordered macroporous carbons may also be useful as photonic bandgap materials. [†]

2.4.3 Macroporous silica-alumina composites with meso-porous walls

Table 2.4.1 lists the compositions of the various samples prepared by us. In Figure 2.4.9(a) we show the SEM image of the templating PMMA spheres employed by us. The spheres are of uniform diameter and are ordered into arrays. In Figure 2.4.9(b) we show the SEM image of sample B after the spheres were treated with the silica-alumina gel, dried and calcined. The networks are fairly well ordered. The diameter of the pores is slightly smaller (150 nm) than that of the initial PMMA spheres. The shrinkage occurs during the removal of the template during calcination. The SEM image of the samples A and C too were similar to the image in Figure 2.4.9(b). There was no noticeable change in the external morphology on increasing the amount of aluminum in the samples. The SEM images clearly establish the presence of macropores probably connected in three dimensions.

[†]A paper based on this study has appeared in Mat. Res. Bull., (2001).
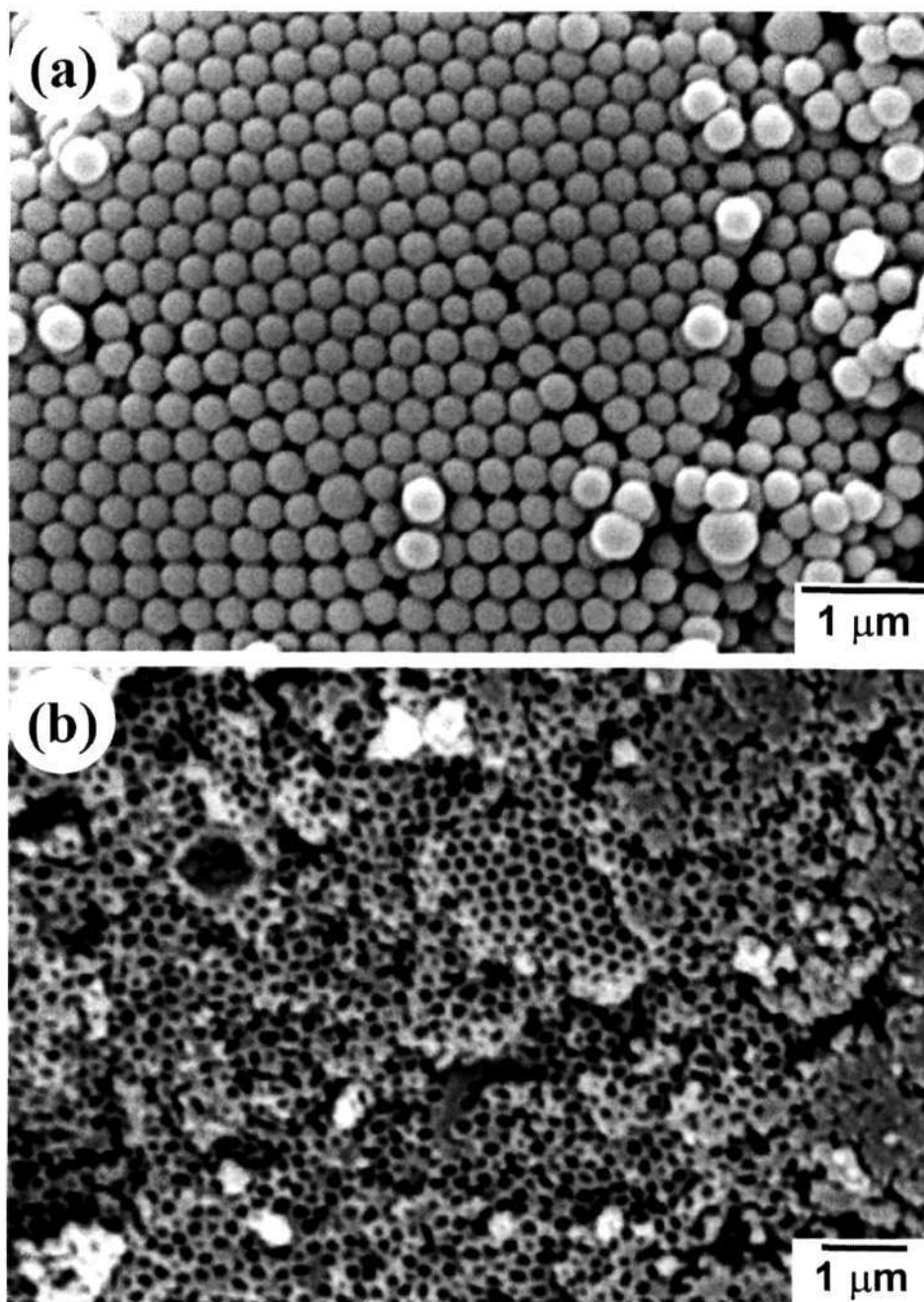
Figure 2.4.9: SEM images of (a) PMMA spheres and (b) sample B after removal of the template.
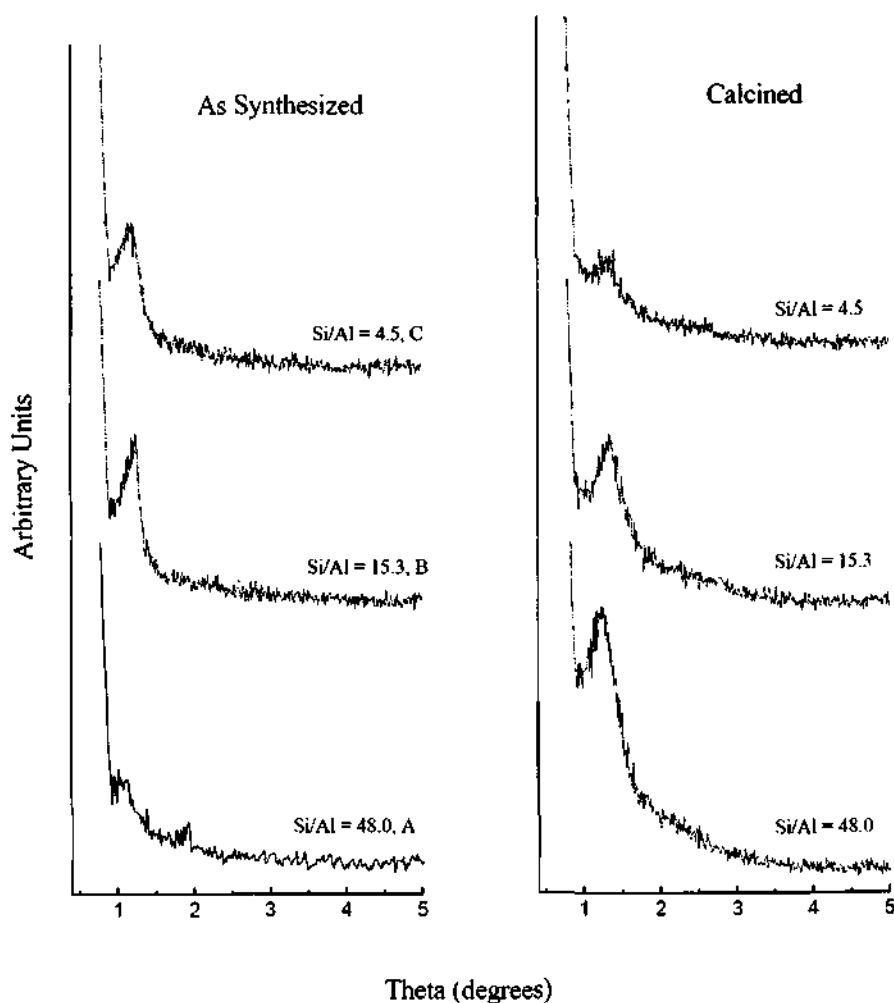
Figure 2.4.10: XRD patterns of the as-synthesized and calcined samples A, B and C.

XRD patterns of the as-synthesized and calcined samples are presented in Figure 2.4.10. The as-synthesized samples of A, B and C show single peaks with d-values 38.94, 35.26 and 38.15 Å respectively. The low-angle peak is similar to that shown by hexagonal mesoporous solids. There is a decrease in the d-value after calcination due to removal of template CTAB molecules, d-values being 35.5, 32.64 and 33.52 Å respectively for A, B and C. The presence of the low angle peak after calcination indicates that the mesoporous phase is reasonably intact after removal of the template. We know of three materials, A, B, and C, which are macroporous-mesoporous.

TGA curves of the aluminosilicates A and C are shown in Figure 2.4.11. The

178

as-synthesized samples show a single weight loss from 250–350 °C due to the loss of the PMMA and CTAB templates. The weight loss above 350 °C is due to the condensation of the silanol that occurs after 350 °C . The TGA curve for the calcined samples show a single weight loss corresponding to the adsorbed water. The amount of template removed was calculated to be above 95%.

We performed MAS NMR studies to determine the co-ordination of aluminium and silicon in the framework. ^{29}Si MAS NMR of the as-synthesized sample A showed two broad peaks at -101 and -110 ppm corresponding to the Q^3 and Q^4 species respectively. The intensity of the Q^3 species was greater than the Q^4 species indicating that the silanol groups had not condensed fully. On calcination, the relative intensity of the Q^4 species increased, showing that on calcination the silanol groups condense to form Si-O-Si species. ^{27}Al MAS NMR of the calcined sample A showed a large narrow peak at -7 ppm corresponding to octahedrally co-ordinated aluminium species and a very small, broad feature centered at 46 ppm due to tetrahedrally co-ordinated aluminium. On integrating these peaks, the areas under the peaks were found to be in the ratio of 1:0.2 of the octahedral to the tetrahedral species. It appears only 20% of the Al is present in the framework. Most of the Al is therefore present as Al_2O_3 in composite form with SiO_2. This is because of the limitation due to the pH and temperature employed in the preparation. We may therefore consider A, B, and C as composites of SiO_2 and Al_2O_3 with a small proportion of aluminosilicate. Even though the amount of aluminium in the framework is small, the composite materials that we have made have macroporous-mesoporous characteristics described earlier.

Nitrogen adsorption isotherms of the samples A, B and C are presented in Figure 2.4.12. These are typical Type IV isotherms characteristic of mesoporous materials. The isotherms exhibit little or no hysteresis, showing thereby that the pores may not be very ordered. The surface areas calculated by the BET method are in the range of 676-1038 m^2g^{-1} for the three samples. There is a decrease in the surface area with the increasing aluminum content, consistent with the observations of Janicke et al. [66], who observed that the surface areas decrease with a decrease in the Si/Al ratios.
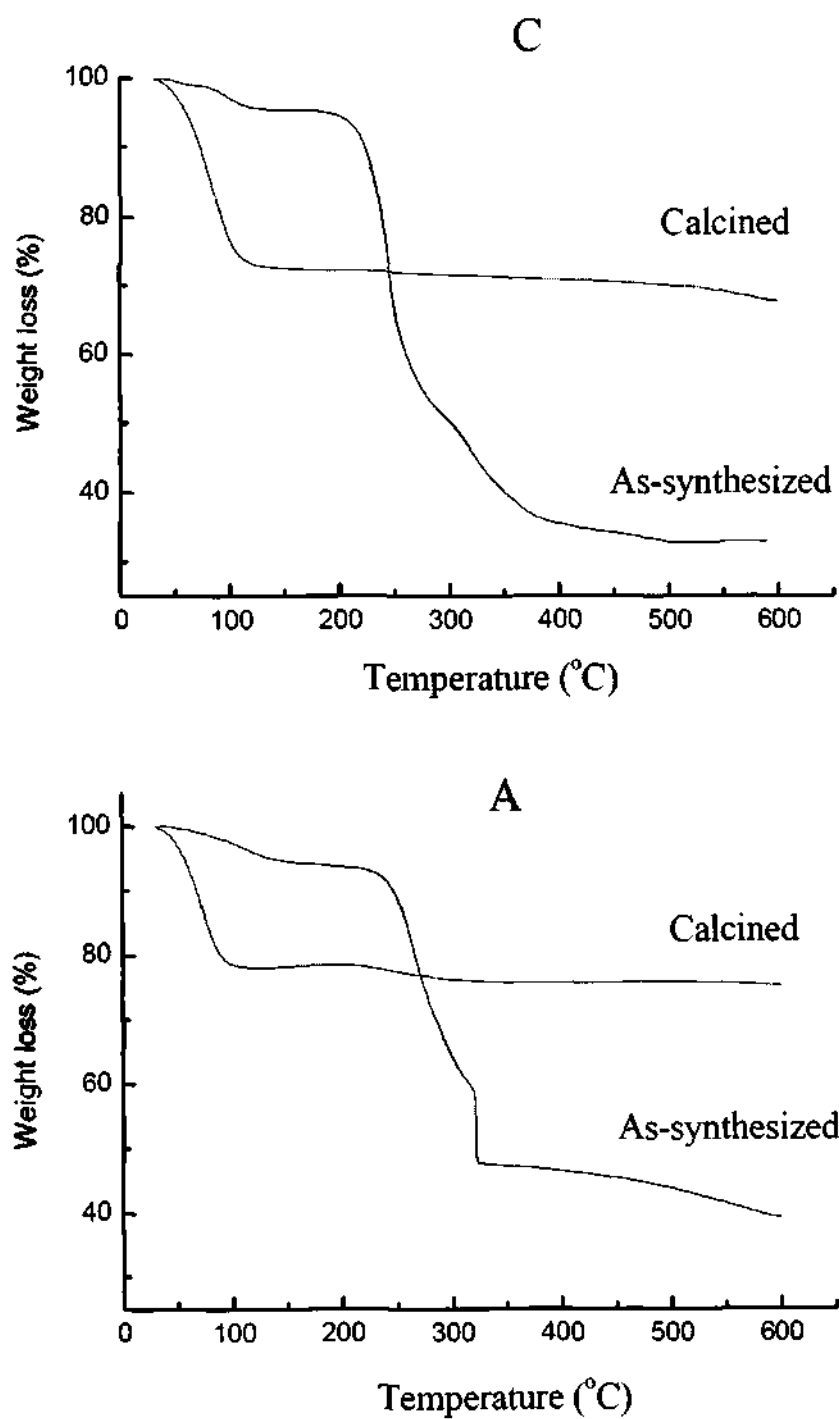
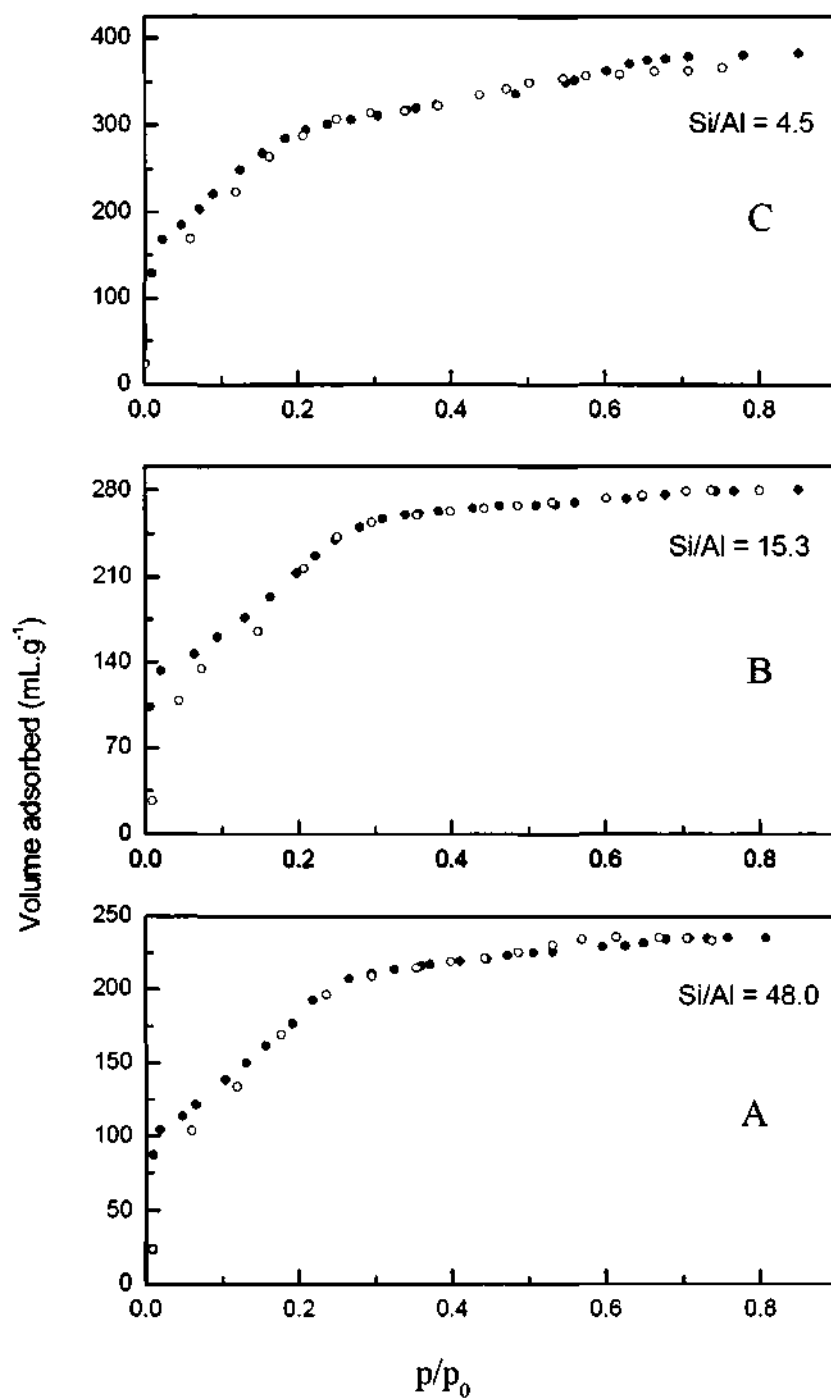Figure 2.4.11: TGA curves of the aluminosilicate samples A and C.

Figure 2.4.12: N_2 adsorption isotherms for A, B and C. Dark circles represent adsorption cycle and open circles represent desorption cycle.

Table 2.4.2: Properties of mesoporous aluminosilicate spheres

Sample	Si/Al[a]	d_{100}[b] (Å)	Particle diameter (μm)	Surface area (m^2g^{-1})	Pore diameter (Å)
A	14 (49)	35.8 (36.2)	0.35	970	18
B	24 (82)	36.8 (35.3)	0.40	510	15
C	40 (132)	34.8 (30.6)	0.30	700	19
D	Infinity	31.3 (29.6)	0.43	1100	20

[a]The values in parenthesis are obtained after taking into account the Al in the framework.

[b]d-value of the low angle reflection in the XRD pattern. The values in brackets were obtained after calcination at 473 K for 4h. After calcination at 473 K for 4h, the % template removed in the sample is 87–95%.

In summary, we have demonstrated the synthesis of macroporous aluminosilicates containing mesoporous walls. Though the amount of aluminium in the framework is small, the presence of macropores as well as mesopores makes these composites suitable as catalyst supports. The presence of macropores would aid in the diffusion of species to the active sites of the catalyst. [‡]

2.4.4 Submicron-sized mesoporous aluminosilicate spheres

Table 2.4.2 lists the compositions of the various samples prepared by us.

Calcination of the spherical aluminosilicates (A-C) and silica (D) at 200 °C for 4 h removed most of the surfactant template as will be demonstrated later. In Figure 2.4.13, we show the SEM images of the two aluminosilicate samples with Si/Al ratios of 14 and 40 (A and C respectively). The as-synthesized sample of A with a Si/Al ratio of 14 shows spherical morphology as revealed by the SEM images. There is little agglomeration of particles. The spherical morphology is retained even after calcination at 200 °C as can be seen from Figure 2.4.13(b). This was true of the other two aluminosilicate samples (B and C) as well, as demonstrated

[‡]A paper based on this study has appeared in Bull. Mater. Sci., (2001).
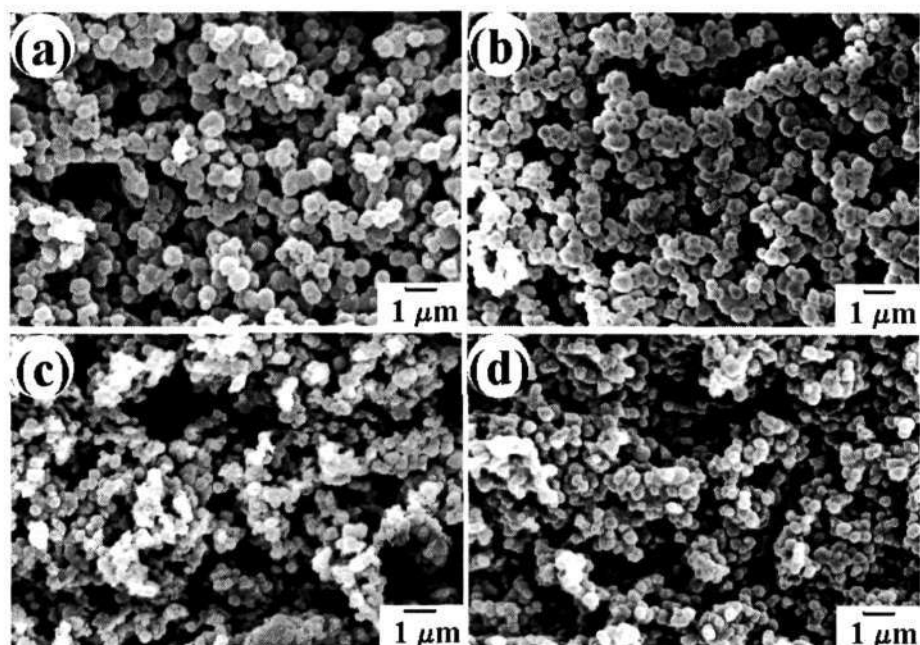
Figure 2.4.13: SEM images of aluminosilicate samples (a) A, as-synthesized, (b) A, calcined, (c) C, as-synthesized and (d) C, calcined.

in Figure 2.4.13(d) in the case of sample C. The particles show a narrow size distribution with average diameters of 0.35 and 0.30 μm in the case of A and C respectively. The particle sizes of all the samples are listed in Table 2.4.2.

Powder XRD patterns of the as-synthesized aluminosilicate and silica spheres are presented in Figure 2.4.14(a). The XRD patterns show a single feature at 2θ values of 2.46° , 2.38° , 2.54° and 2.81° respectively for A, B, C and D. The low-angle peaks are similar to those of hexagonal mesoporous solids. The powder XRD patterns of the samples after calcination at 200 °C for 4 hours exhibit single broad peaks at 2θ values of 2.44° , 2.5° , 2.88° and 2.98° respectively for A, B, C and D as revealed in Figure 2.4.14(b). The shift in the peak positions after calcination is due to the removal of the template. The presence of the low-angle reflection after calcination indicates that the mesophase is reasonably intact even after the removal of the template, although the intensity is considerably diminished in the case of the samples A and B. The spherical morphology is, however, retained as mentioned earlier. It appears that the Al-rich samples are more disordered.

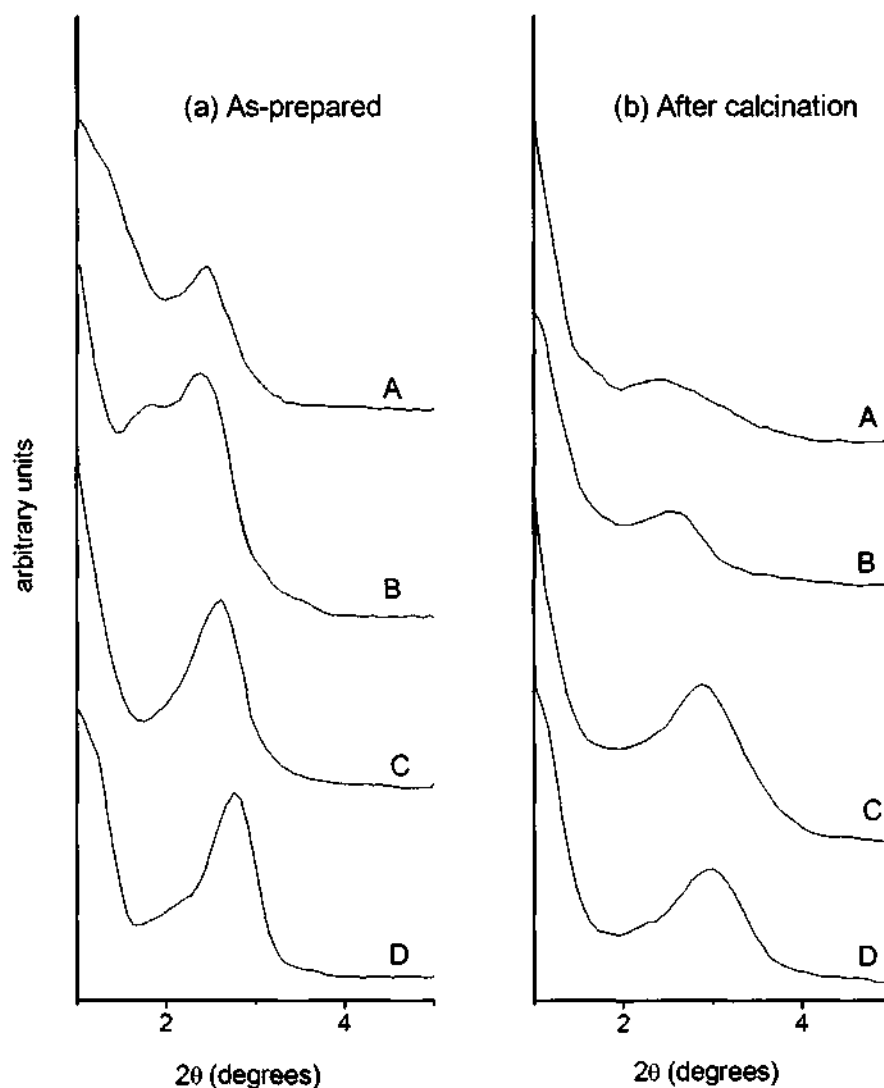TGA curves of the aluminosilicates A and C are shown in Figure 2.4.15. The

Figure 2.4.14: XRD patterns for the aluminosilicate (A, B and C) and pure silica (D) spheres.

as-synthesized samples show one major mass loss in the temperature range 200–300 °C . The mass loss is around 40%, where most of the template is removed. Thus, the sample calcined at 200 °C for 4h, only shows a mass loss (<20%) due to adsorbed water around 100 °C . The TGA curves confirm that most of the template is removed on calcination at 200 °C for 4h. We did not calcine the samples at higher temperatures in order to ensure that the morphology and surface area of the samples are not badly affected. The values of the percentage template removed on calcination 200 °C are listed in Table 2.4.2. The values are in the range of 87–95%.

^{29}Si and ^{27}Al MAS NMR spectra of sample C are shown in Figure 2.4.16. The ^{29}Si NMR spectrum of the as-synthesized sample shows two peaks at -100 and -108 ppm due to the Q^3 and Q^4 silicate species respectively. The intensity of the Q^3 species is greater than that of the Q^4 species indicating that the silanol groups have not condensed fully. On calcination, however, the relative intensity of the Q^4 species increases, showing that the silanol groups condense to form the Si-O-Si species. The ^{27}Al NMR spectrum of the as-synthesized samples show two peaks at 47 and 9.5 ppm. These are due to the tetrahedrally and octahedrally co-ordinated species respectively. After calcination, the relative proportion of the peaks corresponding to the tetrahedral and the octahedral species remains the same. Taking account of only the tetrahedral species to be a part of the framework, we estimate the percentage of aluminium in the framework to be around 30%. The Si/Al ratios calculated on this basis are listed in Table 2.4.2.

Nitrogen adsorption isotherms of samples A and C are presented in Figure 2.4.17. These are typical type IV adsorption isotherms. The BET surface areas of the samples calculated from N_2 adsorption are in the range 500–1000 m^2g^{-1} (Table 2.4.2). In general, the surface area of the aluminosilicate spheres is smaller than that of the pure silica spheres. The pore size distribution was calculated using the BJH method. In Figure 2.4.18, we show the plots of the pore size in case of samples A and C. The particles have a narrow pore size distribution, the values of the pore diameters being in the range of 15–20 Å (Table 2.4.2). The pore size of the aluminosilicate spheres is smaller than that of the pure silica spheres. We could estimate the diameter of the pores from the low-angle XRD peaks by making use of the relation $a_o=(2d_{100})/(3)^{1/2}$. The values of the diameter obtained are considerably larger than the pore diameter from adsorption measurements, since the former includes the wall thickness. We have estimated the wall thickness from the difference in the XRD (a_o) and adsorption pore diameters. These values are in the 7-13 Å range, the thickness increasing with Al content.

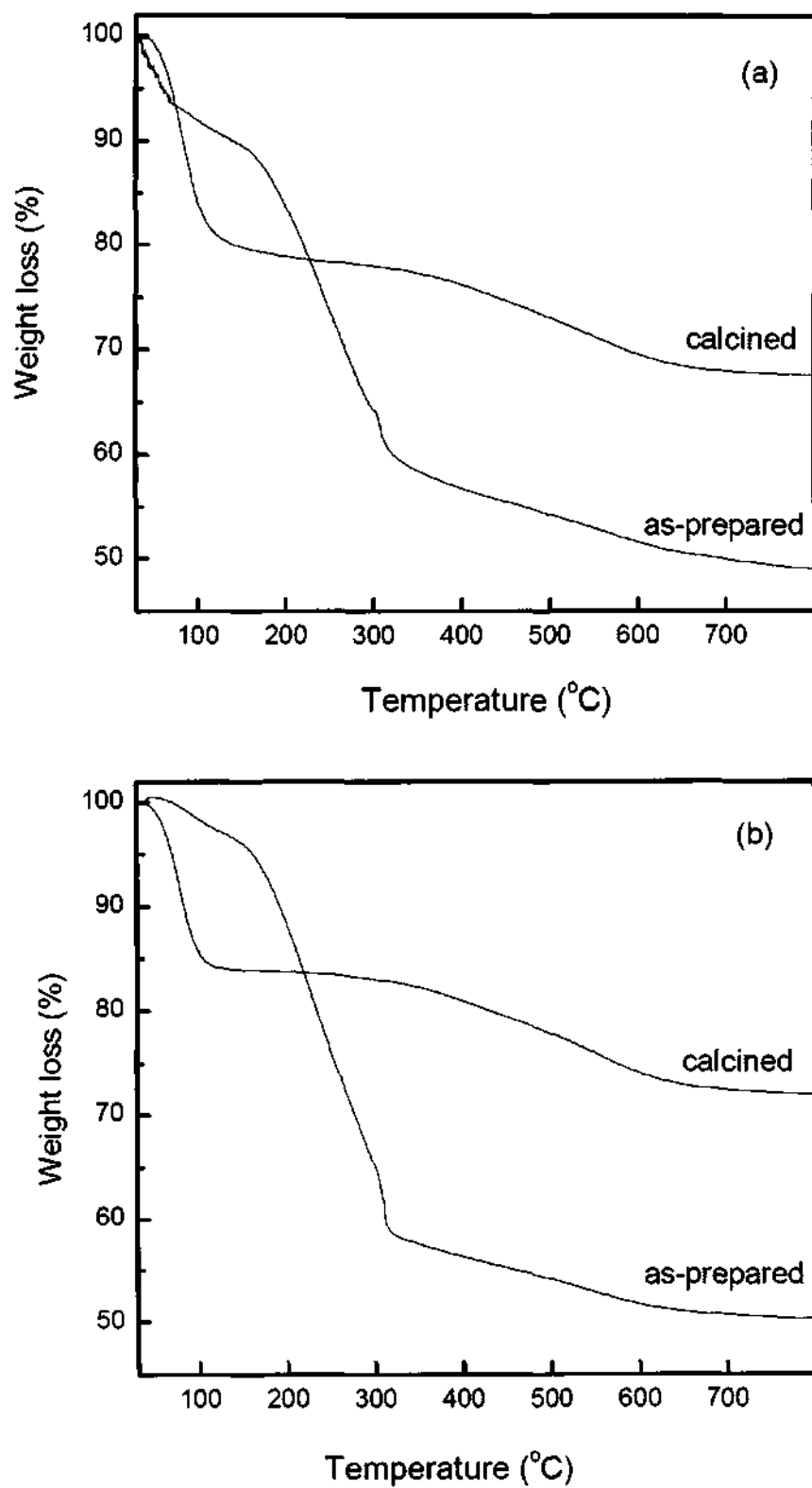In summary, the present work demonstrates that it is possible to prepare

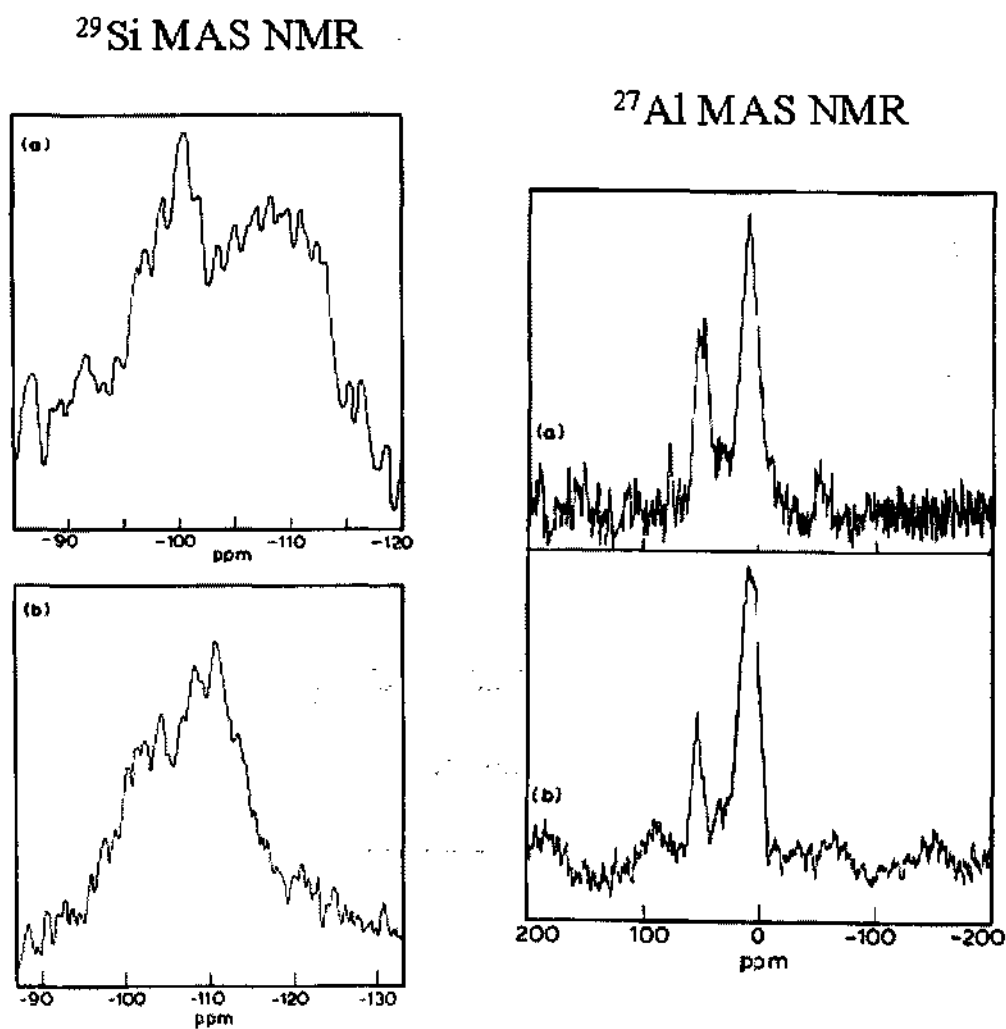Figure 2.4.15: TGA curves of the aluminosilicate samples A and C.

^{29}Si MAS NMR

^{27}Al MAS NMR

Figure 2.4.16: MAS NMR spectra of sample C (a) as-synthesized and (b) after calcination.

submicron-sized mesoporous spheres of aluminosilicates by using surfactant templating. [§]

187
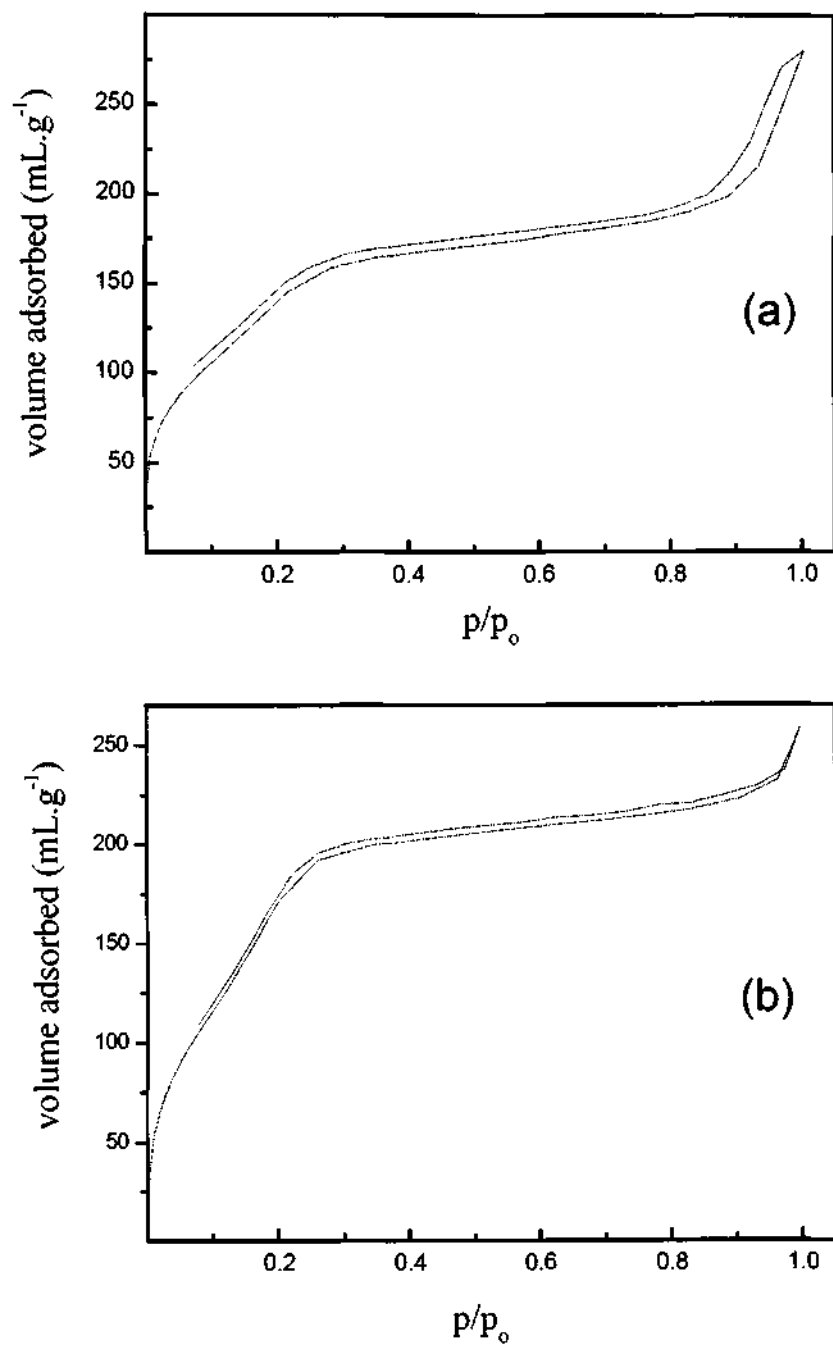
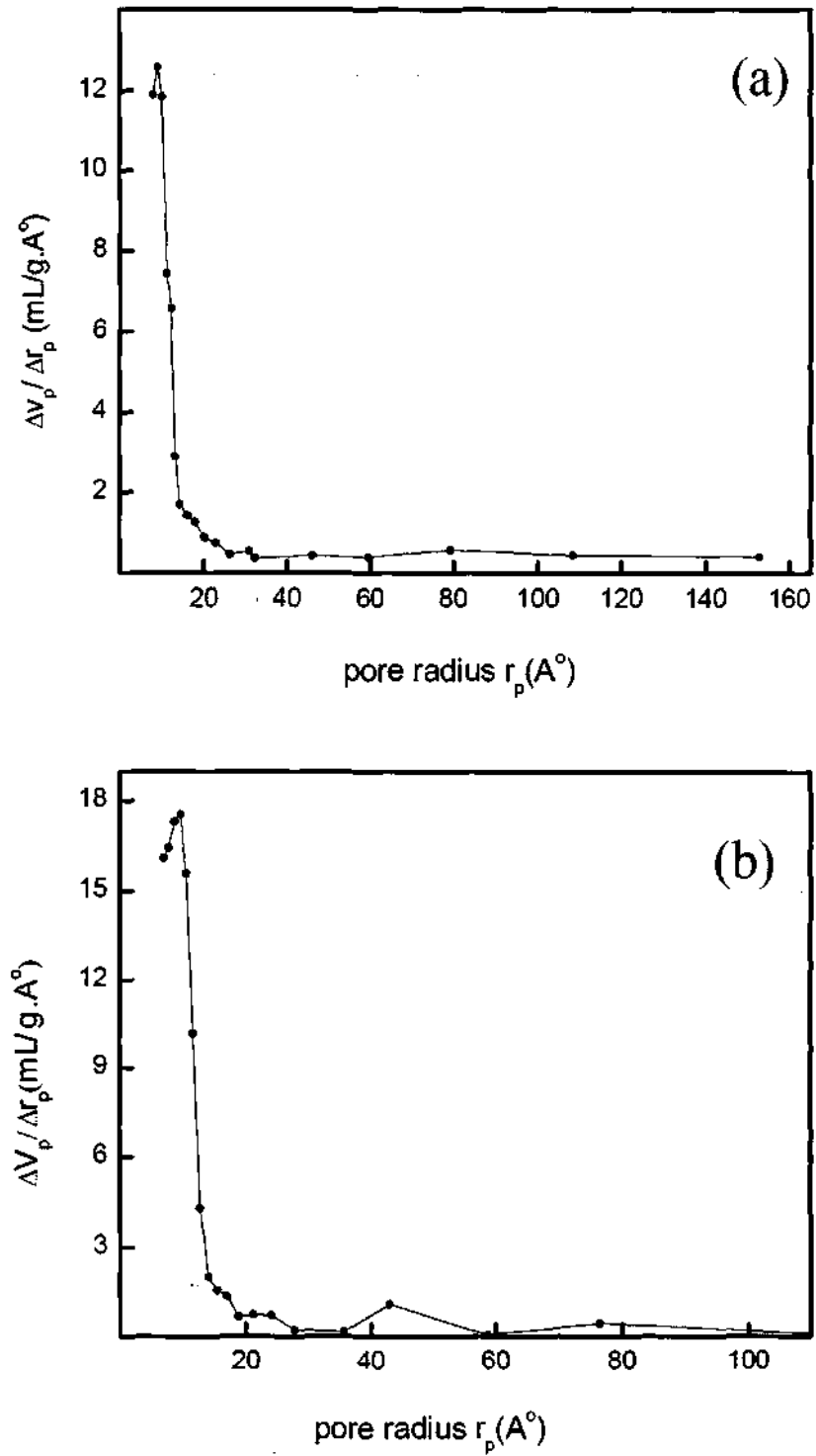**Figure 2.4.17:** Nitrogen adsorption isotherms for samples (a) A and (b) C.

Figure 2.4.18: Pore size distribution for the samples (a) A and (b) C.

2.5 Conclusions

In summary, we have been able to successfully obtain macroporous networks of various materials. Macroporous networks with interconnected pores of binary as well as ternary oxides have been obtained using PS spheres as the template. Since gels give good macroporous solids, the scope of this technique is immense. It appears that washing with a solvent is a better way of removing the template from these structures. The macroporous structures of ferroelectric materials may indeed find useful applications.

Macroporous carbons, using porous as well as non-porous silica spheres have been successfully prepared. These may be useful as photonic bandgap materials. The high surface area carbon networks obtained using mesoporous silica spheres seem useful candidates as catalyst supports.

Materials with dual porosity, namely macroporous aluminosilicate networks with mesoporous walls have been obtained using an ordered array of PMMA spheres as a template. The study opens up scope for preparing macroporous-mesoporous structures by doping other transition metals such as Ti, V, Cr, etc. into the silica framework. The only limiting factor is that the reaction has to be carried out at a temperature below which the template decomposes.

Submicron-sized mesoporous spheres of aluminosilicates have been synthesized by varying the amount of aluminium. Although the sample crystallinity is not as high as in the case of pure silica spheres prepared by a similar procedure, the high surface areas and desirable pore diameters of the aluminosilicate spheres make them good candidates for use in catalysis, sorption and related applications.

References

[1] R. R. Bhave, *Inorganic Membranes: Synthesis, Characteristics and Applications*, Van Nostrand Reinhold, New York, 1991.

[2] D. E. Fain, *MRS Bull.*, 1994, **19**, 40.

[3] V. S. Lin, K. Motesharei, K. S. Dancil, M. J. Sailor and M. R. Ghadiri, *Science*, 1997, **278**, 840.

[4] J. D. Joannopoulos, P. R. Villeneuve and S. Fan, *Nature*, 1997, **386**, 143.

[5] D. W. Schaefer, *MRS Bull.*, 1994, **19**, 14.

[6] M. E. Davis and R. F. Lobo, *Chem. Mater.*, 1992, **4**, 756.

[7] J. M. Thomas, *Angew. Chem. Int. Ed.*, 1999, **38**, 3588.

[8] A. K. Cheetham, G. Ferey and T. Louseau, *Angew. Chem. Int. Ed.*, 1999, **38**, 3588.

[9] C. T. Kresge, M. E. Leonowicz, W. J. Roth, J. C. Vartuli and J. S. Beck, *Nature*, 1992, **359**, 710.

[10] J. S. Beck, J. C. Vartuli, W. J. Roth, M. E. Leonowicz, C. T. Kresge, K. D. Schmidt, C. T. W. Chu, D. H. Olson, E. W. Sheppard, S. B. Mccullen, J. B. Higgins and J. L. Schlenker, *J. Am. Chem. Soc.*, 1992, **114**, 10834.

[11] P. Behrens, *Angew Chem Int. Ed. Engl.*, 1996, **35**, 515 and references therein.

[12] S. A. Bagshaw and T. J. Pinnavaia, *Angew. Chem. Int. Ed.*, 1996, **35**, 1102.

[13] D. M. Antionelli and Y. J. Ying, *Angew. Chem. Int. Ed.*, 1995, **34**, 2014.

[14] S. Ayyappan, N. Ulagappan and C. N. R. Rao, *J. Mater. Chem.*, 1996, **6**, 1737.

[15] N. Ulagappan and C. N. R. Rao, *Chem. Commun.*, 1996, 1685.

[16] S. Neeraj and C. N. R. Rao, *J. Mater. Chem.*, 1998, **8**, 1631.

[17] S. Neeraj, M. Eswaramoorthy and C. N. R. Rao, *Mat. Res. Bull.*, 1998, **38**, 1549.

[18] B. Chakraborty, A. C. Pullikottil, S. Das and B. Viswanathan, *Chem. Commun.*, 1997, 911.

[19] P. Feng, Y. Xia, J. Feng, X. Bu and G. D. Stucky, *Chem. Commun.*, 1997, 949.

[20] S. Schacht, Q. Hou, I. G. Voigtmartin, G. D. Stucky and F. Schüth, *Science*, 1996, **273**, 768.

[21] H. Yang, N. Coombs, I. Sokolov and G. A. Ozin, *Nature*, 1996, **381**, 589.

[22] H. Yang, V. Gregory, N. Coombs, S. Igor and G. A. Ozin, *J. Mater. Chem.*, 1998, **8**, 743.

[23] K. Schumacher, M. Grün and K. K. Unger, *Micro. and Meso. Mat.*, 1999, **27**, 201.

[24] C. Y. Chen, S. L. Burkett, H. X. Li and M. E. Davis, *Microporous Mat.*, 1993, **2**, 27.

[25] Q. Huo, D. I. Margolese, U. Ciesla, D. G. Demuth, P. Feng, T. E. Gier, P. Sieger, A. Firouzi, B. F. Chmelka, F. Schüth and G. D. Stucky, *Chem. Mater.*, 1994, **6**, 1176.

[26] R. C. Furneaux, W. R. Rigby and A. P. Davidson, *Nature*, 1989, **337**, 147.

[27] R. J. Tonucci, B. L. Justus, A. J. Campillo and C. E. Ford, *Science*, 1992, **258**, 783.

[28] M. Yoshida, M. Asano, T. Suwa, N. Reber, R. Spohr and R. Katakai, *Adv. Mater.*, 1997, **9**, 757.

[29] G. Widawski, M. Rawiso and B. Francois, *Nature*, 1994, **369**, 387.

[30] D. J. LeMay, R. W. Hopper, L. W. Hrubesh and R. W. Pekara, *MRS Bull.*, 1990, **15**, 19.

[31] B. Gates, Y. Yin and Y. Xia, *Chem. Mater.*, 1999, **11**, 2827.

[32] P. Jiang, K. S. Hwang, D. M. Mittleman, J. F. Bertone, and V. L. Colvin, *J. Am. Chem. Soc.*, 1999, **121**, 11629.

[33] A. A. Zakhidov, R. H. Baughman, Z. Iqbal, C. Cui, I, Khyarullin, S. O. Dantas, J. Marti and V. G. Rakihenko, *Science*, 1998, **282**, 897.

[34] J. E. G. J. Wijnhoven and William L. Vos, *Science*, 1998, **281**, 802.

[35] O. D. Velev, T. A. Jede, R. F. Lobo and A. M. Lenhoff, *Nature*, 1997, **389**, 447.

[36] B. T. Holland, C. F. Blanford, T. Do and A. Stein, *Chem. Mater.*, 1999, **11**, 795.

[37] A. Imhof and D. J. Pine, *Nature*, 1999, **389**, 948.

[38] H. Yan, C. F. Blanford, W. H. Smyrl and A. Stein, *Chem. Commun.*, 2000, 1477.

[39] E. Matijevic, *Acc. Chem. Res.*, 1981, **14**, 22.

[40] W. Stöber and A. Fink, *J. Colloid. Interface Sci.*, 1968, **26**, 62.

[41] R. K. Iler, *The Chemistry of Silica*, Wiley, New York, 1979.

[42] D. H. Everett, *Basic Principles of Colloid Science*, Royal Society of Chemistry, London, 1988.

[43] J. V. Sanders, *Nature*, 1964, **204**, 1151.

[44] H. Miguez, F. Meseguer, C. Lopez, A. Mifsud, J. S. Moya and L. Vazquez, *Langmuir*, 1997, **13**, 6009.

[45] D. H. Van Winkle and C. A. Murray, *Phy. Rev.*, 1986, **34**, 562.

[46] S. Park and Y. Xia, *Langmuir*, 1999, **15**, 266.

[47] H. Yan, C. F. Blanford, W. H. Smyrl and A. Stein, *Chem. Commun.*, 2000, 1477.

[48] A. Blanco, E. Chomski, S. Grabtchak, M. Ibisate, S. John, S. W. Leonard, C. Lopez, F. Meseguer, H. Miguez, J. P. Mondia, G. A. Ozin, O. Toader and H. M. Van Driel, *Nature*, 2000, **405**, 437.

[49] D. Joannopoulos, R. D. Meade and J. N. Winn, *Photonic Crystals*, Princeton University Press, Princeton, NJ, 1995.

[50] S. John, *Phy. Rev. Lett.*, 1987, **58**, 2486.

[51] E. Yablonovitch, *Phy. Rev. Lett.*, 1987, **58**, 2059.

[52] E. Yablonovitch, T. Gmitter and K. Leung, *Phy. Rev. Lett.*, 1991, **67**, 2295.

[53] J. F. Bertone, P. Jiang, K. S. Hwang, D. M. Mittleman and V. L. Colvin, *Phy. Rev. Lett.*, 1999, **83**, 300.

[54] B. Gates, S. H. Park and Y. Xia, *J. Lightwave Technol.*, 1999, **17**, 1956.

[55] B. T. Holland, C. F. Blanford and A. Stein, *Science*, 1998, **28**, 538.

[56] R. Ryoo, S. H. Joo and S. Jun, *J. Phy. Chem. B*, 1999, **103**, 7743.

[57] B. T. Holland, L. Abrams and A. Stein, *J. Am. Chem. Soc.*, 1999, **121**, 4309.

[58] K.K Unger, H. Giesche and J.N. Kinkel, *German Patent DE-3534*, 143.2, 1985.

[59] C. Kaiser and K. K. Unger, *German Patent DE-195*, 30031 A1, 1997.

[60] G. Büchel, K. K. Unger, A. Matsumoto and K. Tsutsumi, *Adv. Mater.*, 1998, **10**, 1036.

[61] Q. Huo, J. Feng, F. Schüth and G. D. Stucky, *Chem. Mater.*, 1997, **9**, 14.

[62] L. Qi, J. Ma, H. Cheng and Z. Zhao, *Chem. Mater.*, 1998, **10**, 1623.

[63] M. Grün, I. Lauer and K. K. Unger, *Adv. Mater.*, 1997, **9**, 254.

[64] S. D. Park, Y. H. Cho, W. W. Kim and S. J. Kim, *J. Solid State Chem.*, 1999, **146**, 230.

[65] J. F. Bryne and H. Marsh, *Porosity in Carbons*, ed. J. W. Partick, (Edward Arnold, London), 1995, Great Britain.

[66] M. T. Janicke, C. C. Landry, S. C. Christiansen, S. Birtalan, G. D. Stucky and B. F. Chmelka, *Chem. Mater.*, 1999, **11**, 1342.

620.116
Pol.